Characterization of the dielectric strength in vacuum of RF drivers for fusion neutral beam injectors

Coordinator: Prof. Paolo Bettini
Supervisors: Prof. Francesco Gnesotto, Dr. Elena Gaio

Ph.D. student: Alberto Maistrello

Padova, January 2018

JOINT Doctorate and NETWORK in Fusion Science and Engineering

Network Partners:
- Instituto Superior Técnico (IST) Lisboa, Portugal
- Universitá degli studi di Padova, Italy
- Ludwig Maximilians University Munich, Germany

In collaboration with:
- Consorzio RFX, Italy
- IPP Garching, Germany

Table of Contents

List of figures

List of tables

Acronyms and definitions

AGPS	Acceleration Grid Power Supply
BP	Bias Plate
BS	Beam Source
CODAS	COntrol and Data Acquisition System
DC	Driver Case
DUT	Device Under Test
ED	Electron Dump
EG	Extraction Grid
ELISE	Extraction from a Large Ion Source Experiment
EMS	ElectroMagnetic Shield
ESR	Equivalent Series Resistance
FS	Faraday Screen
Gap	minimum distance between electrodes of a pair
GG	Grounded Grid
GIP	Gas Injection and Pumping system
GRPS	Ground Related Power Supplies
HVD	High Voltage Deck
HVPTF	High Voltage Padova Test Facility
HVRFTF	High Voltage Radio Frequency Test Facility
IPP	Max-Planck-Institut für Plasmaphysik
ISEPS	Ion Source and Extraction Power Supplies
LD	Driver equivalent inductance
MAMuG	Multi Aperture Multi Grids
MITICA	Megavolt ITER Injector and Concept Advancement
n.a.	Not Available
NBI	Neutral Beam Injector
NBTF	Neutral Beam Test Facility
PCE	Planar Circular Electrodes
PDS	DUT composed of a Planar electrode, a Dielectric disk and a Spherical electrode
PG	Plasma Grid
Pn	Nominal power
PRIMA	Padua Research on ITER Megavolt Accelerator
PS	Power Supply
RD	Driver equivalent series resistance
RFX	Reverse Field eXperiment
RID	Residual Ion Dump
SE	Shielding Effectiveness
SEEA	Secondary Electron Emission Avalanche
SINGAP	Single aperture single gap

SPIDER   Source for the Production of Ions of Deuterium Extracted from an RF plasma
TBC   To be confirmed
TBD   To be defined
VD   Driver Voltage
Vn   Nominal Voltage
VV   Vacuum Vessel

Abstract

The two projects of the ITER Neutral Beam Test Facility (NBTF) [1] in Padova are MITICA, the full scale prototype of the heating Neutral Beam Injector (NBI) and SPIDER, the full-size negative ion source of the NBI. Both include a Radio Frequency (RF) Ion Source where plasma is produced by the inductive coupling with coils wound around vacuum chambers called drivers. Each coil is fed at 1 MHz up to a power of 100 kW, which corresponds to a voltage of about 12 kV rms, with nominal plasma parameters.

The ion source design derives from the R&D carried out at the Max-Planck-Institut für Plasmaphysik (IPP) during the past years [2] [3], with additional improvements to achieve the desired performance in long duration pulses (up to 1 h) on a full ITER-size device, in a vacuum environment and with optimized beamlet optics [4] [5] [6] [7].

Among the various issues connected to the fulfillment of the requirements for ITER, special attention should be paid to those related to the voltage hold off in vacuum of the beam source components; not only for the acceleration grids subjected to very high dc voltage but also for the RF circuits of the ion source and in particular the RF drivers.

Some concern in this regard has arisen since several years ago and in fact, also in IPP, the last two test facilities RADI and ELISE have been realized in such a way the areas containing the drivers that can be put under vacuum (lower than 10^{-4} mbar [8]) to better simulate the ITER operating condition [9] [10]. For the ITER heating NBI the concern is deeper, since the rear side of the ion source, where the drivers are located, is not directly pumped and the pressure at the moment is only estimated by means of simulation. The voltage hold off of the driver coils is essential to operate the ion source at full power and thus to reach the full performance.

The topic of the PhD activity belongs to the framework of the RF R&D task of the NBTF workprogramme, and was focused on the development of a simple, accessible and flexible device called "High Voltage Radio Frequency Test Facility" (HVRFTF) to characterize the dielectric strength in vacuum of the RF drivers of SPIDER and MITICA ion sources and to effectively address the issues related to their voltage hold off when subjected to radiofrequency E-fields at low pressure.

The experimental arrangement worked out to reproduce the desired operating conditions consists in a vacuum vessel capable to host different types of driver mock-ups, called Devices Under Test (DUT) in the thesis, a gas injection and pumping system to supply the desired gas species up to the test pressure and a RF circuit designed to produce the high voltage.

The HVRFTF allows the variation of the quantities which influence the voltage hold off, such as the pressure, geometry and materials of the DUTs, in order to perform parametric analyses.

The idea behind this flexibility is not only to execute tests relevant for the verification of the driver insulation design, but also to quantify operative margins and to identify possible improvements or hints for the design of new drivers.

Part of the thesis work was the identification of the requirements of the HVRFTF, consisting in analyses carried out to identify the driver operating conditions relevant to the voltage hold off (geometry, materials and pressure).

I estimated the voltage applied to the RF coil of the drivers at full power, and the related E-field, with the identification of the most stressed area.

I conceived several driver mockups to be tested within the HVRFTF: the best configuration worked out for the scope is based on a couple of electrodes (one plane and one spherical) with a dielectric material in between. However, the studies highlighted that a single sphere diameter is not sufficiently accurate to cover the entire gap range of interest; in particular the sphere diameter has to be increased as far as the gap increases. Nevertheless, three of these DUTs allow reproducing the desired E-field trend.

I decided to test at first a planar circular electrode pair with Rogowski profile, even if it is not suitable as driver mock-up, since it is a test configuration widely treated in the literature and it generates the most reproducible experimental regime, thus allowing a validation of the basic test arrangement.

As far as the RF high voltage generation is concerned, the feasibility study led me to work out a resonant circuit matched through a reversed L-type network, supplied by a low voltage amplifier. As a first design approach, the load of the circuit to be matched to the low voltage amplifier output impedance could be the DUT, but the practical implementation of this concept in the design of the RF circuit is complex due to the variation of the DUT impedance during the test campaign and the effect of stray impedances of circuit components. From the electrical point of view, the DUT represents a capacitance with an equivalent series resistance; both depend on the geometry of the electrode pair, on the gap between the two electrodes, and on the properties of the dielectric material in between.

The selected approach was to design a suitable inductor to be connected in parallel to the DUT and to use their equivalent impedance as the load impedance to be matched. With this method and once verified that the real part of the load impedance is lower than the real part of the amplifier output impedance, the matching network can be composed by capacitors only, that were designed to assure the matching condition at the nominal frequency. Variable capacitors can be adopted in order to modify the resonance frequency and maintain the matching condition in the whole frequency range of interest.

Another important phase of my design work was the development of the electrical model of the components to be used, in order to verify and quantify the real power requirements as a function of the voltage to be reached with the HVRFTF.

The realization of the HVRFTF was completed in 2016 with a first RF circuit composed of fixed capacitors and supplied by a RF amplifier rated for a limited power, both already available at Consorzio RFX. The test campaigns on a stainless steel planar circular electrode pair proved the correct operation of the overall plant and allowed obtaining the first experimental results, including in particular the achievement of a voltage up to 10 kV rms. Moreover the tests gave the opportunity to improve the knowledge in this field, discover unexpected issues relevant to specific operating conditions and investigate on possible solutions. Another important fallout of the tests was the validation of the models developed during the design phase, essential for the continuation of the R&D work.

The thesis is organized as follows:
- Chapter 1 presents the thesis background: starting from the identification of the need for sustainable energy sources, nuclear fusion is identified as a suitable contributor. ITER is the next step toward nuclear fusion and PRIMA, the ITER neutral beam test facility is one of the main supporting R&D projects, with its two experiments SPIDER and MITICA. The experiments are introduced with a brief description.

- Chapter 2 enters more in details in one of the components of SPIDER and MITICA beam sources which is considered critical as far as the voltage holding is concerned: the driver. Its operating conditions are described in this chapter.
- Chapter 3 presents the High Voltage Radio Frequency Test Facility (HVRFTF), a small, accessible and flexible testbed to experimentally characterize the dielectric strength in vacuum of the driver.
- Chapter 4 reports on the analyses carried out for the definition of the devices to be tested within the HVTFTF, relevant mockups of the drivers.
- Chapter 5 reports on the studies and the design of the circuit used in the HVRFTF for the generation of high voltage at radiofrequency.
- Chapter 6 presents the experimental results obtained so far with the HVRFTF.
- Conclusions.

Sommario

La stazione sperimentale Neutral Beam Test Facility (NBTF) dell'esperimento ITER [1], in costruzione a Padova presso il Consorzio RFX, ospita due esperimenti: MITICA, il prototipo in scala 1:1 del sistema di iniezione di particelle neutre per il riscaldamento del plasma in ITER (NBI) e SPIDER, il prototipo della sorgente ionica impiegata dal NBI.

Entrambi i progetti impiegano 8 "driver" a radiofrequenza (RF), ovvero sorgenti di plasma, per la generazione di ioni; ciascun driver è costituito da una camera da vuoto cilindrica su cui è avvolta una bobina che si accoppia induttivamente con il plasma.

Ogni bobina è alimentata da un'onda sinusoidale di tensione a 1 MHz, con una potenza fino a 100 kW alla quale corrisponde, con i parametri nominali di plasma, un valore efficace di tensione tra i terminali di circa 12 kV rms.

La soluzione progettuale della sorgente ionica deriva dall'attività di ricerca e sviluppo effettuata al Max-Planck-Institut für Plasmaphysik (IPP) negli scorsi anni [2] [3], ulteriormente studiata e sviluppata per raggiungere le prestazioni desiderate per ITER ed in particolare quelle legate al miglioramento dell'ottica del fascio e al funzionamento in vuoto con impulsi di durata prolungata fino ad un'ora [4] [5] [6] [7].

Tra le varie problematiche legate al soddisfacimento dei requisiti per ITER, particolare attenzione è rivolta alla tenuta della tensione in vuoto dei componenti e dei circuiti dell'iniettore, non solo per le griglie di accelerazione che sono soggette a tensioni dc fino a 1 MV, ma anche per i circuiti RF della sorgente e in particolare dei driver.

La consapevolezza della criticità di questo aspetto è maturata negli ultimi anni e di conseguenza è cresciuta l'attenzione al problema: anche i più recenti esperimenti presso IPP (RADI ed ELISE) prevedono la possibilità di mettere in vuoto (con pressione inferiore a 10^{-4} mbar [8]) il volume contenente i driver, per poter simulare meglio le condizioni operative di ITER [9] [10].

Per l'iniettore di neutri di ITER la preoccupazione è anche maggiore, poiché non vi potrà essere controllo diretto della pressione nella regione dei driver; al momento essa è stimata per mezzo di simulazioni numeriche. La tenuta di tensione della bobina dei driver è essenziale al fine di operare la sorgente alla piena potenza, requisito per il raggiungimento delle piene prestazioni dell'iniettore.

L'argomento del dottorato ricade nell'ambito della task "RF R&D" del programma di lavoro della NBTF ed è focalizzato allo sviluppo di un esperimento semplice, accessibile e flessibile chiamato "High Voltage RadioFrequency Test Facility" (HVRFTF), indirizzato allo studio delle problematiche legate alla tenuta di tensione in vuoto dei driver RF delle sorgenti di SPIDER e MITICA.

Il setup sperimentale di HVRFTF consente di ricreare le condizioni operative delle bobine dei driver e consiste in una camera da vuoto capace di ospitare diversi dispositivi in prova, chiamati Device Under Test (DUT) nella tesi, un sistema di pompaggio e immissione gas in grado di regolare la pressione e la specie di gas all'interno della camera e di un circuito a radiofrequenza in grado di produrre l'alta tensione.

HVRFTF permette la variazione delle grandezze fisiche che influenzano la tenuta di tensione, come ad esempio la pressione, la geometria e i materiali dei dispositivi in prova, al fine di poter effettuare analisi parametriche.

Questa flessibilità permette non solo di verificare il progetto dell'isolamento dei driver, ma anche di quantificarne i margini operativi e di identificare possibili miglioramenti o spunti per il progetto elettrico di nuovi driver.

Parte del lavoro di tesi è stato dedicato alla definizione dei requisiti di HVRFTF, a partire dallo studio della sorgente e delle condizioni operative dei driver che ne influenzano la tenuta di tensione.

Ho stimato la tensione applicata alla bobina RF dei driver a piena potenza e ricavato la relativa mappa di campo elettrico, che mi ha consentito di identificare la regione maggiormente stressata.

In seguito ho concepito diversi possibili modelli di driver da testare all'interno di HVRFTF: il migliore è basato su una coppia di elettrodi (un piano e una sfera) tra i quali è interposto un disco di materiale dielettrico. Tre sfere di diametro direttamente proporzionale al gap sono necessarie per riprodurre l'andamento del campo elettrico nell'intero intervallo di variazione del gap. Per le prime prove con HVRFTF ho deciso di testare degli elettrodi piani circolari con profilo di Rogowski, anche se non rappresentano un buon modello del driver, al fine di validare il setup sperimentale. L'uso di questo tipo di elettrodi è infatti ampiamente diffuso e documentato in letteratura, perché essi sono in grado di generare condizioni sperimentali riproducibili.

Per la generazione di alta tensione a radiofrequenza, tra possibili soluzioni ho adottato un circuito risonante adattato all'impedenza di uscita dell'amplificatore che lo alimenta, attraverso una rete a L rovesciato. In prima istanza, il carico da adattare potrebbe essere l'impedenza del DUT, che dal punto di vista elettrico risulta essere una capacità in serie ad una resistenza, entrambe dipendenti dalla geometria degli elettrodi, dalla loro distanza (gap) e dalle proprietà del materiale dielettrico interposto tra loro.

Tuttavia l'implementazione pratica di quest'approccio è complessa: l'impedenza del DUT durante la campagna sperimentale è variabile; inoltre i componenti del circuito di adattamento (almeno uno dei quali dovrebbe essere un induttore), introducono impedenze parassite non note, a loro volta da compensare.

Una soluzione ragionevole che ho infine elaborato consiste nel collegare in parallelo al DUT un induttore di caratteristiche opportune e di utilizzare l'impedenza equivalente come carico da adattare. Con questo approccio, una volta dimensionati i componenti in modo tale che la parte reale dell'impedenza di carico sia minore della parte reale dell'impedenza di uscita dell'amplificatore, la rete di adattamento a L rovesciato risulta composta da soli condensatori, le cui capacità si ricavano imponendo il vincolo di adattamento di impedenza e la frequenza di risonanza. L'utilizzo di condensatori aventi capacità regolabile permette infine di modificare la frequenza di risonanza in modo da poter operare in tutto l'intervallo di frequenze di interesse.

Per il progetto del circuito RF ho sviluppato modelli elettrici dettagliati per ogni componente impiegato, al fine di verificare e quantificare i requisiti di potenza attiva in funzione della tensione da raggiungere con HVRFTF.

La realizzazione preliminare di HVRFTF è stata completata nel 2016 con un circuito a radiofrequenza composto da condensatori aventi capacità fissa, alimentato da un amplificatore RF di potenza limitata; sia i condensatori che l'amplificatore erano già disponibili al Consorzio RFX.

La campagna di prove sperimentali con la coppia di elettrodi piani in acciaio ha dimostrato il corretto funzionamento dell'impianto sperimentale con il raggiungimento della tensione di 10 kV, ha consentito di ottenere i primi risultati sperimentali e di validare i modelli sviluppati durante la fase di progetto.

Il lavoro presentato in questa tesi è così organizzato:

- Capitolo 1: si presenta il contesto tematico all'interno del quale è stata sviluppata la tesi; a partire dal problema energetico, una possibile soluzione è un mix di fonti sostenibili tra cui la fusione nucleare. Si presentano in seguito ITER, il prossimo passo verso la fusione e "ITER Neutral Beam Test Facility", uno dei principali progetti a supporto di ITER con i suoi due esperimenti: SPIDER e MITICA.
- Capitolo 2: si descrive in dettaglio uno dei componenti delle sorgenti ioniche di SPIDER e MITICA, ritenuto critico dal punto di vista della tenuta di tensione: il driver. Si presentano le analisi eseguite per derivare le sue condizioni operative.
- Capitolo 3: si presenta l'esperimento "High Voltage Radio Frequency Test Facility" (HVRFTF), un piccolo impianto per la caratterizzazione sperimentale della rigidità dielettrica in vuoto dei driver.
- Capitolo 4: si presentano le analisi effettuate per la definizione dei dispositivi da testare con HVRFTF, con l'obiettivo che essi possano riprodurre condizioni operative simili a quelle del driver per lo studio della problematica di interesse .
- Capitolo 5: si riportano gli studi per la generazione di alta tensione a radiofrequenza e il progetto del circuito risonante adottato per HVRFTF.
- Capitolo 6: si presentano i risultati ottenuti con HVRFTF.
- Conclusioni.

Resumo

Os dois projetos do ITER Neutral Beam Test Facility (NBTF) [1] em Padova são MITICA, o protótipo de escala completa do Injetivador de feixe neutro de aquecimento (NBI) e SPIDER, a fonte de íons negativos de tamanho completo do NBI. Ambos incluem uma fonte de íon de radiofreqüência (RF), onde o plasma é produzido pelo acoplamento indutivo com bobinas enroladas em câmaras de vácuo chamadas condutores. Cada bobina é alimentada a 1 MHz até uma potência de 100 kW, o que corresponde a uma tensão de cerca de 12 kV, com parâmetros nominais de plasma.

O design da fonte de íons deriva da R&D realizada no Max-Planck-Institut für Plasmaphysik (IPP) nos últimos anos [2] [3], com melhorias adicionais para alcançar o desempenho desejado em pulsos de longa duração (até 1 h) em um dispositivo de tamanho ITER completo, em um ambiente de vácuo e com óptica de feixe otimizada [4] [5] [6] [7].

Entre os vários problemas relacionados ao cumprimento dos requisitos para o ITER, há também aqueles relacionados à tensão de retenção no vácuo dos componentes da fonte do feixe; não apenas para as grelhas de aceleração sujeitas a uma tensão de corrente muito alta, mas também para os circuitos RF da fonte de íons e, em particular, os drivers de RF.

Algumas preocupações neste sentido surgiram desde há vários anos e, de fato, também no IPP, as duas últimas instalações de teste RADI e ELISE foram realizadas com as áreas que contêm os drivers que podem ser colocados sob vácuo (inferior a 10^{-4} mbar [8]) para melhor simular a condição de operação do ITER [9] [10]. Para o aquecimento do ITER NBI, a preocupação é maior, uma vez que o lado traseiro da fonte de iões não é diretamente bombeado e a pressão no momento só é estimada por meio da simulação. A força de retenção das bobinas do condutor é essencial para operar a fonte de íons em plena potência e, assim, atingir os desempenhos completos.

O tema do PhD é o quadro da tarefa de R & D de RF do programa de trabalho do NBTF e foi focado no desenvolvimento de uma instalação de teste simples, acessível e flexível chamada "Instalação de Teste de Radiofrequência de Alta Tensão" (HVRFTF) para caracterizar o dielétrico força ao vácuo dos drivers de RF das fontes de íons SPIDER e MITICA e efetivamente lida com os problemas relacionados à sua tensão, quando são submetidos a campos E de radiofreqüência a baixa pressão.

O HVRFTF permite a variação das quantidades que influenciam a retenção de tensão, como a pressão, geometria e materiais dos dispositivos em teste, para realizar análises paramétricas.

A idéia por trás dessa flexibilidade não é apenas executar testes relevantes para a verificação do projeto de isolação do driver, mas também quantificar as margens operacionais e identificar possíveis melhorias ou sugestões para o projeto de novos drivers.

Parte do trabalho de tese foi a identificação dos requisitos da HVRFTF, consistindo em análises realizadas para identificar as condições de operação dos condutores relevantes para a retenção de tensão (geometria, materiais, impedância e pressão).

Eu avaliei a tensão aplicada à bobina de RF dos drivers em plena potência, e o campo E relacionado, com a identificação da área mais estressada.

Eu concebi várias modelos de driver para serem testados no HVRFTF: a melhor configuração estabelecida para o escopo é baseada em um par de eletrodos (um plano e um esférico) com um material dielétrico no meio. No entanto, os estudos evidenciaram que um único diâmetro da esfera não

é suficientemente preciso para cobrir toda a distância de interesse; em particular, o diâmetro da esfera deve ser aumentado até o intervalo aumentar. No entanto, três dessas DUTs podem permitir reproduzir a tendência de campo E desejada.

Decidi testar em primeiro lugar um par de eléctrodos circular plano com perfil de Rogowski, que é uma configuração de teste amplamente tratada na literatura. Eu selecionei mesmo que não seja bom como maquete do driver, pois gera o regime experimental mais reprodutível, permitindo assim uma validação da avaliação básica do teste.

No que diz respeito à geração de alta tensão de RF, o estudo de viabilidade me levou a descobrir um circuito ressonante combinado através de uma rede de tipo L invertida, fornecida por um amplificador de baixa tensão. Como uma primeira abordagem de design, a carga do circuito a ser compatível com a impedância de saída do amplificador de baixa tensão pode ser o DUT, mas a implementação prática deste conceito no projeto do circuito RF é complexa devido à variação da impedância DUT durante a campanha de teste e o efeito das impedâncias dispersas dos componentes do circuito. Do ponto de vista elétrico, o DUT representa uma capacitância com uma resistência série equivalente; ambos dependem da geometria do par de eletrodos, do espaço entre os dois eletrodos e das propriedades do material dielétrico no meio.

A abordagem selecionada foi projetar um indutor adequado para ser conectado em paralelo ao DUT e usar sua impedância equivalente à medida que a impedância de carga seja combinada. Com este método e uma vez verificado que a parte real da impedância de carga é menor do que a parte real da impedância de saída do amplificador, a rede de correspondência pode ser composta somente por capacitores, que foram projetados para garantir a condição de correspondência na freqüência nominal. Os capacitores variáveis podem ser avaliados para manter a correspondência em toda a faixa de freqüência de interesse.

Outra fase importante do trabalho de design foi o desenvolvimento do modelo elétrico dos componentes a serem utilizados, a fim de verificar e quantificar os requisitos de energia real em função da tensão a ser alcançada com HVRFTF.

A realização do HVRFTF foi concluída em 2016 com uma primeira rede de correspondência composta por condensadores fixos, já disponível no Consorzio RFX. As campanhas de teste em um par de eletrodos circulares planar de aço inoxidável provaram o funcionamento correto da planta geral e a realização de uma tensão de até 10 kV rms com o amplificador de RF disponível e permitiu a validação dos modelos desenvolvidos durante a fase de projeto.

A tese está organizada da seguinte forma:

- O Capítulo 1 apresenta os antecedentes da tese: a partir da identificação da necessidade de fontes de energia sustentáveis, a fusão nuclear é identificada como uma resposta adequada. O ITER é o próximo passo em direção à fusão nuclear e PRIMA, a instalação de teste de feixe neutro do ITER é um dos principais projetos de P & D de apoio, com seus dois experimentos SPIDER e MITICA. Os experimentos são apresentados com uma breve descrição.
- O Capítulo 2 envia mais detalhes em um dos componentes das fontes do feixe SPIDER e MITICA que é considerado crítico para a tensão: o driver. Suas condições operacionais são descritas neste capítulo.
- O Capítulo 3 apresenta a Instalação de Teste de Radiofrequência de Alta Tensão (HVRFTF), uma pequena experiência para caracterizar experimentalmente a força dielétrica no vácuo do motorista.
- O Capítulo 4 relata as análises realizadas para a definição dos dispositivos a serem testados dentro do HVTFTF, substituto relevante dos drivers.

- O Capítulo 5 relata os estudos e o projeto do circuito utilizado na HVRFTF para geração de alta tensão em radiofreqüência.
- O Capítulo 6 apresenta os resultados experimentais obtidos até agora com HVRFTF.
- Conclusões.

1 Thesis background

1.1 Energy demand and the thermonuclear fusion option

The world energy demand is expected to rise in the next years due to the rise of world population and to the increased per-capita energy consumption in the developing countries. In fact demographic projections of United Nations foresee the increment of the world population (two out of three predictions, as shown in Figure 1-1 a) in the next decades, concentrated mostly in underdeveloped and developing countries.

There is a strong correlation between a country development and its energy consumption for the majority of the world countries, as can be seen in Figure 1-1 b, where the per capita energy consumption (PCEC) is expressed in kg of oil equivalent per year and HDI is the Human Development Index. The HDI is a composite index measuring average achievements in three basic dimensions of human development: a long and healthy life, knowledge and a decent standard of living [11].

a)

b)
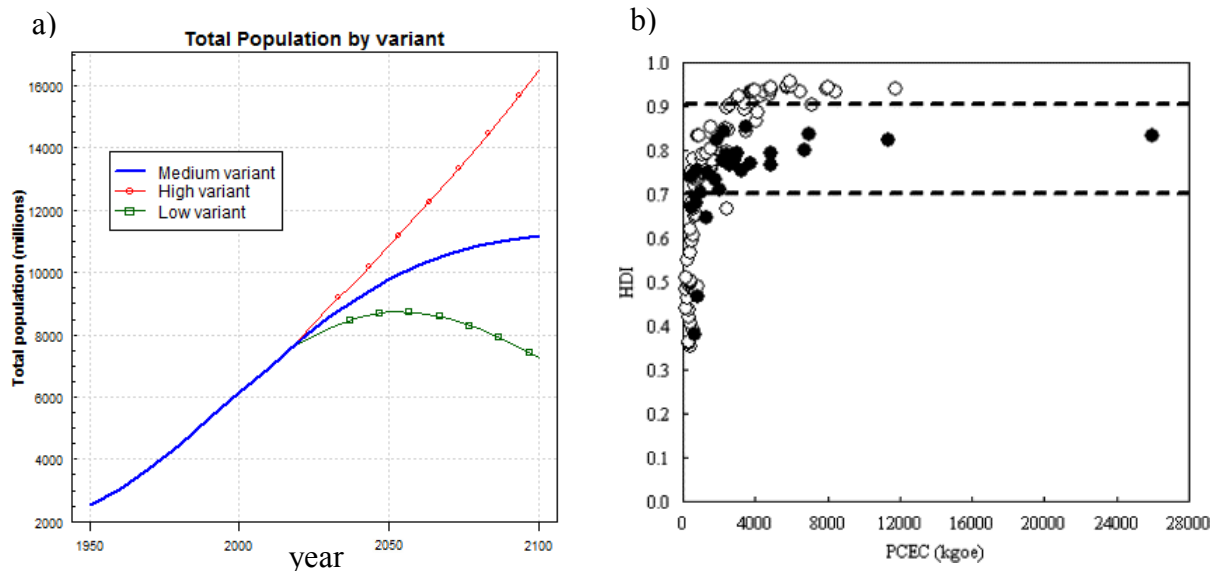
Figure 1-1 – a) UN world population prediction [12], b) Human Development Index as a function of the energy consumption [13] (The black circles corresponds to countries that are major net energy exporters and many members of the Former Soviet Union.)

Within the HDI curve three regions can be identified:

- a steeply rising region for HDI < 0.7, representing energy poor nations, for which there is a very strong dependence of HDI on the energy access.

- a region located near the derivative change for HDI in between 0.7 – 0.9, representing nations that overcame the threshold between poor development and high development;
- a saturated region for HDI > 0.9, representing very advanced developed nations residing in the industrialized world, and indicating that little improvement in human welfare can be achieved with larger energy consumption.

Favorable HDI in between 0.7 and 0.9 can be reached with moderate energy consumption (less than 4000 kgoe per person per year).

It is reasonable to allow nations seeking an improvement of their HDI, and, since among these nations there are highly populated countries like China, India, Brazil, …, an increment in the world energy demand is foreseen by most projections [14].

One of the goals of the 2030 agenda for sustainable development [15] adopted on 25th September 2015 by Heads of State and Government at a special UN summit is to "Ensure access to affordable, reliable, sustainable and modern energy for all", which is linked to many of the other development goals.

Fossil fuels presently satisfy more than 80% [16] of the primary energy demand, but their impact on the environment through greenhouse gas emission is clearly not sustainable. In the near future, fossil fuels can be replaced only by a mix of options that includes renewable energy, nuclear fission and carbon capture and sequestration. In a long term perspective, the development of alternative primary energy sources is crucial for mankind, and one possibility is represented by nuclear fusion energy.

In 2012 EFDA (European Fusion Development Agreement) presented to the European Commission a technical roadmap [17] to nuclear fusion energy for electricity production by 2050, with up to 30% of electricity production by 2100.

In the roadmap ITER is the key facility and its success remains the most important overarching objective, but the realization of fusion as sustainable and secure energy supply requires the development of an intermediate demonstrative device called DEMO, the first demonstration Fusion Power Plant.

1.2 ITER

ITER is a scientific experiment which aims at demonstrating the scientific and technical feasibility of fusion energy for peaceful purposes [18], currently under construction in St. Paul lez Durance in the south of France, Europe.

According to the official ITER schedule, the first plasma will be achieved in 2025.

Figure 1-2 – Aerial view of ITER construction site, 2017

It is the world's largest and most advanced tokamak, the first magnetic confinement device producing a net surplus of energy from nuclear fusion, built thanks to a major international collaboration

involving China, the European Union (plus Switzerland), India, Japan, the Russian Federation, South Korea and the United States.

In summary, the main technical objectives and performance specifications require ITER [19]:

- to achieve extended burn in inductively-driven deuterium-tritium plasma operation with $Q \geq 10$ (Q is the ratio of fusion power to additional power injected into the plasma), with an inductive burn duration of more than 400 s;
- to demonstrate steady state operation using non-inductive current drive with $Q \geq 5$;

In terms of engineering performance and testing, the design should:

- demonstrate availability and integration of essential fusion technologies;
- test components for a future reactor;
- test tritium breeding concepts with 14 MeV-neutrons, power load on the first wall $\geq$ 0.5 MW/m^2 and fluence $\geq$ 0.3 MW/m^2.

The main parameters of ITER are listed in Table 1-1.

Table 1-1 – ITER main parameters [19]

Total Fusion Power	500 MW (700 MW)
Q — fusion power/additional heating power	≥ 10
Average 14MeV neutron wall loading	0.57 MW/m^2 (0.8 MW/m^2)
Plasma inductive burn time	≥ 400 s
Plasma major radius (R)	6.2 m
Plasma minor radius (a)	2.0 m
Plasma current (I p)	15 MA (17 MA)
Vertical elongation @95% flux surface/separatrix (κ 95)	1.70/1.85
Triangularity @95% flux surface/separatrix (δ 95)	0.33/0.49
Safety factor @95% flux surface (q 95)	3.0
Toroidal field @ 6.2 m radius (B T)	5.3 T
Plasma volume	837 m^3
Plasma surface	678 m^2
Total additional heating/current drive power	73 MW

A cross section of ITER tokamak is shown in Figure 1-3.
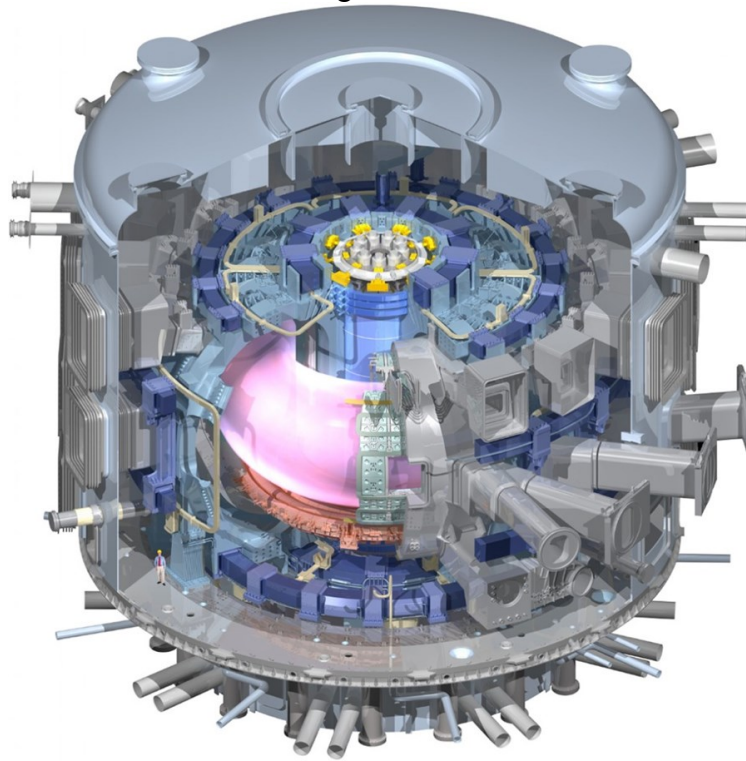
Figure 1-3 – ITER cut view [20]

In ITER additional heating and current drive systems are required to achieve the foreseen operative scenarios.
The injected power of each ITER additional heating system is listed in Table 1-2.

Table 1-2 – ITER Heating and Current Drive Systems [19]

	Neutral Beam (1 MeV)	Electron Cyclotron (170 GHz)	Ion Cyclotron (~50 MHz)	Lower Hybrid (5 GHz)
Power injected per unit equatorial port [MW]	16.5	20	20	20
Number of units for the first phase	2	1	1	0
Total power for the first phase [MW]	33	20	20	0
(Optional) Number of units for subsequent phases	3	1	1	1
(Optional) Total power for subsequent phases [MW]	~50	20	20	20

A total plasma heating power up to 110 MW can be available in subsequent operation phases, with the installation of an additional Neutral Beam Injector and a Lower Hybrid Current Drive system.

1.3 ITER Heating Neutral Beam Injector

A neutral beam can enter the magnetic confined plasma of a tokamak and transfer its energy to plasma electrons and ions; in fact energetic neutral particles travel along straight lines, unaffected by magnetic field.

A conceptual scheme of a neutral beam injector is shown in Figure 1-4:

- ions are created within an ion source;
- the ions are extracted from the ion source and accelerated by means of electrostatic grids, creating an ion beam;
- the ion beam is neutralized by collision with neutral ions within a neutraliser;
- the neutralization efficiency is not 100%, therefore the neutraliser output is composed of a neutral beam and a residual ion beam;
- the residual ion beam is deflected and dumped within a residual ion dump, so that at the output there is only a neutral beam which can enter the tokamak plasma.
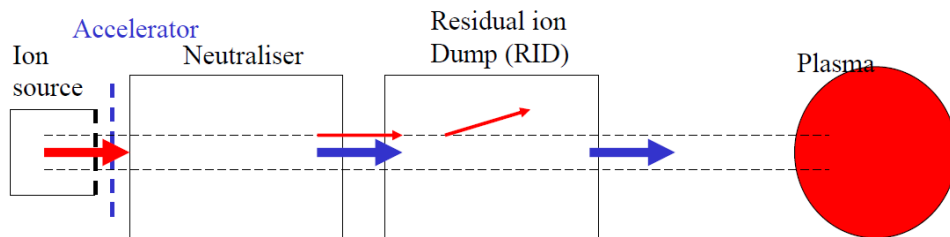
Figure 1-4 – Conceptual scheme of a neutral beam injector
(red arrows represent ion beams, blue arrows represent neutral beams)

The neutralization is a fundamental process which happens through charge exchanges, however there is also a re-ionization process as competing reaction which takes place, as follows:

Charge exchange

$$D^+ + D_2 \rightarrow D + D_2^+$$

Ion beam   gas   Desired neutral beam   Slow ion

(1)

Ionization

$$D + D_2 \rightarrow D^+ + D_2 + e$$

Neutral beam   gas   Unwanted Ion beam   gas   Released electron

(2)
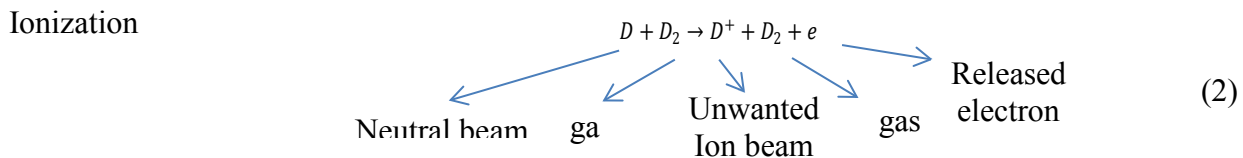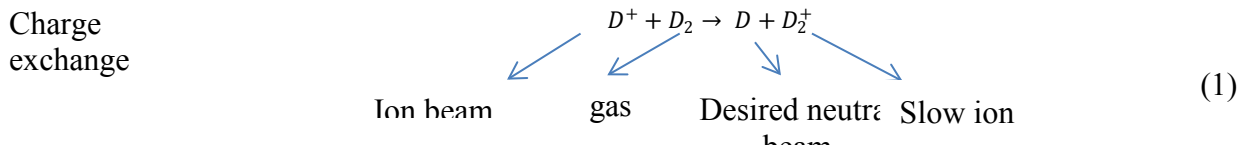
Figure 1-5 shows the deuterium and hydrogen neutralization efficiency as a function of the beam energy. The Deuterium neutralization efficiency is higher than 80% for both positive and negative ions for beam energies lower than 20 keV; for higher energies the neutralization efficiency drops steeply for positive ions and it is only 20% at 200 keV, while it reduces to about 60% for negative ions up to 1 MeV.
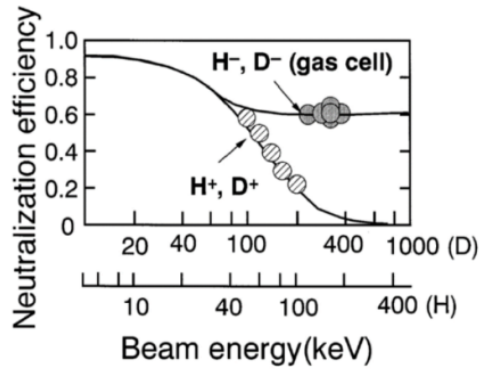
Figure 1-5 - Neutralization efficiency for Deuterium and Hydrogen as a function of the beam energy [21]

The generation of negative ions is very difficult, and the system efficiency is reduced due to the presence of electrons extracted from the beam source together with the negative ions. Therefore positive ion beams are preferred for low energy beams, while for high energy beams negative ion sources are mandatory, as in ITER.

The negative ion generation can be a volume production (attachment of low energy electrons to excited molecules), or a surface production (attachment of surface electrons to incident atoms). In the latter case, Cs injection greatly increases negative ion yield, as it decreases surface material work function. The survival length for negative ions is a few centimeters due to volume processes (mutual neutralization in collision with positive ions, electron detachment in collision with electrons, associative detachment in collision with atoms); therefore the formation of negative ions must be close to the extraction system.

As far as the ion source is concerned, two technologies are commonly used for NBI: arc chamber ion sources and RF driven ion sources.

With the arc chamber ion sources (Figure 1-6 a) the plasma is produced by arc discharges between tungsten filaments (cathode) and the source body (anode). Permanent magnets are necessary on the source body to create a suitable magnetic field for plasma confinement and to increase the overall efficiency of the source. A plasma grid confines the plasma and allows the surface generation of negative ions.

There is a large experience all over the world with this kind of ion sources, since they are commonly implemented in the NBI of tokamaks. The main drawback of this technology is the presence of the filaments, which require periodic maintenance and consequently frequent shutdowns.

With the RF ion sources (Figure 1-6 b) the plasma is generated within so called RF drivers by inductive coupling with external coils, and expands within a vacuum chamber toward the plasma grid where negative ions are produced by surface process, as with arc ion sources.

The RF ion sources were developed mainly at Max-Planck-Institut für Plasmaphysik (IPP) on several testbeds: Batman, Manitu, RADI, ELISE [2] [10].

The main advantages of RF ion sources are that they do not require frequent shutdowns for filament maintenance and that the Cs consumption is lower than with arc ion source; the drawback is that there is less experience with fusion devices.

For ITER the required negative ion current density to be extracted from the plasma source ranges from 290 A/m^2 in D$_2$ (D$^-$) to 350 A/m^2 in H$_2$ (H$^-$) and these values should be obtained at the lowest admissible neutral pressure in the plasma source volume, nominally at 0.3 Pa.

Both arc and RF ion sources can potentially fulfill these requirements, but the lower Cs consumption and the simpler maintenance led to select the RF ion source for ITER.
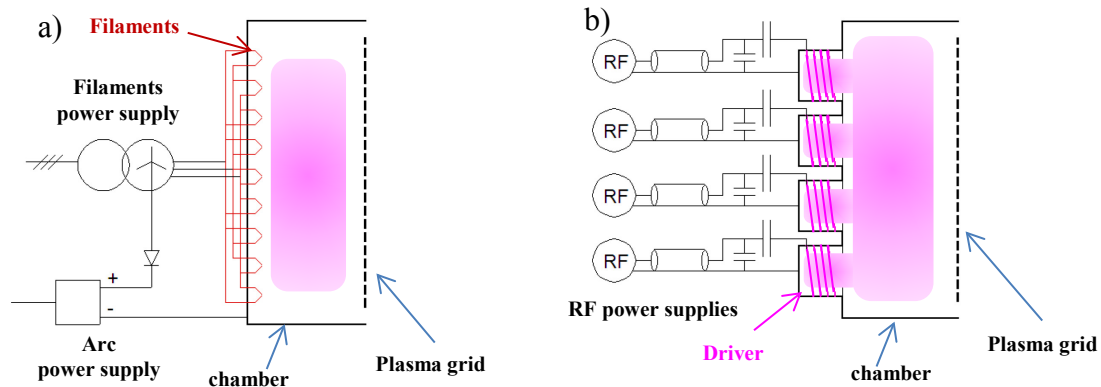
Figure 1-6 – Conceptual scheme of arc ion sources a) and RF ion sources b), with power supplies sketched

The extraction of ions and their acceleration is performed by electrostatic grids. Two configurations have been developed for high energy beams: MAMuG (Multi Aperture - MUlti Grids) and SINGAP (SINGle Aperture - SINgle GAP), as shown in Figure 1-7 with reference to ITER requirements.

With MAMuG the ions are accelerated with intermediate steps of potential applied to intermediate multi aperture grids, each having the same aperture pattern of the plasma and extraction grids. This requires power supplies at intermediate voltage to feed each grid and the related water cooling.

With SINGAP [22] the ions are pre-accelerated with energies of about 60 keV, and then accelerated to the final energy in one single step towards the final grid at ground potential (GG) characterized by large apertures. SINGAP reduces the gas load in the accelerator and greatly simplifies the design of accelerator and power supplies; the main technical issue is related to the vacuum voltage hold off of the large gap which is subjected to almost the total accelerating voltage [23].

For ITER NBI the MAMuG configuration has been selected.
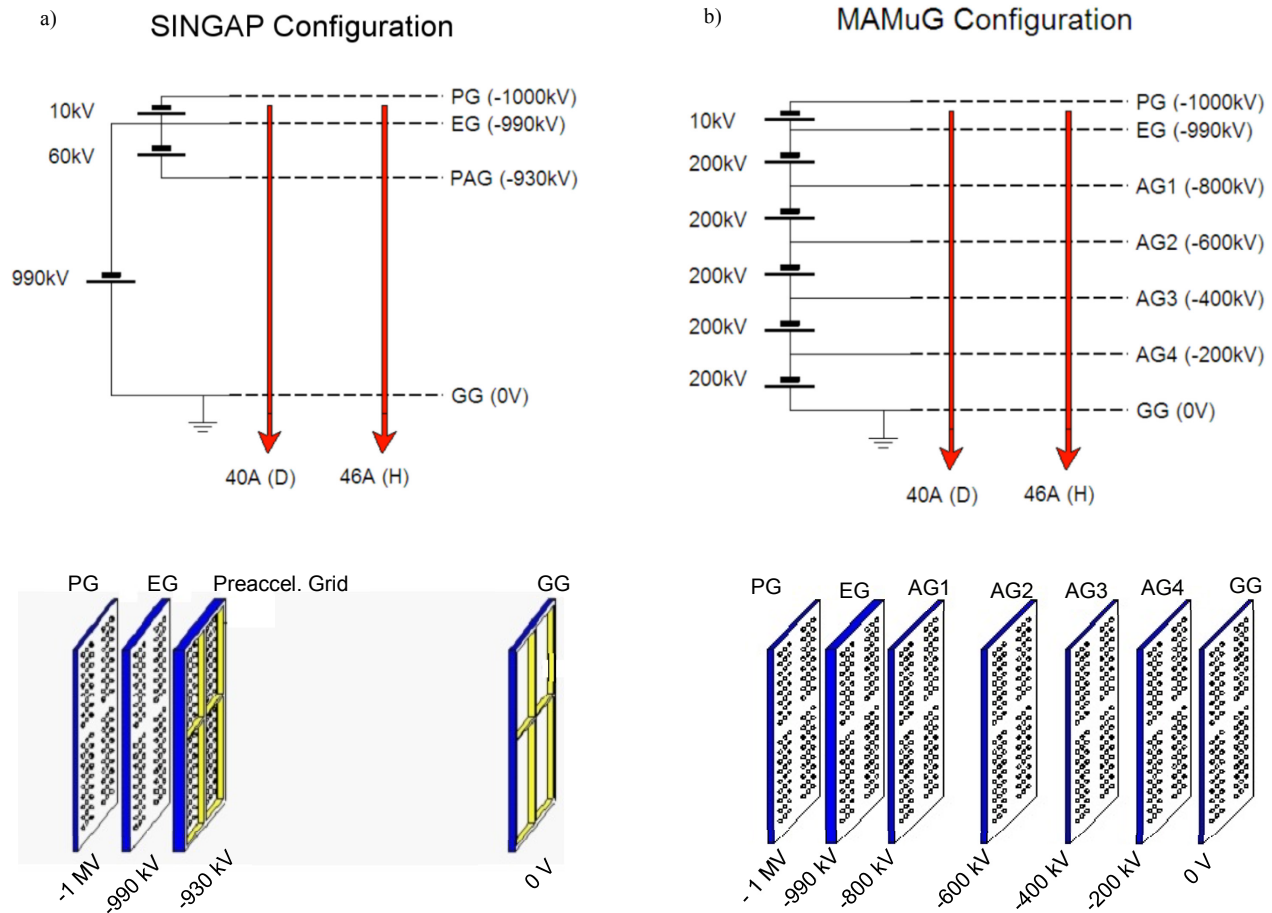
Figure 1-7 - SINGAP a) and MAMuG b) configruations

The Residual Ion Dump filters the charged beam that exits from the neutralizer by deflection with electrostatic field (or magnetic field) and dump on actively cooled panels. The electrostatic field was selected for ITER NBI.

At the exit of the residual ion dump the desired neutral beam can enter the plasma or can be dumped on a V shaped calorimeter during commissioning and conditioning phases. The calorimeter can have diagnostic purpose (for instance if arrays of thermocouples are installed on it) to verify the correct beam generation and its uniformity.

In ITER, the heating Neutral Beam Injectors are required to achieve "H-mode" operation, characterized by higher temperature and density, thus by improved plasma confinement, and also for current drive purposes.

Figure 1-8 a) shows a cut view of the ITER heating NBI placed in the tokamak building, while b) shows the space allocated for the ITER NBI system (one diagnostic NBI, and three heating NBIs).

The performance requested from the heating NBI is listed in Table 1-3.
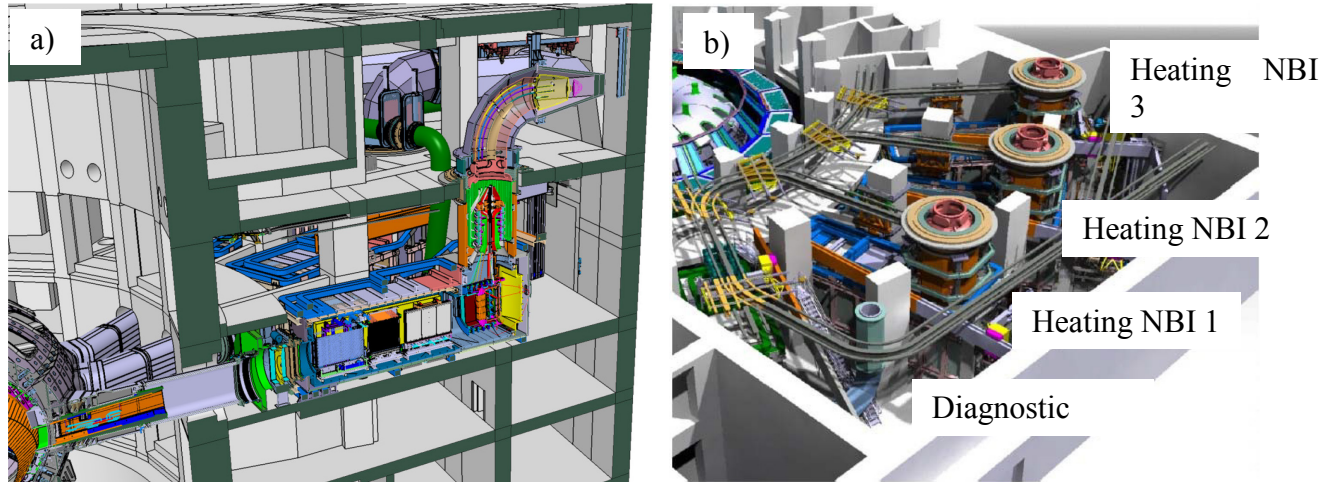
Figure 1-8 – a) Cut view of the ITER Tokamak building with focus on one Heating NBI, b) 3D view of ITER Tokamak building where up to three heating NBIs and one diagnostic beam can be hosted

Table 1-3 – Performance requested to each ITER Heating NBI

Parameter	Unit	H operation	D operation
Beam energy	[keV]	870	1000
Acceleration current	[A]	49	40
Maximum beam source pressure	[Pa]	0.3	0.3
Beamlet divergence	[mrad]	≤ 7	≤ 7
Beam on time	[s]	3600	3600
Co-extracted electron fraction (e^-/H^- or e^-/D^-)	[-]	< 0.5	< 1

This performance presents several challenging issues on physics and technology, and was never met before all together in a single device.

"All the development of the ITER accelerators and ion sources has been carried out on relatively low powered test stands, particularly so for the accelerator. Thus there remains the need to finalize the development of the full size, full power ion source, and accelerator at full pulse length. Experience gained from the development of the high power positive ion based systems has made very clear the advantages of having a full power test bed, the main one being that all development can be carried out independently of the final user, the tokamak plasma." [24]

1.4 PRIMA: the ITER Neutral Beam Test Facility

In the framework of the strategy for the development of the Heating Neutral Beam Injectors for ITER, it has been decided to build in Padova the ITER Neutral Beam Test Facility called PRIMA (Padua Research on ITER Megavolt Accelerator) [25] [26] [27] [1], including two experimental devices: SPIDER, the full size ion source with low voltage extraction and MITICA the full size NB injector at full beam acceleration voltage (1 MV), both designed for the full pulse length foreseen in ITER.

These two different devices will separately address the main scientific and technological issues of the 16.5 MW NBI for ITER.

The SPIDER test bed aims at the mitigation of the manufacturing and operational issues in advance of the operation on a full scale ITER heating Neutral Beam Injector.

MITICA is the prototype of the full ITER injector and has the following aims: to study beam uniformity and high voltage holding; to investigate beam particle trajectories in the accelerator and in the neutralization process; to test beam line components at full power; to prove correct operation of the residual ion dump; to fully test the power supplies; to verify the overall reliability of the NBI.

Figure 1-9 – Panoramic picture of PRIMA, Euganean hills background
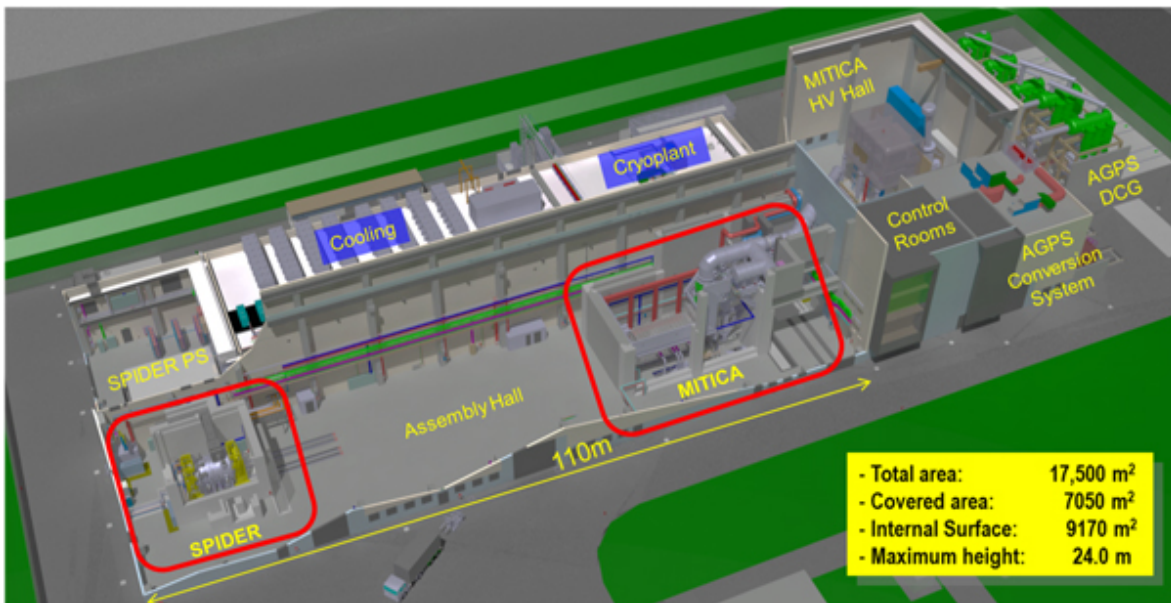
Figure 1-10 – 3D cut view of PRIMA

1.4.1 SPIDER

SPIDER will address the ITER performance requirements to the ion source in terms of current density and uniformity, limitation of the electron/ion ratio and stationary operation at full current with high reliability and constant performance for the whole operating time up to 1 h.

The performance requested to SPIDER is listed in Table 1-4.

Table 1-4 – Performance requested to SPIDER

Parameter	Unit	H operation	D operation
Beam energy	[keV]	100	100
Maximum beam source pressure	[Pa]	0.3	0.3
Uniformity	%	±10	±10
Extracted current density	[A/m^2]	> 350	> 290
Beam on time	[s]	3600	3600
Co-extracted electron fraction (e$^-$/H$^-$ or e$^-$/D$^-$)	[-]	< 0.5	< 1

SPIDER is basically composed of a beam source placed within a vacuum vessel (VV) 6 m long and 4 m in diameter (see Figure 1-12), together with a water-cooled beam dump rated for the maximum power and pulse duration, and a high-spatial-resolution air cooled calorimeter called STRIKE, rated for a pulse of few seconds, as shown in Figure 1-11.

The VV is evacuated to the nominal pressure of 10 mPa by means of 3 turbomolecular pumps and 8 cryopumps with nominal H$_2$ pumping speed of 9 m^3/s and 96 m^3/s respectively [28].
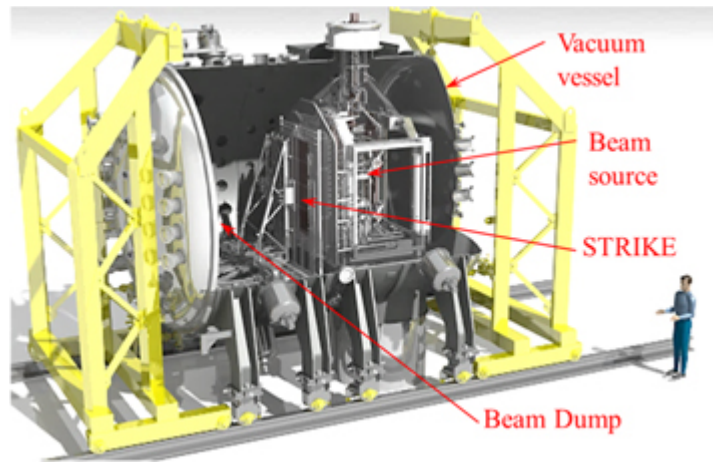
Figure 1-11 - SPIDER 3D cut view
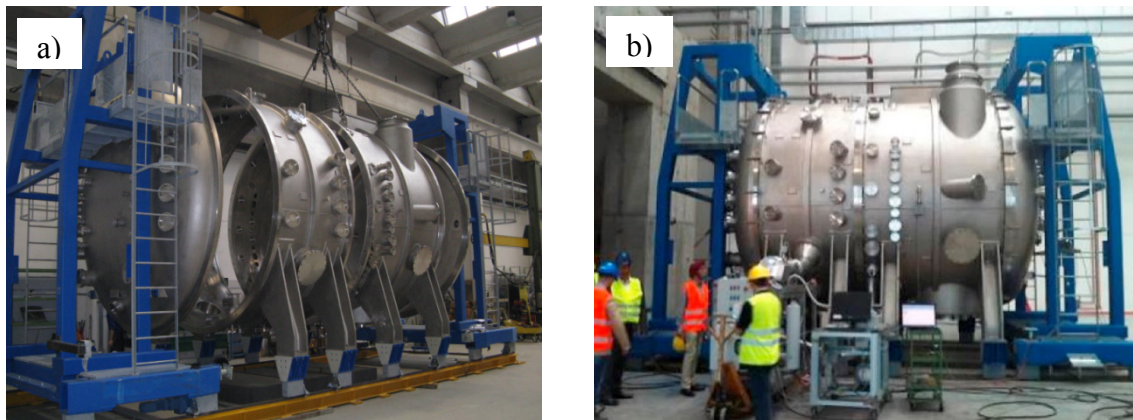
Figure 1-12 – Pictures of SPIDER vacuum vessel: a) at manufacturer premises, b) during vacuum test at PRIMA [27]

The beam source (BS) is the most complex component of SPIDER. The RF plasma source and the extraction grids are topologically identical to those to be provided for MITICA and ITER heating Neutral Beams.

The BS is composed of a Plasma Source and an ion extraction system, forming the so-called ion source, and of ion acceleration grids. The plasma source is composed of eight cylindrical chambers called driver cases, where gas (hydrogen or deuterium) is injected at a pressure of about 0.3 Pa and ionized by RF inductive coupling with coils wound around the driver cases, for a total power of 800 kW at 1 MHz. The drivers will be further described in section 2, where the operating conditions which influence the voltage hold off will be detailed.

The impedances of the RF coils are matched to the output impedance of the RF voltage sources (see paragraph 1.4.1.1) by means of a matching network, whose components are installed on the rear side of the plasma source [29] [30].

The plasma generated within the drivers diffuses into an expansion chamber towards the plasma grid (PG), where the majority of negative ions are generated by surface process; in fact, three caesium ovens inject fresh caesium into the expansion chamber in order to lower the work function so that the impinging hydrogen/deuterium atoms are more easily turned into negative ions.

A bias plate (BP) is mounted 10 mm upstream of the PG, with the function to absorb electrons and thus optimize the electric field distribution to improve the performance.

The voltage applied between the PG and the extraction grid (EG) extracts the negatively charged beams from the plasma through the apertures located in the PG.

The negative ions are subjected to a further acceleration voltage, between the EG and the grounded grid (GG), so that they are accelerated to full energy.

An electron dump (ED), just outside the accelerator, made of several vertical pipes suitably arranged, is designed to absorb most of the power associated to electrons exiting the accelerator.

Figure 1-13 shows an exploded view of SPIDER beam source, where all the described components are highlighted.
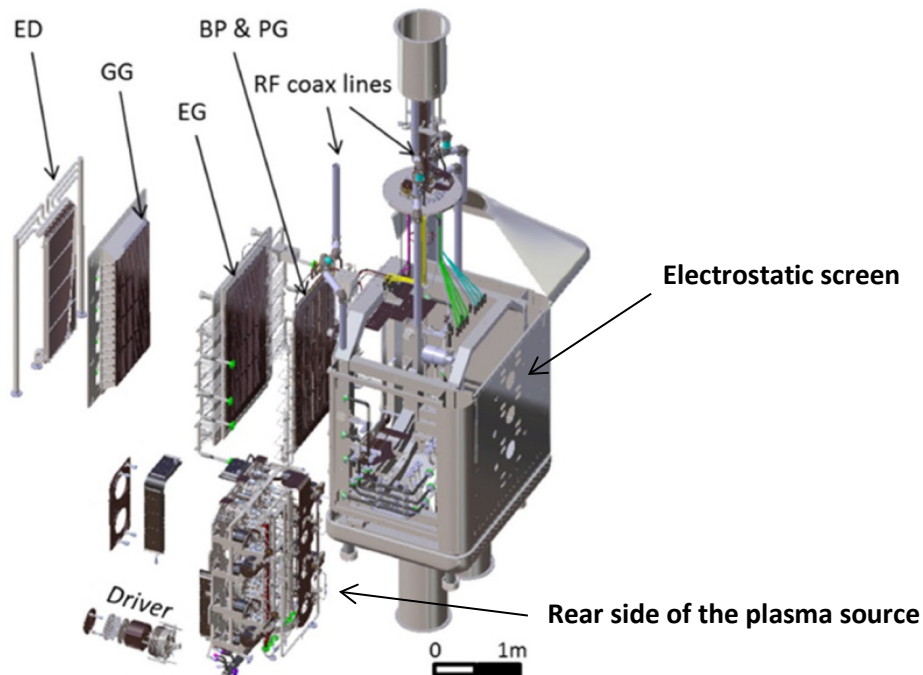
Figure 1-13 – Exploded view of the SPIDER beam source [1] ("ED" is the "Electron Dump", "GG" is the "Grounded Grid", "EG" is "Extraction Grid", "BP & PG" is the "Bias Plate and Plasma Grid")

Figure 1-13 also shows that the ion source is enclosed within an electrostatic screen at source potential to prevent breakdown between ion source components and the VV which is grounded. The electrostatic screen is composed of drilled plates to allow the evacuation of the gas from the ion source to the pumping system.

Figure 1-14 shows some of the beam source components during the manufacturing phase, and in particular the RF driver (c), the electrostatic screen (d), the plasma grid segments (e) and the ion source expansion chamber (f).

Figure 1-15 shows a front view and lateral-rear view of the beam source at PRIMA.
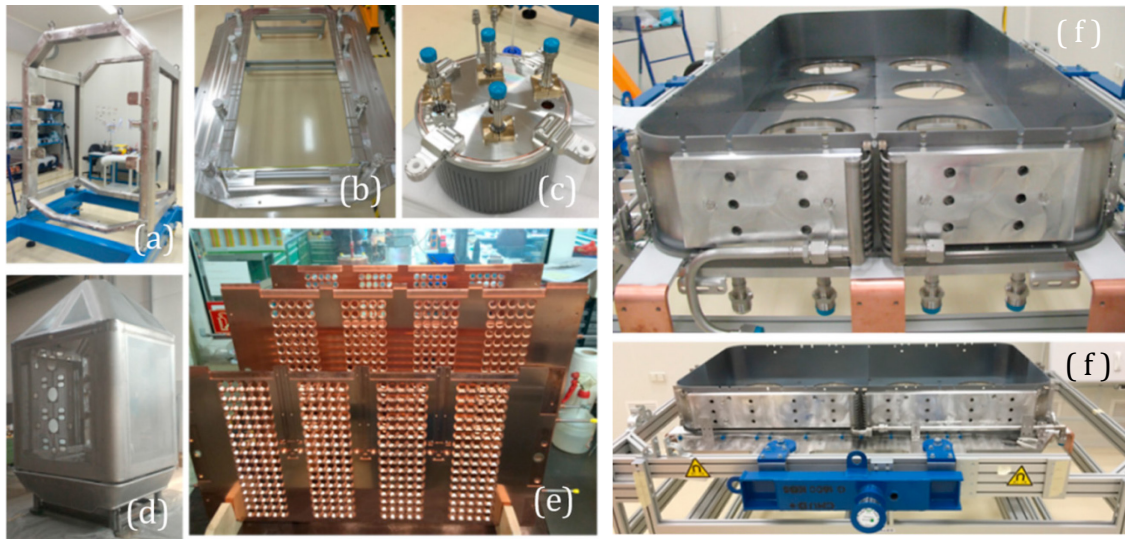
Figure 1-14 – SPIDER beam source components during manufacturing [27]: support frames (a)(b), RF driver (c), overall electrostatic screen (d), plasma grid segments (e) and ion source expansion chamber (f)
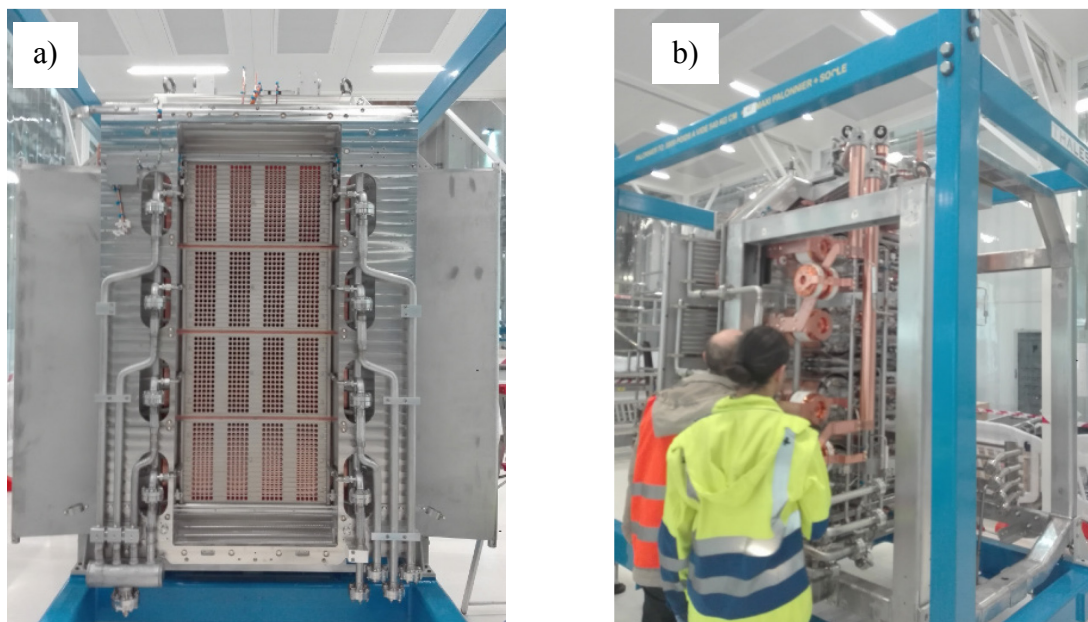
Figure 1-15 – SPIDER beam source within a clean room at PRIMA (November 2017): a) front view (ED not installed), b) lateral-rear view

1.4.1.1 Power supplies

SPIDER power supplies are rated for the full pulse length, and can be grouped into the ion source and extraction grid power supply (ISEPS), and the acceleration grid power supply (AGPS).
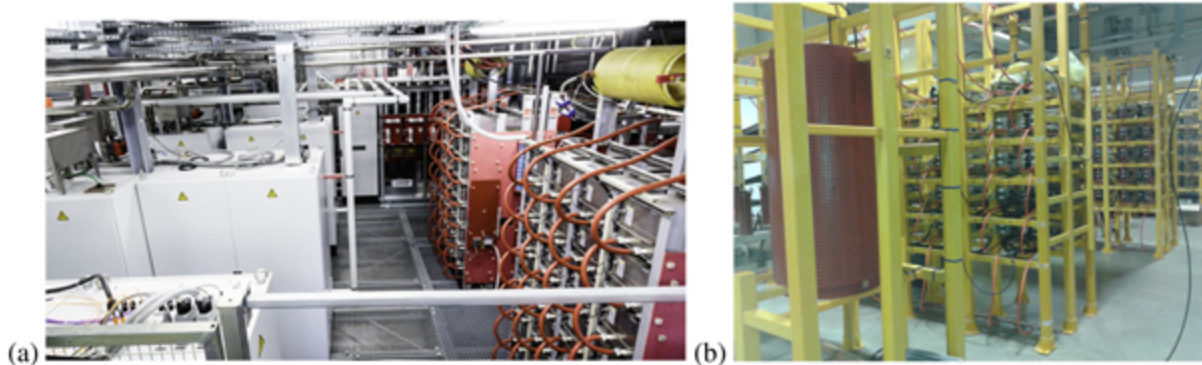
Figure 1-16 – Pictures of SPIDER ISEPS (a) and SPIDER AGPS (b)

ISEPS is placed within a Faraday Cage called "High Voltage Deck" [31] at the EG potential with respect to ground. An air insulated transmission line connects ISEPS and AGPS to the beam source [32].

The ISEPS system is supplied through three multi-secondaries transformers, insulated for 100 kV, and includes the main power generators [33]:

- ISRF composed of a common high voltage dc power supply (ISRF-TE) feeding four independent RF oscillators, each feeding two RF coils connected in series, serving two drivers (more details in paragraph 2.2);
- ISEG is the Extraction Grid power supply, which applies a voltage between Plasma and Extraction Grids;
- ISPG is the Plasma Grid Filter power supply, which generates a dc current flowing through the plasma grid inducing a magnetic field aimed at reducing the extraction of electrons;
- ISBI is the Bias power supply, which applies a voltage between the Plasma Grid and the Ion Source Body in order to favour the extraction of ions;
- ISBP is the Bias plate power supply, which applies a voltage between the Bias Plate and the Ion Source Body to suppress the co-extracted electrons;
- other auxiliary PS (i.e. filament PS, caesium oven PS, etc.).

The main performance requested to ISEPS is listed in Table 1-5.

Table 1-5 – ISEPS main performance specification [33]

Power supply	Output ratings
ISEG	−12 kV, ripple < ±1%, 140 A dc
ISRF-TE	12 kV, ripple < ±0.25%, 140 A dc
ISRF	4 units, 200 kW each f = 0.9 – 1.1 MHz, 50 Ω load
ISBI	30 V, 600 A dc
ISBP	30 V, 150 A dc
ISPG	15 V, 5 kA dc

The AGPS, based on Pulse Step Modulator architecture, provides the voltage between the grounded grid and the extraction grid, for the full beam acceleration. The main performance requested to AGPS is listed in Table 1-6.

Table 1-6 – AGPS main performance specification

Parameter	Unit	Value
Dc output voltage	[kV]	From -20 to -96
Output Current	[A]	71
Voltage control accuracy	[-]	±1% of the maximum value
Voltage ripple	[-]	±1% of the maximum value

1.4.2 MITICA

MITICA is the full scale prototype of the ITER Heating Neutral Beam Injector, with the same plasma source of SPIDER,

5 stage acceleration system by means of water cooled Cu grids at different electrical potentials (200 kV each), a neutralizer, a residual ion dump and a calorimeter for the dissipation of the beam energy. Its requirements are the same of ITER heating NBI, already listed in Table 1-3.

A 3D cut view of MITICA is shown in Figure 1-1.
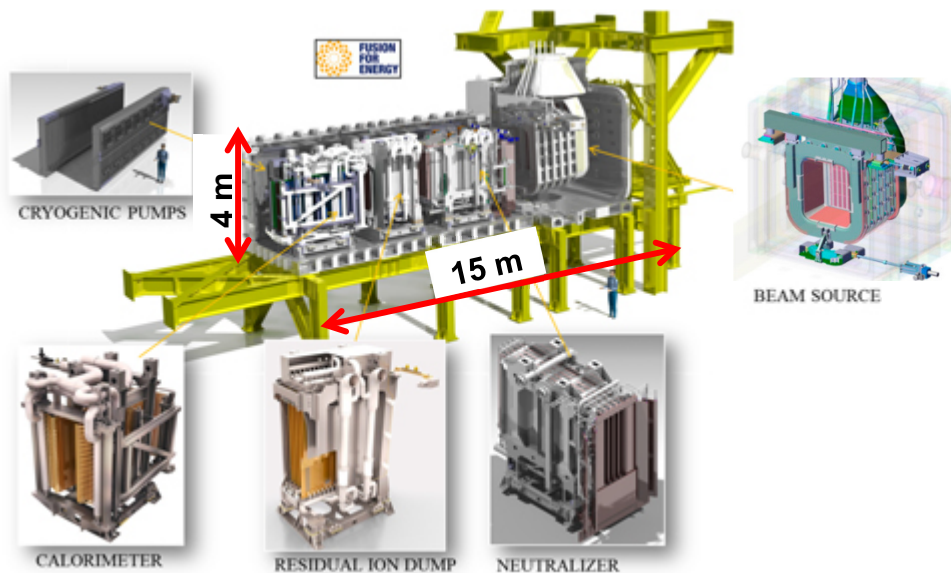
Figure 1-17 – 3D cut view of MITICA

1.4.2.1 NBI efficiency

The present process of Neutral Beam generation and transmission is characterized by very low efficiency, due to substantial losses both inside the beam source and along the path towards the plasma.

For ITER NB Injectors about 59 MW are necessary to deliver 16.5 MW to the plasma, for a net efficiency of 28%. This (in) efficiency is not acceptable for a fusion power plant, but it is the best achievable performance when assuming negative ions with present knowledge and technologies.
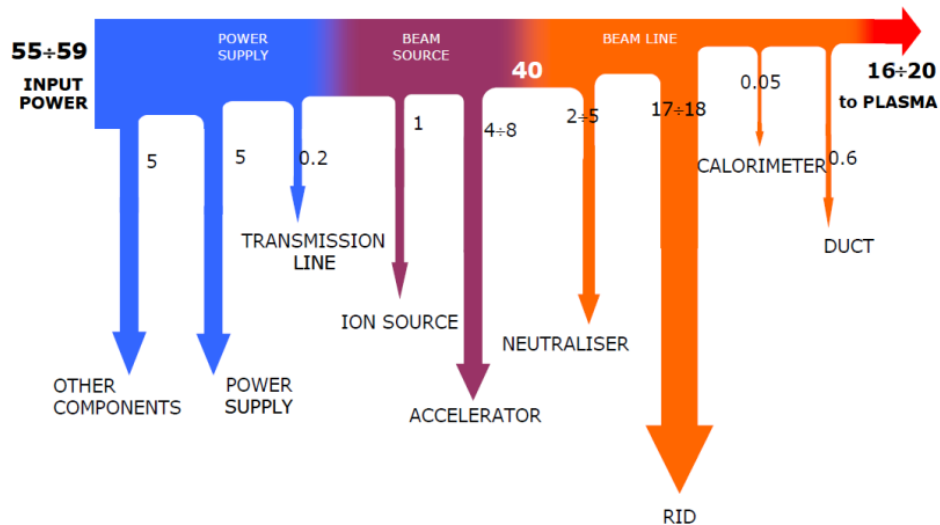
Figure 1-18 – NBI power losses

1.4.2.2 Power supplies

MITICA power supplies, whose scheme is shown in Figure 1-19, are grouped in three groups:
- ISEPS for the supply of the ion source and the extractor, as in SPIDER;
- AGPS for the supply of the accelerator composed of a so called "Conversion System" and "DC generators";
- Ground related power supplies (GRPS) for the supply of the residual ion dump (RID).

On MITICA ISEPS is supplied by a transformer insulated for 1 MV to ground, and it is placed within a Faraday Cage called "High Voltage Deck 1" [34] at the EG potential with respect to ground. The High Voltage Deck 1 is 12.5 m long, 8.4 m large, 9.6 m high and it is sustained by 8 fiberglass insulators 6 m long. A "High Voltage Deck 2" hosts the pipes for the ion source and the grids cooling.

The AGPS conversion system [35] is used to supply the 5 step up transformers with square voltage waveform at 150 Hz, with the capability to fast switch off the power.

The transformers outputs are rectified with diodes bridges to generate -200 kV and feed the accelerating grids.

The power is transmitted to the ion source and the acceleration grids via a high voltage transmission line, SF_6 insulated for 1 MV dc to ground [36].

The 3D layout of MITICA and its power supplies is shown in Figure 1-20.
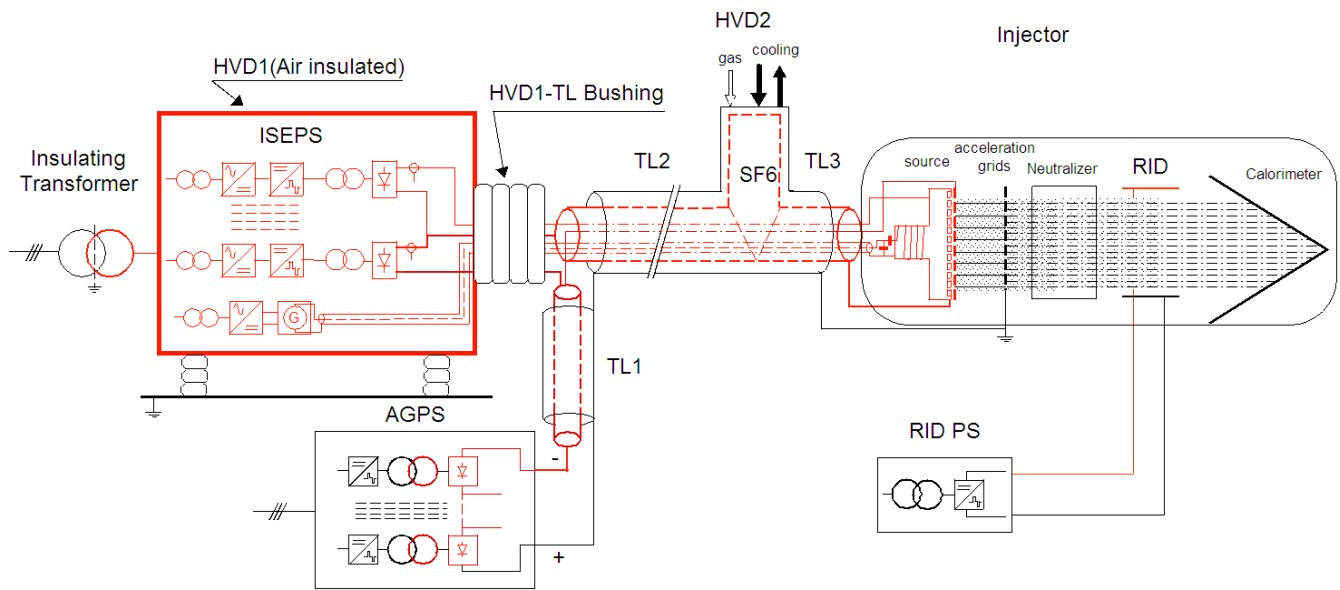
Figure 1-19 – MITICA Power Supplies conceptual scheme
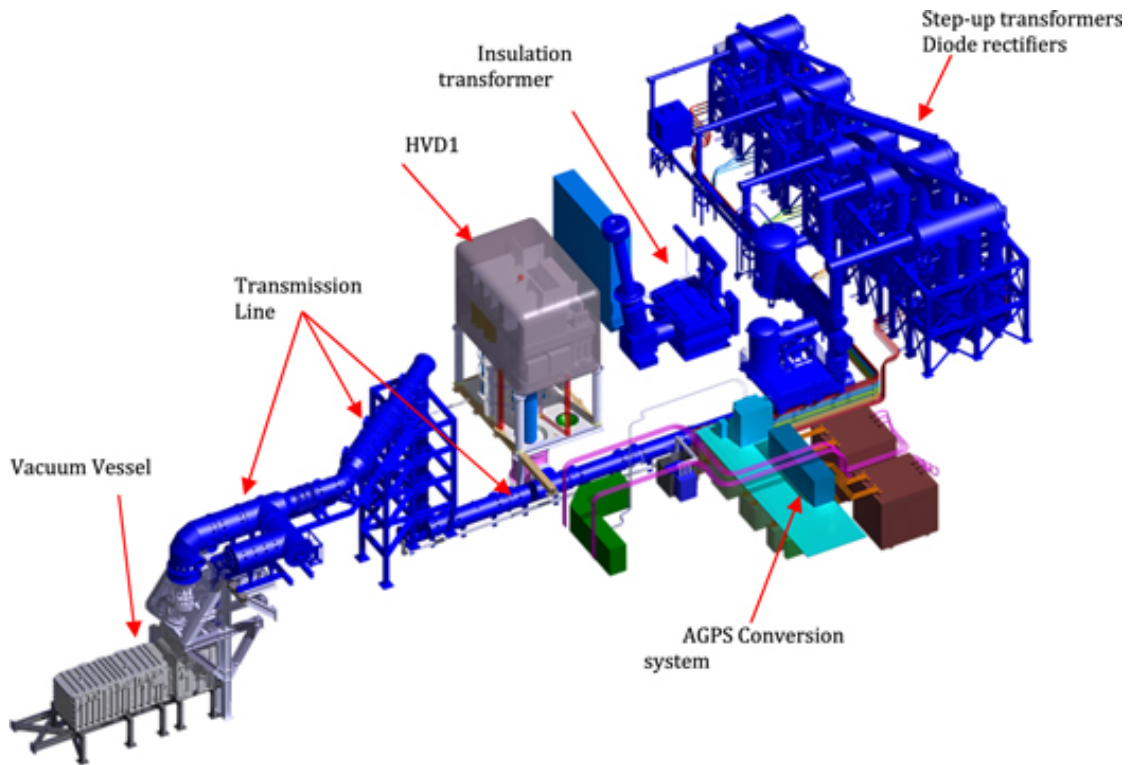
Figure 1-20 - MITICA Power Supplies 3D layout

2 Analysis of SPIDER and MITICA drivers operating conditions

2.1 Detailed description of the driver

Within the beam source the 8 drivers are arranged in a 2x4 matrix, as shown in Figure 2-1. The electrical circuits which supply the drivers are on the rear side of the source and comprise the RF coils, the matching capacitors and the RF transmission lines.

The rear side of the beam source is quite crowded; in fact, besides the presence of the RF circuits, it houses the cooling circuits and manifolds, gas inlet pipes, cables for diagnostics and other auxiliary equipment, such as the feeder for the starting filaments.
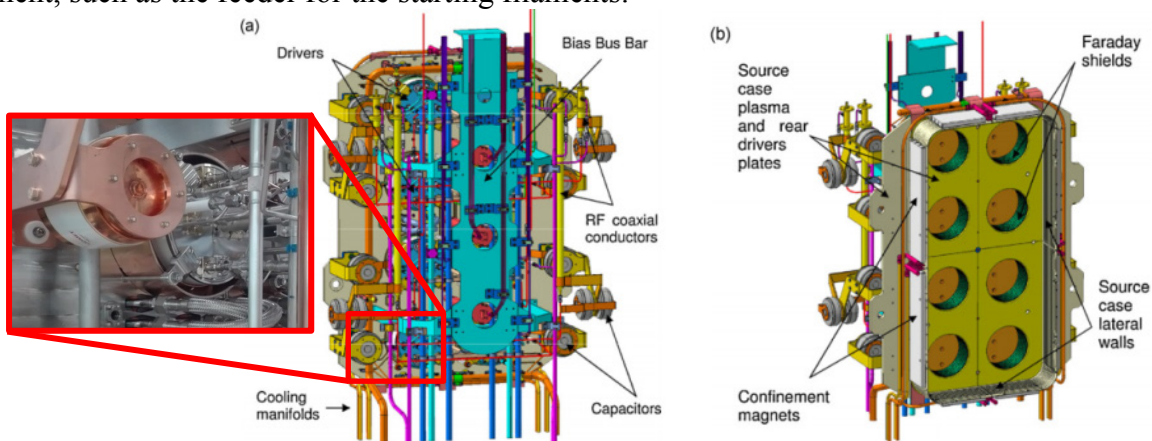
Figure 2-1 – SPIDER RF beam source: a) rear side, b) front side

To describe in detail the design of the driver, reference is made to the 3D CAD view of one driver with the indication of the main components shown in Figure 2-2 a); a close view of the driver is shown by a picture in Figure 2-2 b).

Starting from the external region, the main components of a driver are:

- four support rods relatively displaced by 90° to mechanically hold the components;
- the Electromagnetic shield (EMS) [37], at the ion source potential, surrounding the coil and actively cooled;
- four so called "combs" made of Vespel SP-1 to support the coil;
- the actively cooled copper coil;
- the insulating driver case (DC) made of Aluminum Oxide;
- the copper Faraday Screen (FS) at ion source potential coated with a Molybdenum layer to reduce the plasma etching [5] [10];
- at the top there are the backplate and the back cover.

The geometrical parameters of the SPIDER ion source driver are listed in Table 2-1.

The two clearances gap1 and gap2 indicated in Figure 2-3 are of particular interest for the analyses presented in the following paragraphs. Gap1 is the distance between the FS lateral wall and the Driver Case and it is nominally equal to 2 mm; gap2 is the distance between the coil and the Driver Case and it nominally equal to 0 mm, since the coil is tightly wound around the DC. However, because of mechanical tolerances of component, it is expected that the Gap2 can be equal to zero just in some points. Gap1 is inside the Driver Case, where plasma is produced at the nominal pressure of 0.3 Pa, while gap2 is outside the driver and its working pressure is the one at the backside of the beam source.
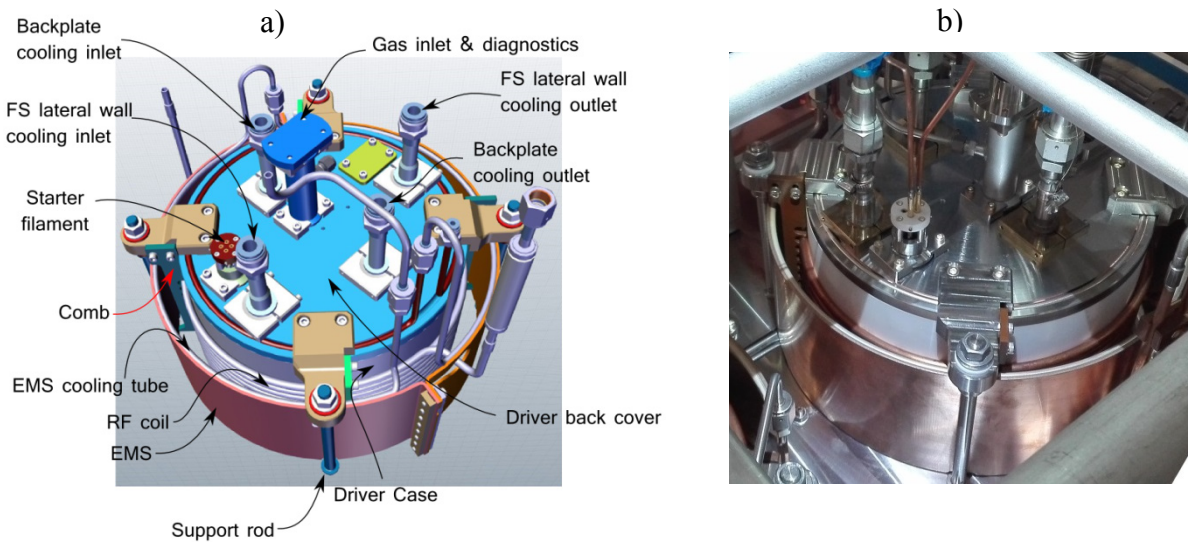
Figure 2-2 – a) 3D CAD view of the driver with the indication of the main components, b) picture of one driver installed in the beam source.
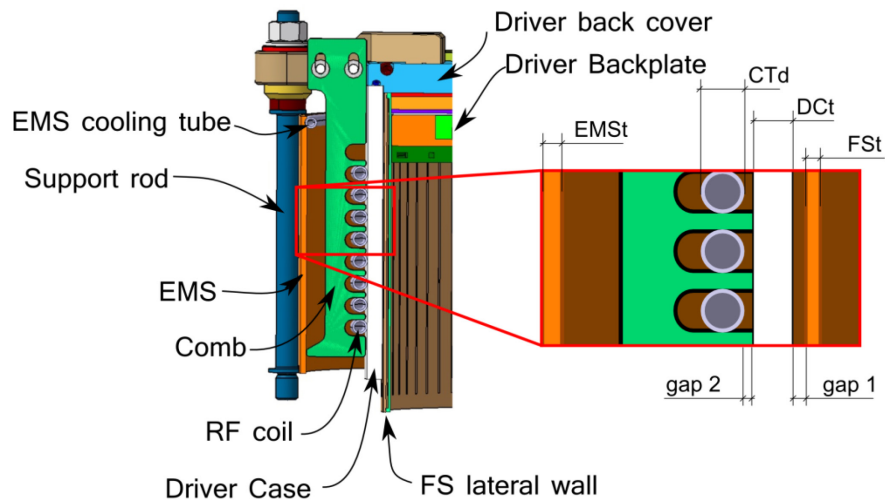
Figure 2-3 - Cross section of the driver with the indication of the main components.

Table 2-1 - Geometrical parameters of SPIDER ion source driver

Geometrical parameters	id	[mm]
Height of the EMS		140.5
Inner EMS diameter		366.0
Distance of EMS from RF coil		25.0
EMS thickness	EMSt	3.0
Comb thickness		6.0
RF coil diameter (axis of the tube)		308.0
RF coil tube outer diameter	CTd	8.0
Distance of RF coil from driver case	gap2	0
Driver case outer diameter		300.0
Driver case thickness	DCt	8.0
Distance of driver case from FS	gap1	2.0
FS outer diameter		280.0
FS thickness	FSt	2.5

2.2 RF coil working pressure

The H_2 pressure distribution on the internal surface of the SPIDER vacuum vessel and on its in-vessel components, calculated in [28], is shown in Figure 2-4:
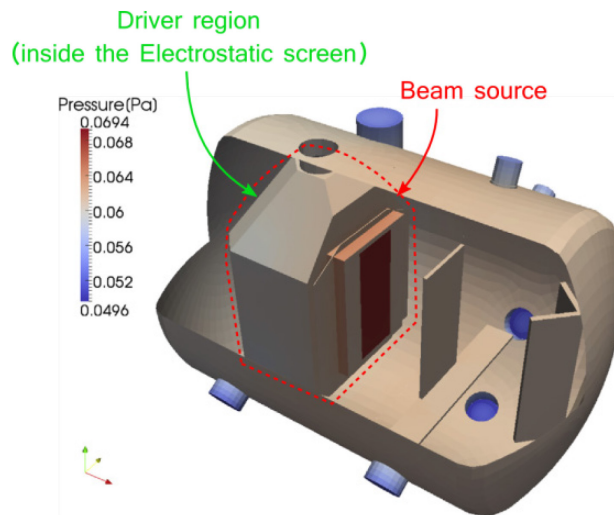
Figure 2-4 - H₂ pressure distribution at the surface of SPIDER vacuum vessel and internal components [28]

The total pressure at the electrostatic screen outer surface has been estimated to be around 65 mPa [28], given by two contributions: the partial pressure of hydrogen which is 61 mPa and the pressure due to surface outgassing which is up to 4 mPa at room temperature.

Because of outgassing the components within the electrostatic screen are expected to be characterized by higher pressure.

2.3 RF circuit supplying the drivers

The 8 drivers of the beam source are arranged in 4 couples, each fed by two RF coils connected in series, and matched to the characteristic impedance of the transmission line through a normal L-type matching network [38] composed of vacuum capacitors [30].

The identification of the ratings for the matching capacitors and the matching conservation during operation are not trivial since the drivers' coils are magnetically coupled with the plasma, therefore their resistance and inductance depend on the plasma parameters. The strategy adopted for SPIDER is to vary the frequency of the oscillators to adjust the matching, as plasma parameters change [29].

It has to be mentioned that the RF coils are not only coupled with the plasma, but also to the other passive structures of the driver and of the BS such as the Faraday shield, the EMS, the backplates.

Each RF circuit is referenced to the potential of the Body source through an impedance Z, whose value is still to be defined.

Figure 2-5 shows the 3D layout of the RF coils and of the matching capacitors placed on the back side of the beam source.

The single line diagram of the RF circuit which supplies the drivers is highlighted in Figure 2-6, which also shows the electrical circuit of the ISEPS.
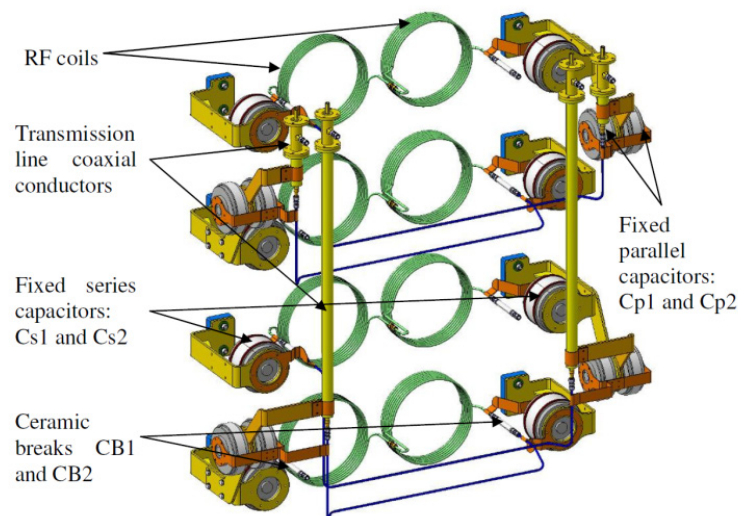
Figure 2-5 - View of the matching network and drivers RF coil
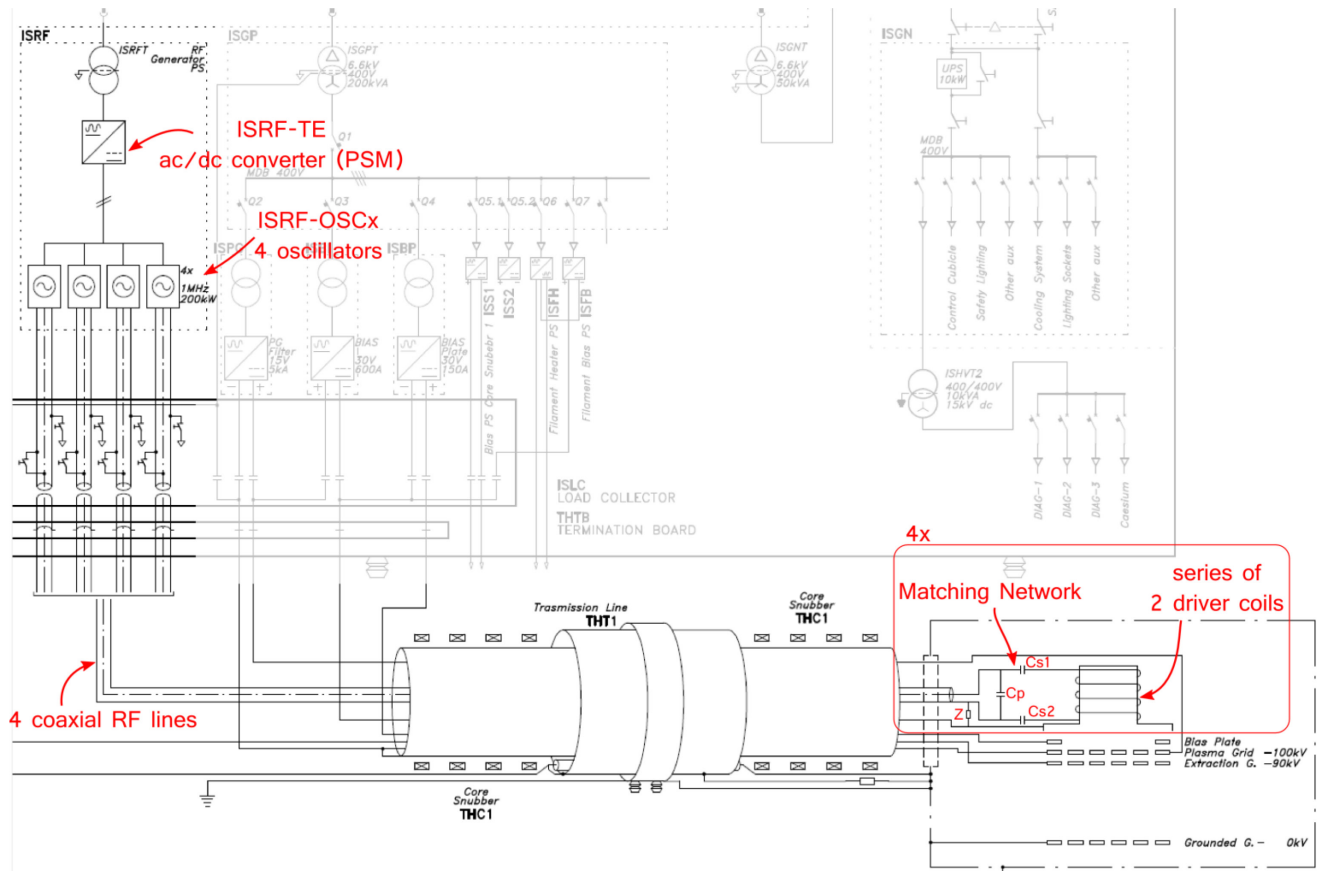
Figure 2-6 - Single line diagram of the RF circuit

In particular four oscillators ISRF-OSCx (with x=1,2,3,4) are connected to the matching networks through four RF coaxial transmission lines (3⅛") having a characteristic impedance Z_0 = 50 Ω.

Each oscillator is rated to deliver a power of 200 kW to a 50 Ω load, and its frequency is adjustable in the range 0.9 MHz – 1.1 MHz.

The complete SPIDER RF circuit is shown Figure 2-7, where also the voltage source and the potentials of the grids are indicated.
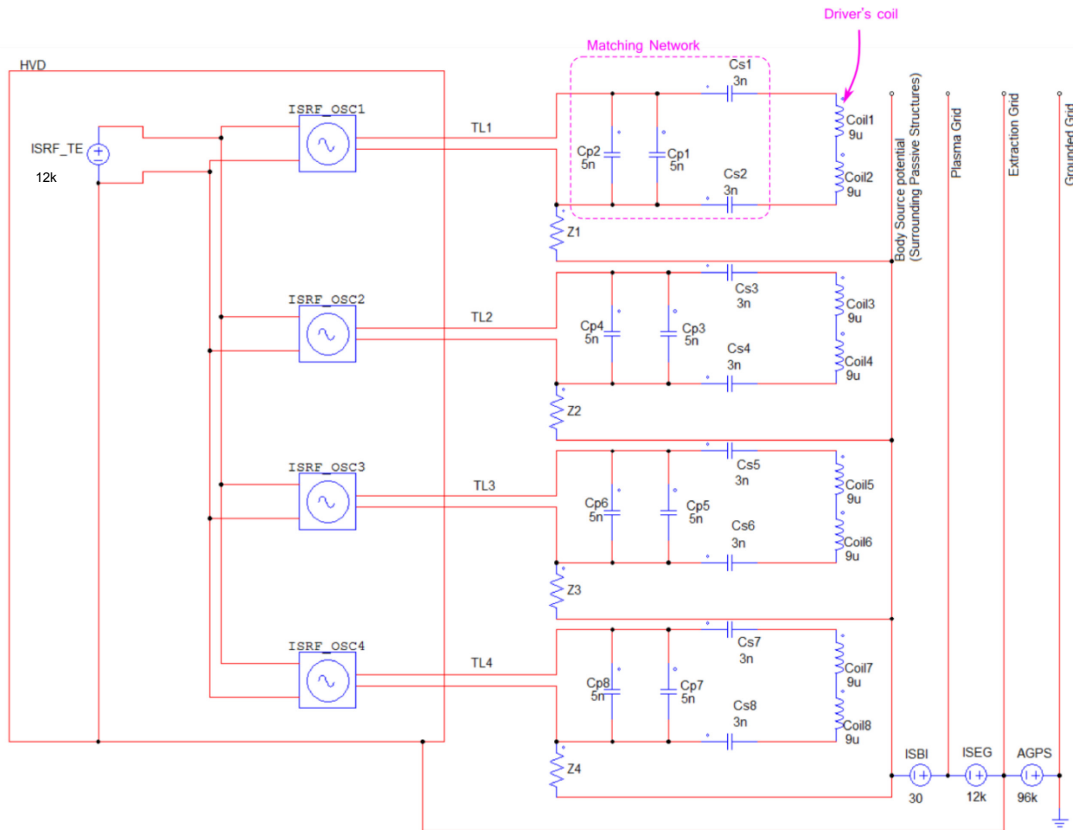
Figure 2-7 - SPIDER RF Circuit

The main parameters of the circuit are reported in Table 2-2.

Table 2-2 - Main parameters of SPIDER RF circuit

parameter	Id	value	unit
ISRF-OSCx rated power	Pn	200	kW
ISRF-OSCx frequency range		0.9 – 1.1	MHz
ISRF-OSCx max output voltage with a load of 50 Ω[1]	Vn	3160	V
ISRF-OSCx output impedance		50	Ω
Z_0 of TL		50	Ω
Cp (composed of a couple of capacitors Cp1 and Cp2)		10	nF
Cs (composed of the Cs1 and Cs2 series capacitor)		1.5	nF
RF estimated coil inductance (when coupled with plasma)		9	μH
RF coil estimated equivalent resistance (when coupled with plasma)		2.3	Ω
Z (impedance used to link the RF circuit to the Body Source)		Ratings still under study	Ω

---

[1] This is calculated from the rated power and its nominal output impedance.

2.4 Expected driver voltage

The voltage across each RF coil (VD) depends on the values of its inductance and effective resistance, which are affected by uncertainties since they depend on the coupling with the plasma, thus on its variable plasma parameters.

The expected value for the driver inductance (LD) is 9 µH and for the driver resistance (RD) is 2.3 Ω with nominal plasma parameters and nominal frequency of 1 MHz.

The expected driver voltage was estimated by means of numerical analyses considering the circuit of Figure 2-7 and the ISRF-OSC working at its maximum performance (with maximum power output, maximum output voltage, see Pn and Vn of Table 2-2) within its frequency range, for different values of RD and LD:

- Nominal RD value was assumed, and a variation of LD was considered;
- Half RD value was assumed, and a variation of LD was considered;
- Double RD value was assumed, and a variation of LD was considered.

This approach allows disregarding physics of plasma and its coupling with the RF coil, it considers that the driver equivalent series resistance could have been underestimated or overestimated by 100%. The limits on the LD values, then, are imposed by the operating frequency range of the generators.

Table 2-3 summarizes the results of the simulations; in particular the operating frequency and the voltage across each RF coil (rms value) are reported as a function of the RD and LD values. The ISRF-OSC reached limit is highlighted too.

Table 2-3 – Expected voltage across each RF coil terminals

LD	RD	f	VD (rms)	P	Reached limit
[µH]	[Ω]	[MHz]	[kV]	[kW]	
Varying LD, while keeping RD to the nominal value					
7	2.3	1.100	10.1	200	Pn
8	2.3	1.096	11.5	200	Pn
9	2.3	1.033	**12.2**	200	Pn, Vn
10	2.3	0.979	12.7	195	Vn
11	2.3	0.933	12.8	181	Vn
11.8	2.3	0.900	13.0	174	Vn
Varying LD with RD half of the nominal value					
7	1.15	1.100	14.3	200	Pn
8	1.15	1.093	13.3	136	Vn
9	1.15	1.028	13.9	131	Vn
10	1.15	0.971	14.9	137	Vn
11	1.15	0.922	16.0	145	Vn
11.4	1.15	0.904	**16.6**	151	Vn
Varying LD with RD double of the nominal value					
7	4.6	1.100	7.2	200	Pn
8	4.6	1.092	8.1	200	Pn
9	4.6	1.030	8.6	200	Pn
10	4.6	0.977	9.1	200	Pn
11	4.6	0.931	9.5	200	Pn
11.7	4.6	0.903	9.9	200	Pn

With RD at its nominal value the LD can vary in the range 7-11.8 µH: higher inductance values would require an operating frequency below 900 kHz, lower inductance values would require operating frequencies higher than 1.1 MHz.

Both the power and the voltage limits are reached when RD and LD are at their nominal value; in that case the rms value of the voltage across each coil is 12.2 kV.

Doubling the value of RD with respect to the nominal one would reduce the voltage across each coil; halving the value of RD would increase the voltage value across the coil up to 16.6 kV rms.

2.5 E-field calculation

A simplified 2D axisymmetric finite element model has been developed with FEMM [39], according to the driver geometry presented in Figure 2-3 and in Table 2-1, in order to calculate the electrostatic field in the driver region. The model includes the geometry of the driver components and the materials properties. The peak value of the coil voltage expected with nominal plasma parameters was assumed, with the hypothesis of linear distribution among the coil turns.

The present design of the SPIDER driver assumes zero gap between the driver case and the RF coil (gap2 = 0 mm); a realistic value for gap2 is in the range 0-0.5 mm and the value of 10 µm was assumed in the model.

The analysis results show an intense Electric field (E-field) in the two gaps region, as shown in Figure 2-8, where it is possible to appreciate maximum E-field values between the highest voltage turn of the RF coil and the DC.
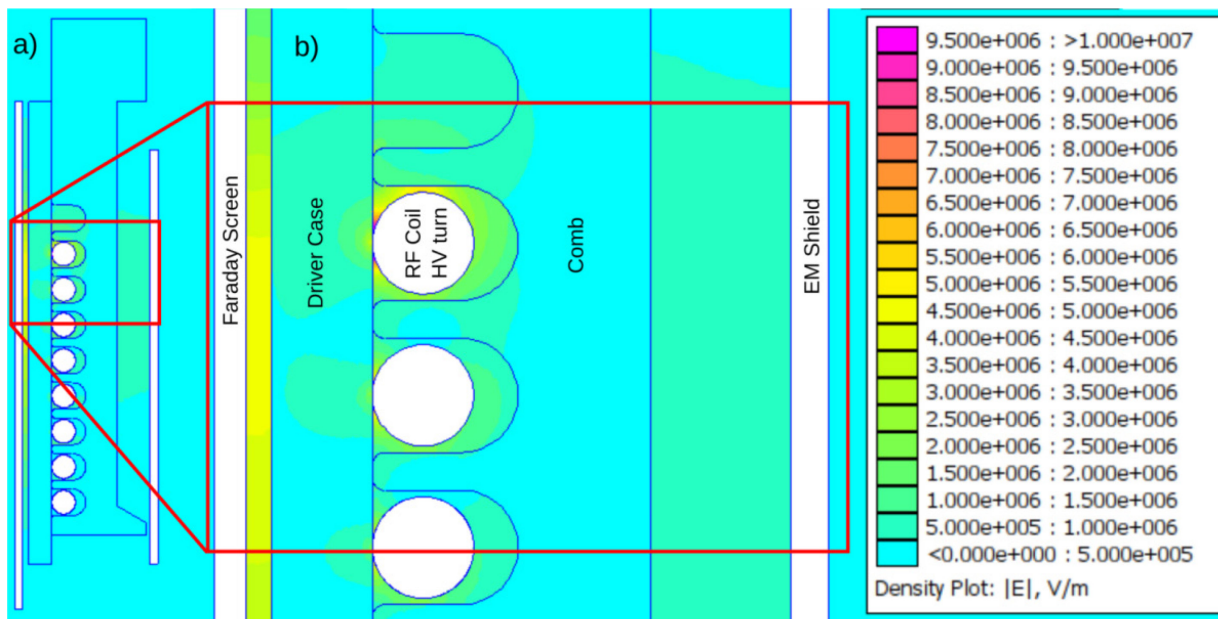
Figure 2-8 - a) Driver E-Field density plot (hypothesis: 12.2 kV rms, linear distribution among turns, gap of 10 µm between RF coil and Driver Case); b) zoomed view on the region characterized by the highest E-field.

The analyses were repeated with the same model when gap2 width varies in the range 10µm - 1 mm, and the resulting maximum E-field in the two gaps as a function of the gap2 width are shown in Figure 2-9: it can be seen that the decrease of gap2 width causes a strong increase of the E-field in the gap2 region (green triangle markers) and much lower in the gap1 region (orange triangle markers).
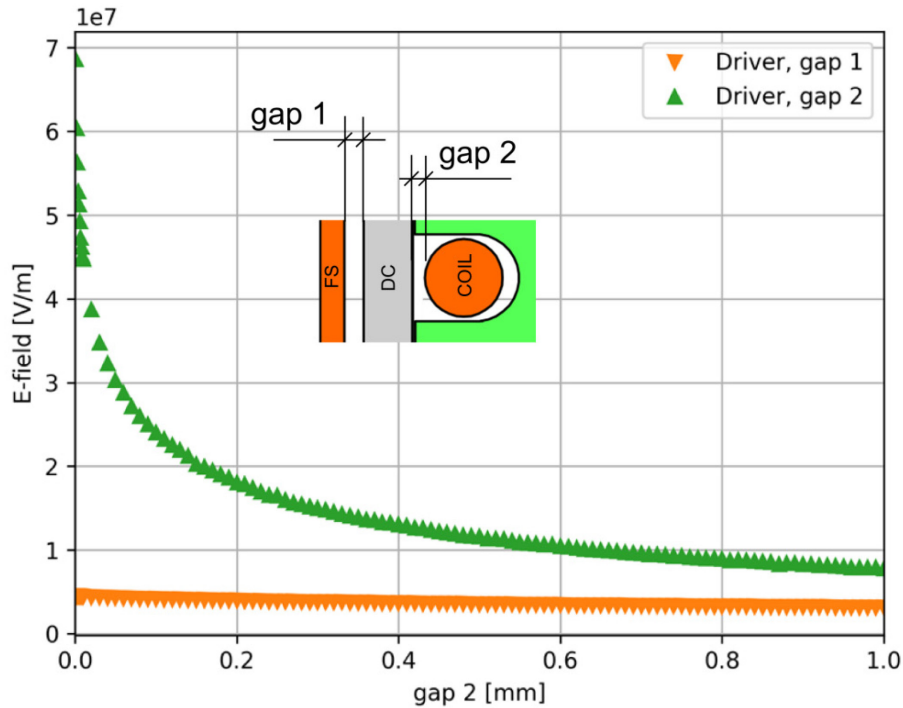
**Figure 2-9 - Maximum E-Field in on gap1 and gap2 as a function of the gap2
(with the hypothesis of 12.2 kV rms applied to the RF coil)**

With 16.6 kV across the coil the E-field in the gap2 region would be in the range 14-95 MV/m.

2.6 Driver voltage hold off

The E-field strength is in general the primary factor for a breakdown to occur and it is most likely to occur where the E-field is highest, but it is not always the case and other factors need to be considered (materials, gas type, pressure, temperature, surface finishing, gap, …).

The gas pressure in the RF circuits and driver coils region is far from values typical of Ultra High Vacuum, preferable for voltage holding, but since the distances between metallic parts at different potential inside the beam source are shorter than the mean free path of the electrons, the Townsend discharge regime is not expected.

The RF circuit and the coils therefore work at the left side of the Paschen curve, so only vacuum discharges are possible: "Isolation sous vide" region of Figure 2-10. That curve was derived for planar circular stainless steel electrodes with a gap of 1 cm in between.
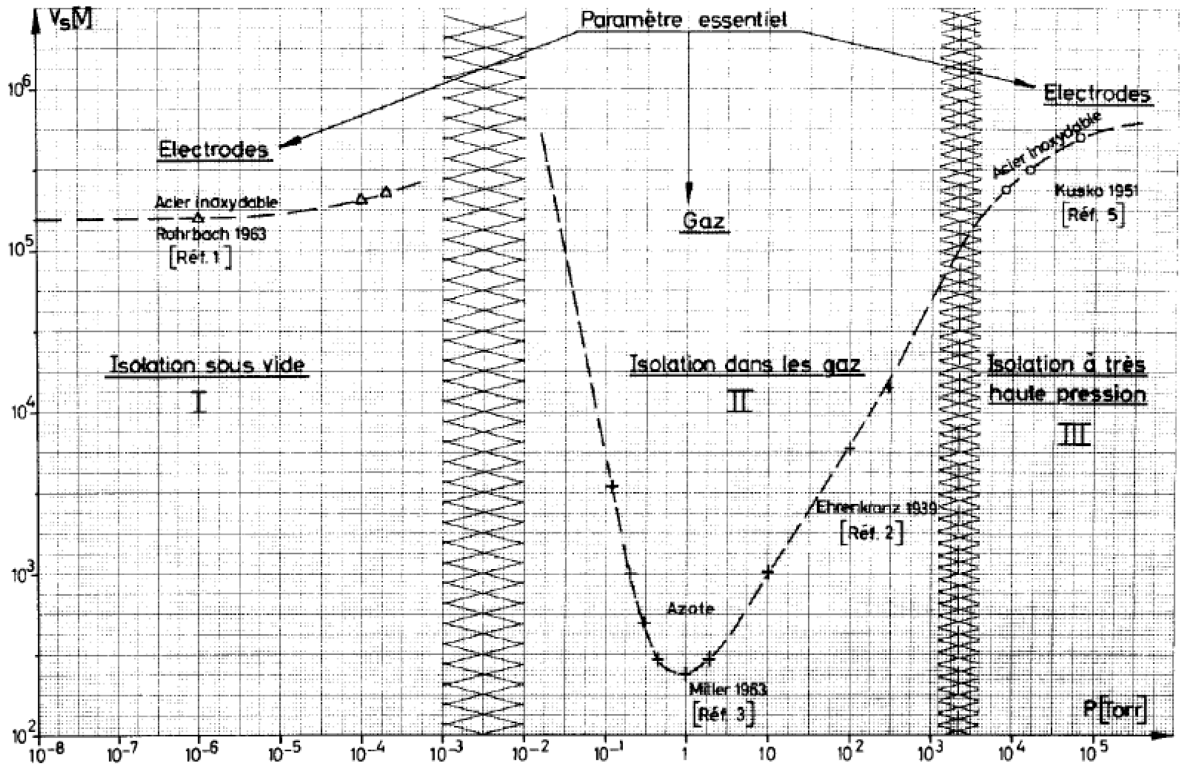
Figure 2-10 – Paschen curve derived for Planar Stainless Steel Electrodes, direct voltage, gap = 1 cm [40]

Actually, the breakdown voltage for gas discharge depends on the product of the pressure and the gap, in fact usually in the literature the Paschen curve presents the breakdown voltage as a function of that product.

For the vacuum insulation the breakdown voltage is little higher than 100 kV, corresponding to a macroscopic electric field higher than 10 MV/m. This value is much lower than the expected E-field in the driver; nevertheless it has to be considered that the E-field required for a breakdown tends to increase for shorter gaps, while for longer gaps it tends to decrease; in other words the breakdown voltage is not linear with the gap, but tends to saturate for long gaps [41].

The mechanisms of vacuum breakdown have been investigated for decades, and many theories and models were developed for both "vacuum gap" configuration (metallic electrodes separated by a vacuum gap) and for mixed configuration in which a solid insulator bridges the gap [42].

In general the presence of a solid dielectric reduces the voltage hold off capability, due to the intrinsic formation of "triple junctions" (metal, vacuum, dielectric).

Triple junctions are characterized by local intensification of the E-field, with possible associated electron emission.

The free electrons impinging on the dielectric surface can develop a secondary electron emission avalanche (SEEA), and can desorb and ionize the gas trapped in the surface outer layer. This process can result in a surface flashover and so to a complete breakdown [43] [44] [45].

For the purpose of the thesis the focus is maintained on the particular case of the driver.

The geometry of the driver is quite different from a couple of planar electrodes in vacuum (typical for the investigation of vacuum breakdown mechanism) and from a couple of electrodes bridged by a solid

insulator. Figure 2-11 proposes a sketch of the top part of the driver, an in particular the turns at higher voltage.

The regions which configure as triple junctions are identified as "A1" and "A2, the E-field value in correspondence to "A1" is produced by the voltage applied between the top turn and the FS (V_{TG} in Figure 2-11).

The electrons emitted in the triple junction regions can be accelerated by the E-field due to the turn to turn voltage (V_{TT} in Figure 2-11), bridged by the DC surface or by the comb surface (not represented in the sketch).
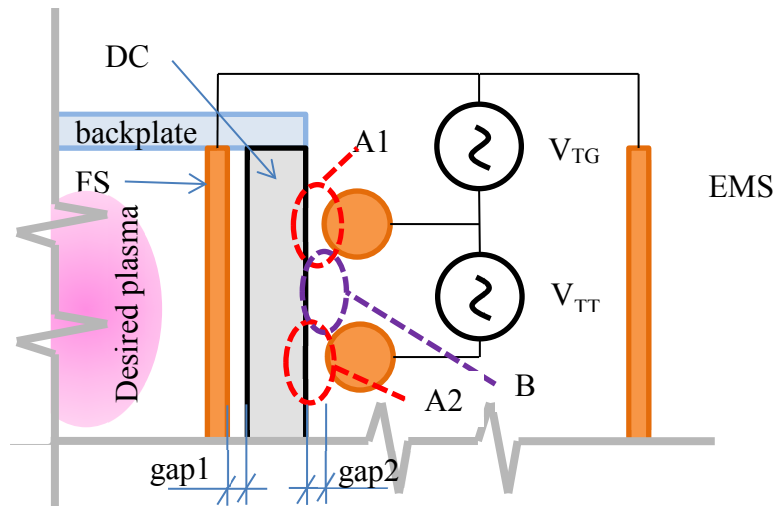
Figure 2-11 – Sketch of the top part of the driver: the high E-field regions are highlighted

The RF drivers adopt a design very similar to that of ELISE [10] in terms of geometry and materials, which experienced breakdowns in the ion source backside [46]. These breakdowns occurred randomly outside of the drivers and limited the RF power injected into the plasma and thus the ion source performance.

To increase the voltage hold off capability of the drivers the best idea is to reduce as much as possible the E-field: some hints for possible design improvements (increase the distance between the coil and the driver case) can be derived by the results shown in Figure 2-9.

However, the results of FEM analysis only are not sufficient for the verification of the driver insulation design since other macroscopic parameters such as the total voltage [47] [48], the operational frequency (most of the literature is for dc, industrial frequency, lightning impulse or for f > 100 MHz), the electrode materials, the residual pressure [49] [50], can play a role in the voltage hold off and need to be taken into account.

For this reason the development of a test facility (presented in chapter 3) suitable to experimentally investigate the driver insulation design and to perform parametric studies versus the cited macroscopic parameters was launched.

This approach allows to complement the FEM analyses with experimental results on suitable mockups of the SPIDER driver, whose design is presented in chapter 4.

3 High Voltage Radio Frequency Test Facility

The High Voltage RadioFrequency Test Facility (HVRFTF) has been developed with the aim to be a simple, accessible and flexible device to characterize the dielectric strength in vacuum of the RF drivers of SPIDER and MITICA ion source and to effectively addresses the issues related to their voltage hold off when subjected to their operating radiofrequency E-fields and pressure.

The operative conditions of SPIDER and MITICA in terms of voltage, pressure, E-field and materials are summarized in Table 3-1 together with the HVRFTF requirements, generally larger so that it will be possible to derive also operational limits.

Table 3-1 - SPIDER and MITICA operating conditions, HVRFTF requirements

PARAMETER	UNIT	SPIDER/MITICA	HVRFTF
Gas species	-	H_2, D_2	Ar, N_2, He, H_2, D_2
Pressure	Pa	0.065-0.070	$0.005\text{-}10^5$
Voltage (rms)	kV	12.2	up to 17
Frequency	MHz	0.9-1.1	0.9-1.1
Conducting materials	-	Cu, Stainless Steel	Cu, Stainless Steel
Dielectric materials	-	Alumina C799, Vespel SP-1	Alumina C799 Vespel SP-1 Fused Quartz

The properties of the dielectric materials which will be tested are listed in Table 3-2.

Table 3-2 - Dielectric materials properties at 1 MHz

PARAMETER	UNIT	ALUMINA C799 [51]	VESPEL SP-1 [52]	FUSED QUARTZ [51]
Dielectric constant	-	9.6 (@10 MHz)	3.55	3.78
Dissipation factor	-	$1 \cdot 10^{-3}$	$3.4 \cdot 10^{-3}$	$1.4 \cdot 10^{-3}$
Dielectric strength	MV/m	17	22	n.a.
Volume resistivity at 20 C	Ω m	10^{12}	$10^{14}\text{-}10^{15}$	10^{20}
Surface resistivity	Ω	n.a.	$10^{15}\text{-}10^{16}$	n.a.

As far as the dielectric materials are concerned, fused quartz at the moment is not used in SPIDER and MITICA drivers, but was considered as possible candidate for the driver of ELISE [10].

3.1 Experimental arrangement

The experimental arrangement worked out to reproduce the operating conditions of Table 3-1 consists of: a vacuum vessel capable to host different types of Devices Under Test (DUT), a gas injection and pumping system to supply the desired gas species up to the test pressure and to evacuate the vacuum vessel, and a RF circuit designed to produce the high voltage.

The voltage is supplied to the DUT by means of air–vacuum feedthroughs, placed on the top and the bottom of the vacuum vessel. The top feedthrough is mounted on a linear translator, and can be axially shifted to adjust the gap of the DUT.

A simplified block scheme of the experimental setup is shown in Figure 3-1, including ancillary systems such as baking system and EM shielding box.
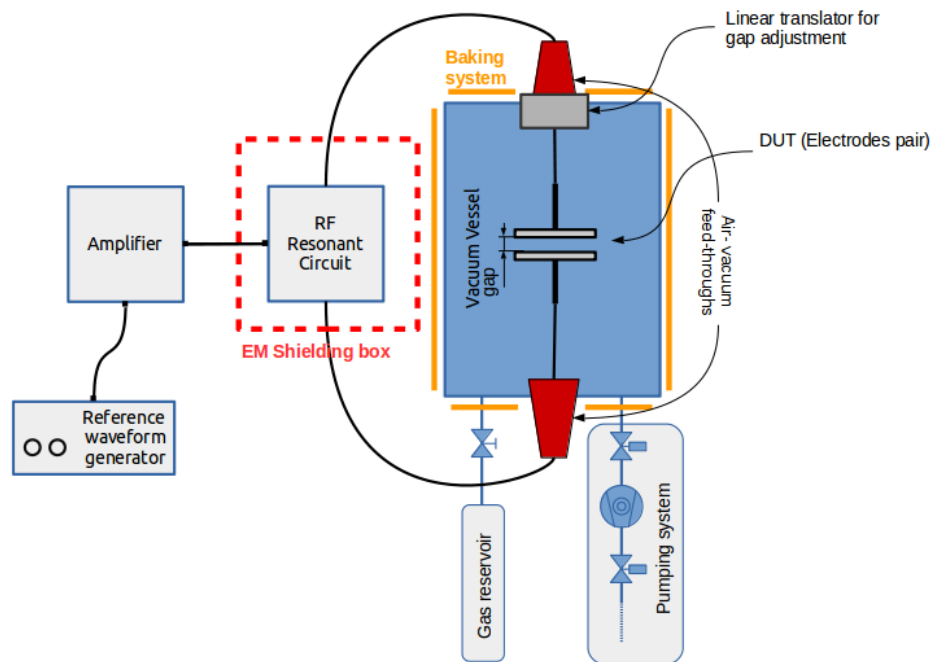
Figure 3-1 - Simplified block scheme of the HVRFTF experimental arrangement

The different parts of the HVRFTF have been designed such that they can be subjected to different specific conditions experienced by the driver coils, in particular:

- The DUTs, placed inside the vacuum vessel, can be made of different materials and characterized by various shapes for the production of E-fields with different magnitude and field line patterns.
- The RF circuit can generate the sinusoidal voltage waveform with the desired amplitude and frequency to be applied to the DUT.
- The gas injection and pumping system can provide to the DUT environmental conditions similar to those experienced at the backside of the ion source, in the driver region, in terms of gas type and pressure.

In the development of the HVRFTF, the two main issues faced have been: the working out of suitable DUT able to reproduce the driver's operating conditions under study and the development of an efficient RF circuit capable to generate the desired high voltage to the DUT, with low power losses. These topics are addressed in chapters 4 and 5 respectively, while the other parts of the experimental setup are described in detail in the following paragraphs.

3.1.1 RF voltage source

A RF amplifier rated for 300 W is available at Consorzio RFX and is used for the preliminary setup of the experimental arrangement. The amplifier is driven by a waveform generator with a sinusoid in the frequency range 0.9-1.1 MHz.

The voltage waveform generator used to produce a sinusoidal waveform is a Tektronix AFG3021B, whose characteristics are:

- Output voltage: 0.01-10.0 V
- Voltage step: 0.01 V
- Frequency range: 0.1 mHz – 25 MHz
- Sampling rate: 250 MS/s
- Output channels: 1, BNC
- Output impedance: 50 Ω
- Source voltage and frequency: 100 - 240 V, 47 – 63 Hz
- Control interface: USB/LAN/GPIB

The broadband RF amplifier is an E&I A300, whose main characteristics are:

- Rated/saturated output power: 300 W / 450 W
- Frequency range: 300 kHz – 35 MHz
- Gain: 55 dB
- Input and output connectors: type N
- Input impedance: 50 Ω
- Output impedance: 50 Ω
- Maximum input signal: 13 dBm (1 V rms), for all output load condition
- Power output meter: ±3% of full scale
- Source voltage and frequency: 100 - 240 V, 47 – 63 Hz
- Control interface: RS232

A 20 dB attenuator is connected to the input of the amplifier to avoid exceeding the tolerable voltage with the waveform generator.

A BNC to N adapter is used to connect the attenuator to the amplifier.

The coaxial cable used is a standard RG58, BNC terminated.
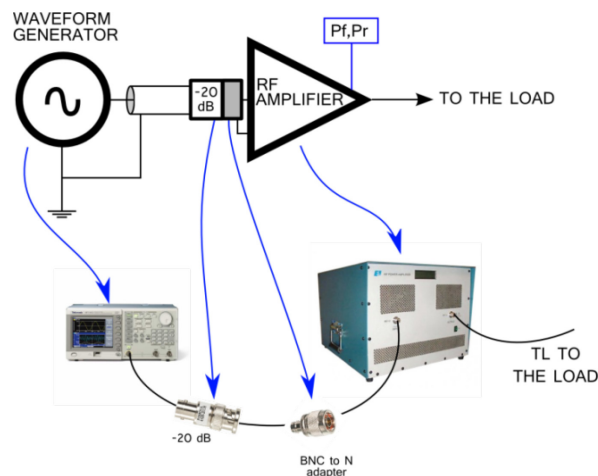
Figure 3-2 - Setup for the generation of RF voltage

3.1.2 Vacuum system

3.1.2.1 Vacuum vessel

The vertical axis cylindrical vacuum chamber is made of Stainless Steel AISI 304L, 760 mm long and 960 mm in diameter, with a detachable top lid, four ports on the equatorial plane, and two co-axial ports at the top and at the bottom.

Figure 3-3 shows the top view and the cut view of the VV.
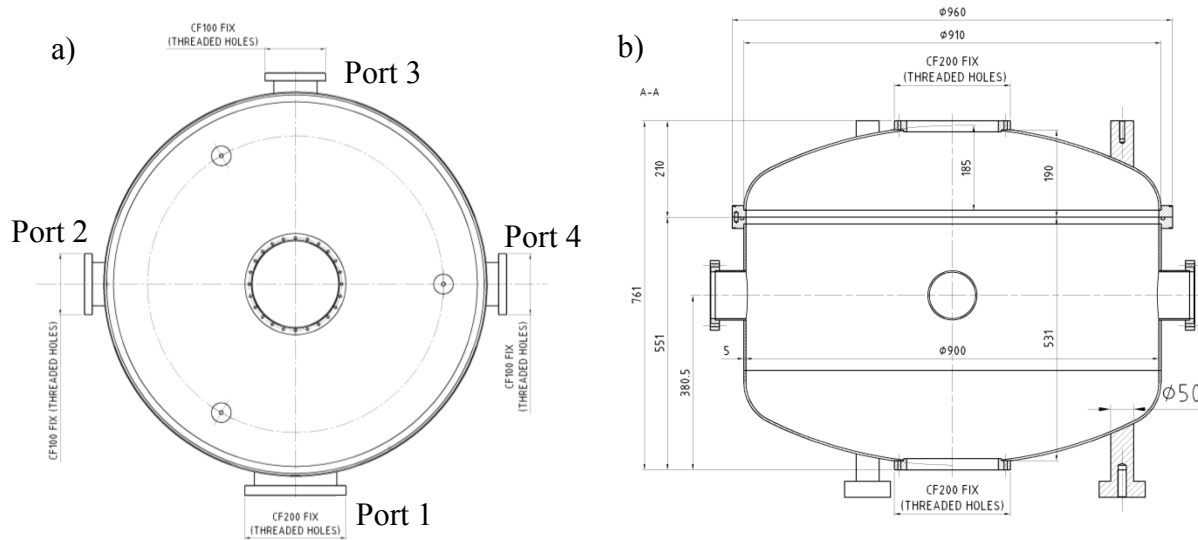
Figure 3-3 – Top view of the VV (a), cut view of the VV (b)

The dimension and flange type of the VV apertures are listed in Table 3-3.

Table 3-3 – VV port list

Port	Flange type and dimension	Note
Top lid	KF 960 mm	
Equatorial port 1	CF 200 mm	Pumping system
Equatorial port 2	CF 100 mm	Viewing port
Equatorial port 3	CF 100 mm	Gas injection port
Equatorial port 4	CF 100 mm	VV pressure measurement
Top coaxial port	CF 200 mm	Linear translator and feedthrough
Bottom coaxial port	CF 200 mm	Bottom feedthrough

A pumping system, a gas inlet valve, two vacuum gauges and a window are mounted on the equatorial ports.

A baking system consisting of three independent heating cables, mounted respectively at the top, bottom, and lateral walls is used to heat the chamber up to 100 °C, a temperature sufficient to promote the outgassing of impurities from the vessel walls.

3.1.2.2 Vacuum-air feedthroughs

The electrical feedthroughs main characteristics are:
- Rated voltage: 150 kV dc;

- Insulating Material: Alumina A-479 (99% Al_2O_3);
- Metallic parts (flange, central rod and Faraday screen): AISI 304L;
- Central rod: diameter 24 mm, M8 threaded connection.

A drawing is shown in Figure 3-4.
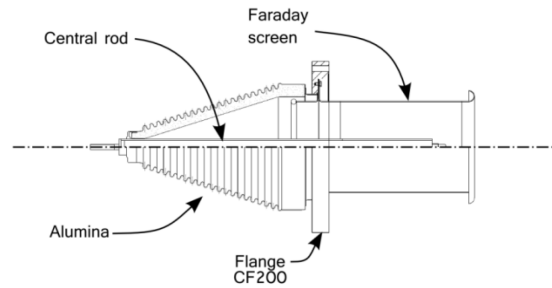
Figure 3-4 – Feedthrough

The Faraday screens mounted on the feedthroughs were designed to control and shape the E-field near the central rod. They have been removed in HVRFTF for a couple of reasons:

- The first is that the HVRFTF voltage is one order of magnitude lower than their rated voltage, so the control of the E-field shape for voltage hold off in that area is not required;
- The second is that the Faraday screens introduce ground stray capacitances to the RF circuit.

3.1.2.3 Translator for distance adjustment

The top feedthrough is mounted on a linear translator for the adjustment of the gap between the electrodes, as shown in Figure 3-5.

The characteristics of the translator are:

- Working stroke 50 mm;
- Max. planarity error between flanges 0.2 mm;
- Hand actuated;
- Material AISI 304.
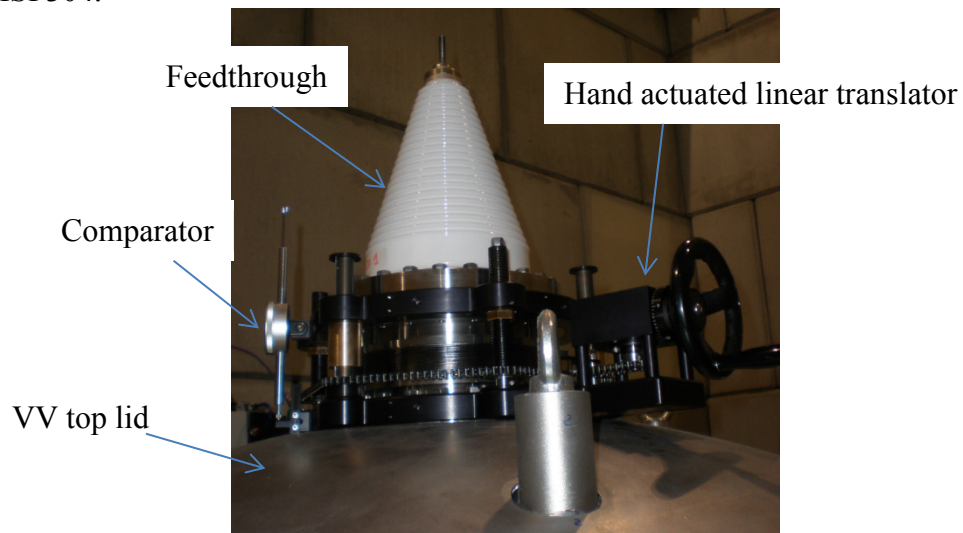
Figure 3-5 - Picture of the top feedthrough mounted on the linear translator

A comparator integrated with the feedthrough measures the distance with respect to the top lid, which corresponds to the DUT gap. The characteristics of the comparator are reported in paragraph 3.1.5.

3.1.2.4 Baking system

To promote the outgassing of impurities from vacuum vessel walls a consolidated technique consists in the bake-out of the vessel (with pumping system turned on).

The HVRFTF VV is equipped with a baking system consisting of three independent heating cables, each one heating respectively the bottom, the lateral wall and the top lid of the VV. The temperature of each part is measured by thermocouples and it is regulated in feedback by a PID controller, with setpoint at 110 °C, temperature sufficient for the purpose.

3.1.3 Gas injection and pumping system

The HVRFTF is equipped with a gas injection and pumping (GIP) system to provide suitable environment condition for the high voltage tests. A scheme of the whole system is reported in Figure 3-6.
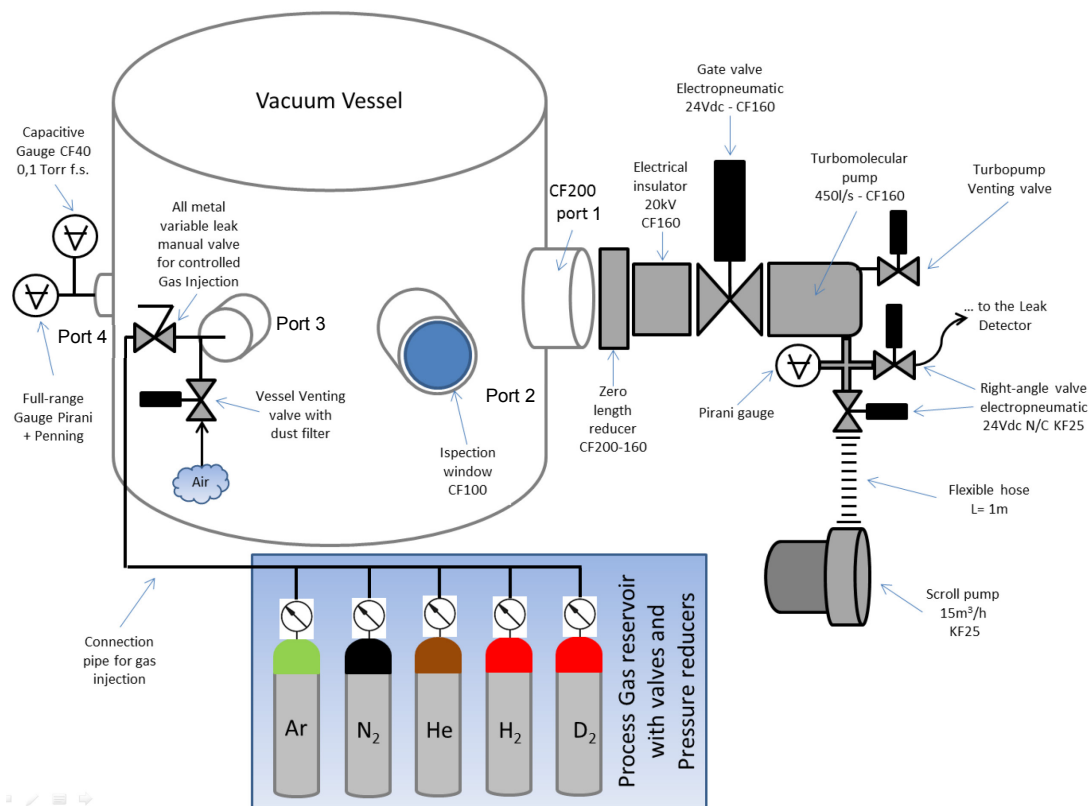
Figure 3-6 – Overview of the gas injection and pumping system

All components of the GIP system are insulated with respect to the vacuum vessel by means of ceramic breaks, and they are grounded independently.

A description of the main components of the GIP system is reported in the following paragraphs.

3.1.3.1 Pumping system

The pumping system is composed of a primary pump (15 m^3/h) and a turbomolecular pump (400 l/s) connected in series and provides a pressure below 10^{-5} Pa.

The pumping system is connected to the vacuum chamber through a gate valve.

The pumping system and the vacuum vessel can be vented independently, for maintenance or during shutdown.

The pressure within the vessel is monitored by a full-range Pirani + Penning gauge, while the pressure at the output of the turbomolecular pump is measured by a Pirani gauge. Since these pressure gauges are robust they are preferred to monitor the plant, nevertheless their measurements are coarse and gas species dependent, thus they are not the best choice for the experimental point of view. Therefore a capacitive gauge, whose measuring range is limited to the one of interest, is connected to the vacuum vessel to measure its pressure more precisely. The capacitive gauge is composed of two small vacuum chambers, one connected to the VV and the other sealed, separated by a membrane which deflects depending on the pressure difference between the two chambers and modifying the capacitance, the quantity used to derive the pressure. The reading of the capacitive gauge does not depend on the gas species.

During experiments the gate valve can be either closed or open, depending on the test pressure: for pressures lower than 0.5 Pa the gate valve is open; for higher pressures the gate valve is closed to prevent wearing of the turbomolecular pump due to gas frictional load.

The main components of the pumping system are listed in Table 3-4.

Table 3-4 – List of the main pumping system components

Component	Description	Note
Full range gauge	Edwards wide range WRG-S-CF40	Measuring range $1000 - 10^{-9}$ mbar
Gate valve	Gate valve s.s. GVC060 CF160	Electro-pneumatic (24 V dc) with position indicators
Turbopump	nEXT400D CF160	Pumping speed (N_2) 400 l/s, Ultimate vacuum $< 10^{-10}$ mbar
Oil free primary pump	Scroll pump nXDS15i	Peak pumping speed 15.1 m^3/h ultimate vacuum: 0.007 mbar
Pirani gauge	Edwards NW25	Measuring range 1000-10^{-3} mbar
Pumping control system	TIC TURBOCONTROLLER 100W	Serial port RS232 to control the turbopump, 3 channels for active sensors
Active sensor controller	Oerlikon Leybold vacuum GRAPHIX ONE	-
Active sensor/Transmitter	Oerlikon Leybold vacuum CERAVAC CTR100N	Capacitive gauge $10^{-5} - 10^{-1}$ mbar

3.1.3.2   Gas injection system

The process gases to be used for the experiments are stored within gas reservoirs equipped with pressure reduction valves and connected to the VV through a gas inlet line.

The regulation of the gas flow to the vacuum chamber is provided by an all-metal variable leak manual valve that allows a fine adjustment of the VV pressure.

With reference to Table 3-3 the valve is mounted on the port 3, positioned about 90° away from both the pressure gauges on the port 4 and the pumps on the port 1.

Two different operative conditions are possible depending on the status of the gate valve which separates the vacuum vessel from the pumping system, as shown in Figure 3-7.
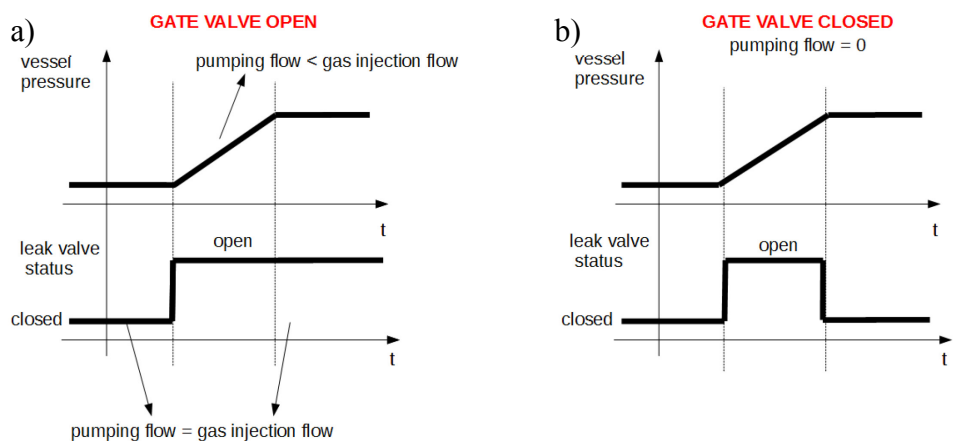
Figure 3-7 - Gas injection system operation

The gate valve can be operated only if the differential pressure is lower than 3 kPa.

When the gate valve is open the pressure within the vessel depends on the difference between the gas injection flow and the pumping flow; while when the gate valve is closed the static pressure depends on the quantity of injected gas. When working at relatively low pressures the outgassing from solid surfaces of many gas species concurs with the desired gas species injected on purpose, therefore the operation with the gate valve open is preferable. The operation with the gate valve closed can be exploited at intermediate pressures, when the outgassing rate does not increase the static pressure. The main advantage of this second operating condition is that the tests can be performed at relatively high pressure (>0.5 Pa) with the pumping system switched on without damages or stresses.

3.1.4 EM shielding box

The E-field and H-field produced by the HVRFTF are estimated to be 1000 V/m and 2.0 A/m at the distance of 2 m [53] from the center of the VV, where researchers operate the facility; these values exceed the exposure limits imposed by the Italian regulation at 1 MHz, therefore an EM shield is necessary.

A convenient arrangement is sketched in Figure 3-8 a): the RF circuit is placed below the VV, so that the VV support structure can also be used as support for the grounded passive structures of the EM shield (Figure 3-8 b); the live electrode is the bottom one, so that its E-field is screened by the VV.
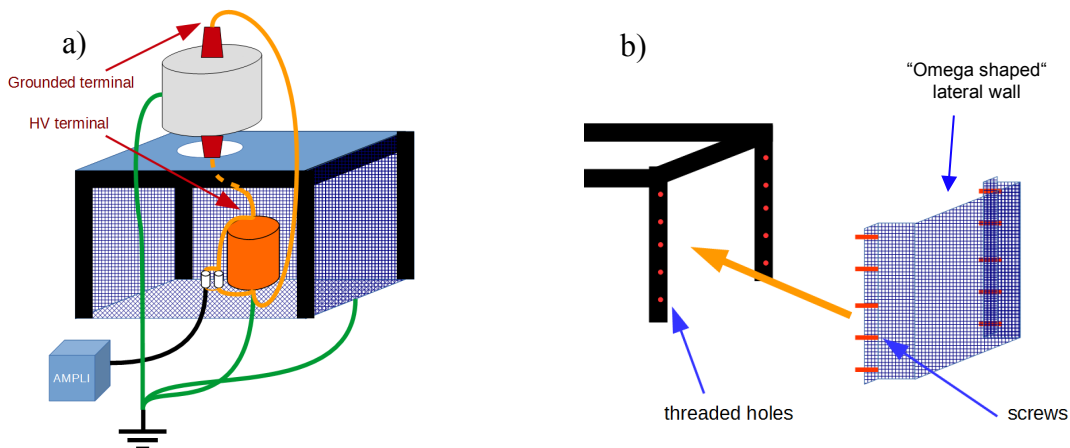
Figure 3-8 - Conceptual setup of the EM shield

The EM shielding box walls are made of perforated aluminum sheet to allow the natural air flow for the cooling of the internal components. The shielding effectiveness (SE) for H-field and E-field required to the EM shielding box, and the SE provided by a perforated sheet placed at 0.5 m from the source and evaluated at 2 m, are listed in Table 3-5.

Table 3-5 - Requirements for the EM shield

	E-field	H-field
Value of field @ 2 m from source	1000 [V/m]	2.01 [A/m]
Law limit @ 1 MHz	87 [V/m]	0.73 [A/m]
Shielding Effectiveness required to the shield	21.2 [dB]	8.8 [dB]
Shielding Effectiveness of perforated aluminum sheet 2 mm thick (placed at 0.5 m from the source and evaluated at 2 m)	178 [dB]	99 [dB]

The lateral walls of the EM shielding box are "Omega shaped" to increase the distance from the RF circuit components, to reduce the stray capacitance and the magnetic coupling.

3.1.5 Measuring equipment

The HVRFTF is equipped with instruments having appropriate bandwidth for the measurements of the experimental data and for monitoring the correct operation of the auxiliary systems.
Figure 3-9 shows the HVRFTF measuring points, each described in Table 3-6.
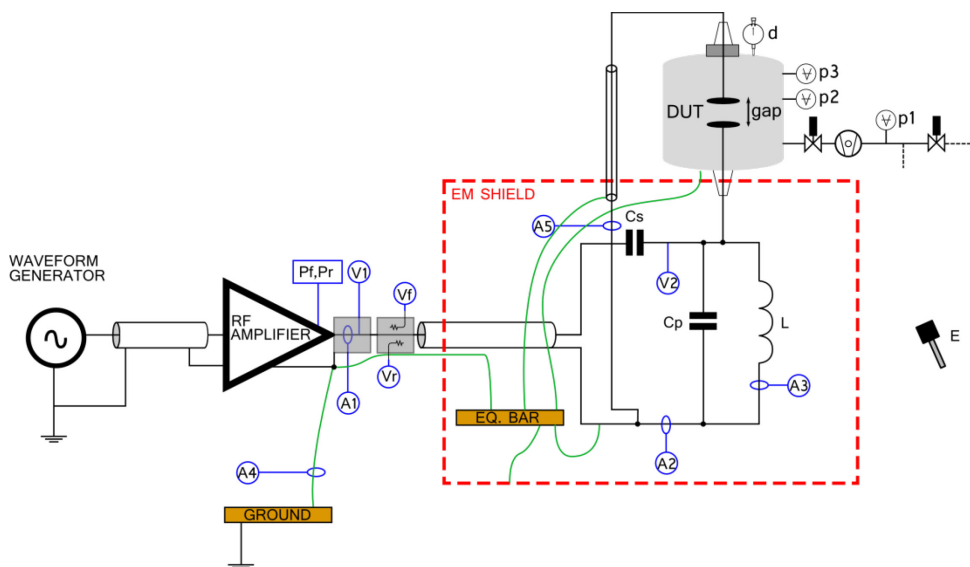
Figure 3-9 - Measuring points

Table 3-6 - List of measuring points and related instrument

Id	Measured quantity	Item	Model	Unit	Range	Sensitivity	Bandwidth
V1	Amplifier output voltage	Voltage probe	Yokogawa scope probe 700988	[V]	0- 600	n.a.	dc – 400 MHz
V2	Voltage applied to the DUT	Voltage probe	North Start PVM-5	[kV]	0 – 60	n.a.	dc – 80 MHz
Vf, Vr	Forward and reflected voltage	Dual directional coupler	Werlatone C5959-10	[V]	0 – 2	n.a.	0.1 – 30 MHz
Pf, Pr	Forward and reflected power	Amplifier	-	[W]	0 – 450	1	n.a.
A1	Amplifier output current	Current probe	Tektronix TCP312 + Tektronix TCPA300	[A]	0 - 5	0.001	dc – 100 MHz
A2	Current on the parallel branch (Cp//L)	Current probe	Tektronix TCP303 + Tektronix TCPA300	[A]	0 - 25	0.005	dc – 15 MHz
A3	Inductor current	Current probe	Pearson 301X	[A]	0 - 400	0.1	5 Hz – 2 MHz
A4	Ground current	Current probe	Tektronix TCP312 + Tektronix TCPA300	[A]	0 - 5	0.001	dc – 100 MHz
A5	DUT current	Current probe	Tektronix TCP312 + Tektronix TCPA300	[A]	0 - 25	0.005	dc – 15 MHz
p1	Primary pump pressure	Pirani gauge	Edwards NW25	[mbar]	$10^{-3} – 10^3$	10^{-3}	n.a.
p2	Vessel pressure	Full range pressure gauge	Edwards wide range WRG-S-CF40	[mbar]	$10^{-9} – 10^3$	10^{-9}	n.a.
p3	Vessel pressure	Capacitive pressure gauge	Oerlikon Leybold CERAVAC CTR100N	[Pa]	0.001 - 10	0.001	n.a.
d	Gap between electrodes	Comparator	Peacock 1361	[mm]	0 – 50	0.01	n.a.

Id	Measured quantity	Item	Model	Unit	Range	Sensitivity	Bandwidth
E	Electric field near operators	Electric field probe	NARDA 8718 + NARDA 8761D 300 kHz - 3 GHz, 20 mW/cm^2	[V/m]	0 – 200	0.001	300 kHz – 3 GHz

For the voltage holding characterization in particular the following measurements are required:
- Voltage applied to the DUT (V2);
- Gap between electrodes (d);
- Vessel pressure (p3);
- DUT current (A5).

The DUT pre breakdown current is usually employed with dc tests for the characterization of the materials and the geometry [42]. In HVRFTF the DUT current before the breakdown is orders of magnitude higher than with dc tests, due to the DUT stray capacitance; it is used as breakdown detection.

In HVRFTF the voltage applied to the DUT is used to detect the breakdown: in fact at the breakdown it reduces to the arc voltage.

The forward and reflected power can be used as well since at the breakdown the RF circuit mismatch, with a variation of both measurements.

The gap and the pressure identify a particular operating condition of the DUT. To be noted that the vessel pressure is measured via a capacitive pressure gauge, whose reading is independent of the gas type.

3.1.6 Operation of the facility
The HVRFTF finite states machine is shown in Figure 3-10.
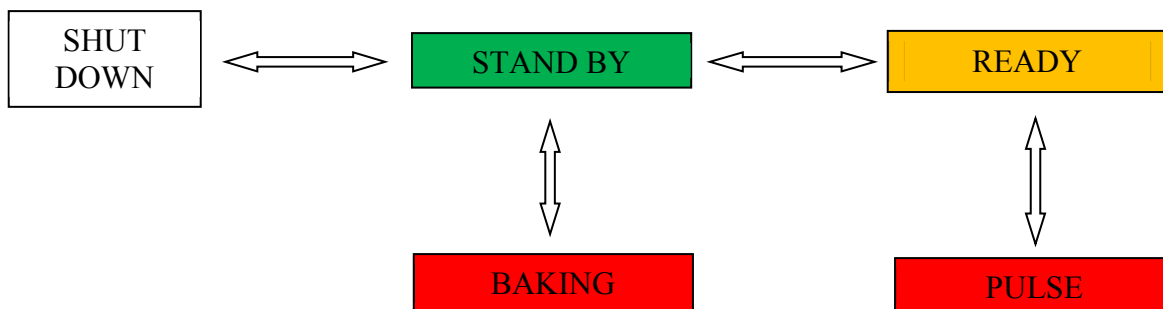
Figure 3-10 – HVRFTF finite states machine

Each state foresees the ON, OFF or DISCONNECTED status of different plant components as shown in Table 3-7.

Table 3-7 – Status of the plants with respect to the HVRFTF state

State	Pumping system	Control system	Baking system	RF amplifier
SHUT DOWN	DISCONNECTED	DISCONNECTED	DISCONNECTED	DISCONNECTED
STAND BY	ON	ON	DISCONNECTED	DISCONNECTED
BAKING	ON	ON	ON	DISCONNECTED
READY	ON	ON	DISCONNECTED	OFF
PULSE	ON	ON	DISCONNECTED	ON

A customized check-list has been prepared to assure safe transition from one state to the other.

To perform the experimental activity the HVRFTF has to be in the "READY" state; the comparator "d" (Figure 3-9) and the capacitive pressure gauge "p3" (Figure 3-9) have to be reset, in particular:

- The gap is set to 0 mm acting on the linear translator, and the continuity is verified with a multimeter. Then the comparator "d" is reset.
- The pumping system should work for at least a couple of days; the pressure on the vacuum vessel measured with the full range valve "p2" has to be lower than 10^{-7} mbar. Then the capacitive gauge "p3" can be reset.

The HVRFTF operation is pulsed; with reference to the time sequence shown in Figure 3-11 for each pulse the following operations are performed, starting from the READY state:

- t<t0: The gap and the pressure are adjusted to the desired value;
- t=t0: The RF amplifier is switched ON (transition from "READY" to "PULSE");
- t=t1: The waveform generator (which drives the amplifier) is switched on and drives the RF amplifier with a sinusoidal waveform with 0.5 V amplitude at the frequency of 1 MHz;
- t1<t<t2: The frequency is varied to seek the resonance, at which the high voltage (V2) is maximized and the reflected voltage/power are minimized;
- t2<t<t3: The high voltage is increased up to the desired value acting on the waveform generator output voltage;
- t3<t<t4: The high voltage is maintained for the test time
- t4<t<t5: Then high voltage is decreased to 0 V;
- t = t5: The waveform generator and the RF amplifier are switched OFF.
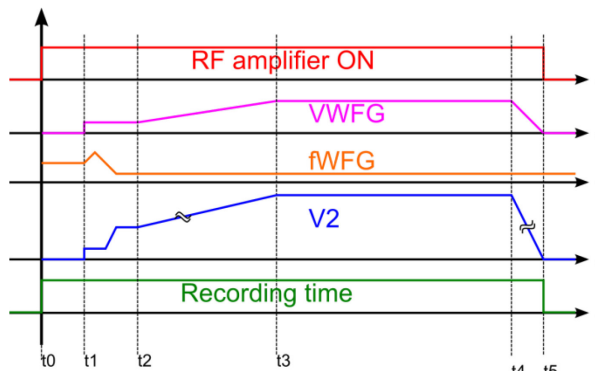
Figure 3-11 – Time sequence of a HVRFTF pulse.
Red curve: RF amplifier status
Magenta curve: waveform generator output voltage (rms value)
Orange curve: frequency of the waveform generator output voltage
Green curve: Recording time

In the event of a breakdown the time sequence is modified: from the breakdown time there is a jump to t4.

3.1.7 Control and data acquisition system

The HVRFTF control and data acquisition system (CODAS) conceptual scheme is shown in Figure 3-12. The signals exchanged with the field are listed in Table 3-8.
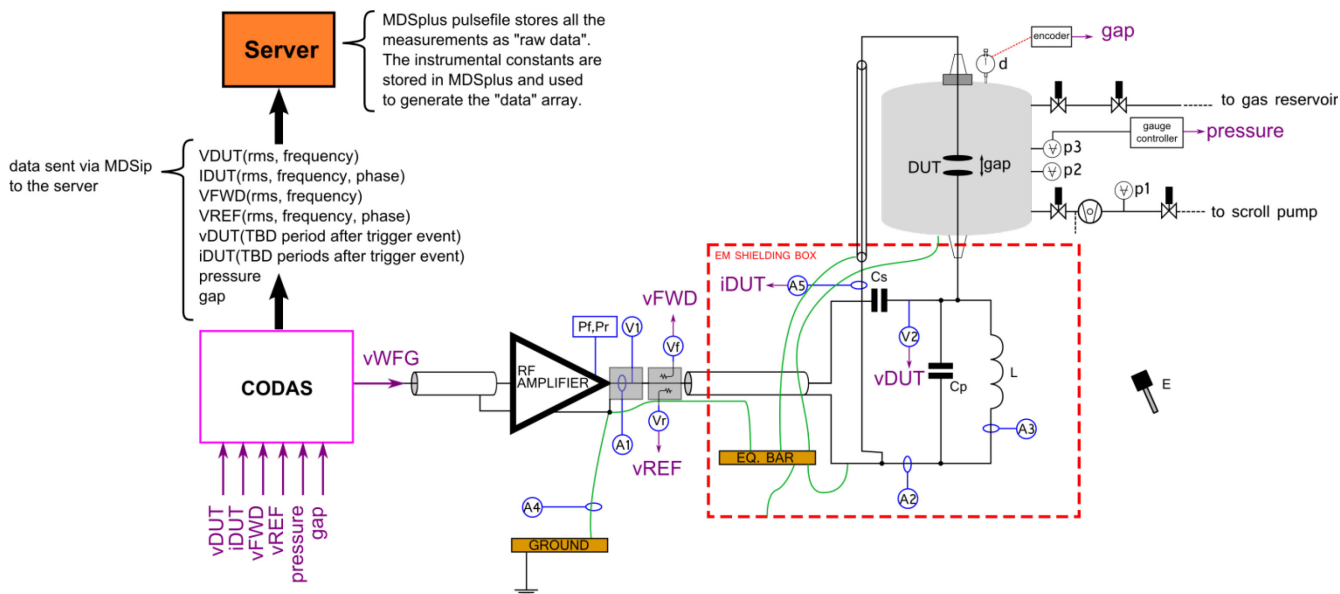
Figure 3-12 – CODAS conceptual scheme

Table 3-8 - Signals from/to the field elaborated by CODAS

Signal id	Description	Sampling frequency	Type	Note
vDUT	Instantaneous voltage applied to the DUT	125 MS/s	Input	
iDUT	Instantaneous current flowing in the DUT	125 MS/s	Input	
vFWD	Instantaneous forward voltage measured by Dual Directional Coupler	125 MS/s	Input	
vREF	Instantaneous reflected voltage measured by Dual Directional Coupler	125 MS/s	Input	
vWFG	Instantaneous reference voltage for the RF amplifier	125 MS/s	Output	
pressure	Instantaneous VV pressure	10 S/s	Input	Controller response time 100 ms
gap	Instantaneous Gap distance	0.1 S/s	Input	

At the moment CODAS is still under development and only the part related to the data acquisition of fast signals is commissioned and working; the slow signals are not acquired and the sinusoidal waveform which drives the RF amplifier is not generated by CODAS but manually through a waveform generator instead.

The instantaneous value of the fast signals of Table 3-8 acquired from the field are elaborated by CODAS to calculate the corresponding rms value, frequency and phase delay which are then stored on a MDSplus server [54] [55].

Other measurements from the field (listed on Table 3-6) are acquired and visualized on oscilloscopes for diagnostic purpose and are not recorded by default.

The hardware architecture of CODAS is shown in Figure 3-13:

- A server runs MDSplus;
- The fast signals are acquired by means of two Redpitaya STEMlab 125-14 boards [56], sent to the HMI and stored in the MDSplus server;
- The slow signals are acquired by a RaspberryPi board [57] with an R-adapt shield [58], sent to the HMI and stored to the MDSplus server;
- A pc is used to visualize the HMI, while the stored data can be visualized with jScope [59];
- The different devices communicate via cabled network through an Ethernet switch.
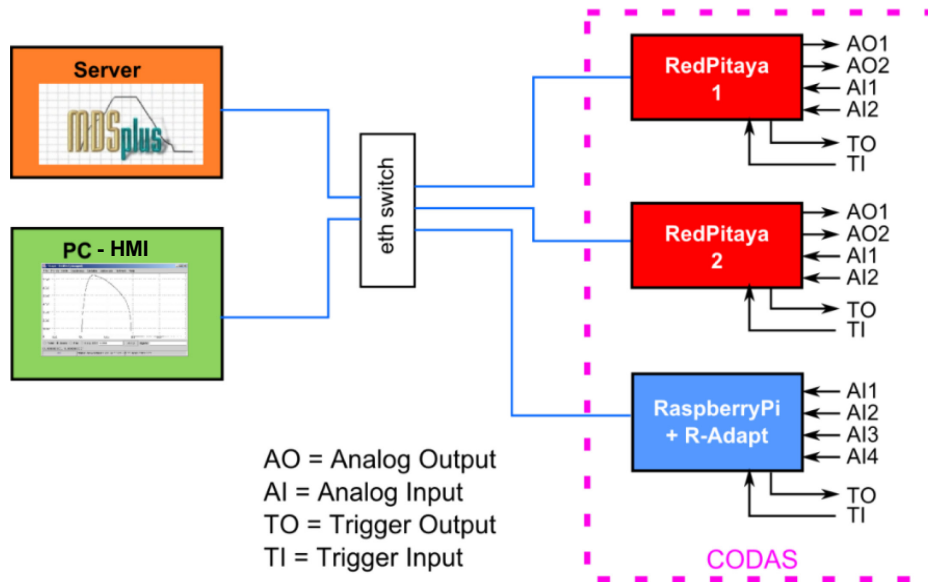
Figure 3-13 – CODAS hardware architecture

3.1.8 Low voltage distribution system

The different electrical loads of the HVRFTF are supplied by a low voltage distribution system whose conceptual scheme is shown in Figure 3-14.

Two racks serve the HVRFTF equipment:

- Rack 1 serves the control section (for the pumping system, the baking system, the amplifier) and it is placed near the operator desk;
- Rack 2 serves the RF amplifiers, the data acquisition boards and the auxiliary electronics for the transducers; it is placed near the vacuum vessel.
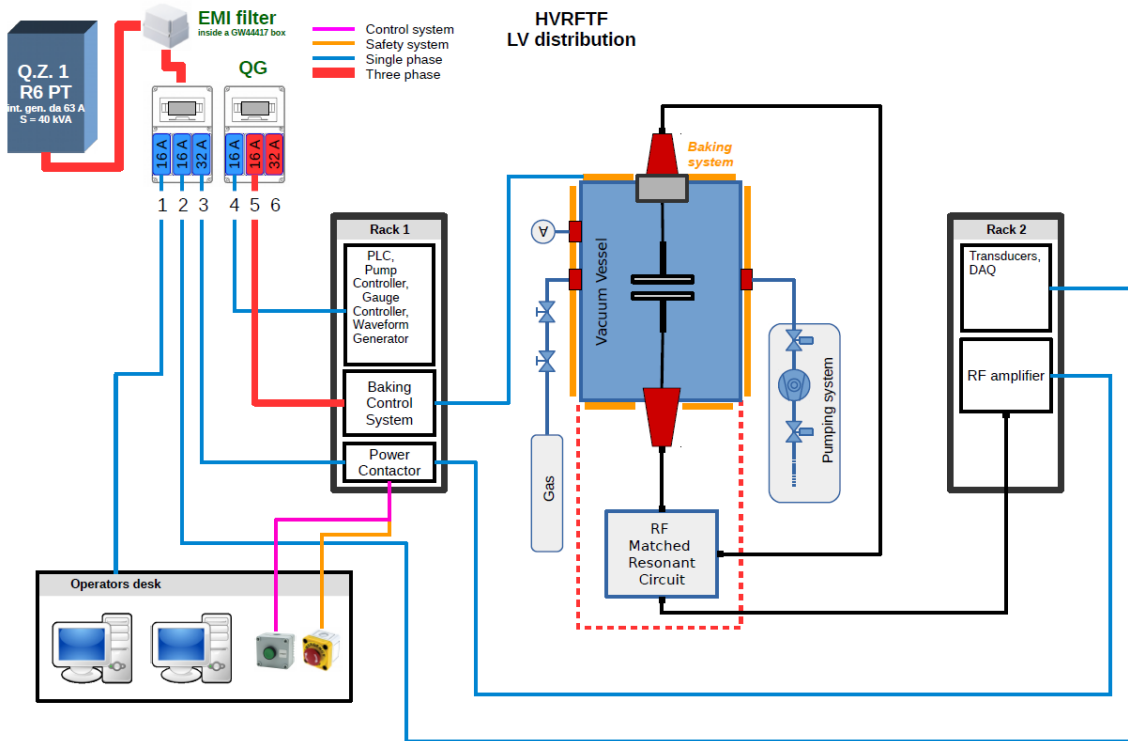
Figure 3-14 – Conceptual scheme for the low voltage distribution system

The operators desk hosts the computers with the HMI for the experiment and the control buttons for the switch ON and OFF of the RF amplifier.

3.2 Final layout

A top view of the layout of the HVRFTF is shown in Figure 3-15, and a picture of the facility is shown in Figure 3-16
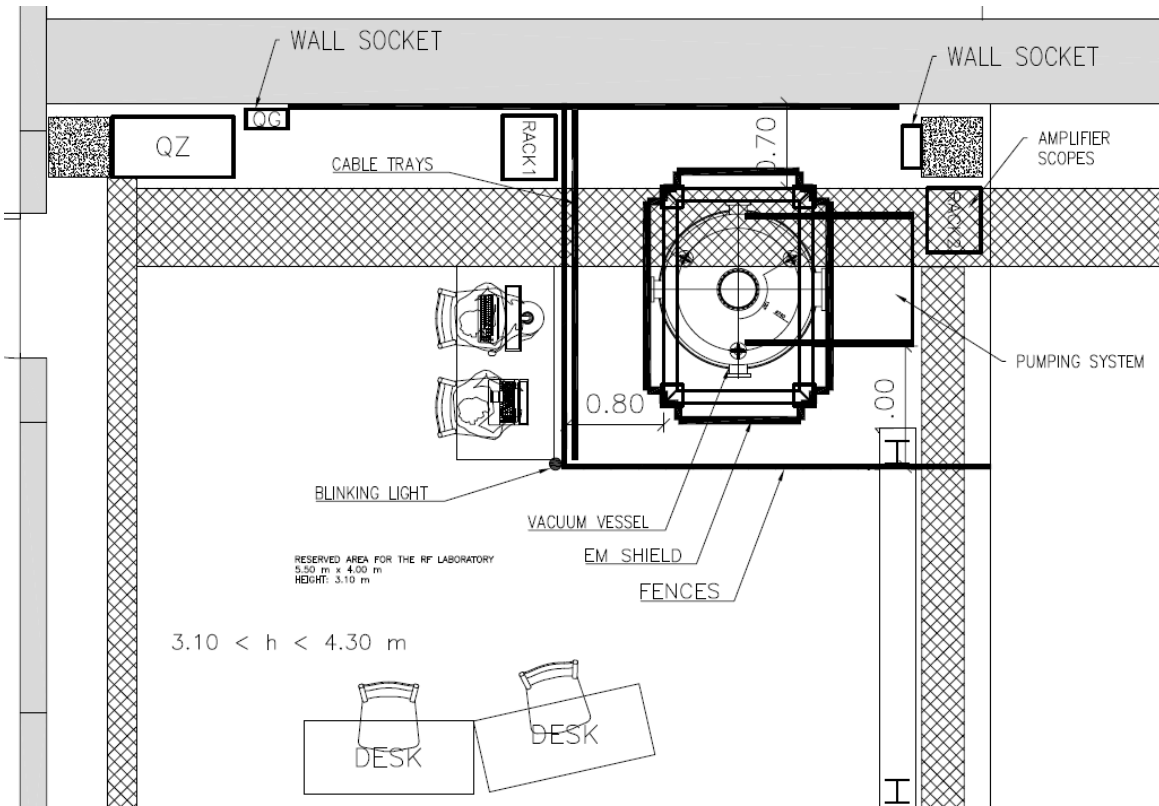
Figure 3-15 - Top view of the HVRFTF layout

Figure 3-16 – Picture of the HVRFTF (early 2017)

4 Studies for the definition of the Device Under Test

In order to verify the voltage hold off of a driver, it is necessary to recreate its working conditions when inside the ion source (gas species, pressure, sinusoidal voltage at the operating frequency), and to test it by increasing the applied voltage amplitude up to the breakdown.

Nevertheless, besides the complexity and cost of this type of Device Under Test (DUT), this approach prevents to test different design solutions in terms of geometry and materials and also the possibility to perform parametric studies, for instance with a varying gap .

On the contrary, simpler DUT geometries in a flexible arrangement allow these opportunities, and thus they are preferable, provided that they are able to reproduce with sufficient accuracy the operating conditions of interest.

Figure 4-1 shows the cross section sketch of several geometries of electrode pairs, which have been studied; their suitability for the DUT to be tested with HVRFTF is discussed below.
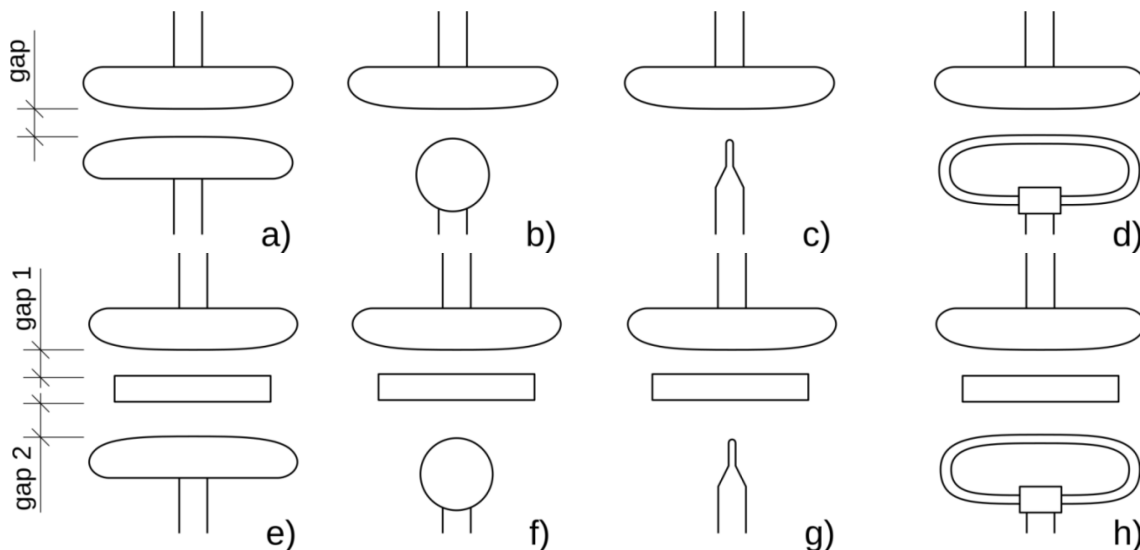
Figure 4-1 - Sketch of the cross section of different DUT: a) Planar circular electrodes, b) plane-sphere DUT, c) plane-tip DUT, d) plane-tube DUT. The same configurations with a dielectric slab in between the electrodes are e),f),g),h).

They can be grouped into two categories of DUT:
- DUT composed only of electrodes without dielectric material (a,b,c,d of Figure 4-1);
- DUT composed of electrodes with a dielectric material interposed in between them (e,f,g,h of Figure 4-1).

The DUTs of first group do not have a dielectric material between the electrodes (first difference with respect to the driver) and are characterized by a single gap (second difference); nevertheless, they are simple and in particular configurations a) and b) are commonly used to perform voltage hold off tests.

The second group is considered more suitable to be a mockup of the driver since it can simulate the triple junction which is present in the driver configuration; in fact, the electrodes can represent the driver Faraday Screen (FS) and the RF coil turn at high voltage respectively, while the dielectric disk can represent the driver case (DC). The gap between the top electrode and the dielectric disk is called gap1 and the gap between the dielectric disk and the bottom electrode is called gap2 for similarity with the gaps inside the SPIDER driver described in section 2.5.

It is worth noting that the RF coil of the driver is fed by a voltage applied across its terminals, and that the coil turns are at intermediate voltage values; while in the configurations shown in Figure 4-1 one electrode is grounded and the other is at the voltage applied to the high voltage terminal of the RF coil.

In the following, each geometry is described and the related E-field map obtained with a 2D finite element electrostatic model (FEM) is shown. Each FEM model is also used to derive the E-field value as a function of the gap in the range of 0-1 mm for the DUT without dielectric and for a gap2 in the range of 0-1 mm with a fixed gap1 of 2 mm for the DUT with the dielectric.

The dimensions assumed for each configuration are listed in Table 4-1.

Table 4-1 - Geometry assumed for the analyses

Configuration	Component	parameter	unit	value	note
a, e	Top electrode	Diameter	mm	108	Planar electrode
		Thickness	mm	22	
		Edge	-	-	Rogowski profile [60]
	Bottom electrode	Diameter, Thickness, edge	-	-	Same as top electrode
b, f	Top electrode	Diameter, thickness, edge	-	-	Same as top electrode of configuration a)
	Bottom electrode	Diameter	mm	40	Spherical electrode
c, g	Top electrode	Diameter, thickness, edge	-	-	Same as top electrode of configuration a)
	Bottom electrode	diameter	mm	8	Hemispherical tip
d, h	Top electrode	Diameter, thickness, edge	-	-	Same as top electrode of configuration a). Note that the analysis is carried out with a 2D planar model for this configuration
	Bottom electrode	diameter	mm	8	Tubular electrode
		length	mm	TBD	Infinite length is assumed in the planar model, for both the electrodes.
		edge radius	mm	TBD	

All the analyses for the configurations a,b,c,d, are run with a voltage of 12.2 kV rms applied to the bottom electrode, 0 V applied to the top electrode and a gap in the range of 0-1 mm.

The studies on the E-field for the configurations e,f,g,h, are carried out by applying the same voltage and assuming an alumina dielectric disk 8 mm thick, gap1 of 2 mm and gap2 in the range of 0-1 mm.

4.1 Metal-Vacuum-Metal DUT

4.1.1 Configuration a): Planar circular electrodes

The configuration a), which is composed of two planar circular electrodes (PCE) with a Rogowski profile [60], creates an uniform electric field in between the electrodes and avoids the intensification at the edge as can be seen on Figure 4-2, for the gap width of 0.1 mm. The E-field value depends on the gap and on the applied voltage, and is easy to be calculated analytically as $E=V_{DUTp}/gap$, where V_{DUTp} is the peak voltage applied to the DUT.

This configuration is widely treated in literature since it generates the most reproducible experimental regime to identify physical processes influencing the breakdown conditions.
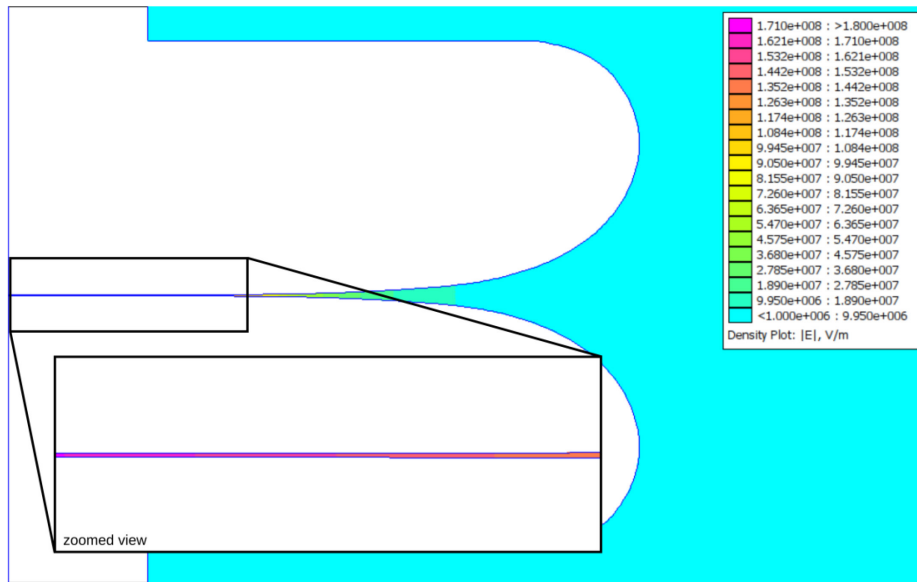
Figure 4-2 – DUT configuration a): E-field map
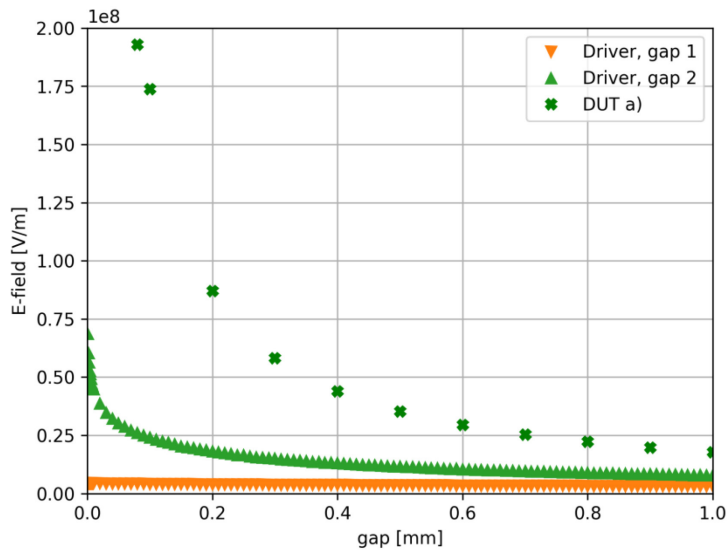
Figure 4-3 - DUT configuration a): E-field as a function of the gap

The E-field produced by this configuration (green cross markers of Figure 4-3) is much higher than the E-field at the turn at highest voltage in the driver (green triangle markers of Figure 4-3), therefore the

configuration a) is not directly relevant for the driver; however, it is interesting to teste it since the results can be compared to those documented in the literature for the validation of the basic test assessment.

4.1.2 Configuration b): Plane-sphere electrodes

The configuration b) is composed of a plane and a spherical electrode. The generated E-field is not uniform in between the electrodes, on the contrary it intensifies as the distance between the electrodes reduces (due to the curvature of the sphere): at the axis where the distance is the minimum, the value of the E-field is the maximum. Figure 4-4 shows the E-field map for the gap width of 0.1 mm and a sphere of 40 mm. With equal gap and applied voltage, the width of the region at high E-field depends on the radius of the sphere, and the maximum value is close to the one reached with configuration a) when the sphere radius is sufficiently higher than the gap. The plane-sphere configuration has been widely used with dc or pulse tests to verify the effect of the intensification of the E-field at the electrodes.
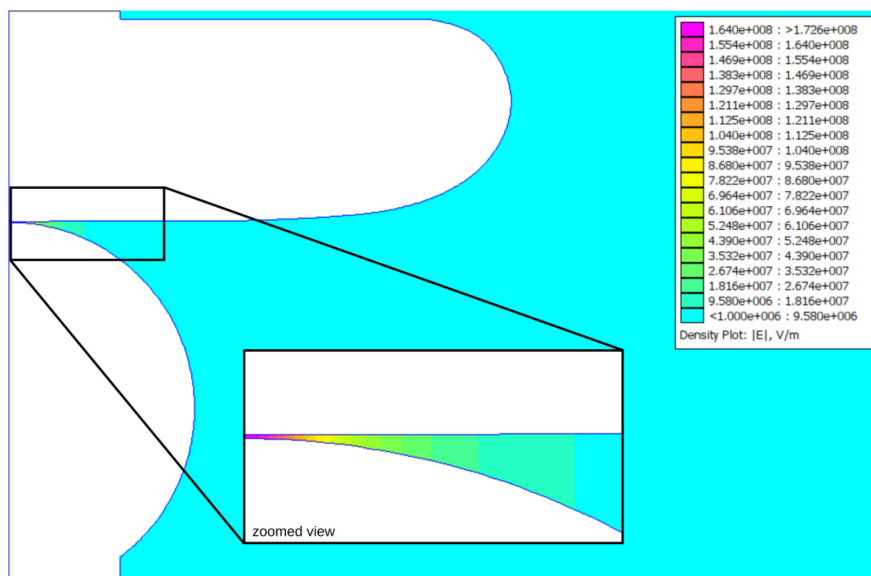
Figure 4-4 - DUT configuration b): E-field map
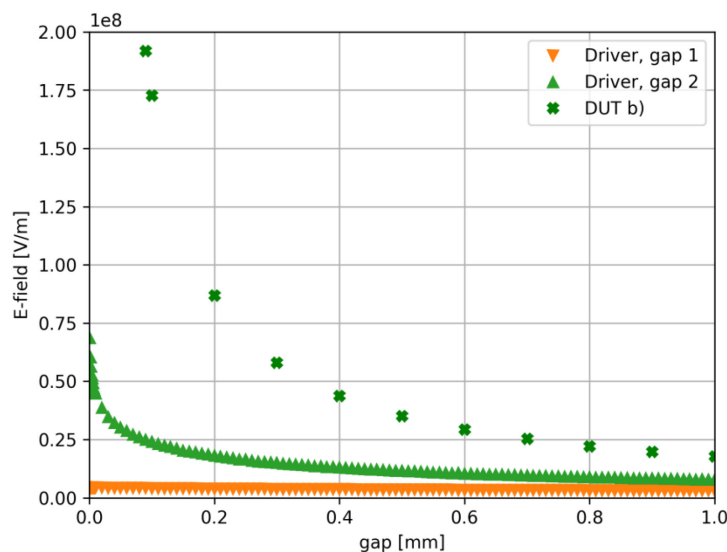
Figure 4-5 - DUT configuration b): E-field as a function of the gap

The E-field produced by this configuration at the minimum distance between the electrodes (green cross markers of Figure 4-5) is very similar to the one of configuration a), and therefore much higher than the E-field at the turn at highest voltage of the driver coil (green triangle markers of Figure 4-5).

4.1.3   Configuration c): Plane-tip electrodes

The configuration c) is conceptually the same as b), but in this case the sphere radius is the radius of support, thus the electrode has the shape of a tip with a hemispherical edge. The E-field map produced by a tip having the radius of 4 mm with a gap 0.1 mm is shown in in Figure 4-6. In this case the high E-field region is narrower with respect to the one generated by configuration b), while the maximum E-field value is very similar.
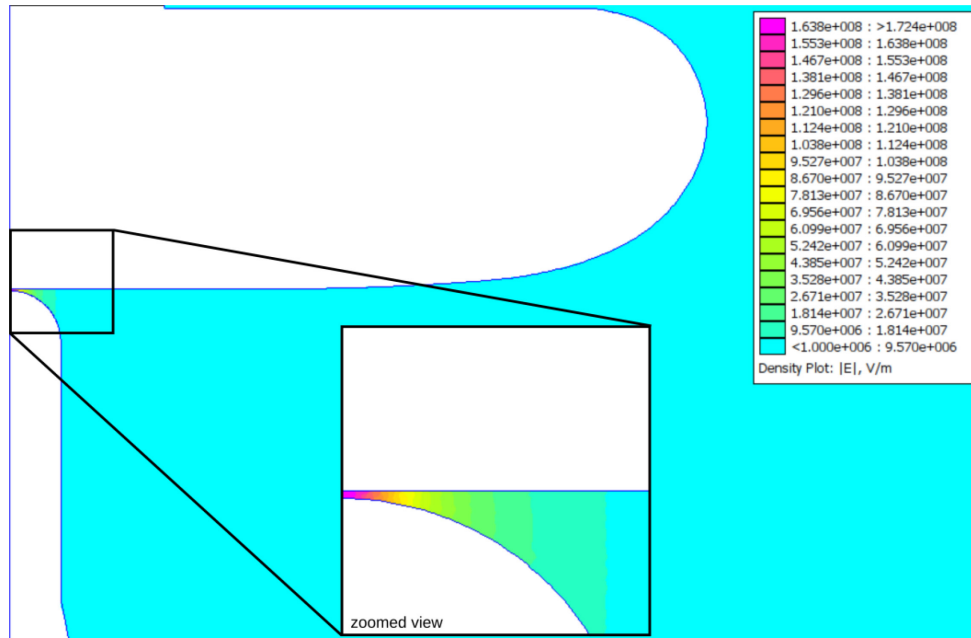
Figure 4-6 - DUT configuration c): E-field map
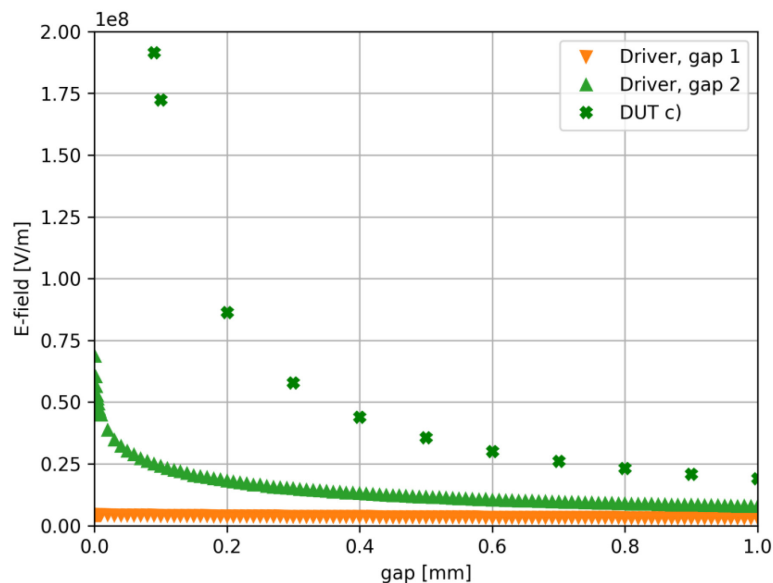
Figure 4-7 - DUT configuration c): E-field as a function of the gap

49

The E-field produced by this configuration at the minimum distance between the electrodes (green cross markers of Figure 4-7) is similar to the one of configurations a) and b), and therefore much higher than the E-field at the turn at highest voltage of the driver coil (green triangle markers of Figure 4-7).

4.1.4 Configuration d): Plane-tube electrodes

The configuration d) is composed of a planar electrode and a tubular electrode. It is more similar to the driver, where the planar electrode represents the Faraday Screen and the tubular electrode represents the RF coil conductor. The intensification of the E-field in this case is not on the axis since the configuration is not axisymmetric; the intensification is instead along the tube and depends on the radius of the tube. In Figure 4-8 the E-field map derived with a 2D planar finite element model, for a tube having a radius of 4 mm and a gap of 0.1 mm, is shown. A 3D model which takes into account the tube edge effects would be more precise in the calculation of the E-field.
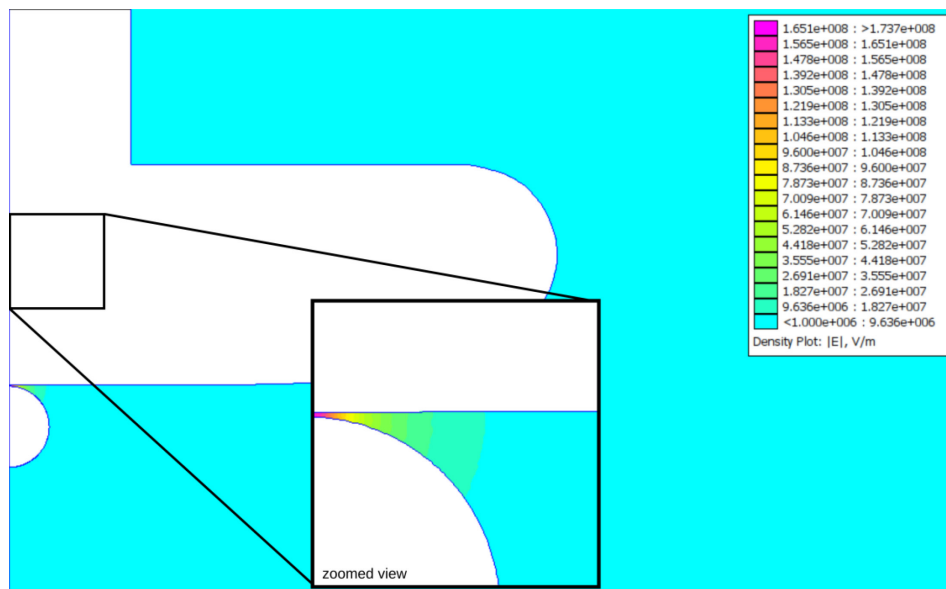
Figure 4-8 - DUT configuration d): E-field map
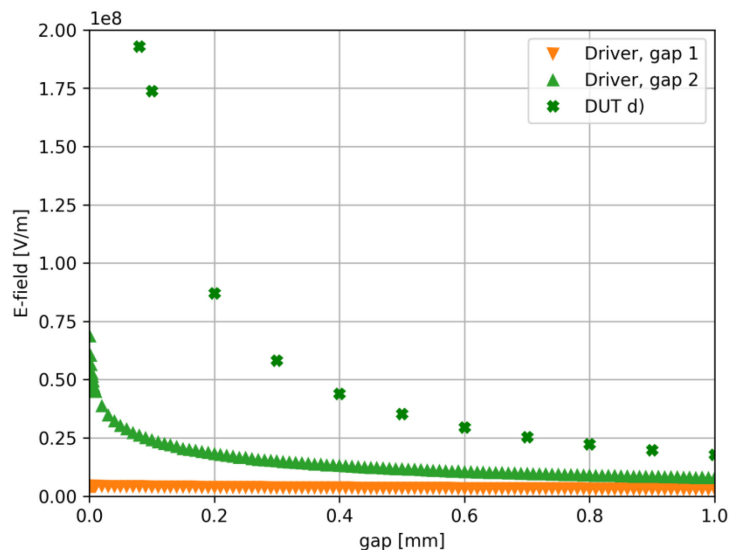
Figure 4-9 - DUT configuration d): E-field as a function of the gap

The E-field produced by this configuration at the minimum distance between the electrodes (green cross markers of Figure 4-9) is similar to the one of configurations a), b) and c), and therefore much higher than the E-field at the turn at highest voltage of the driver coil (green triangle markers Figure 4-9).

4.1.5 Remarks

These analyses show that the E-field trend in the DUT gap remains substantially the same changing the bottom electrode shape and that all these configurations are not suitable for reproducing the E-field in the gap regions of the SPIDER driver.

4.2 Metal-Dielectric-Metal DUT

4.2.1 Configuration e): Plane-disk-plane

The relatively high dielectric constant of the disk inserted between the electrodes expels the E-field from the dielectric material; for configuration e) the E-field is given by

$$E = \frac{V_{DUTp}}{gap^*} = \frac{V_{DUTp}}{gap1 + gap2 + \dfrac{DielThick}{\varepsilon_r}} \tag{3}$$

Where:
- V_{DUTp} is the peak voltage applied to the DUT;
- DielThick is the dielectric thickness;
- ε_r is the dielectric relative permittivity.

The E-field map is shown in Figure 4-10 for gap2 of 0.1 mm, while the E-field calculated on gap1 and gap2 as a function of gap2, with a fixed gap1 of 2 mm, is shown in Figure 4-11.
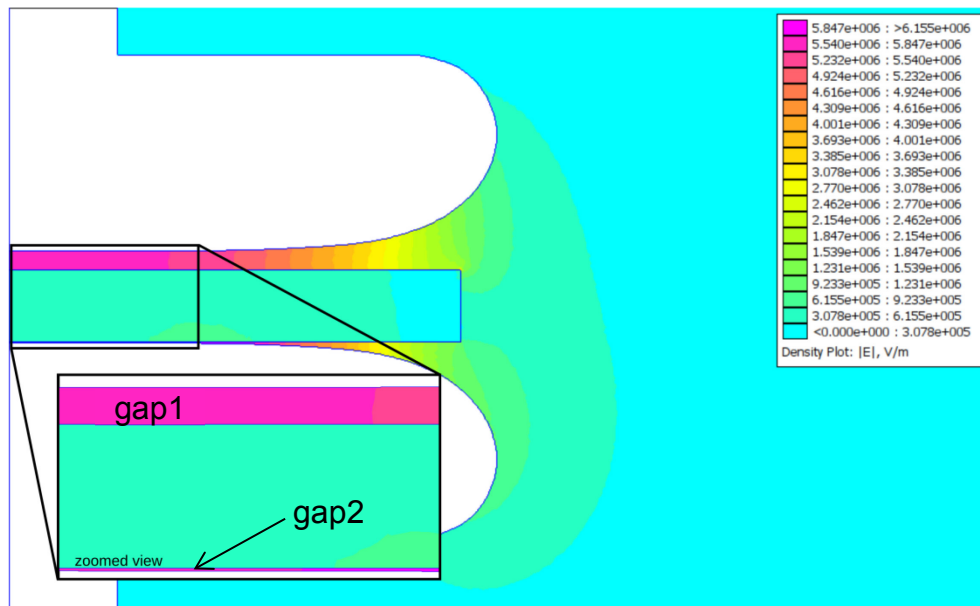
Figure 4-10 - DUT configuration e): E-field map
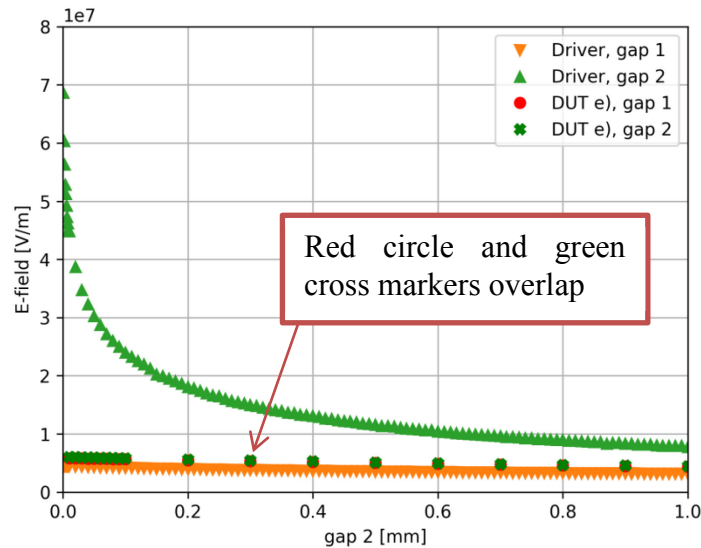
Figure 4-11 - DUT configuration e): E-field as a function of the gap

The E-field produced by the DUT is equal for gap1 and gap2 (red circle and green cross markers overlap in Figure 4-11), and it is different from the one of the driver on both gaps (triangle markers of Figure 4-11). Thus configuration e) is not relevant for the test purpose and it is excluded.

4.2.2 Configuration f): Plane-disk-sphere

Configuration f) produces an intensification of the E-field at the surface of the spherical electrode facing the dielectric disk, similar to what happens in the driver for gap2.

The E-field map is shown in Figure 4-12 for gap2 of 0.1 mm, while the E-field as a function of gap2 is shown in Figure 4-13. It is worth noting that the trend of the E-field obtained with this DUT is similar to the one of the driver, and in particular for a gap2 of 10 μm it is the same: in fact green cross and green triangle markers overlap.

On the contrary the E-field on gap1 is lower with respect to the one of the driver; however, it has to be pointed out that in the driver that gap is not in vacuum but in the area filled with gas at about 0.3 Pa.
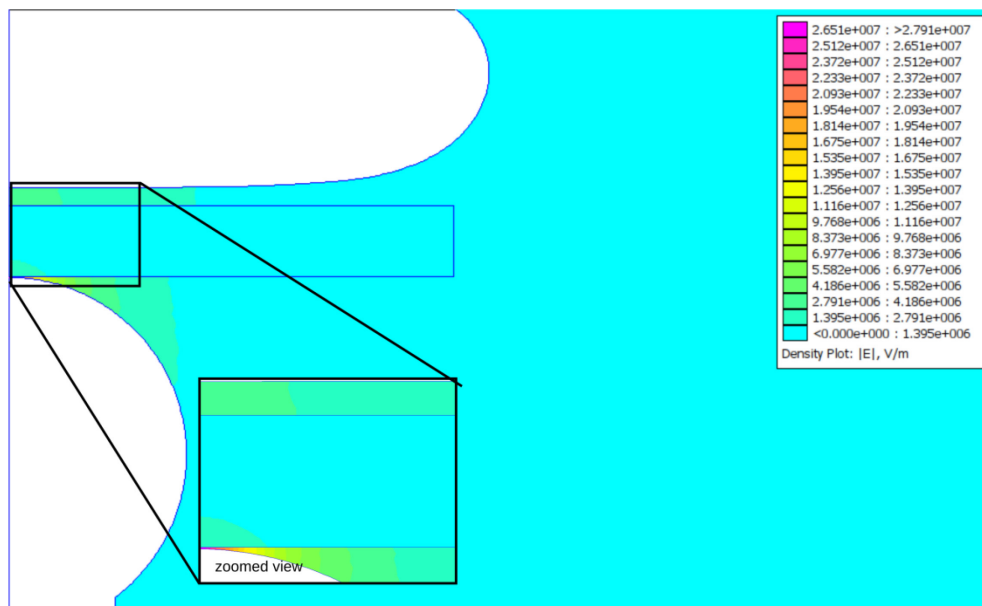
Figure 4-12 - DUT configuration f): E-field map
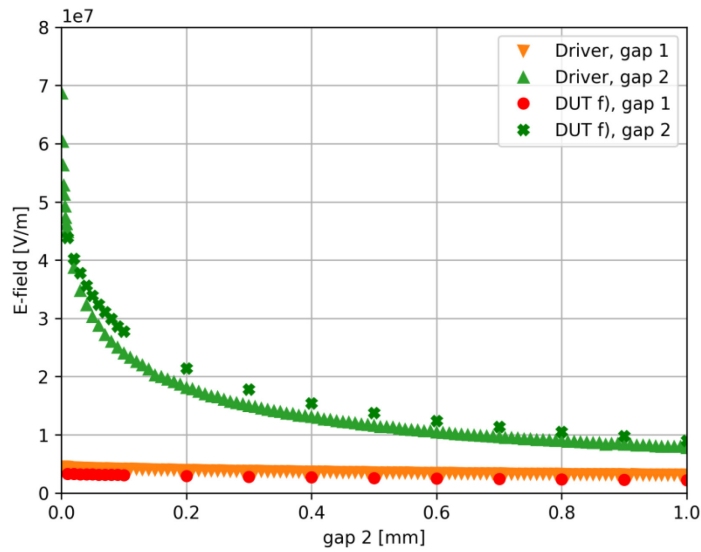
Figure 4-13 - DUT configuration f): E-field as a function of the gap

4.2.3 Configuration g): Plane-disk-tip

Configuration g) is characterized by a local intensification of E-field at the tip surface. The E-field values are much higher than those of the driver in gap2, while they are lower in gap1.

The E-field map is shown in Figure 4-14 for gap2 of 0.1 mm, while the E-field as a function of gap2 is shown in Figure 4-15.
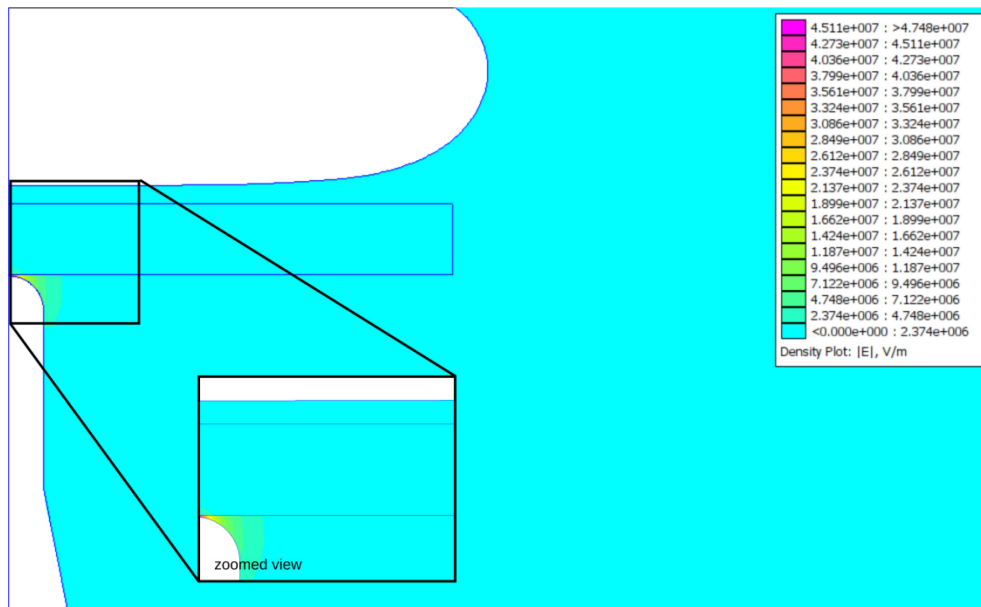
Figure 4-14 - DUT configuration g): E-field map
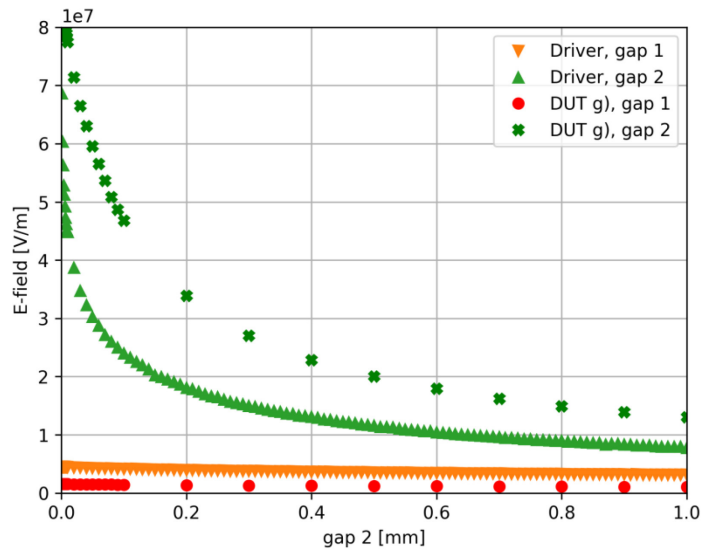
Figure 4-15 - DUT configuration g): E-field as a function of the gap

4.2.4 Configuration h): Plane-disk-tube

Configuration h) is the most similar to the driver geometry, provided that the driver radius is much larger than the radius of the coil conductor. The E-field map is shown in Figure 4-16 for gap2 of 0.1 mm, while the E-field as a function of gap2 is shown in Figure 4-17: as can be seen, the E-field is similar to the one produced by the driver for gap2 in the order of 0.1 mm.
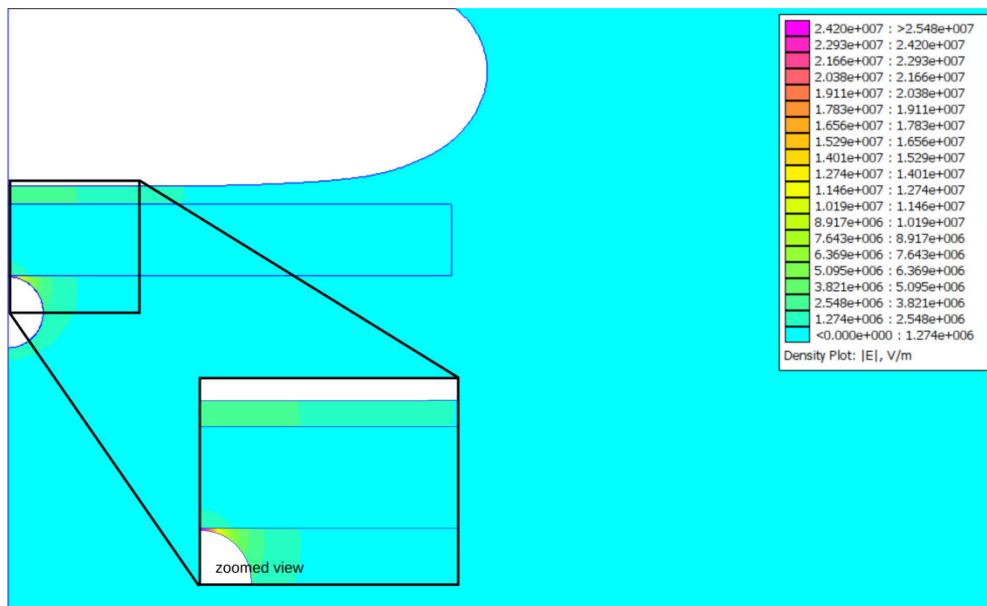
Figure 4-16 - DUT configuration h): E-field map
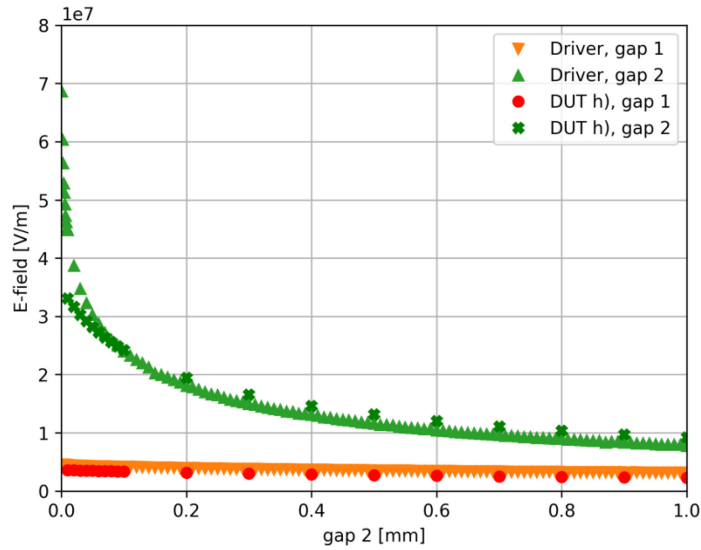
Figure 4-17 - DUT configuration h): E-field as a function of the gap

4.2.5 Remarks

The results show that none of the configurations is able to reproduce the E-field on gap2 for all the gap2 range. Configurations f) and h) produce the E-field closest to the one of the driver for gaps of about 10 μm and 100 μm respectively. Configuration g) could also be considered as DUT, since it produces E-field values larger than in the driver thus representing a worst case.

Configuration f) is much simpler than configuration h) which may introduce edge effects, and it is preferred as configuration to be further explored to find out diameters of the sphere at which the E-field produced is similar to the one of the driver (for the gap2 width covering at least the range expected in the driver).

4.3 Further studies of configuration f)

The aim of these studies is to identify the diameters of the spheres which are required to obtain E-field values similar to that ones of the driver. In particular three gaps have been considered for the analyses: 10 μm, 100 μm and 300 μm.

A 2D electrostatic axisymmetric FEM model has been built assuming an alumina disk 8 mm thick (the thickness of the driver case) interposed in between the two electrodes, fixed gap1 of 2 mm, fixed gap2 of 10 μm and the diameter of the sphere ranging from 5 mm to 65 mm. The E-field is calculated by applying 12.2 kV rms to the sphere and 0 V to the planar electrode.

The E-field trends at the DUT gaps (solid lines) as a function of the sphere diameter are shown in Figure 4-18; the figure shows also E-field at the driver gaps (dashed lines), with gap1 of 2 mm and gap2 of 10 μm.
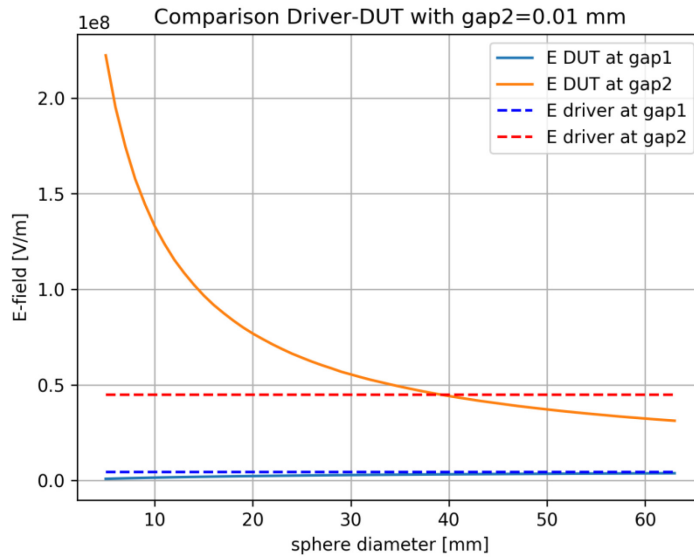
Figure 4-18 – E-fields at gap1 and gap2, as a function of the sphere radius, with gap2 = 10 µm

The sphere diameter which makes the E-field similar to the one of the driver for gap2=10 µm is of 39 mm. The diameter of 40 mm is taken as reference.

The same procedure is repeated for gap2=0.1 mm, and the E-field at the DUT and driver gaps as a function of the sphere diameter is shown in Figure 4-19.
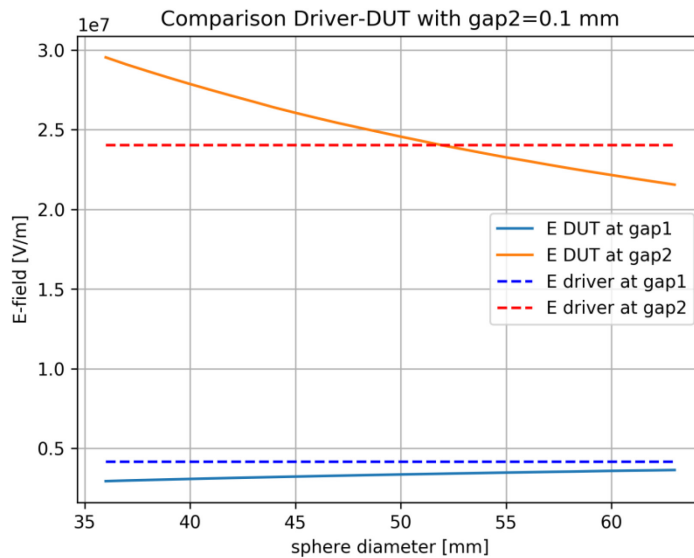
Figure 4-19 – E-fields at gap1 and gap2, as a function of the sphere radius, with gap2 = 0.1 mm

The sphere diameter which makes the E-field similar to the one of the driver for gap2=100 µm is of 52 mm. The diameter of 50 mm is taken as reference.

For gap2 width of 0.3 mm the E-field as a function of the sphere radius is shown in Figure 4-20.
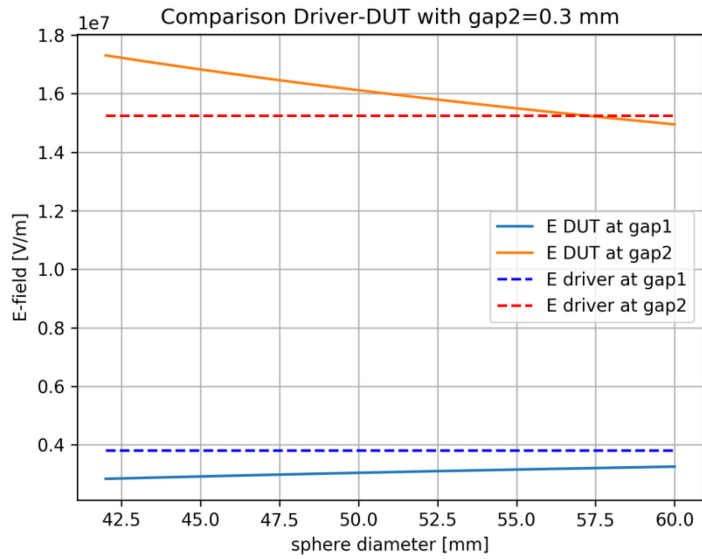
Figure 4-20 – E-fields at gap1 and gap2, as a function of the sphere radius, with gap2 = 0.3 mm

The sphere diameter which makes the E-field similar to the one of the driver for gap2=300 μm is of 57.5 mm. The diameter of 60 mm is taken as reference.

Figure 4-21 shows the plot of the E-field on gap2 as a function of gap2 produced by the driver, by the f) type DUT having the sphere diameter of 40 mm, 50 mm and 60 mm:
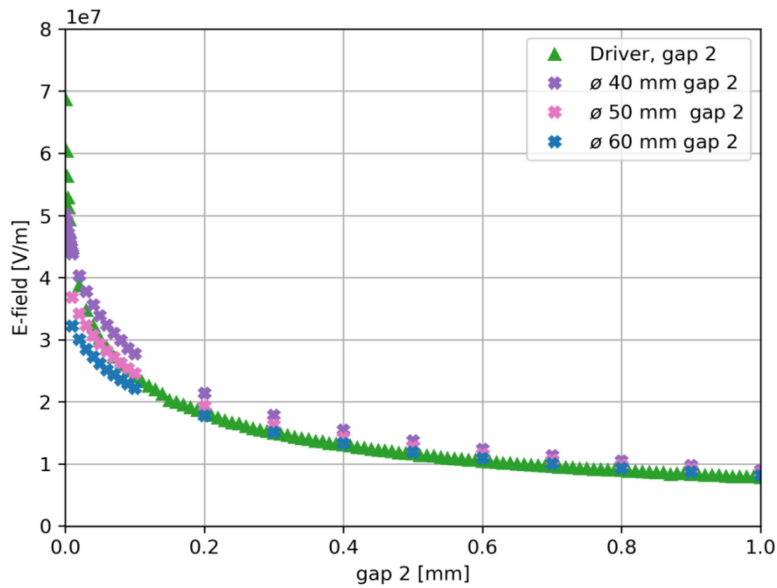
Figure 4-21 – E-field produced on gap2 by the driver and by the DUT f) having the sphere diameter of 40 mm, 50 mm and 60 mm

Figure 4-22 shows the relative difference between the E-field produced by the DUTs and by the driver with the same gap2 width.
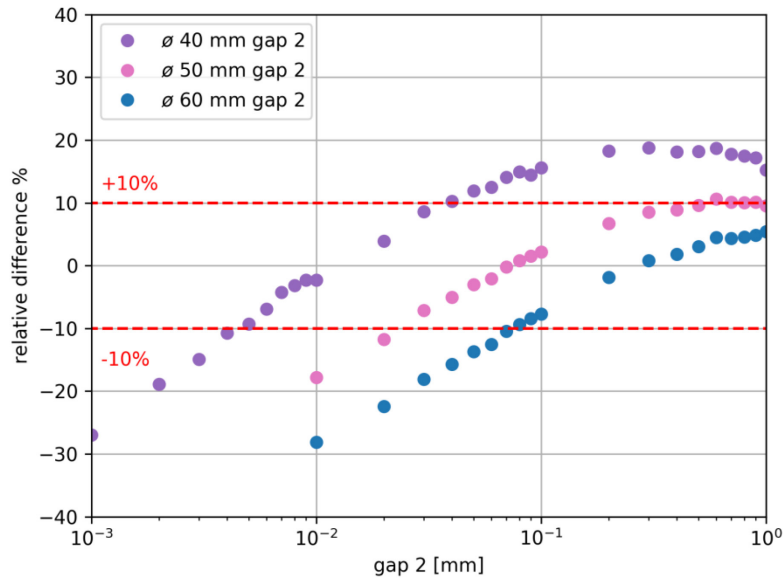
Figure 4-22 – E-field produced on gap2 by the driver and by the DUT f) having the sphere diameter of 40 mm, 50 mm and 60 mm

The set of the three spheres considered for DUT f) produces E-field values showing a relative difference of less than ±10% from those of the driver in the entire gap2 range from 40 µm to 1 mm. The calculation results indicate that a single DUT is not able to reproduce the whole E-field curve with gap2 ranging from 0 mm to 1 mm, but the combination of three type f) DUTs having spheres with different radius allow a satisfactory approximation of driver operating conditions in terms of applied voltage, E-field amplitude and gap width.

4.4 Device under test in the HVRFTF

For the HVRFTF the plan is to perform tests on:
- Planar Circular Electrodes (geometry described in paragraph 4.1.1), identified as PCE;
- Plane Disk Sphere DUT (geometry described in paragraph 4.2.2), with sphere diameters:
  - 40 mm, identified as "PDS40";
  - 50 mm, identified as "PDS50";
  - 60 mm, identified as "PDS60";
- Plane Disk Tip DUT (geometry described in 4.2.3), with a hemispherical tip of 8 mm in diameter, identified as "PDS8".

The DUT materials were already listed in Table 3-2.

4.4.1 DUT equivalent electric circuit

From an electrical point of view, the DUT can be represented by a capacitance with an equivalent series resistance (Figure 4-23 a)); both depend on the geometry of the electrode pair, on the gap between the two electrodes, and on the properties of the dielectric material in between. In particular,

the capacitance depends on the permittivity of the dielectric material while the resistance depends on its loss angle.

The parallel representation of the DUT, shown in Figure 4-23 b), is convenient to be used in some cases.

$$\dot{Z}_{DUT}=R_{DUT} - jX_{C_{DUT}}$$
$$X_{C_{DUT}}=-j(\omega C_{DUT})^{-1}$$

$$\dot{Z}_{DUT}=[(R_{DUT}*)^{-1} +(- jX_{C_{DUT}}*)^{-1}]^{-1}$$
$$X_{CDUT}*=-j(\omega C_{DUT}*)^{-1}$$
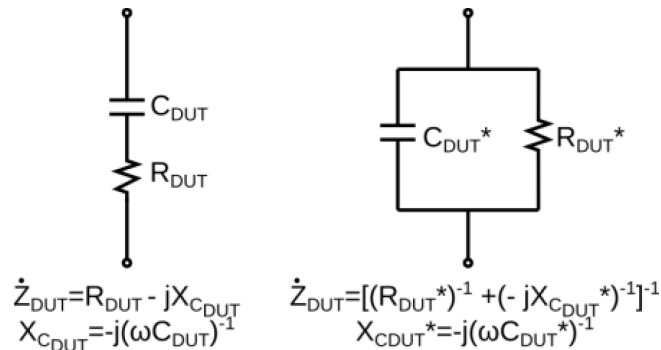
Figure 4-23 – Series and parallel equivalent circuital representation of the DUT

The geometry, the gap and the dielectric materials are parameters that can be varied during the experimental campaigns. Moreover, the vacuum vessel acts as a third electrode too, and creates an additional capacitance in parallel to the DUT impedance. The equivalent impedance of DUT and vacuum vessel are taken into account for the design of the circuit used to generate the high voltage described in chapter 5.

The capacitance and resistance of the DUTs considered suitable for the HVRFTF have been calculated through electrostatic and current flow analyses respectively, with the help of 2D axisymmetric finite elements models. The electrical parameters of the PCE have been calculated for a gap of 100 μm and 50 mm, while for the Plane-Disk-Sphere DUTs they have been calculated with disk thickness of 8 mm, fixed gap1 = 2 mm and for gap2 of 10 μm and 50 mm. Alumina was assumed as dielectric material, since it is the material used in SPIDER for the driver case, and furthermore it is characterized by the highest permittivity (see Table 3-2) resulting in the highest capacitance.

The obtained values for the capacitance and the resistance, for both the series and parallel representations are reported in Table 4-2. The loss angle of Alumina is not the highest and in principle with Vespel or Quartz the equivalent series (parallel) resistance could be higher (lower), but it is clear that the DUT resistance can be neglected when looking at the values in Table 4-2.

Table 4-2 - Electrical parameters of the DUTs with alumina as dielectric material (where C_{DUT} and R_{DUT} refer to the series representation, $C_{DUT}{}^*$, $R_{DUT}{}^*$ to the parallel representation)

DUT ID	Description	Gap	C_{DUT}	R_{DUT}	$C_{DUT}{}^*$	$R_{DUT}{}^*$
PCE	Planar Circular Electrodes diam. 108 mm	100 μm – 50 mm	177 – 12 pF	0 Ω	177 – 12 pF	-
PDS8	Plane - Dielectric Disk - Sphere diam. 8 mm	10 μm – 50 mm	11 – 10 pF	67 mΩ – 1.9 mΩ	11 – 9 pF	> 1 GΩ
PDS40	Plane - Dielectric Disk - Sphere diam. 40 mm	10 μm – 50 mm	13 pF – 10 pF	162 mΩ – 7.8 mΩ	13 pF – 10 pF	> 1 GΩ
PDS50	Plane - Dielectric Disk - Sphere diam. 50 mm	10 μm – 50 mm	14 – 10 pF	164 mΩ – 3.6 mΩ	14 – 10 pF	> 1 GΩ
PDS60	Plane - Dielectric Disk - Sphere diam. 60 mm	10 μm – 50 mm	15 – 11 pF	157 mΩ – 4.2 mΩ	15 – 11 pF	> 1 GΩ

5 Studies for the generation of High Voltage

Radiofrequency high voltage sources are not industrial products. Common RF voltage sources available in the market are oscillators or RF amplifiers and they are specifically designed for laboratory, broadcasting and induction heating applications. For our application the use of RF amplifiers is preferable, since they are full controllable voltage source and, differently from the oscillators, their operation is not influenced by the load.

Both oscillators and RF amplifiers are available for a wide range of power and for relatively low load impedances, usually 50 Ω resistance, which is very different from the DUT impedance listed in Table 4-2.

The exploitation of the resonance principle to produce the required high voltage was identified as a viable solution, with the constraint that the impedance seen by the amplifier has to be matched to its output impedance to extract its full power. The description of the general approach and its application for the design of the RF circuit are given in the following paragraphs.

5.1 Matched resonant circuit

A L-type matching network is composed of a couple of reactances jX_1 and jX_2, two kinds of L-type matching networks are possible, as shown in Figure 5-1:
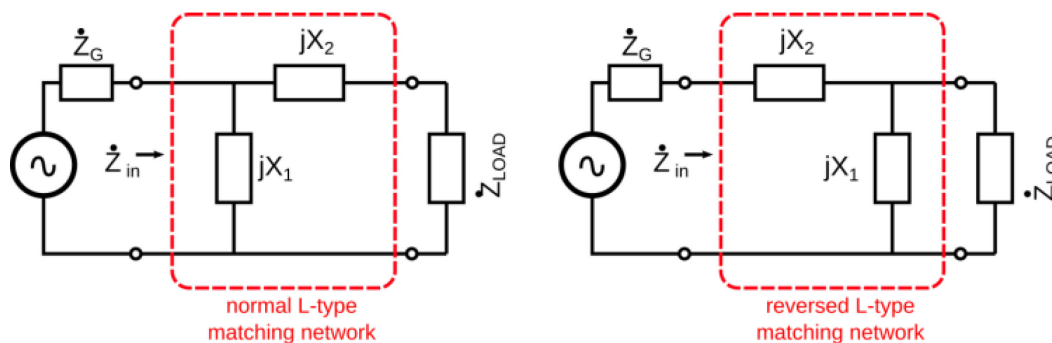
Figure 5-1 – Normal and reversed L-type matching network

An arbitrary load impedance Z_{load} may be matched to any impedance [38] by a normal L-type matching network or by a reversed L-type matching network. Sometimes both normal and reversed types allow the desired matching.

The reversed L-network was selected for our scope; it is characterized by a series resonance between jX_2 and the parallel of jX_1 and Z_{LOAD}..

A key point is related to the definition of the Z_{load}: the first choice could be the assumption of the DUT impedance, but a variable capacitance as load would require a variable inductor as matching network component, which is not convenient neither for the construction, nor for the operation point of view. In addition the inductor would introduce a significant variable stray resistance, to be considered in the design of the matching network itself, making the design even more complex. In fact, not only the reactances, but also the stray resistances contribute to the modification of the input port equivalent impedance (Z_{in}), thus to the achievement and maintenance of the matching conditions.

The approach followed was to connect an inductor in parallel to the DUT and to assume their equivalent impedance as Z_{load}: $\dot{Z}_{Load} = R_{Load} + jX_{Load}$.

The inductance of the inductor has been selected such that the X_{load} reactance remains inductive in the full ranges of the operating frequency and of the DUT capacitance; this condition can be formulated as:

$$\sqrt{(L \cdot C_{DUTmax})^{-1}} > \omega_{max} \tag{4}$$

Where:
- L is the inductance of the inductor [H];
- C_{DUTmax} is the maximum capacitance of the DUTs (the one of the PCE with the smallest foreseen gap) [F];
- ω_{max} is the maximum foreseen angular frequency [rad/s];

This design solution allows avoiding variable inductors in the matching network, which can be composed by capacitors only.

The resulting circuit topology is shown in Figure 5-2.
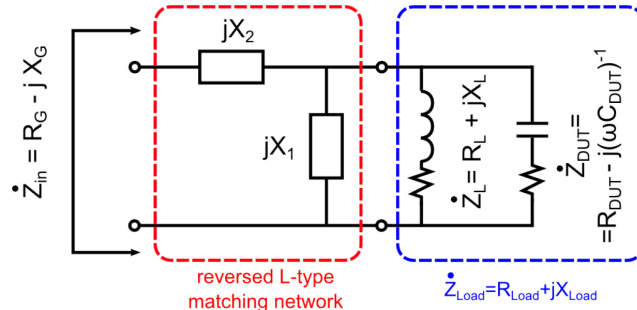
Figure 5-2 - Scheme of the reversed L-type network with the inductor in parallel to the DUT as load

To simplify the schematization, it has been preferred to convert the inductor and DUT series impedances to the parallel representation as in Figure 5-3, using the following equations

$$R_L^* = \frac{R_L}{\cos^2(\text{atan}(X_L/R_L))} \tag{5}$$

$$X_L^* = \frac{X_L}{\sin^2(\text{atan}(X_L/R_L))} \tag{6}$$

$$R_{DUT}^* = \frac{R_{DUT}}{\cos^2(\text{atan}(X_{DUT}/R_{DUT}))} \tag{7}$$

$$X_{DUT}^* = \frac{X_{DUT}}{\sin^2(\text{atan}(X_{DUT}/R_{DUT}))} \tag{8}$$

Where:
- R_L is the stray resistance of the inductor with the series representation [Ω];
- X_L is the reactance of the inductor with the series representation [Ω];
- R_{DUT} is the stray resistance of the DUT with the series representation [Ω];
- X_{DUT} is the reactance of the DUT with the series representation [Ω];
- The symbol * identify the aforementioned parameters with the parallel representation.

Both the DUT and the inductor impedances are characterized by a reactance much higher than the resistance $X_L \gg R_L$, $X_{DUT} \gg R_{DUT}$, which allows the simplifications $X_L^* \approx X_L$ and $X_{DUT}^* \approx X_{DUT}$, as in Figure 5-3.
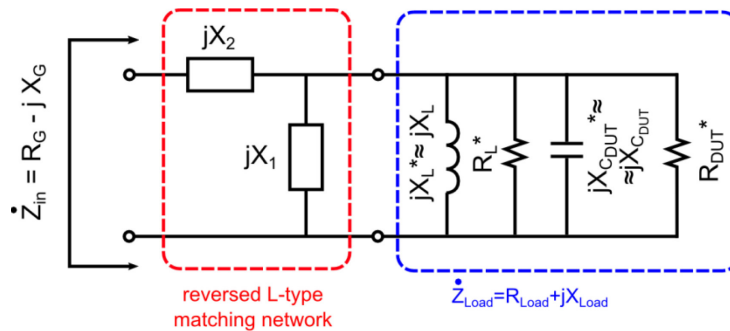
Figure 5-3 - Scheme of reversed L-type network with parallel representation of the DUT and inductor impedances

The reactances jX_1 and jX_2, are calculated as follows:

$$X_1 \mid Re\left(\frac{jX_1 \cdot \dot{Z}_{Load}}{jX_1 + \dot{Z}_{Load}}\right) = Re\left(\dot{Z}_G\right) \tag{9}$$

$$X_2 = -Im(\dot{Z}_G) - Im\left(\frac{jX_1 \cdot \dot{Z}_{Load}}{jX_1 + \dot{Z}_{Load}}\right) \tag{10}$$

Where $\dot{Z}_G = R_G + jX_G$ is a generic voltage source impedance.

If the load impedance is inductive and the resistive part is lower than the real part of $\dot{Z}_G$, both X_1 and X_2 result capacitive reactances.
The selection of vacuum capacitors, characterized by a low ESR, as matching components, allows to disregard their stray resistances and to assume pure capacitances, simplifying their schematization as shown in Figure 5-4.
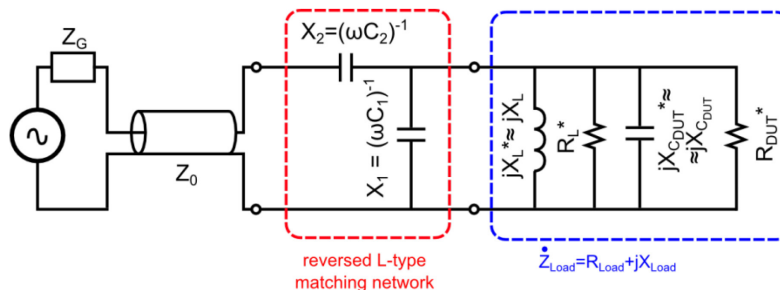
Figure 5-4 – Simplified scheme of the complete RF circuit

The compensation of the DUT capacitance and resistance variation surely requires that C_1 is a variable capacitance. Furthermore a variable C_1 is necessary to cover the working frequency range. Looking at equation (10), it can be appreciated that also C_2 should be variable, since it is a function of the variable load impedance.

5.2 Design of the RF circuit

The amplifier output impedance and the estimation of the load impedance are necessary to design the matching network components.

As far as the amplifier output impedance is concerned, the value of 50 Ω is assumed. While for the estimation of the load impedance it is necessary to define the inductor ratings.

Once all the circuit components are defined, the performances of the circuit in terms of voltage gain and power requirements can be calculated.

5.2.1 Inductor

5.2.1.1 Identification of the inductance value

The inductor is the component characterized by the highest power losses, defined as:

$$P = R_L \left(\frac{V_{target}}{|\dot{Z}_L|} \right)^2 \tag{11}$$

Where:
- P is the power dissipated in the inductor [W];
- R_L is the inductor stray resistance [Ω];
- Z_L is the inductor impedance [Ω];
- V_{target} is the target voltage to be reached across the DUT [V].

Assuming $R_L \ll X_L$, it is possible to derive the following relationship:

$$P \propto \frac{R_L}{X_L^2} = \frac{R_L}{(\omega L)^2} = \frac{1}{\omega L Q} \tag{12}$$

Where:
- X_L is the inductor reactance [Ω];
- L is the inductor inductance [H];
- $Q = X_L/R_L$ is the inductor quality factor [-].

The relation (12) highlights that a high reactance is desirable, thus the inductance for a fixed frequency, even if it can imply an increase of the winding stray resistance and a reduction of the quality factor.

However, there is an upper limit for the inductance value that can be derived by equation (4) and expressed as follow:

$$L < \frac{1}{\omega_{max}^2 \cdot C_{DUTmax}} \tag{13}$$

The highest DUT capacitance, which is the one offered by the PCE for the lowest gap, is equal to 170 pF; thus, the maximum value for the inductance, calculated at the maximum frequency of 1.1 MHz (see Table 3-1) is equal to 149 μH.

To leave margin for the conservation of the matching condition by varying C1, L should be sufficiently lower than the limit of equation (13). In addition, there are feasibility constraints related to the inductor size, which further limit the maximum inductance. An inductance value around 70 μH at 1 MHz was selected.

5.2.1.2 Manufacturing design

Dimensions of about 0.5 m (diameter) x 0.5 m (height) have been considered reasonable; as for the construction method, an air core single layer solenoid has been adopted to reduce as much as possible the stray capacitances [61] with an air gap between turns sufficient to avoid low self-resonance frequency and to sustain the turn to turn voltage.

A high frequency single layer solenoid electrical model was developed (see appendix paragraph I) to predict the impedance of the inductor at the desired frequency and its natural resonance frequency. The model was validated against measurements on inductor samples built on purpose or available at Consorzio RFX; see appendix paragraph 0.

The model predicts the impedance and the inductance at 1 MHz with a relative error lower than 15%; the natural resonance frequency is underestimated which means that the stray capacitances are overestimated. The predicted stray resistance is lower than the measured one (error up to 50%).

These results highlighted the need of building the inductor and to characterize its impedance before designing the matching network.

During the inductor test campaign, solenoids built with different approaches were built and characterized with the aim to reduce the inductor stray resistance: litz wire (paragraph II.ii.l) and rectangular cross section wire (paragraph II.ii.m) were tested, but with poor results (paragraphs II.iv II.v respectively).

A more effective design was identified in a small scale inductor composed of two identical single layer solenoids turn to turn insulated, magnetically coupled and with terminals connected in parallel (paragraph II.ii.j): the measured stray resistance of the inductor was 1.6 times lower than the resistance of a single solenoid (paragraph II.ii.i), while the inductance is only slightly reduced. The test was repeated on an inductor composed of four identical single layer solenoids (paragraph II.ii.k), the measured stray resistance in this case was a third of the one of the single solenoid.

The inductor designed and manufactured for the HVRFTF is composed of two insulated single layer solenoids, magnetically coupled and connected in parallel, as shown in Figure 5-5.
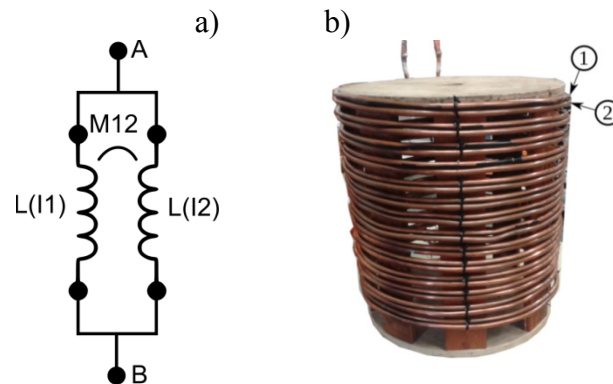
Figure 5-5 - Conceptual scheme of the HVRFTF inductor a), picture of the HVRFTF inductor b)

The inductor characteristics are listed in Table 5-1.

Table 5-1 – HVRFTF construction characteristics

Material	Copper
Diameter of the inductor [cm]	49
Height of the inductor [cm]	47
Diameter of the wire [cm]	1.2
Distance between the two solenoids [mm] (approximatively)	0.1
Pitch [cm]	3.5
Number of turns	14

The impedance meter HP4194A was used to characterize the inductor and measure both its inductance and resistance at high frequency.

Figure 5-6 shows the inductor impedance absolute value and the phase measured outside the EM shielding box with floating terminals and with a grounded terminal (red and green curves), and inside the EM shielding box with floating terminals and with a grounded terminal (blue and yellow curves). It is possible to appreciate the influence of the grounding and of the passive structures on the inductance value.
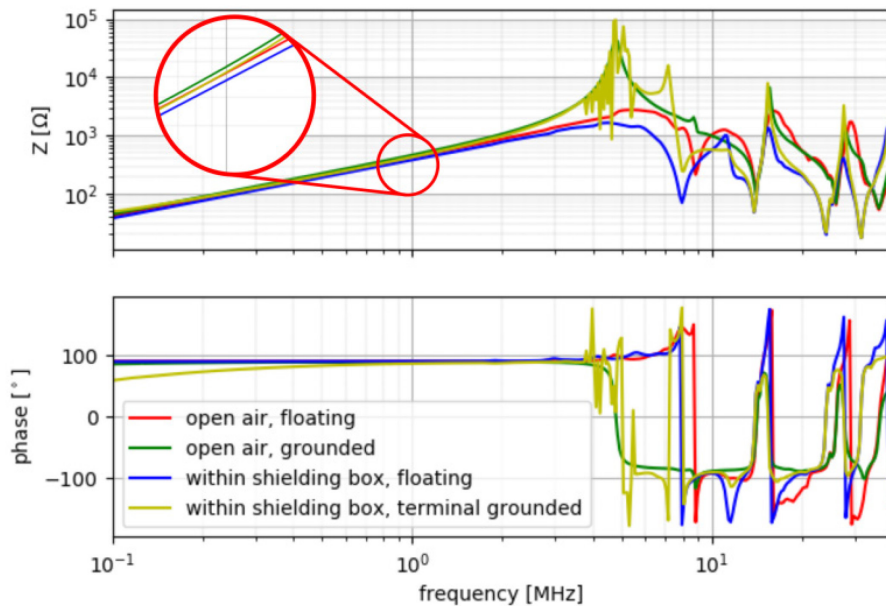
Figure 5-6 – HVRFTF inductor measured impedance: top plot absolute value of the impedance, bottom plot phase.
Red curve: inductor outside the EM shielding box, with floating terminals
Green curve: inductor outside the EM shielding box, one terminal grounded
Blue curve: inductor inside the EM shielding box, with floating terminals
Yellow curve: inductor inside the EM shielding box, one terminal grounded

The measurements utilized for the design of the matching network were performed with the inductor in its final position (yellow curve of Figure 5-6) within the EM shielding box and with one terminal grounded as in the circuit.

In these conditions the average measured inductance in the frequency range 0.9 MHz – 1.1 MHz is 67.79 μH with a standard deviation of 0.12 μH. The inductor stray resistance is 1.34 Ω, measured at 1.1 MHz, using the resonant circuit described in paragraph II.i of the appendix. It is higher than 0.90 Ω, measured outside the EM shielding box.

The stray resistance depends on the skin depth which varies with the frequency:

$$\delta = \sqrt{\frac{2\rho}{\omega\mu_0\mu_r}} \tag{14}$$

With the hypothesis that the skin depths δ is much lower than the conductor diameter, the following relationship can be written:

$$R_L' \sim R_L \sqrt{\frac{f'}{f}} \tag{15}$$

Within the operative frequency range the maximum δ is about 69 μm at 900 kHz (assuming copper conductor, and a temperature of 20 °C), thus (15) can be use to calculate the inductor stray resistance at any operative frequency.

Table 5-2 reports the inductor stray resistance for the minimum, maximum and central HVRFTF operating frequencies (900 kHz, 1 MHz and 1.1 MHz), and for both the series and parallel representation of the resonant circuit of Figure 5-4:

Table 5-2 – HVRFTF inductor parameters for series (R_L, L) and parallel (R_L*,L*) representation

Frequency [MHz]	0.9	1	1.1
L=L* [μH]	67.79		
R_L [Ω]	1.21	1.28	1.34
R_L* [kΩ]	121	142	164

5.2.2 Matching network capacitors

Once known the load impedances (parallel of the DUT and the inductor impedance), and the voltage source impedance, it is possible to calculate the reactances required to match the RF circuit impedance to the voltage source impedance using equations (9) and (10).

Among the DUTs to be used with HVRFTF the PCE, characterized by the largest value of capacitance and the widest variation with the gap, is assumed for the calculation of the load impedance.

Figure 5-7 shows the capacitance values of the PCE (orange curve), C_1 (blue curve) and C_2 (green curve) to obtain a perfect matching at 1 MHz to the voltage source impedance, as a function of the DUT gap in the range 10 μm – 50 mm.
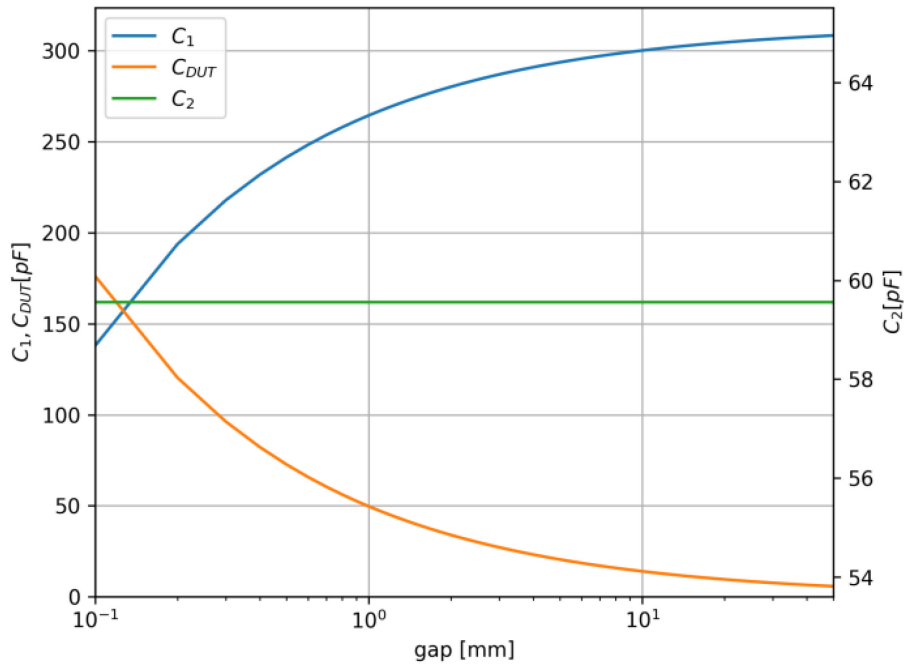
Figure 5-7 – C_1 and C_2 values for PCE as a function of the gap

The variation of the DUT capacitance is compensated by the variation of C_1, so that the parallel impedance of the load and C_1 is constant at the operating frequency. With a constant parallel impedance the capacitance C_2 is constant.

Figure 5-8 shows the capacitance values of C_1 and C_2 for the entire range of frequency, assuming the minimum and the maximum gap for PCE.
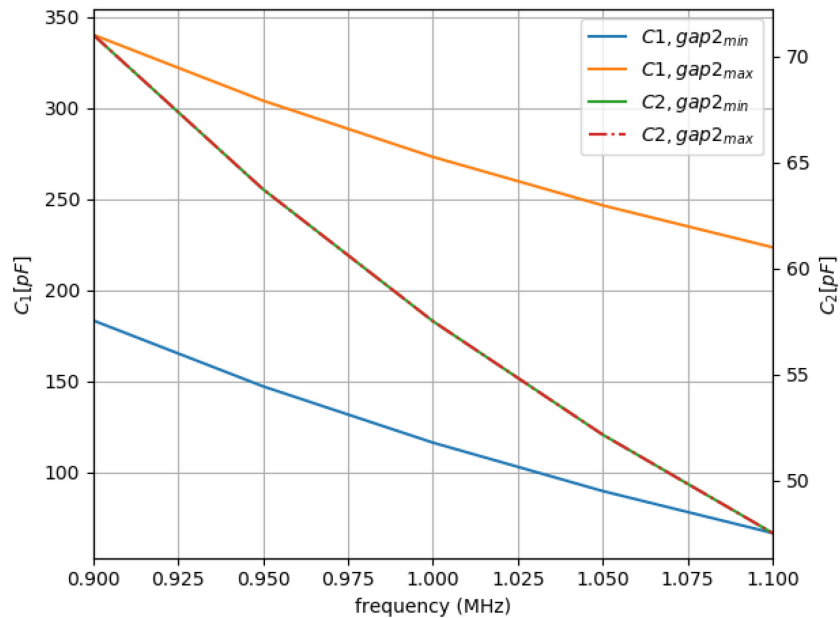
Figure 5-8 - C_1 and C_2 value as a function of frequency, for the minimum and maximum gap 2

In this case both the C_1 and C_2 should be variable to allow the circuit operates in all the specified frequency range. It is once again pointed out that C_2 does not depend on the gap (green solid line and red broken line overlap).

Table 5-3 lists the values required to C_1 and C_2 for the matching with the impedance of the inductor alone and of the load composed of the inductor and the foreseen DUT in parallel, for the frequencies of 900 kHz, 1 MHz and 1.1 MHz.

Table 5-3 – C_1 and C_2 values for the matching

| LOAD | 900 kHz | | 1 MHz | | 1.1 MHz | |
	C1 [pF]	C2 [pF]	C1 [pF]	C2 [pF]	C1 [pF]	C2 [pF]
Inductor	389	72	314	60	258	50
Inductor and PCE gap2 min	213	72	137	60	81	50
Inductor and PCE gap2 max	377	72	302	60	246	50
Inductor and PDS8 gap2 min	379	72	303	60	247	50
Inductor and PDS8 gap2 max	380	72	304	60	248	50
Inductor and PDS40 gap2 min	377	72	301	60	245	50
Inductor and PDS40 gap2 max	380	72	304	60	248	50
Inductor and PDS50 gap2 min	376	72	300	60	244	50
Inductor and PDS50 gap2 max	380	72	304	60	248	50
Inductor and PDS60 gap2 min	375	72	299	60	243	50
Inductor and PDS60 gap2 max	379	72	303	60	247	50

The perfect matching in the frequency range of 0.9 MHz-1.1 MHz, for all the DUTs is assured by a C_1 variable in the range $82 - 378$ pF and a C_2 variable in the range $49 - 74$ pF. To that purpose a couple of vacuum variable capacitors rated for C=25-450 pF and 24 kV (peak working voltage) have been selected.

The equivalent series resistances of the vacuum capacitors are orders of magnitude lower than the stray resistance of the inductor, thus they do not influence the values of the matching capacitance listed above.

5.2.3 Voltage gain and power requirements

The voltage gain of the RF circuit is defined as the ratio between the voltage at the output port and the voltage at the input port of the circuit, as indicated in Figure 5-9.
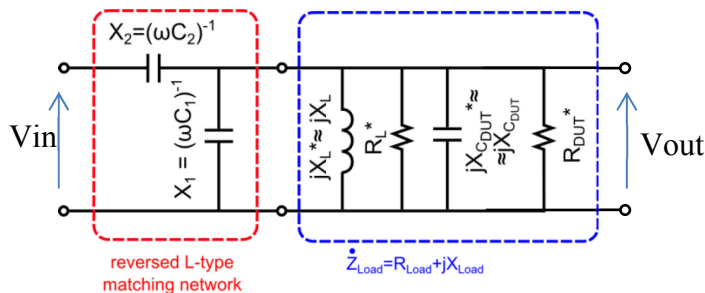
Figure 5-9 – RF circuit: input and output voltage highlighted

The voltage divider equation is exploited to express the voltage output as a function of the voltage input, so that the gain can be formulated as the ratio of the circuit impedances, as follows:

$$gain = \frac{V_{out}}{V_{in}} = \frac{\dot{Z}_{Load}||(-jXC_1)}{[\dot{Z}_{Load}||(-jXC_1)] - jXC_2} \tag{16}$$

The equation (16) is used to calculate the gain in the frequency range 0.9 MHz – 1.1 MHz, for all the DUTs, assuming the capacitance values C_1 and C_2 allowing the perfect matching for each one (Table 5-3).
The power absorbed at the input port is calculated as follows:

$$S = \frac{V_{in}^2}{Z_{in}} = \frac{\left(\frac{V_{out}}{gain}\right)^2}{Z_{in}} \xrightarrow{Z_{in}=Z_G} P \tag{17}$$

where the voltage input is expressed as the ratio between the target voltage and the voltage gain, while the impedance at the input port is $Z_{in} = Z_G = 50+j0\ \Omega$, since the circuit is a matched load for the amplifier and active power only is absorbed in this condition.
The power losses do not depend on the capacitance introduced by the DUT; they are affected only by the equivalent load resistance and they depend on the working frequency.
The gain, expressed in [db], as a function of frequency is shown in Figure 5-10 (blue curve), while the power required to reach the target voltage of 17 kV is indicated by the green curve.
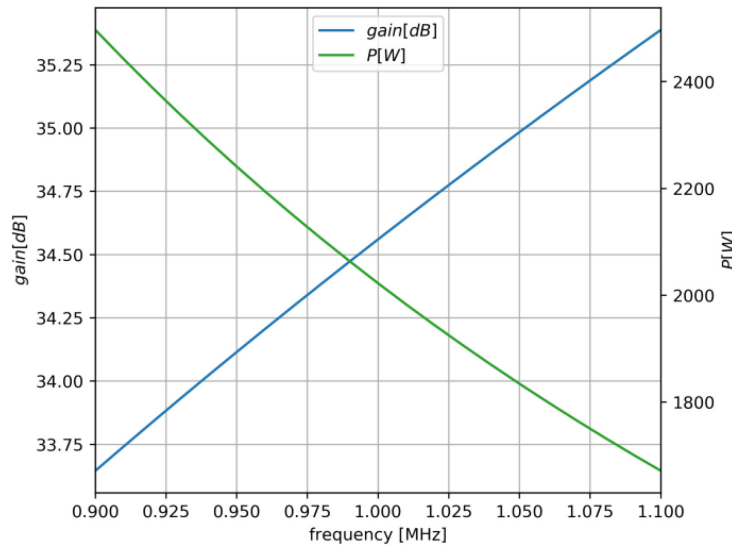
Figure 5-10 – gain and power losses of the RF circuit as a function of tuning frequency

The maximum power absorbed by the circuit is 2.5 kW at the minimum operating frequency; this would require a more powerful RF amplifier with respect to the one presently available at Consorzio RFX.

5.3 Preliminary HV circuit

A preliminary setup of the RF circuit was arranged with the RF amplifier rated for 300 W as described in paragraph 3.1.1 and vacuum capacitors available at Consorzio RFX; this allowed the validation of the design approach and the possibility to perform tests while procuring the amplifier with the required power and the required capacitors.

A capacitor rated for 25 pF was used as series capacitance (C_2), and a capacitor rated for 250 pF was used as parallel capacitance (C_1).

The main issue with the capacitance values used is that the impedance seen by the amplifier is not matched to the amplifier output impedance; this does not allow the complete power transfer and causes higher voltage on the RF coaxial line.

The absolute value of the impedance seen by the amplifier as a function of the gap is shown in Figure 5-11, with the assumptions:

- PCE as DUT;
- Operating frequency at which the voltage gain is the highest;
- The amplifier output voltage is the maximum (230 V, experimentally observed);
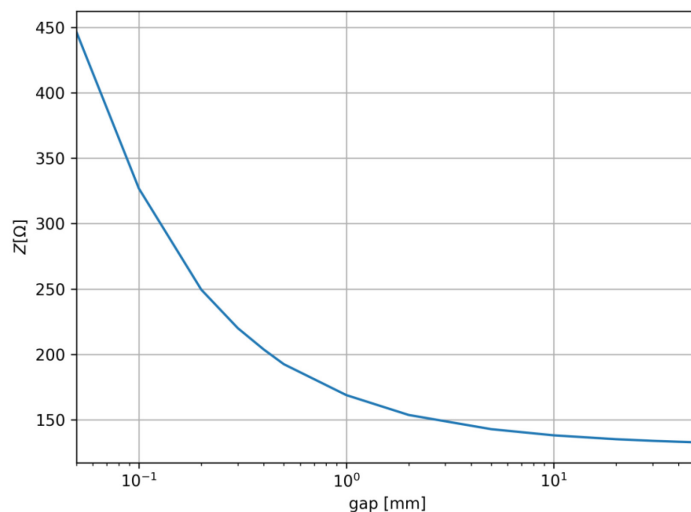
Figure 5-11 – Impedance seen by the amplifier as a function of the gap

The expected DUT voltage and operating frequency as a function of the DUT gap, assuming 300 W as the power supplied by the amplifier, is shown in Figure 5-12.
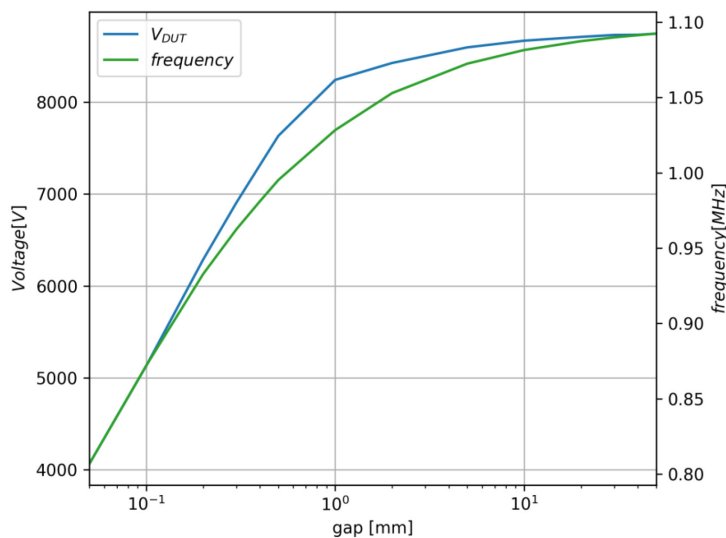
Figure 5-12 – DUT voltage and operating frequency with the preliminary RF circuit ($C_1 = 250$ pF, $C_2 = 25$ pF) supplied with 300 W

The maximum expected DUT voltage is about 8.6 kV rms: a value lower than the one required to HVRFTF because of the underrated RF amplifier and of the mismatch.

Nevertheless since the amplifier can deliver up to 450 W on 50 Ω (out of its class of operation), higher DUT voltage values could be reached.

5.3.1 RF circuit construction

The simplified scheme of the RF circuit is shown in Figure 5-13.
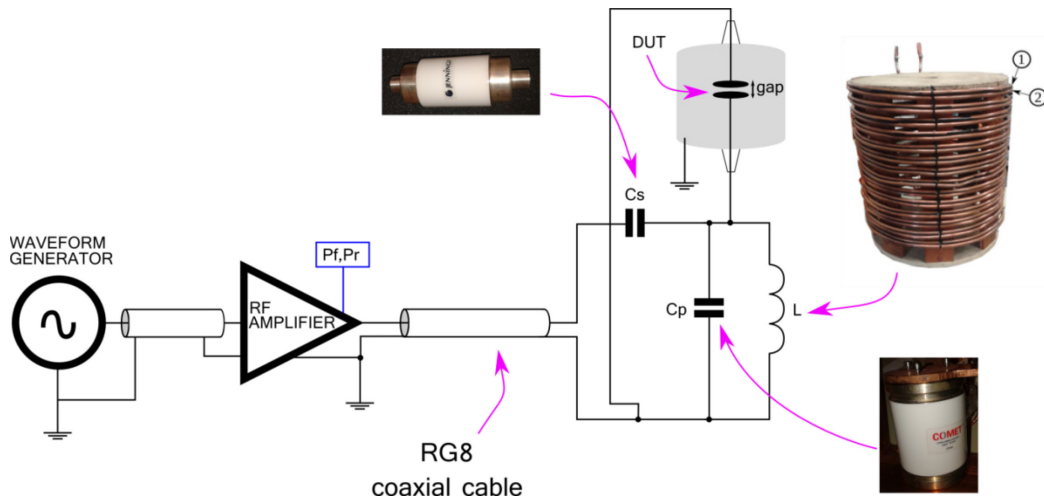
Figure 5-13 – HV generation conceptual scheme

The resonant circuit and matching network are mounted on a polyethylene slab and the connections among the different components are made of copper pipes with a diameter of 16 mm.
A N-type connector is mounted at the input port of the circuit, and represents the interface with the amplifier (transmission line).
The 3D view of the resonant circuit and a picture during the realization on the workbench is shown in Figure 5-14.
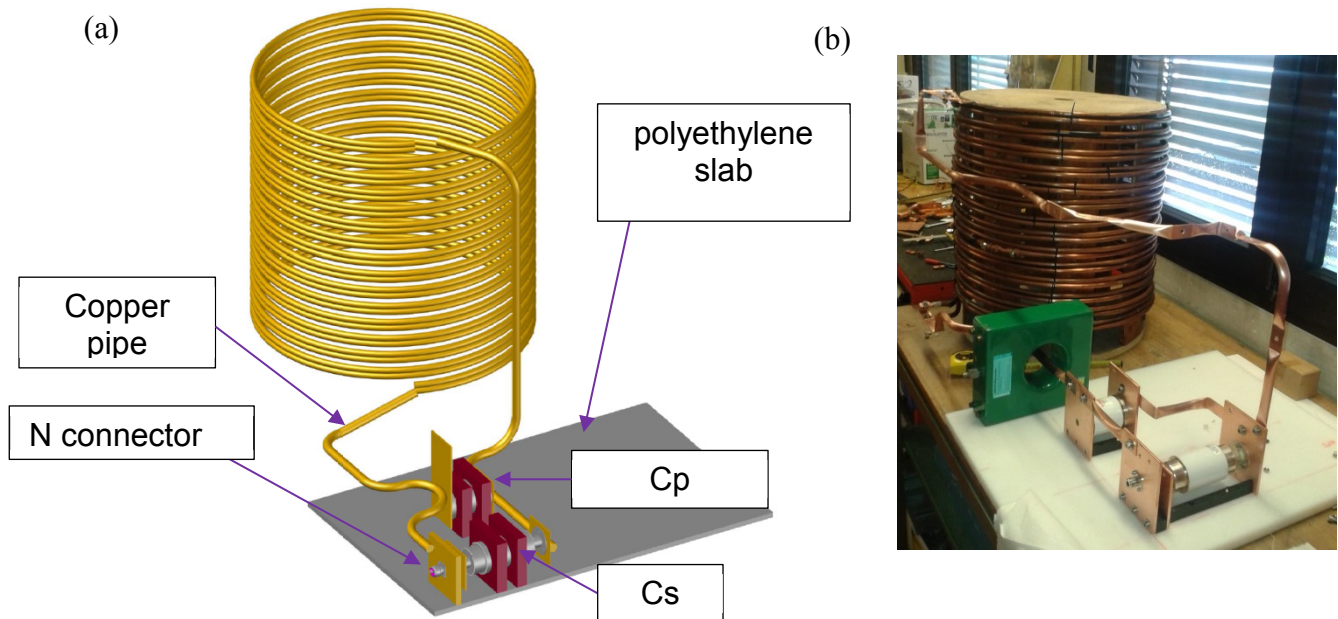
Figure 5-14 – 3D view (a) and picture (b) of the resonant circuit

6 HVRFTF experimental results

As planned, the operation of the HVRFTF started with stainless steel planar circular electrodes with a diameter of 108 mm, (the DUT identified as "PCE" in paragraph 4.4). Two test campaigns were performed on PCE.

The first test campaign included tests aimed at the verification of the correct operation of the facility both with vacuum tests (pressure below 10^{-3} Pa, without gas injection) in order to characterize the behaviour of the RF circuit once connected to the DUT, and tests with injection of Argon at pressures up to 100 Pa. With these tests we verified the pressure limit of the test facility, represented by the left vertical asymptote of the Paschen curve with the appearance of a glow discharge between the high voltage electrode and the vacuum vessel.

After the first test campaign the improvements identified were implemented on both the RF circuit and on the vacuum system to extend the operating pressure range.

The second test campaign was carried out with small gaps to intensify the E-field between the electrodes and Argon injection up to the pressure at which the glow discharge appeared.

The experimental activity, besides the collection of data relevant for the main HVRFTF scope, allowed detecting specific issues related to the setup and operation of the facility. In the following paragraphs the issues arisen and the strategies adopted to face them are discussed in addition to the description of the experimental results obtained so far.

6.1 First test campaign (2016)

Figure 6-1 summarizes the results obtained in 145 shots: the rms voltage applied to the DUT ("V_{DUT}" – blue curve), the pressure within the vessel ("pressure" – green curve) and the distance between the two electrodes ("gap" – magenta curve). With reference to the V_{DUT} in particular, the blue dot markers represent the maximum voltage achieved in each pulse, while the red dots are plotted if the voltage caused a breakdown).

The abrupt reduction of the V_{DUT} and the complete mismatch of the load seen by the amplifier identified the breakdown events, which were detected for gas pressures higher than 0.5 Pa.

After each breakdown a glow discharge surrounded the high voltage electrode (the bottom one); an example can be seen in Figure 6-2 b). Figure 6-2 a) is a picture of the electrodes taken just after their installation, for reference.

The glow discharges interested both the rod supporting the bottom electrode and the electrode, but not the space in between the two electrodes. In fact, when the pressure, starting from vacuum, is high enough to reach the Paschen left vertical asymptote, the discharge appears between the high voltage electrode (and its support) and the vacuum vessel, for a given pressure the breakdown voltage is lower for larger gaps (see Figure 2-10, assuming that the x axis reports the product of pressure and gap).

The pressure at which these glow discharges start is one order of magnitude higher than the pressure foreseen in the backside of the ion source, thus not of interest to characterize the drivers' voltage holding. Nevertheless provisions to try to extend the pressure at which the discharge happens were developed, as presented in paragraph 0

Breakdowns due to discharges between the electrodes were not detected.

In the following when speaking about the high voltage electrode it is made reference to both the electrode and its support.
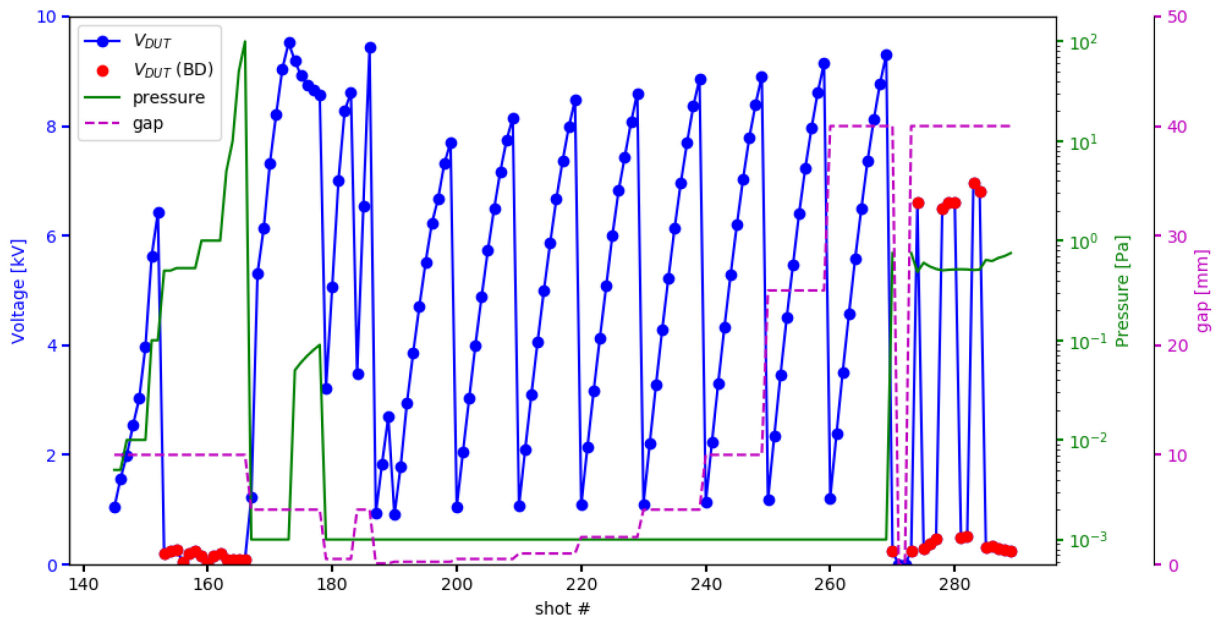
Figure 6-1 – First test campaign
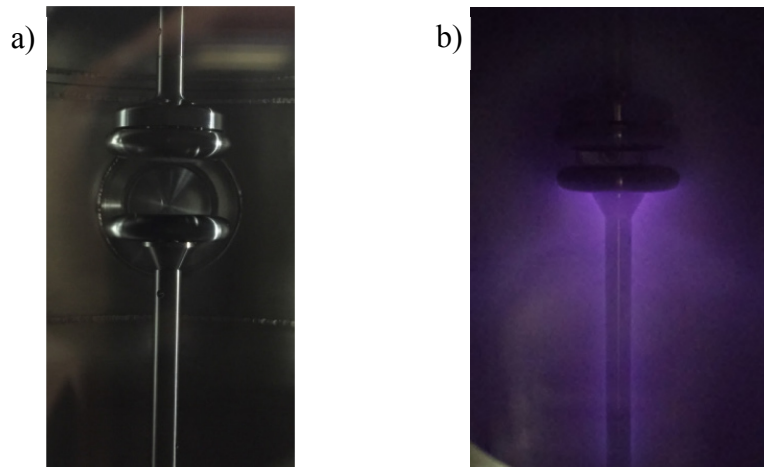
Figure 6-2 – Pictures taken during the first test campaign: a) PCE after installation (lighting from the outside), b) glow discharge around the bottom electrode and its support

6.1.1 Vacuum tests

It is pointed out that the vacuum tests, shots #179-269, corresponding to the shots in the central part of Figure 6-1, are presented first, since they are the most significant for the system characterization before introducing the gas.

The main aim of the tests was to find out the operating frequency and the voltage capability of the RF circuit supplying PCE, for a wide range of gaps (0.1, 0.25, 0.5, 1, 2.5, 5, 10, 25, 40 mm).

Once the gap between the electrodes was set, the voltage was increased in subsequent pulses up to the maximum value (limited by the RF amplifier power). Figure 6-3 reports the operating points recorded for the tests: the blue dots are the voltages applied to the DUT and the orange dots are the voltage frequencies.

The operating frequency of the circuit is in the range 0.960 – 1.1 MHz, and it is directly proportional to the gap. This is in line with the expectations, since the operating frequency is related to a resonance and the resonance frequency is proportional to the square root of the capacitance (as the gap increases the DUT capacitance decreases).

As can be seen in Figure 6-3, the voltage reached for gaps in the range 5-40 mm is higher than 9 kV, for gaps in the range of 0.5-5 mm is higher than 8 kV, while for short gaps was limited by us to about 3 kV due to an unexpected audible noise and the modulation of the electrical quantities (this behaviour is analyzed in paragraph 6.1.3).
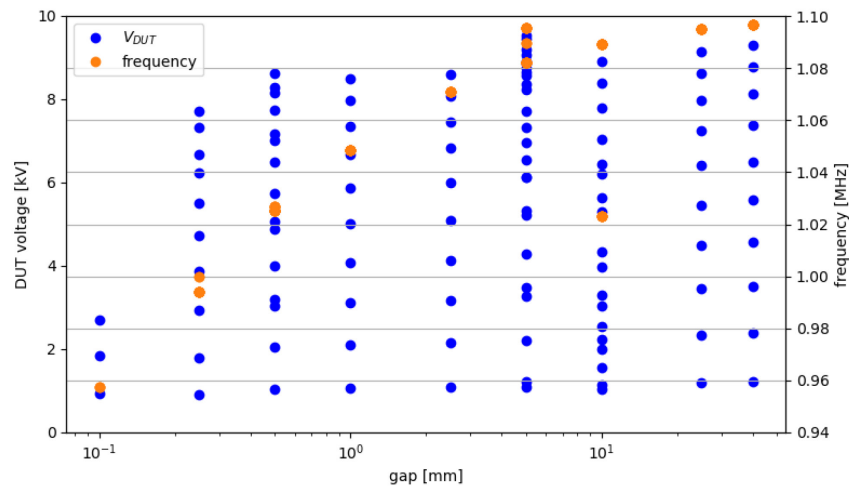
Figure 6-3 – DUT voltage (blue dots) and frequency as a function of the gap (orange dots)

Figure 6-4 shows the peak value of the E-field between the electrodes, calculated as ratio between the peak value of the DUT voltage and the gap, as a function of the gap: the maximum value of 45 MV/m was reached at 0.25 mm.
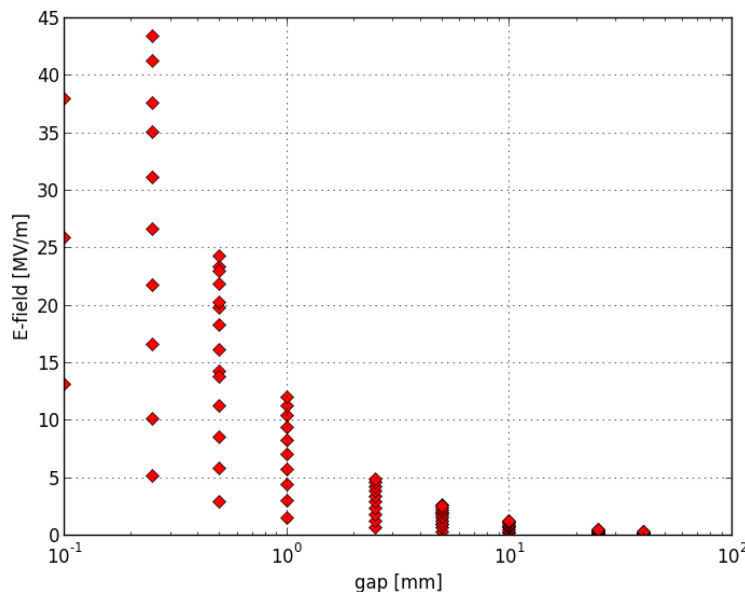
Figure 6-4 – Electric field as a function of the gap

6.1.2 Characterization of the gas discharge

With reference to Figure 6-1, the shots corresponding to gas discharge tests are shots # 145-178 and #270-290.

The tests were carried out for a pressure range of 10^{-3} Pa - 10^{2} Pa, for various gaps. One would expect that breakdown voltages are a function of both pressure and gap, but it is not the case: Figure 6-5 shows the DUT voltage as a function of the pressure, where blue dots are power supply limits, red dots are breakdown voltages.
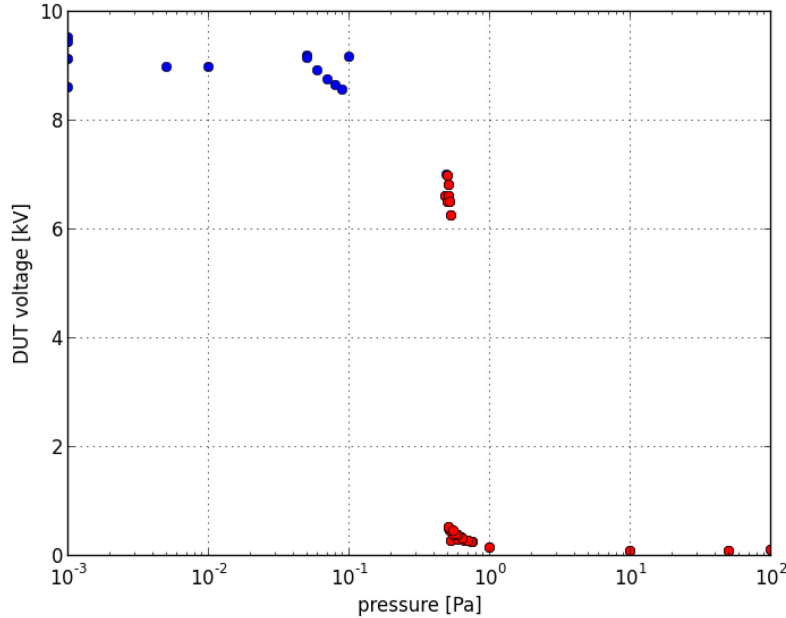
Figure 6-5 – Voltage applied to the DUT as a function of the pressure: red dot markers are breakdown voltages, blue dot markers are power supply limits.

The effect of the gap variation is not visible; a threshold for the breakdown is clearly visible for 0.5 Pa: it is the Paschen left asymptote for a unique gap, which is the maximum distance between the high voltage electrode from the grounded vacuum vessel. In fact the left asymptote of the Paschen curve for Argon (in dc) is at about 0.1 Pa·m [62], therefore the breakdown distance in our case is about 0.20 m, much closer to the VV dimensions than to the gap between the electrodes.

It is interesting noting that for two decades (from 1 Pa to 100 Pa) the breakdown voltage does not increase, differently from what one could expect from the Paschen curve. It has to be considered that to derive the Paschen curve a two electrode system is used; in this case there are three electrodes: the two electrodes of the PCE and the VV. The path of the discharge is the one having the length that multiplied by the pressure is characterized by the lowest breakdown voltage. This means that at 0.5 Pa the discharge formed across the longest path between the electrode and the VV, while increasing the pressure the path modifies and in particular shorten in order to maintain the lowest value of breakdown voltage. Figure 6-6 sketches this effect on the VV: the discharge length "1" is for lower pressure than for discharge path "2".

The availability of multiple path lengths maintains the breakdown voltage to its minimum value over a wide range of pressures, since the discharge happens in the most favorable gap. This behavior was already observed and documented (with dc voltage) for complex geometries [63].

It has to be underlined that the glow discharge between the high voltage electrode and the VV does not compromise the effectiveness and the usability of the HVRFTF for the characterization of the drivers'

voltage holding, since it happens for pressures of about 0.5 Pa, one order of magnitude higher than the RF coil operating pressure.
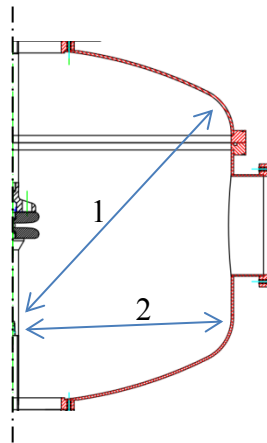
Figure 6-6 – Sketch of the path length variation with pressure: 1 for pressure lower than for 2

6.1.3 Issues and improvements of the HVRFTF arrangement

6.1.3.1 Measurements modulation and noise

A modulation of the measurements at about 500 Hz with associated noise (sine whistle) appeared with short gaps, and it was not possible to reach high DUT voltages. All the measurements are affected by this modulation, with the exception of the amplifier output voltage which is almost not modulated, as can be seen in Figure 6-7.
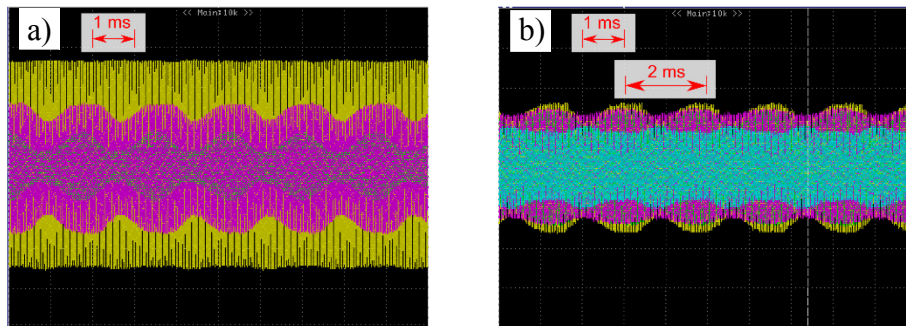
Figure 6-7 – Modulation of the recorded measurements:
a) amplifier voltage output (yellow curve), forward voltage (magenta curve), reflected voltage (green curve);
b) DUT voltage (yellow curve), amplifier output current (magenta curve), DUT current (cyan curve)

This effect happened only for gaps lower than 1 mm.
The hypothesis is that the modulation is due to the mechanical axial vibrations of the electrodes, which would vary the capacitance of the DUT, therefore the electrical quantities.
The reason why it happened for short gaps can be that a slight variation of the gap due to a vibration would cause a substantial variation of the capacitance.

Once the vibration is triggered it is sustained by the electrostatic force acting on the electrodes, which can be calculated as the ratio between the stored energy and the gap, which is proportional to the third power of the gap, as derived in (18).

$$F = \frac{W}{gap} = \frac{1}{2} \cdot C_{DUT} \cdot V_{DUTp}^2 \cdot \frac{1}{gap} \, \alpha \, \frac{1}{gap^2} \tag{18}$$

Where:
- F is the peak electrostatic force [N];
- W is the stored energy [J];
- Gap is the electrodes separation [m];
- C_{DUT} is the DUT capacitance [F];
- V_{DUTp} is the peak voltage applied to the DUT [V].

The PCE capacitance is about 170 pF with a gap of 0.1 mm, therefore the force acting on the electrodes with 3 kV rms is about 15 N.
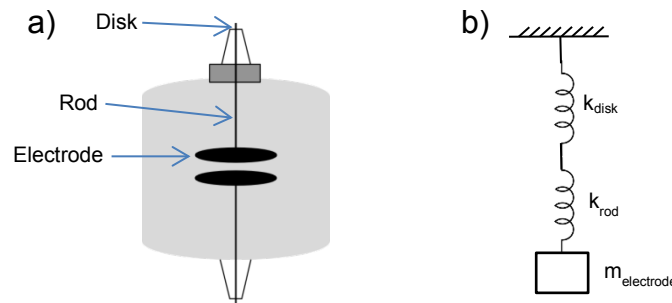
Figure 6-8 – a) sketch of the mechanical system, b) mechanical equivalent scheme

The mechanical system is the same for the top and the bottom electrodes; with reference to Figure 6-8 a), each electrode is supported by a stainless steel rod, which in turn is fastened on a metallic disk brazed on the feedthrough. This configuration can be assumed as a spring-mass system: both the rod and the disk elongate when the electrode is attached.
With the hypothesis of a linear-elastic system and ideal springs with no mass, the mechanical natural resonant frequency can be estimated as in (23):

$$f_0 = \frac{1}{2 \cdot \pi} \sqrt{k_{eq}/m_{electrode}} \tag{19}$$

Where:
- f_0 is the mechanical resonant frequency [Hz];
- k_{eq} is the equivalent elastic constant of the two springs [N/m];
- $m_{electrode}$ is the mass of the electrode [kg].

The elastic constant of the rod and of the disk can be calculated with (20) and (21) respectively, the equivalent elastic constant with equation (22).

$$k_{rod} = E \cdot \frac{A}{L} \tag{20}$$

Where:
- k_{rod} is the elastic constant of the rod [N/m];
- E is the Young's modulus of the material [N/mm²];

- A is the cross section of the rod [mm^2];
- L is the rod length [m].

$$k_{disk} = \frac{4 \cdot \pi \cdot E \cdot s^3}{3 \cdot (1 - \nu^2) \cdot R^2} \cdot 10^3 \qquad (21)$$

Where:
- k_{disk} is the elastic constant of the disk [N/m];
- E is the Young's modulus of the material [N/mm^2];
- s is the thickness of the disk [mm];
- ν is the Poissons's coefficient [-];
- R is the radius of the disk [mm].

The equivalent elastic constant k_{eq} is given by (26):

$$k_{eq} = \left(\frac{1}{k_{disk}} + \frac{1}{k_{rod}} \right)^{-1} \qquad (22)$$

The rod used in HVRFTF is made of AISI 304L Stainless Steel (E=193 GPa=193 kN/mm^2), its cross section is A=452 mm^2 and its length is L=0.8 m: k_{rod} results 109.1 MN/m.
The disk is made of AISI 304L, is 2 mm thick, its diameter is 45.5 mm, ν is 0.3: k_{disk} results 13.7 MN/m.
The equivalent elastic constant is k_{eq} = 12.2 MN/m; the weight of one electrode (of the PCE pair) is $m_{electrode}$=1.25 kg.
The mechanical resonant frequency results f_0 = 497 Hz, in line with the modulation frequency observed.

The main question is what triggers the mechanical vibrations: the pumping system is not the cause, since the modulation was measured also with pumping system switched OFF.
Nevertheless, this limit affects the PCE only since the calculated capacitances of the other DUTs (Table 4-2) with very short gaps are orders of magnitude lower than that of the PCE.

6.1.3.2 Extension of the operating pressure range

It is not possible to avoid the discharge toward the VV, with a metallic VV, for relatively high pressure. But it is possible to extend the operating pressure range by shortening the maximum discharge path length for the high voltage electrode. A couple of Pyrex tubes were placed within the VV for that purpose, as visible in Figure 6-9:

- Tube 1 lays on the ceramic feedtrough and surrounds the rod which support the electrode;
- Tube 2 lays on the metallic flange of the feedtrough and surrounds the electrodes.
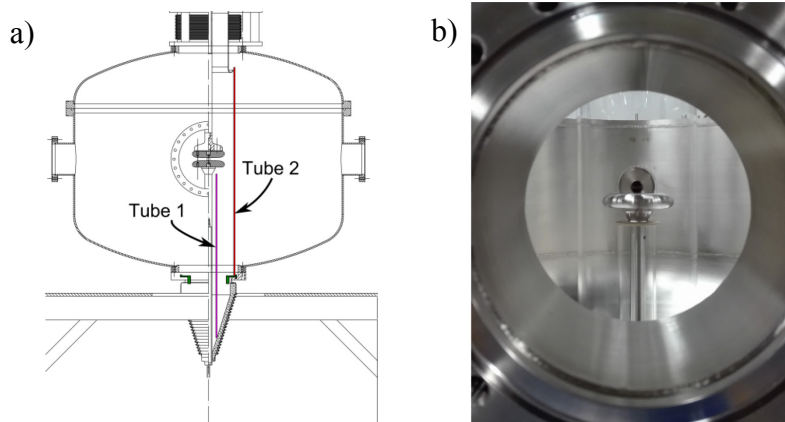
Figure 6-9 – Pyrex tubes for shortening the discharge path

6.2 Second test campaign (2017)

The HVRFTF setup was then improved and the second test campaign was carried out with a refined arrangement:

- Some interesting quantities were measured, recorded during all the pulse and stored on the server;
- The Pyrex tubes for the discharge path modification were installed;
- A fixed capacitance of 50 pF was provided to replace the 25 pF capacitor thus improving the impedance matching and the power transfer from the amplifier to the circuit. The new capacitors were installed during the test campaign from shot #359.

The test campaign was performed for gaps ranging from 0.1 mm to 1 mm with steps of 0.1 mm, with argon as background gas for pressures of 10^{-3} Pa (no gas injection), 10^{-2} Pa, $2.5 \cdot 10^{-2}$ Pa, $5 \cdot 10^{-2}$ Pa, $7.5 \cdot 10^{-2}$ Pa, 0.1 Pa, 0.25 Pa, 0.5 Pa, 0.75 Pa (limit for the turbomolecular pump).

Before each shot the gap and the pressures were adjusted to the desired values, then the voltage was increased up to the maximum reachable amplitude with the available power amplifier and maintained for at least 300 s or up to the breakdown.

The overview of the experimental campaign from pulse #316 to #517 is shown in Figure 6-10: the rms voltage applied to the DUT ("V_{DUT}" – blue curve), the pressure within the vessel ("pressure" – green curve) and the distance between the two electrodes ("gap" – magenta curve). With reference to the V_{DUT} in particular, the blue dot markers represent the maximum voltage achieved in each pulse, while the red dots are plotted if the voltage caused a breakdown).
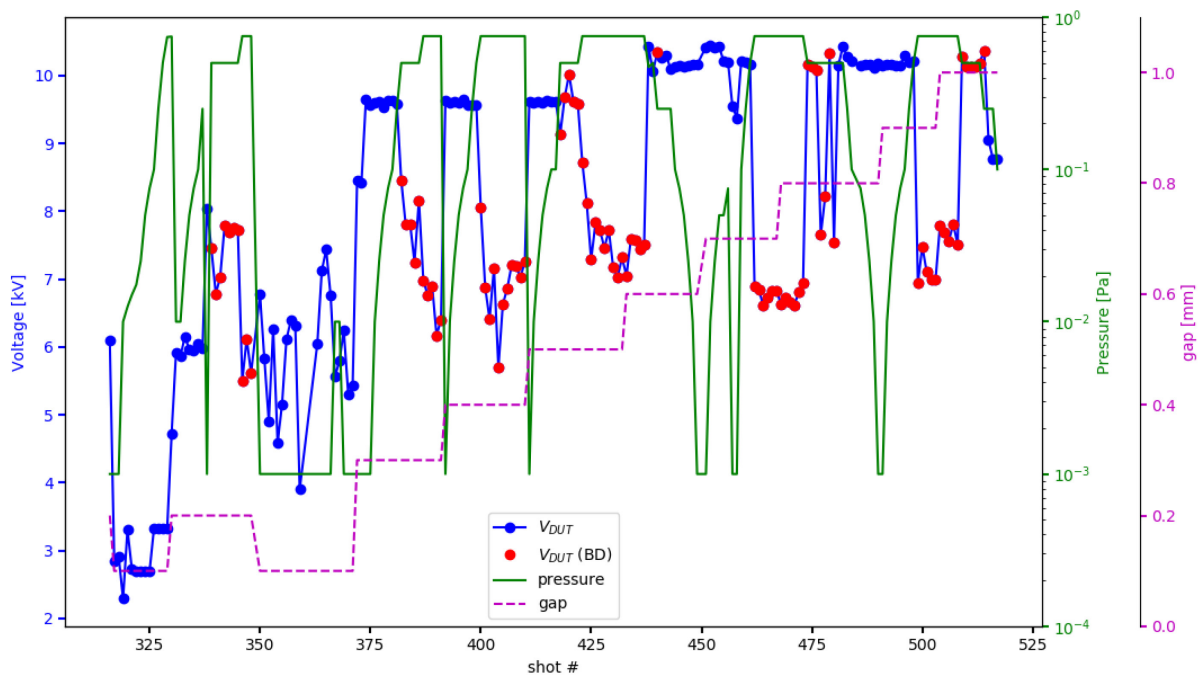
Figure 6-10 – Second test campaign

Also during the second test campaign we observed the abrupt fall of the DUT voltage, which identifies a complete breakdown, associated only to glow discharges between the HV electrode and the VV at relatively high pressure.

As can be seen in Figure 6-11 b) the glow was pushed on the Pyrex tube with larger diameter; sometimes in a fixed position, sometimes slowly turned around the VV vertical axis, and sometimes jumped from a radial position to another. The measurements were not affected by the movement of the glow discharge position, nevertheless it may be that the variation was not detected by the data acquisition system.
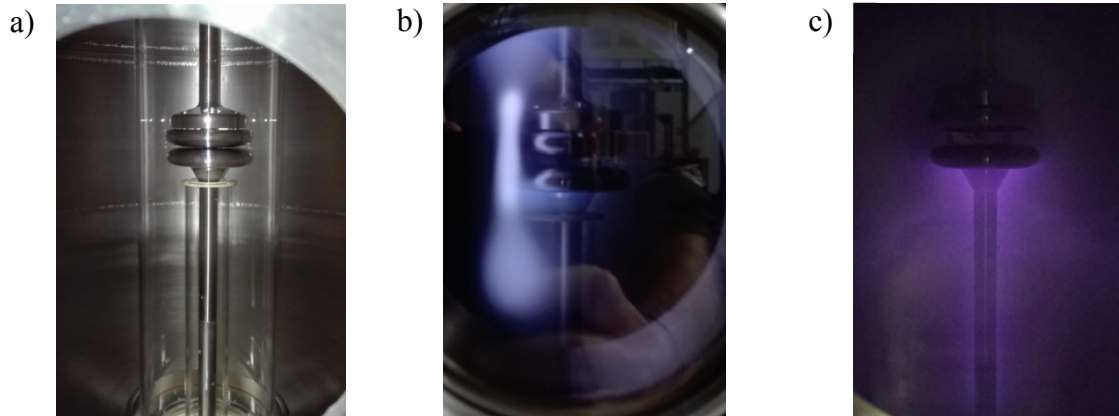
Figure 6-11 – Pictures of the VV inside: a) PCE and tubes after installation (lighting from the outside), b) glow discharge around the bottom electrode and its support confined by the Pyrex tube with larger diameter, c) glow discharge before Pyrex tubes installation for comparison.

At lower pressure no breakdown was observed, not even a transient reduction of the measured voltage was detected; some sparks were noted for gaps of 0.1 and 0.2 mm. Figure 6-12 shows a picture of the sparks, extracted from a video.

**Figure 6-12 – Pictures of sparks between the electrodes
(frame extracted from video, the flange was added to figure out the position of the sparks)**

The data acquisition system allowed recording the pulse evolution with a sample frequency of 4 Hz: Figure 6-13 shows stored signals for a shot with no breakdown, while Figure 6-14 shows the signals for a shot with a breakdown with the associated glow discharge. The pressure within the vessel and the gap were recorded manually.

Each figure shows three plots:
- Top plot: power measured by means of a dual directional coupler (PF= Forward Power, PR= Reflected Power, P = PF-PR)
- Center plot: frequency detected for each measurement (the detection is reliable when the signal amplitude overcomes a threshold)
- Bottom plot: rms values for V_{DUT} voltage and I_{DUT} current in the DUT.
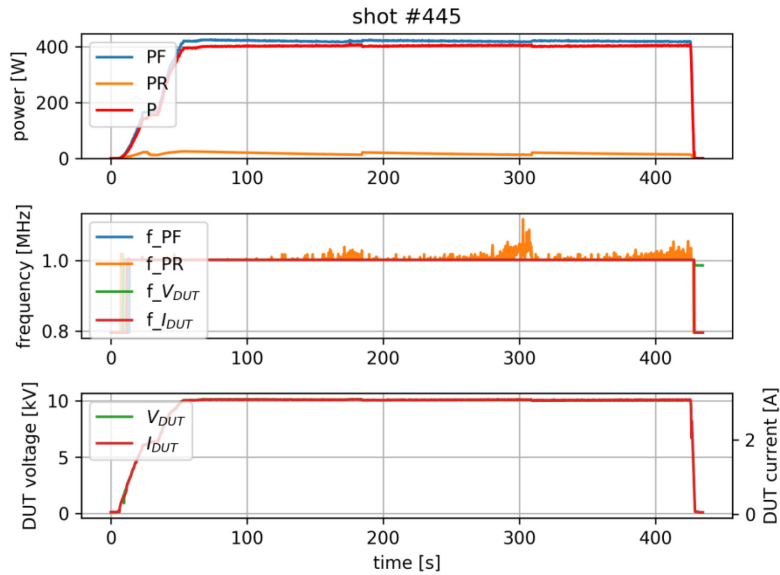
Figure 6-13 – Typical shot with no breakdown (some curves overlie)
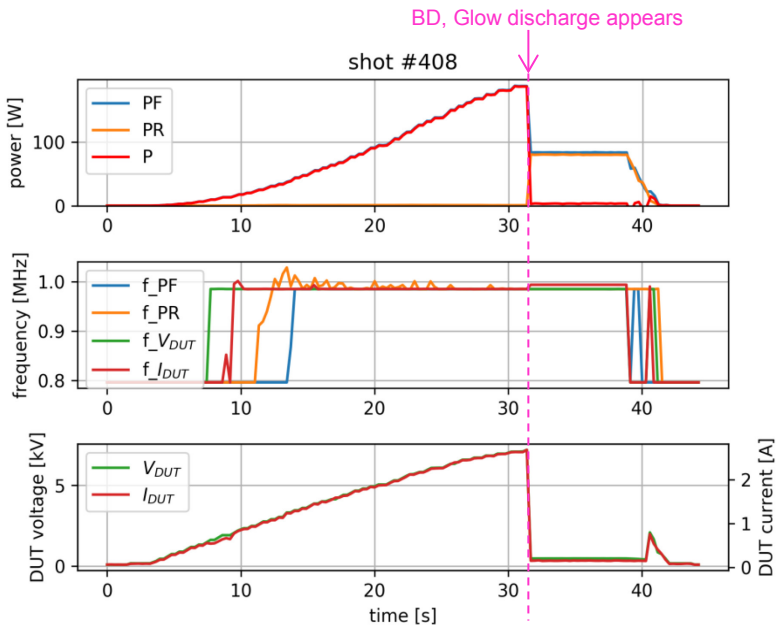
Figure 6-14 - Typical shot with breakdown (some curves overlie)

Looking at the top plot of Figure 6-14 it is interesting to note that in case of breakdown (at about 31.5 s) the load completely mismatches: before the breakdown the Reflected Power is negligible and the Forward Power is delivered to the load; after the breakdown the Reflected Power is almost equal to the Forward Power and the power delivered to the load is negligible. The voltage applied to the DUT, shown in the bottom plot of Figure 6-14, drops after the breakdown to a value lower than 1 kV which is sufficient to sustain the glow discharge. At 38.5 s the RF amplifier output voltage (not shown in the figure) was slowly driven to zero, reached at 42 s. At about 40.5 s the voltage applied to the DUT was not sufficient to maintain the discharge which extinguishes. The reapplied voltage (about 2 kV) was not sufficient to restrike the discharge.

During the second test campaign the issue related to the modulation of the electrical quantities as well as the audible noise was encountered again, as expected. We found out that in order to stop the noise and the modulation for tens of seconds, it was sufficient to reduce the frequency by- ~100 Hz. This effect is shown in Figure 6-15: the 500 Hz modulation is recorded as a disturbance of the measurements, since it is undersampled (4 Hz); in correspondence to the red arrows we acted on the frequency of the signal driving the RF amplifier to stop the disturbance.
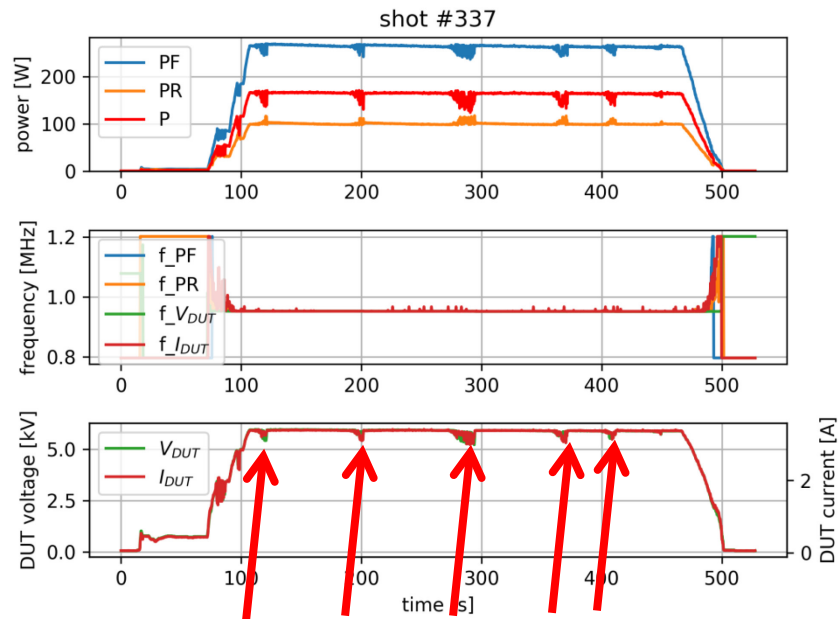
Figure 6-15 – Waveform recorded during shot #337, gap = 0.2 mm, pressure 0.25 Pa (the reflected power is high because the 25 pF capacitor was still mounted on the circuit)

With a gap of 0.1 mm the modulation started at 2 kV and the described method to stop it did not work, as visible in Figure 6-16.
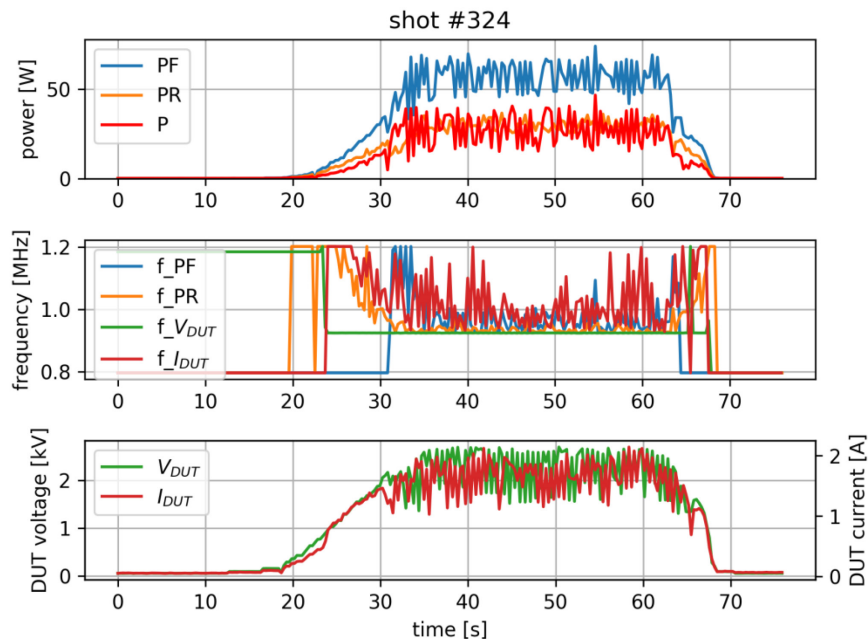
Figure 6-16 - Waveform recorded during shot #324, gap = 0.1 mm, pressure 0.05 Pa

83

A correlation between the modulation of the measurements and the pressure within the vessel was observed, as an example shot #320 is shown in Figure 6-17: the RF amplifier output voltage has been reduced to almost 0 V at 137 s and re-increased at 184 s. Figure 6-17 b) shows the pressure as a function of time (shown by the gauge controller display: red curve on black background). This aspect needs to be analyzed since the correlation can be spurious, due to electric noise pickup.
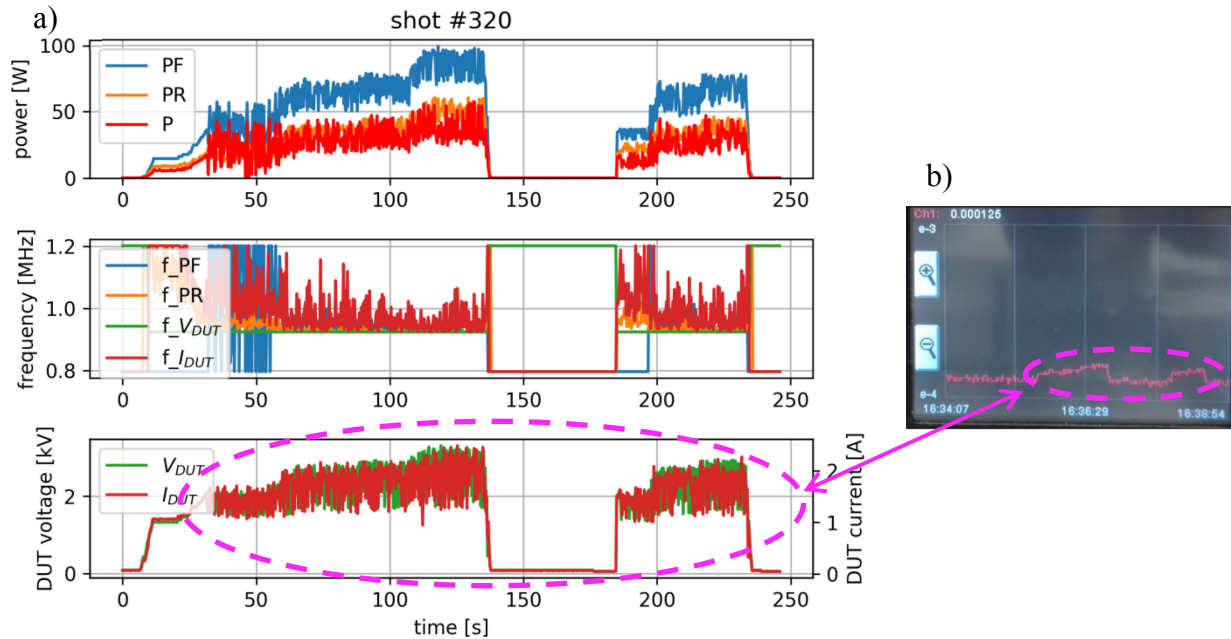
Figure 6-17 – Correlation between the measured VV pressure (b) and the modulation/noise of the RF waveforms (a)

Almost at the end of the experimental campaign, during shot #514, with a gap of 1 mm, a breakdown happened for pressure of 0.25 Pa; it was not the first time, it already happened for shot #440 having a gap of 0.6 mm, but in the case of shot #514 the voltage applied to the DUT (after the breakdown) was about 3 kV, higher than the usual values necessary to sustain the glow discharge.

Figure 6-18 shows the comparison between the two shots: for shot #440 the glow discharge was unexpected (it did not appear before at 0.25 Pa), but the behaviour was similar to previous glow discharges with a voltage necessary to sustain the discharge of about 350 V; this is the reason why the shot was stopped after some seconds. For shot #514, after the breakdown at 222 s, the glow discharge was sustained with about 3 kV and self-extinguished at 445 s when the voltage was about 2.8 kV. Also the power delivered by the RF amplifier was not negligible as during previous discharges, in fact it was of about 100 W. Investigation on this behavior is in progress.
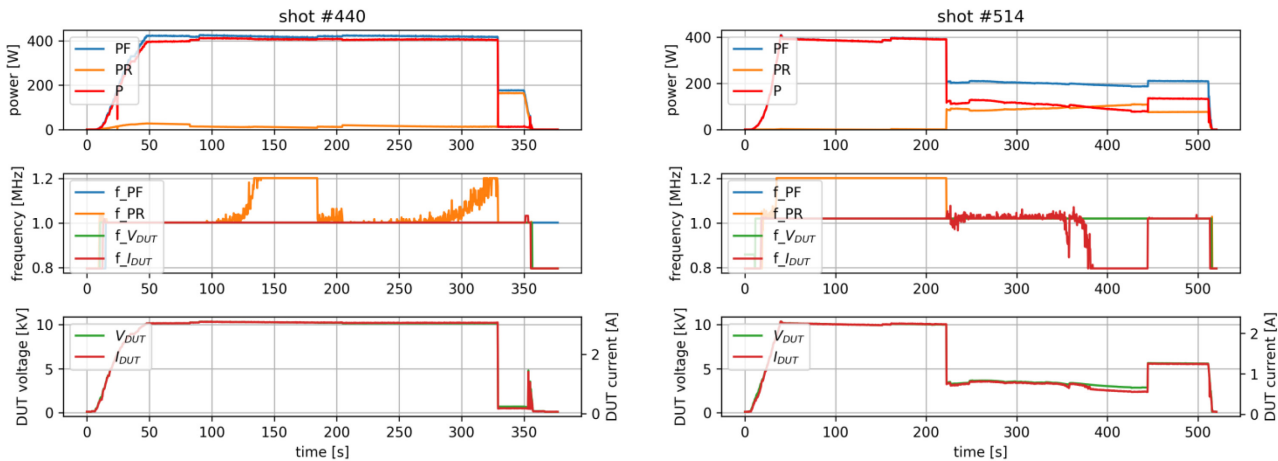
Figure 6-18 – Comparison of shots #440 (gap = 0.6 mm) and #514 (gap = 1 mm), pressure 0.25 Pa

During subsequent pulses the maximum voltage reached by the RF circuit was only of 8.7 kV, against the 10.3 kV of shot #514, and many sparks were observed between the electrodes. The operating frequency decreased by about 1.4 kHz too.

At last the PCE were tested again in vacuum (without gas injection) for gaps of 0.1, 0.2, 0.3 and 0.4 mm and many sparks were generated between the electrodes, which means that the surface of the electrodes was probably crinkled.

To understand the reason of the lower voltage reached by the circuit, each component was inspected. Nothing was noted, and once disconnected from the feedthrough the circuit reached 10.8 kV.

The hypothesis is that the lower voltage issue is related to a modified behaviour of the components placed within the VV; once opened the VV, a blackening of the larger Pyrex tube due to plasma sputtering was observed. The stainless steel sputtered on the tube probably increased the equivalent capacitance of the DUT.

Both the top and the bottom electrodes were visibly damaged after the test campaign as can be seen in Figure 6-19.
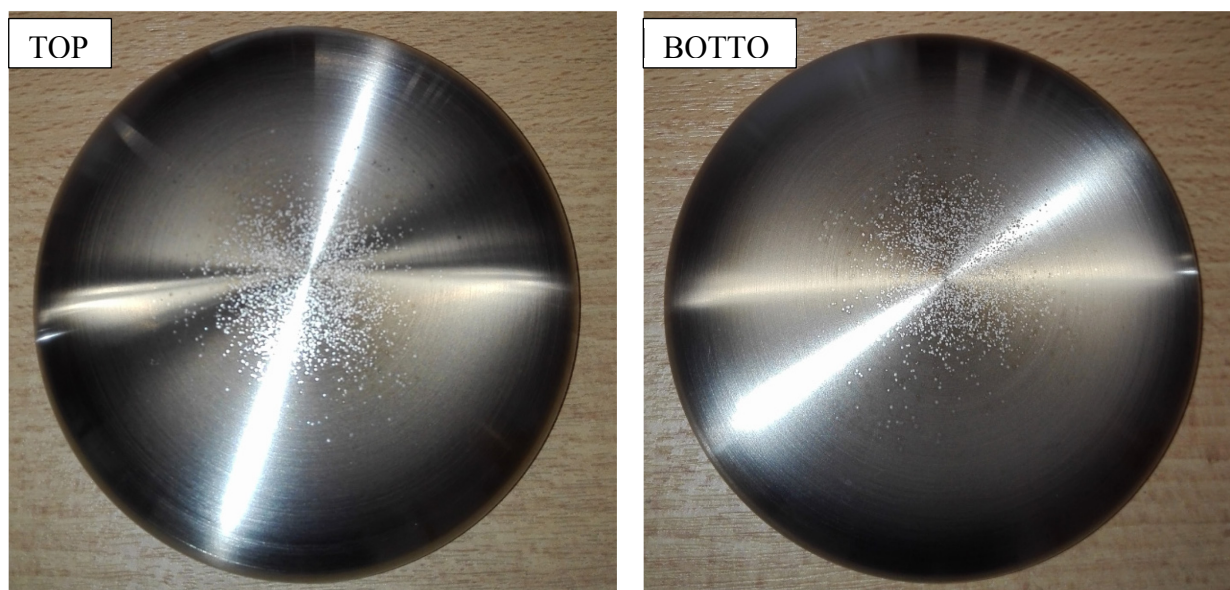
Figure 6-19 - Pictures of PCE after the second test campaign

Both electrodes surface were observed under an optical microscope available at Consorzio RFX. Figure 6-20 shows two typical pictures of the microscope view with the minimum and the maximum magnification. The maximum dimension of the marks is of about 0.5 mm; many marks overlap (many discharges on close points).
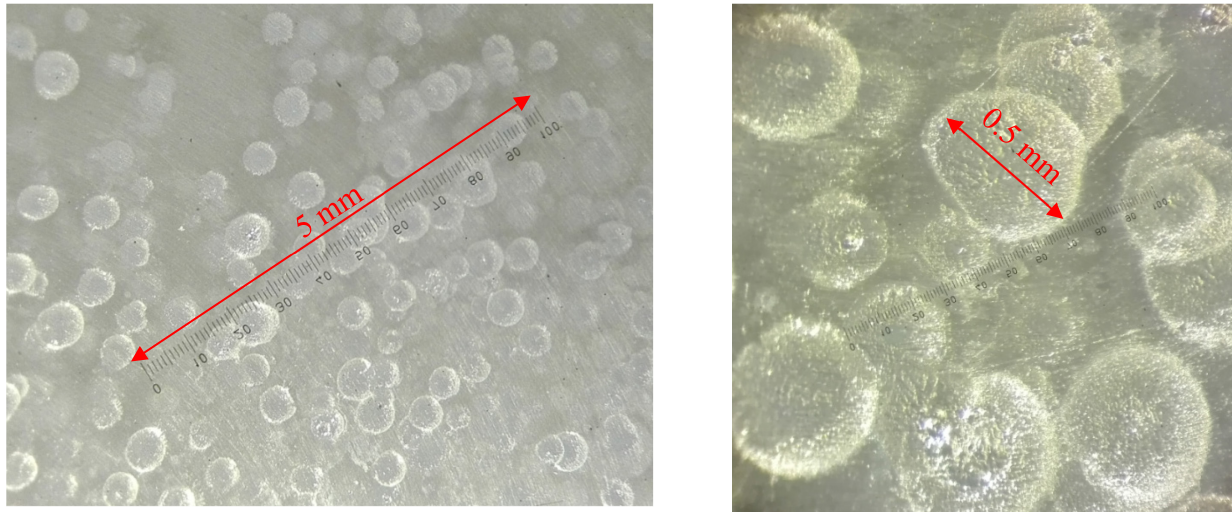
Figure 6-20 – Magnifications of the electrode surface under an optical microscope (pictures taken through the microscope ocular)

6.2.1 RF circuit characterization

The measurements acquired during the experimental campaign are analyzed in the following in order to characterize the behaviour of the RF circuit.

Figure 6-21 shows the voltage applied to the DUT (blue markers) and the operating frequency (magenta markers) as a function of the gap, for pulses when the breakdown was not triggered. The behaviour is similar to the one observed during the first test campaign, the frequency is slightly lower (effect of the series capacitance replacement).
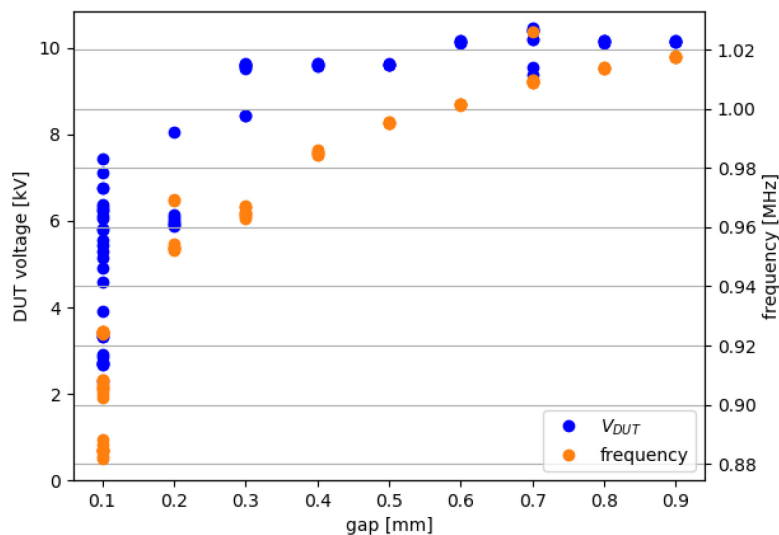
Figure 6-21 – Voltage (blue markers) and frequency (orange markers) as a function of the gap

Figure 6-22 shows the DUT impedance (blue markers), calculated as the ratio between DUT voltage and DUT current, as a function of the gap. The DUT equivalent capacitance (orange markers) is calculated taking into account the frequency dependence of the gap, and with the hypothesis that the DUT impedance is purely reactive.
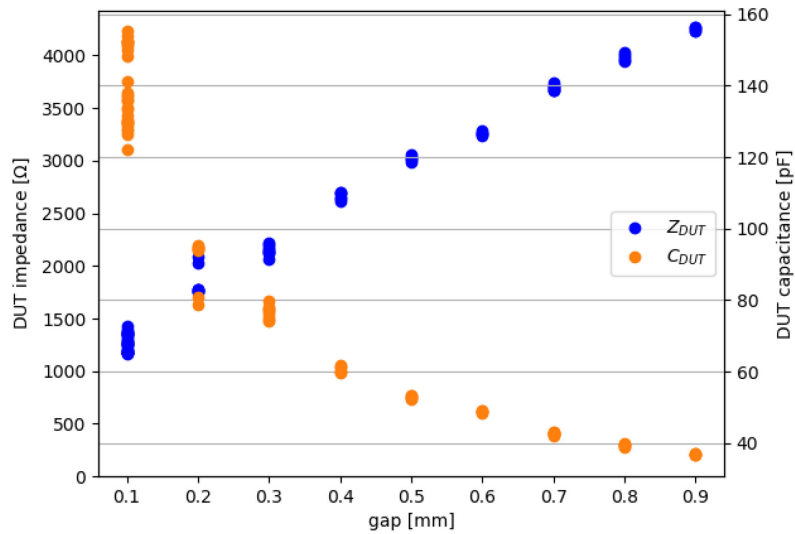
Figure 6-22 – DUT impedance (blue markers) and equivalent capacitance (orange markers) (hypothesis: DUT impedance is purely reactive)

Figure 6-23 shows the peak value of the E-field between the electrodes, calculated as ratio between the peak value of the DUT voltage and the gap, as a function of the gap: the maximum value of about 55 MV/m was reached for a gap of 0.2 mm, while during first test campaign 45 MV/m were reached for a gap of 0.25 mm. The results obtained for 0.1 mm were not used since the measurements were affected by modulation.
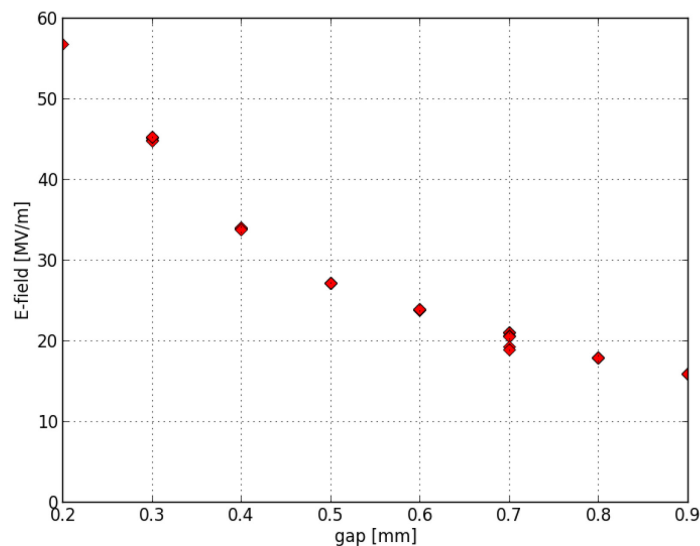
Figure 6-23 – Electric field as a function of the gap

6.2.2 Characterization of the gas discharges

Figure 6-24 shows the DUT voltage as a function of the pressure: blue dots represent the maximum value achievable with the available RF circuit, red dots represent breakdown voltages.
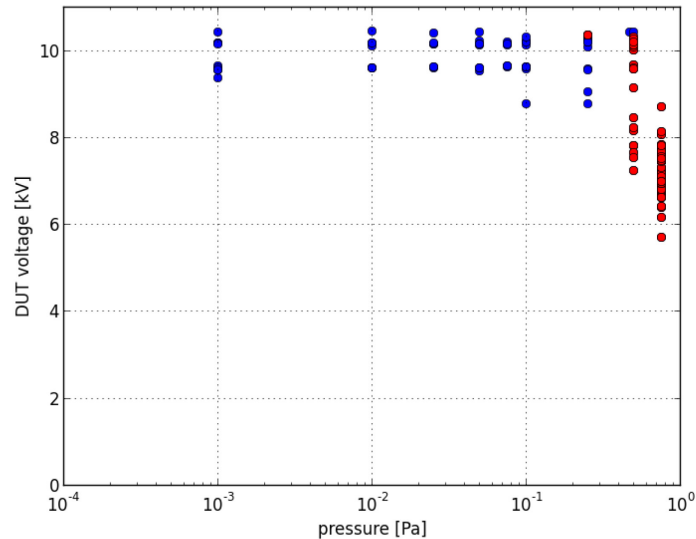
Figure 6-24 - Voltage applied to the DUT as a function of the pressure: red dot markers are breakdown voltages, blue dot markers are power supply limits

The threshold for the breakdown is shifted to the left side with respect to the first test campaign: at 0.5 Pa the breakdown voltage is higher than 7 kV and for some gaps it did not happen; at 0.75 Pa the breakdown voltage is higher than 5 kV, against some hundreds of volts without the Pyrex tubes. Nevertheless the discharge path length did not shorten, in fact the pressure threshold for the calculation of the Paschen left asymptote is still 0.5 Pa.
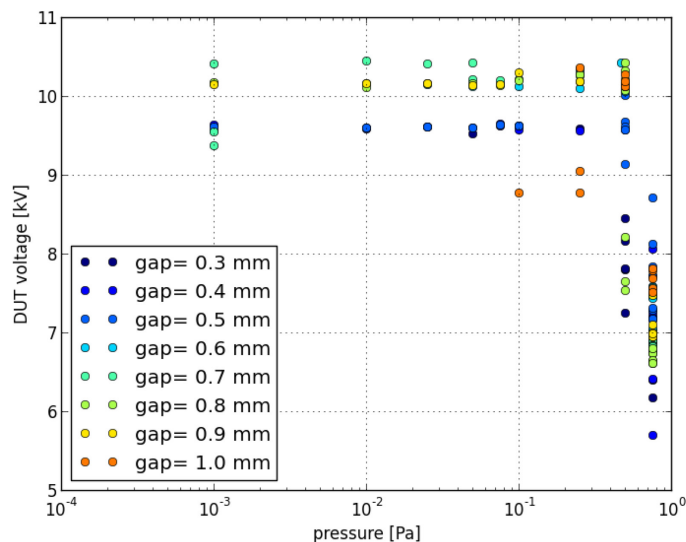
Figure 6-25 - Voltage applied to the DUT as a function of the pressure: markers of different color identify different gaps

Figure 6-25 is the same as Figure 6-24, showing the maximum voltage with different colours in dependence of the gap. This representation allows appreciating the effect of the gap on the breakdown

voltage (red dots in Figure 6-24): the breakdown voltage (for pressures of 0.5 Pa and 0.75 Pa) depends on the gap, even if the tendency is not clear. In fact for the gaps 0.8, 0.9, 1.0 mm the breakdown voltage increases with the gap, but it is lower with respect to the breakdown voltage at 0.5 mm.

6.2.3 Issues and improvements of the HVRFTF arrangement

The results obtained in the second experimental campaign showed the effectiveness of the provisions implemented after the first experimental campaign; in particular a wider operating region has been explored.

However the target to achieve a complete breakdown between the electrodes with small gaps has not been reached yet; instead only sparks were seen without a visible influence on the measurements. This fact is under evaluation: either sparks do not influence the measurements or they are not detected by the transducers (which nevertheless have a large bandwidth) or they are not stored by the data acquisition system.

An improvement of the diagnostics is planned to better detect the sparks, the following provisions will be implemented:

- Increase the sampling frequency of the data acquisition system;
- Installation of a photomultiplier to detect the occurrence of sparks and to measure their light intensity;
- Installation of a CCD camera to capture DUT frames during shots.

Furthermore the instantaneous pressure and the gap are to be acquired by the data acquisition system.

All data coming from the diagnostics will then be stored on the MDSplus server, with a coherent time base.

The other important improvement in progress is the upgrade of the high voltage generation circuit which is necessary to reach the target DUT voltage and to control the operating frequency; its main tasks are:

- The procurement and installation of vacuum variable capacitors (being delivered to Consorzio RFX within the end of 2017)
- The procurement of a powerful amplifier to reach at least the nominal voltage of the driver.

Conclusions

The work carried out during my Ph.D. was addressed to develop a test facility called "High Voltage RadioFrequency Test Facility" (HVRFTF), in order to characterize the dielectric strength of the drivers of the RF ion source of the SPIDER and MITICA projects of the ITER Neutral Beam Test Facility (NBTF).

Basically, the experimental arrangement worked out consists of a vacuum vessel capable to host different types of driver mock-ups (called "Device Under Test", DUT, in the thesis), a gas injection and pumping system to supply the desired gas species, and a RF circuit designed to produce the required high voltage.

My studies were first addressed to identify the HVRFTF requirements. The difficulty in working out a mock-up of the SPIDER RF driver, with a simplified geometry but capable of reproducing similar operating conditions in terms of applied voltage and E-field amplitude, has been faced studying several possible solutions and then working out a configuration of planar-spherical electrodes, with a dielectric disk interposed in between. The analysis carried out showed its capability in reproducing the E-field in the driver, with the same gaps and voltage.

The development of an efficient RF resonant circuit, for the generation of the desired high voltage at 1 MHz to supply the DUT, turned out to be quite challenging, as regards in particular the target of assuring the matching condition against the variable impedance of the load and stray impedances; I worked out a careful design of the circuit components to meet the requirements minimizing the power losses.

I conceived a flexible test arrangement, which allows the variation of the quantities influencing the voltage hold off, such as pressure, geometry and materials of the devices under test, in order to perform parametric analyses which can suggest insights for future driver improvements.

As for the experimental part of the project, a very important goal achieved is that the HVRFTF, developed from scratch, has been completed and entered into operation in 2016. The first experimental campaign with the preliminary RF circuit supplying a couple of planar circular electrodes allowed substantiating the basic test arrangement. The design approach was confirmed experimentally and the models used for the design were validated. Moreover it was possible to gain confidence with the operation of the testbed, to discover issues related to some specific operating conditions and to identify possible provisions.

With the second experimental test campaign, the provisions adopted allowed the extension of the operational range of the facility and the achievement of a voltage up to 10 kV rms. However, the capability to generate and detect the breakdown is still to be improved: currently the only detected breakdowns are related to glow discharges between the high voltage electrode and the vacuum vessel for relatively high pressures (≥ 0.25 Pa), larger than that at which the driver RF coil will operate.

Some sparks between the electrodes were observed for lower pressures and small gaps, but not followed by a complete breakdown. This may be due to a voltage not sufficient to cause and sustain a breakdown or to a not sufficient capability of the data acquisition system to detect and acquire it.

Furthermore, an unexpected behaviour of the RF circuit, characterized by mechanical vibrations of the DUT, further limited the voltage with a gap of 0.1 mm, which otherwise could have been characterized by the highest E-field values.

Presently, the driver mockups and the components for the final circuit are being procured; they will be implemented in the RF circuit for the next test campaigns in 2018. The plans for the next year are to reach the target voltage across the DUT and to investigate breakdown conditions. More in general, the tests will be addressed to provide support to the operation of SPIDER, to the development of the MITICA beam source drivers and to improve skills and knowledge on radiofrequency, in line with the basic scope of the RF R&D task.

Finally, few words about my personal development: this Ph.D. experience has represented a very significant growth under several points of view: in fact, besides an improved capability to carry out both theoretical and experimental research work, I have also grown in the capability of coordinating a research task. In fact, since 2015, I have carried out these activities in the role of Work Package Manager of the RF R&D task of the NBTF workprogramme, thus managing the task work according to the received directives. In this role, I have identified the subtasks regarding the design, realization and operation of the facility and managed the contributions of about six to eight persons among students, researchers and technicians.

References

[1] V. Toigo, S. Dal Bello, E. Gaio, A. Luchetta, R. Pasqualotto, P. Zaccaria, M. Bigi, G. Chitarin, D. Marcuzzi, N. Pomaro, G. Serianni, P. Agostinetti, M. Agostini, V. Antoni, D. Aprile, C. Baltador, M. Barbisan and Battistella, "The ITER Neutral Beam Test Facility towards SPIDER operation," *Nuclear Fusion,* vol. 57, no. 8, 2017.

[2] E. Speth, H. Falter, P. Franzen, U. Fantz, M. Bandyopadhyay, S. Christ, A. Encheva, M. Froeschle, D. Holtum, B. Heinemann, W. Kraus, A. Lorenz, C. Martens, P. McNeely, S. Obermayer, R. Riedl, R. Süss, A. Tanga and Wilhelm, "Overview of the RF source development programme at IPP Garching," *Nuclear Fusion,* vol. 46, no. 6, 2006.

[3] P. Franzen, H. Falter, U. Fantz, W. Kraus, M. Berger, S. Christ-Koch, M. Froschle, R. H. B. H. ,. S. Gutser, S. Leyer, C. Martens, P. McNeely, R. Riedl, E. Speth and D. Wunderlich, "Progress of the development of the IPP RF negative ion source for the ITER neutral beam system," *Nuclear Fusion,* vol. 47, no. 4, pp. 264-270, 2007.

[4] D. Marcuzzi, P. Agostinetti, M. Dalla Palma, M. De Muri, G. Chitarin, G. Gambetta, N. Marconato, R. Pasqualotto, M. Pavei, N. Pilan, A. Rizzolo, G. Serianni, V. Toigo, L. Trevisan, M. Visentin, P. Zaccaria and Zaupa, "Final design of the beam source for the MITICA injector," *Review of Scientific Instruments,* vol. 87, 2016.

[5] D. Marcuzzi, M. Dalla Palma, M. Pavei, B. Heinemann, W. Kraus and R. Riedl, "Detailed design of the RF source for the 1 MV neutral beam test facility," *Fusion Engineering and Design,* vol. 84, no. 7-11, pp. 1253-1258, June 2009.

[6] D. Marcuzzi, P. Agostinetti, M. Dalla Palma, F. Degli Agostini, M. Pavei, A. Rizzolo, M. Tollin and L. Trevisan, "Detail design of the beam source for the SPIDER experiment," *Fusion Engineering and Design,* vol. 85, no. 10-12, pp. 1792-1797, December 2010.

[7] P. Agostinetti, V. Antoni, M. Cavenago, G. Chitarin, N. Marconato, D. Marcuzzi, N. Pilan, G. Serianni, P. Sonato, P. Veltri and P. Zaccaria, "Physics and engineering design of the accelerator and electron dump for SPIDER," *Nuclear Fusion,* vol. 51, 2011.

[8] P. Franzen, B. Heinemann, U. Fantz, D. Wünderlich, W. Kraus, M. Froeschle, C. Martens, R. Riedl, R. Nocentini, A. Masiello, B. Ruf, L. Schiesko and C. Wimmer, "Commissioning and first results of the ITER-relevant negative ionbeam test facility ELISE," *Fusion Engineering and Design,* vol. 88, no. 12, p. 3132–3140, 2013.

[9] P. Franzen, H. Falter, B. Heinemann, C. Martens, U. Fantz, M. Berger, S. Christ-Koch, M. Froeschle, D. Holtum, W. Kraus, S. Leyer, P. McNeely, R. Riedl, R. Süss, S. Obermayer, E. Speth and D. Wünderlich, "RADI—A RF source size-scaling experiment towards the ITER neutral beam negative ion source," *Fusion Engineering and Design,* vol. 82, no. 4, pp. 407-423, June 2007.

[10] B. Heinemann, H. Falter, U. Fantz, P. Franzen, M. Fröschle, R. Gutser, W. Kraus, R. Nocentini, R. Riedl, E. Speth, A. Stäbler, D. Wünderlich, P. Agostinetti and T. Jiang, "Design of the "half-

size" ITER neutral beam source for the test facility ELISE," *Fusion Engineering and Design,* vol. 84, no. 2-6, pp. 915-922, 2009.

[11] UNDP, "Programme United Nations Development - Calculating the human development indices," [Online]. Available: http://hdr.undp.org/sites/default/files/hdr2016_technical_notes.pdf.

[12] "United Nations graphs," [Online]. Available: https://esa.un.org/unpd/wpp/Graphs/DemographicProfiles/.

[13] D. M. Martìnez and B. W. Ebenhack, " Understanding the role of energy consumption in human development through the use of saturation phenomena," *Energy Policy,* vol. 36, p. 1430–1435, 2008.

[14] International Energy Agency, "World Energy Outlook 2017," OECD/IEA, Paris, 2017.

[15] UN, "the 2030 Agenda for Sustainable Development," 2015. [Online]. Available: http://www.un.org/ga/search/view_doc.asp?symbol=A/RES/70/1&Lang=E. [Accessed 30 10 2017].

[16] IEA, "CO2 emissions from fuel combustion highlights 2017," [Online]. Available: https://www.iea.org/publications/freepublications/publication/CO2EmissionsfromFuelCombustion_Highlights_2016.pdf. [Accessed 30 10 2017].

[17] EFDA, "Fusion Electricity A roadmap to the realisation of fusion energy," [Online]. Available: https://www.euro-fusion.org/wpcms/wp-content/uploads/2013/01/JG12.356-web.pdf. [Accessed 30 10 2017].

[18] IAEA, "ITER EDA Agreement and Protocol 2," ITER EDA Documentation Series No. 5, Vienna, 1994.

[19] IAEA, "SUMMARYof the ITER FINAL DESIGN REPORT," ITER EDA DOCUMENTATION SERIES NO. 22, Vienna, 2001.

[20] "ITER organization website," [Online]. Available: https://www.iter.org/.

[21] M. Kuriyama, N. Akino, T. Aoyagi, N. Ebisawa, N. Isozaki, A. Honda, T. Inoue, T. Itoh, M. Kawai, M. Kazawa, J. Koizumi, Mogaki, K., Y. Ohara, T. Ohga, Y. Okumura, H. Oohara, K. Ohshima, F. Satoh, T. Takenouchi, Y. Toyokawa, K. Usui and Watanab, "Operation of the negative-ion based NBI for JT-60U," *Fusion Engineering and Design,* Vols. 39-40, pp. 115-121, 1998.

[22] H. de Esch, R. Hemsworth and P. Massmann, "SINGAP: the European concept for negative ion acceleration in the ITER neutral injectors," *Review of Scientific Instruments,* vol. 73, no. 2, pp. 1045-1047, 2002.

[23] M. Taniguchi, H. P. L. de Esch, L. Svensson, N. Umeda, M. Kashiwagi, K. Watanabe, H. Tobari, M. Dairaku, K. Sakamoto and T. Inoue, "Development of 1 MeV H- Accelerator at JAEA for ITER NB," in *AIP Conference Proceedings*, 2009.

[24] R. S. Hemsworth, A. Tanga and V. Antoni, "Status of the ITER neutral beam injection system," *Review of Scientific Instruments,* vol. 79, no. 2, 2008.

[25] P. Sonato, V. Antoni, M. Bigi, G. Chitarin, A. Luchetta, D. Marcuzzi, R. Pasqualotto, N. S. G. Pomaro, V. Toigo and P. Zaccaria, "Status Of PRIMA, The Test Facility For ITER Neutral Beam Injectors," in *Third International Symposium on Negative Ions, Beams and Sources*, 2012.

[26] V. Toigo and e. al, "Progress in the realization of the PRIMA neutral beam test facility," *Nuclear Fusion,* vol. 55, no. 8, 2015.

[27] V. Toigo and e. al, "A substantial step forward in the realization of the ITER HNB system: The

ITER NBI Test Facility," *Fusion Engineering and Design,* 2016.

[28] E. Sartori, G. Serianni and S. Dal Bello, "Simulation of the gas density distribution in the large vacuum system of a fusion-relevant particle accelerator at different scales," *Vacuum,* vol. 122, 2015.

[29] E. Gaio, W. Kraus, C. Martens, R. Piovan, E. Speth and V. Toigo, "Studies on the radio frequency power supply system for the ITER NB injector ion source," *Fusion Engineering and Design,* vol. 82, pp. 912-919, 2007.

[30] A. Zamengo, M. Recchia, W. Kraus, M. Bigi, C. Martens and V. Toigo, "Electrical and thermal analyses for the radio-frequency circuit of ITER NBI ion source," *Fusion Engineering and Design,* vol. 84, pp. 2025-2030, 2009.

[31] M. Boldrin, L. Grando, A. Pesce, M. Recchia, V. Toigo and e. al, "The 100 kV Faraday cage (High Voltage Deck) for the SPIDER experiment," *Fusion Engineering and Design,* Vols. 96-97, pp. 411-415, 2015.

[32] M. Boldrin, V. Toigo, D. Gutierrez, M. Simon, G. Faoro, E. Maggiora, D. Pedron, A. Guion and H. Decamps, "The Transmission Line for the SPIDER Experiment: From design to installation," *Fusion Engineering and Design,* 2017.

[33] M. Bigi, L. Rinaldi, M. Simon, L. Sita, G. Taddia, S. Carrozza, H. Decamps, A. Luchetta, A. Meddour, M. Moressa, C. Morri, A. Musile Tanzi, M. Recchia, U. Wagner and Zame, "Design, manufacture and factory testing of the Ion Source and Extraction Power Supplies for the SPIDER experiment," *Fusion Engineering and Design,* Vols. 96-97, pp. 405-410, 2015.

[34] M. Boldrin, A. De Lorenzi, H. Decamps, L. Grando, M. Simon and V. Toigo, "Design status and procurement activities of the High Voltage Deck 1 and Bushing for the ITER Neutral Beam Injector," *Fusion Engineering and Design,* vol. 88, no. 6-8, pp. 985-989, 2013.

[35] L. Zanotto, E. Gaio, D. Gutiérrex, M. Simon, H. Decamps, M. Perna, F. Fuarda, C. Panizza, A. Premoli, C. Finotti and C. Brocca, "Final design of the acceleration grid power supply conversion system of the MITICA Neutral Beam Injector," *Fusion Engineering and Design,* 2017.

[36] K. e. a. Watanabe, "Design of a -1 MV dc UHV power supply for ITER NBI," *Nuclear Fusion,* vol. 49, no. 5, 2009.

[37] D. Wünderlich, W. Kraus, M. Froeschle, R. Riedl, U. Fantz and B. Heinemann, "Long pulse, high power operation of the ELISE test facility," in *AIP Conference Proceedings,* 2017.

[38] C. Bowik, RF circuit design, Amsterdam, Boston: Newnes/Elsevier, 2008.

[39] D. C. Meeker, "Finite Element Method Magnetics, Version 4.2 (01 Apr 2009 Build)," [Online]. Available: http://www.femm.info.

[40] F. Rohrbach, "Isolation sous Vide," CERN 71-5 Report, 1971.

[41] L. Cranberg, "The Initiation of Electrical Breakdown in Vacuum," *Journal of Applied Physics,* vol. 23, p. 518, 1952.

[42] R. Latham, High Voltage Vacuum Insulation, Elsevier, 1995.

[43] H. C. Miller, "Flashover of Insulators in Vacuum. Review of the Phenomena and Techniques to Improve Holdoff Voltage," *IEEE nansactions on Electrical Insulation,* vol. 28, no. 4, 1993.

[44] R. Hawley, "Solid Insulators in Vacuum: A Review," *Vacuum,* vol. 18, no. 7, pp. 383-390, 1968.

[45] R. A. Anderson and J. P. Brainard, "Mechanism of pulsed surface flashover involving electron-stimulated desorption," *Journal of Applied Physics,* vol. 51, no. 3, p. 1414, 1980.

[46] B. Heinemann, U. Fantz, W. Kraus, L. Schiesko, C. Wimmer, D. Wünderlich, F. Bonomo, M. Froeschle, R. Nocentini and R. Riedl, "Towards large and powerful radio frequency driven negative ion sources for fusion," *New Journal of Physics,* vol. 19, 2017.

[47] B. Jüttner and H. Wolff, in *7th Int. Cnf. Phenom. Ionised Gases ,* Beograd, 1965.

[48] B. Jüttner, H. Wolff and P. Pech., in *8th Int. Cnf. Phenom. Ionised Gases ,* 1967.

[49] R. Hackham, *J. Appl. Phys.,* no. 46, pp. 3789-99, 1975.

[50] R. Hackham and G. Govindra Raju, *J. Appl. Phys.,* no. 45, pp. 4784-94, 1974.

[51] Springer Handbook Condensed Matter and Materials Data, ISBN 3-540-44376-2.

[52] "DuPont™ Vespel® SP-1 Typical ISO Properties ," [Online]. Available: http://www.dupont.com/content/dam/dupont/products-and-services/plastics-polymers-and-resins/parts-and-shapes/vespel/documents/VPE-A10861-00-B0614.pdf.

[53] A. Maistrello, P. Jain, M. Recchia, F. Baldo and F. Rossetto, "RF R&D report 2015," 2016.

[54] J. A. Stillerman, T. W. Fredian, K. Klare and G. Manduchi, "MDSplus data acquisition system," *Review of Scientific Instruments,* vol. 68, no. 1, pp. 939-942, 1997.

[55] "MDSplus website," [Online]. Available: http://www.mdsplus.org.

[56] "Redpitaya," [Online]. Available: https://redpitaya.com/.

[57] "RaspberryPi," [Online]. Available: https://www.raspberrypi.org/.

[58] G. Serianni, C. Baltador, P. Barbato, L. Baseggio, R. Cavazzana, M. Cavenago, M. De Muri, B. Laterza, L. Migliorato, F. Molon, G. Moro, D. Ravarotto, R. Pasqualotto, P. Patton, M. Recchia, C. Taliercio and P. Veltri, "Acquisition, data retrieval, interlock and control systems for the negative ion source NIO1," in *Fifth International Symposium on Negative Ions, Beams and Sources*, 2017.

[59] G. Manduchi, C. Taliercio and A. Luchetta, "The Java interface of MDSplus: towards a unified approach for local and remote data access," *Fusion Engineering and Design,* vol. 48, no. 1-2, pp. 163-170, 2000.

[60] N. Giao, "Electrode design for testing in uniform Field Gaps," *IEEE Transaction on Power Apparatus & System,* 1980.

[61] G. Grandi, "Optimal Design of Single-Layer Solenoid Air-Core Inductors for High Frequency Applications," *Proceedings of the 40th Midwest Symposium on Circuits and Systems,* 1997.

[62] S. C. Brown, Basic Data of Plasma Physics, New York: American Institute of Physics, 1994.

[63] R. Schnyder, A. A. Howling, D. Bommottet and C. Hollenstein, "Direct current breakdown in gases for complex geometries from high vacuum to atmospheric pressure," *Journal of Physics D: Applied physics,* vol. 46, p. 9, 2013.

[64] G. Grandi, "Stray Capacitances of Single-Layer Solenoid Air-Core Inductors," *IEEE Transactions on Industry Applications,* vol. 35, no. 5, september/october 1999.

[65] A. Massarini, "Self-Capacitance of Inductors," *IEEE Transactions on Power Electronics,* vol. 12, no. 4, 1997.

[66] Python, "https://www.python.org/," [Online].

[67] S. Butterworth, "Eddy current losses in cylindrical conductors with special application to the alternating current resistance of short coils," *Phil. Trans.,* 1922.

[68] S. Butterworth, "Note on the alternating current resistance of single layer coils," 1923.

[69] R. G. Medhurst, "H.F. resistance and self-capacitance of single layer solenoids," *Wireless*

Engineer, 1947.

[70] A. Massarini, "Lumped Parameter Models for Single and Multiple Layer Inductors," *PESC '96 Record., 27th Annual IEEE,* 1996.

[71] A. De Lorenzi, "HVPTF - The high voltage laboratory for the ITER Neutral Beam test facility," *Fusion Engineering and Design,* vol. 86, no. 6-8, p. 742–745, 2011.

[72] L. Pivovar and V. Gordienko, *Sov. Phys-Tech. Phys,* no. 908-12, 1963.

[73] J. M. Meek and J. D. Craggs, "Electrical Breakdown of Gases," 1953.

[74] H. Smith, "Breakdown behaviour in radiofrequency argon discharges," *Physics of plasmas,* vol. 10, no. 3, 2003.

[75] I. Korlov, "Breakdown in hydrogen and deuterium gases in static and radiofrequency fields," *Physics of plasmas,* vol. 22, no. 9, 2015.

[76] P. Dowell, "Effects of eddy currents in transformer windings," in *Proc. Inst. Elect. Eng.,* 1966.

[77] H. de Esch, D. Stork, C. Challis and B. Tubbing, "The optimization of neutral beams for ignition and burn," *Fusion Engineering and Design,* vol. 26, p. 589–604, 1995.

[78] H. C. Miller and F. G.A., "Polarity Effect in Vacuum Breakdown Electrode Conditioning," *Journal ofApplied Physics,* vol. 36, no. 4, pp. 1338-1344, 1965.

7 Appendix

I Air core single layer solenoid model

To design an inductor suitable for the RF circuit of the HVRFTF, it is necessary to take into account not only the inductance but also its stray parameters which strongly influence its impedance (modulus and argument) at high frequency.

One of the fundamental parameters is the resistance of the inductor at the resonance frequency: it reduces the Q factor, thus the voltage gain and it increases the power losses of the circuit. In literature it is found that the single layer solenoid construction type is the best candidate to be used as inductor at high frequency since it presents lower stray capacitance with respect to multiple layer solenoids.

A set of models has been developed in order to:

- calculate the inductance, resistance and stray capacitances of the inductor starting from the geometry of the inductor and from the materials properties;
- calculate the impedance of the inductor versus frequency, starting from the inductor electrical parameters, as previously evaluated.

The input data for the models are the geometry of the inductor (Figure 7-1) and the properties of the materials used to build the inductor.
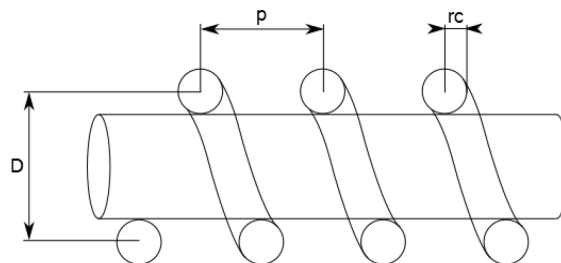
Figure 7-1 - Notation for inductor geometry

The desired output is the impedance as a function of frequency, in the range in which the inductor will be used. A set of models has been developed with Python to achieve this goal: at first the electrical parameters of the inductor are calculated and then they are used to calculate the impedance as a function of frequency.

I.i Resistance

The calculation of the resistance is based on the method proposed by S. Butterworth, and using experimental coefficients found by R.G. Medhurst. This method has been cited recently in [64].
The high frequency resistance is calculated as:

$$R_{hf} = R_{dc} \cdot H \cdot \Phi \tag{23}$$

Where:

- R_{dc} is the dc resistance of the straight wire which will be wound in a coil;
- $H = \frac{\sqrt{2} \cdot z + 1}{4}$, if z > 5, otherwise it is not accurate. H is the ratio between the resistance of the straight wire at high frequency and the dc resistance of the straight wire;
- $z = \frac{dw}{2} \sqrt{\frac{\omega \mu_0}{\rho}}$ is the ratio between the wire diameter and the penetration depth divided by square root of 2;
- dw is the wire diameter in [cm];
- f is the frequency [Hz];
- ρ is the resistivity of the wire [Ω cm];
- Φ is an experimental coefficient ratio between the coil resistance at high frequency and the resistance of the straight wire at the same frequency.

I.ii Inductance

The self-inductance L of the coil is calculated as presented in [61] by G. Grandi et al. exploiting the geometric symmetry and neglecting the influence of skin and proximity effects the inductance:

$$L = N L_1 + 2 \sum_{k=1}^{N-1} (N - k) M_{1,k+1} \tag{24}$$

Where L_1 is the self-inductance of each turn and $M_{1,k+1}$ are the N-1 different mutual inductances between the turns, calculated as:

$$L_1 = \mu_0 \frac{D}{2} \left(\ln \frac{4D}{rc} - \frac{7}{4} \right) \tag{25}$$

$$M_{1,k+1} = \frac{\mu_0 D}{2} \left[\left(\frac{2}{c} - c \right) K(c) - \frac{2}{c} E(c) \right] \tag{26}$$

Where:

- D is the coil diameter;
- rc is the radius of the conductor;
- K(c),E(c) are the elliptic integrals of the first and second kinds;
- $c^2 = \frac{D^2}{D^2 + (kp)^2}$;
- p is the pitch winding.

I.iii Capacitances

The script calculates the stray capacitances of the coil as presented by G. Grandi et al. in [64].

The authors of the paper assumed that the turn to turn stray capacitance C_{tt} can be calculated with the formula of the capacitance per unit length of a couple of infinitely long parallel conductors placed in a homogeneous medium:

$$C_{tt} = \frac{\pi^2 D \epsilon_0 \epsilon_r}{\ln\left[\frac{p}{2\,rc} + \sqrt{\left(\frac{p}{2rc}\right)^2 - 1}\right]} \tag{27}$$

Where:
- D is the coil diameter;
- rc is the radius of the conductor;
- p is the pitch winding.

The turn to shield capacitance C_{ts} is calculated using the formula of the capacitance per unit length between an infinitely long straight conductor and a parallel conducting plane.

$$C_{ts} = \frac{2\pi^2 D \epsilon_0 \epsilon_r}{\ln\left[\frac{hp}{rc} + \sqrt{\left(\frac{h}{rc}\right)^2 - 1}\right]}$$

Where:
- D is the coil diameter;
- rc is the radius of the conductor;
- h is the distance between the shield and the coil winding.

For the inductors without shield the C_{ts} is the capacitance to ground and it is calculated with the same formula, with a distance from the "shield" (the ground) of 2 m. This is a strong approximation, and if necessary in the future the model can be improved.

I.iv Calculation of the impedance of the inductor

The impedance of the inductor at a given frequency is calculated starting from the electrical parameters (resistance, inductance, turn to turn capacitance and turn to shield capacitance), the number of turns and the type of connection symmetric or not with respect to ground (with terminals floating or with a terminal grounded).

Making reference to the Figure 7-2 representing the inductor's equivalent circuit and depending on the type of connection the code calculates the impedance in two different ways:
- In case of symmetric circuit: starting from the equivalent components representing the centre of the inductor's circuit and moving towards the terminals (A and B of Figure 7-2), following the electrical rules;
- In case of asymmetric circuit (if one terminal is grounded): from the equivalent components at ground potential (for instance terminal B of Figure 7-2) moving towards the other terminal (for instance terminal A of Figure 7-2), following the electrical rules.

Note that if one terminal is grounded the capacitance C_{ts} connected to that terminal is short circuited.

$$L_t = L/n$$
$$R_t = R_L/n$$
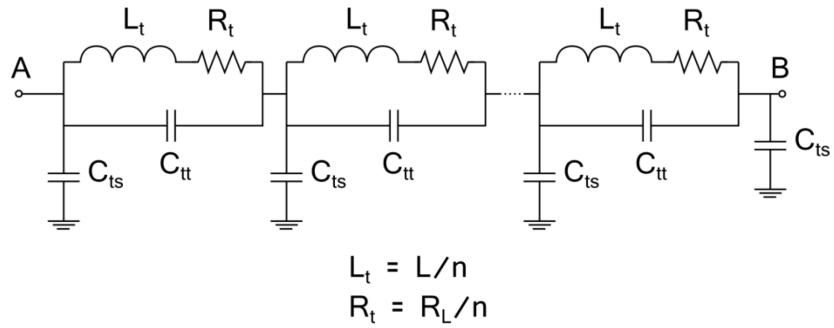
Figure 7-2 - Inductor's equivalent circuit

The calculated impedance Z_L is a complex number. The real part is called "effective resistance" (R_e) and the imaginary part is called "effective reactance": From the latter is possible to calculate the effective inductance L_e. To be noted that the effective resistance can be different with respect to the resistance of the inductor R_L, as well as the inductance.

II   Air core single layer solenoid model validation by means of test campaign

A reliable estimation of the inductor impedance versus frequency is very important to predict its behavior and its suitability to achieve the performances requested to the resonant circuit.

A wide-range test campaign was launched to characterize by a direct measurement of the impedance modulus and argument as a function of frequency some sample inductors realized with circular conductors but different geometries. The main purpose of the test campaign was the validation of the models developed, which are required to design the HVRFTF inductor.

The test campaign included additional tests on inductors built with different design concepts (i.e. rectangular conductor, litz wire, coupled solenoids) in order to understand the relative merit and achieve possible improvements in terms of energy efficiency (reducing the effective resistance).

II.i   Instrument and method

The impedance of the inductor as a function of frequency has been measured with the impedance meter HP4194A, connecting the inductor directly to the "impedance" port (frequency range 100 Hz - 40 MHz).

The data has been acquired with a PC via GPIB port, stored in a csv file and analysed with Python a script.

Table 7-1 - Main characteristics of impedance meter HP4194A

	Min	Max	Resolution
Frequency range	100 Hz	40 MHz	1 mHz
Impedance range	10 mΩ	100 MΩ	100 µΩ

One of the fundamental parameters of the matching resonant circuit for the HVRFTF is the resistance shown by the inductor at the resonance frequency. Its value influences:

- the quality factor (Q factor) and therefore the gain (of voltage) of the resonant circuit;
- the value of capacitances being used for the resonant circuit and matching network;
- the efficiency (power losses to produce high voltage) of the circuit.

The main issue is that the value of the resistance ($\sim 1\ \Omega$) is some orders of magnitude lower than the value of the reactance of the inductor at 1 MHz ($\sim 100\ \Omega$), therefore the direct measurement of the resistance with the impedance meter is not reliable.

To overcome this problem the arrangement of a resonant circuit composed of a series capacitor C_s, a parallel capacitor C_p and the inductor L to be tested in a configuration similar to the one used for HVRFTF is used, as shown in Figure 7-3.

The port AB of the circuit is connected to the impedance meter and the impedance as a function of frequency of the circuit is measured.
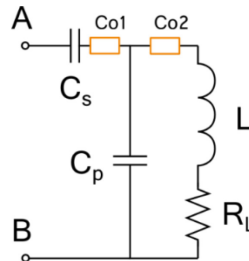
Figure 7-3 - Measurement of the resistance of the sample inductors

The connections Co1 and Co2 affect the impedance seen from port AB, but with the approximation of Figure 7-4 and neglecting the stray parameters of the capacitors, using (28), (29) and (30) it is possible to derive the impedance of the inductor at the resonant frequency.
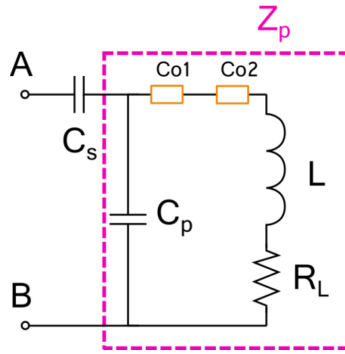
Figure 7-4 - Measurement of the resistance of the sample inductors – simplified equivalent circuit

$$Zp = ZAB - ZCs \qquad (28)$$

$$\frac{1}{ZL} = \frac{1}{Zp} - \frac{1}{ZCp} \qquad (29)$$

$$ZL = RL(f) + j\, 2\pi f L \qquad (30)$$

Where RL (f) is the effective resistance of the inductor at the frequency f.

To measure the value of the resistance RL at different frequencies, different capacitances values (different capacitors) should be used. At the moment only Cs = 25 pF and Cp = 250 pF are available at the laboratory.

II.ii Sample inductors

The geometry of the sample inductors, the measurements and the model results will be presented in the following paragraphs, below details on the design and realization are given.

For each inductor the data are presented as follow:

- Geometry of the inductor with the notation presented in Figure 7-1;
- Electrical parameters calculated with the model (Appendix paragraph I), starting from the geometry and with the assumption of having a terminal grounded;
- A plot showing the measured impedance and the simulated impedance (calculated by numerical simulation) as a function of frequency;
- Electrical parameters derived from both direct measurement using the method explained in paragraph II.i (this measure is not available for all the inductors, since some of them were disassembled before the method was developed) and simulations.

The first inductors which have been tested are air core single layer solenoids of different sizes, made by winding a wire of circular cross section.

Inductors F2, F4, G and H are based on different concepts and in particular:

- F2 (F4) is composed of two (four) single layer solenoids coupled and paralleled;
- G is made by winding a litz wire;
- H is made by winding a wire with rectangular cross section.

They have been tested in order to verify possible improvements in terms of efficiency (smaller effective resistance) with respect to coil made with conductor of circular cross section.

II.ii.a *Inductor 1*

Inductor 1 is the smallest inductor in terms of dimension which has been tested:

Table 7-2 - Inductor 1 geometry

Figure 7-5 - Sample inductor 1
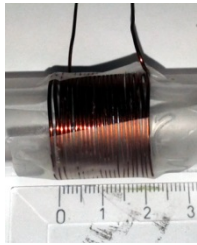
parameter	id	value	unit
Coil diameter	D	0.022	m
Conductor radius	rc	0.00045	m
Pitch	p	0.001	m
Number of turns	n	22	-
resistivity	ro	1.7E-8	Ωm

Table 7-3 - Calculated electrical parameters at 1 MHz of inductor 1

parameter	id	value	unit
Resistance	RL	613	mΩ
	L	7.23	μH
Turn to turn capacitance	Ctt	4.12	pF
Turn to shield capacitance	Cts	0.42	pF
Impedance	ZL	45.5	Ω
Simulated effective resistance	Re	614	mΩ
Simulated effective inductance	Le	7.2	μH
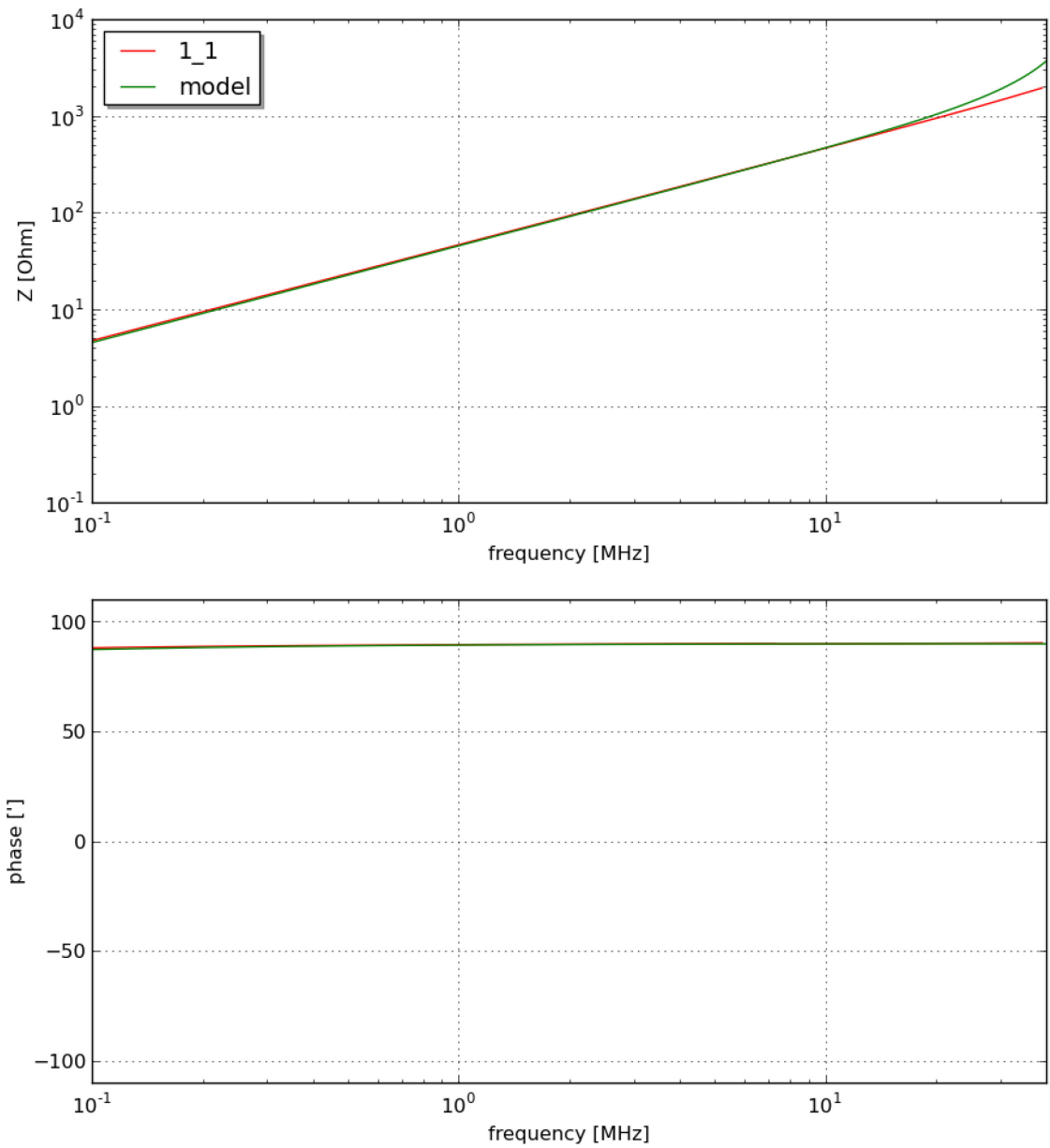
Figure 7-6 - Impedance of inductor 1, measured (red), simulated (green)

Table 7-4 - Electrical parameters of inductor 1

parameter	id	Measured @ 1 MHz	Simulated @ 1 MHz	unit
Impedance	ZL	46.8	45.5	Ω
Effective resistance	Re	n.a.	614	mΩ
Effective inductance	Le	7.4	7.2	µH

The effective resistance derived from direct measurement is not available.

II.ii.b *Inductor 2*

Figure 7-7 - Sample inductor 2

Table 7-5 - Inductor 2 geometry

parameter	id	value	unit
Coil diameter	D	0.0047	m
Conductor radius	rc	0.00045	m
Pitch	p	0.006	m
Number of turns	n	35	-
resistivity	ro	1.7E-8	Ωm

Table 7-6 - Calculated electrical parameters at 1 MHz of inductor 2

parameter	id	value	unit
Resistance	RL	553	mΩ
Inductance	L	13.42	μH
Turn to turn capacitance	Ctt	1.59	pF
Turn to shield capacitance	Cts	0.90	pF
Impedance	ZL	84.4	Ω
Simulated effective resistance	Re	555	mΩ
Simulated effective inductance	Le	13.4	μH
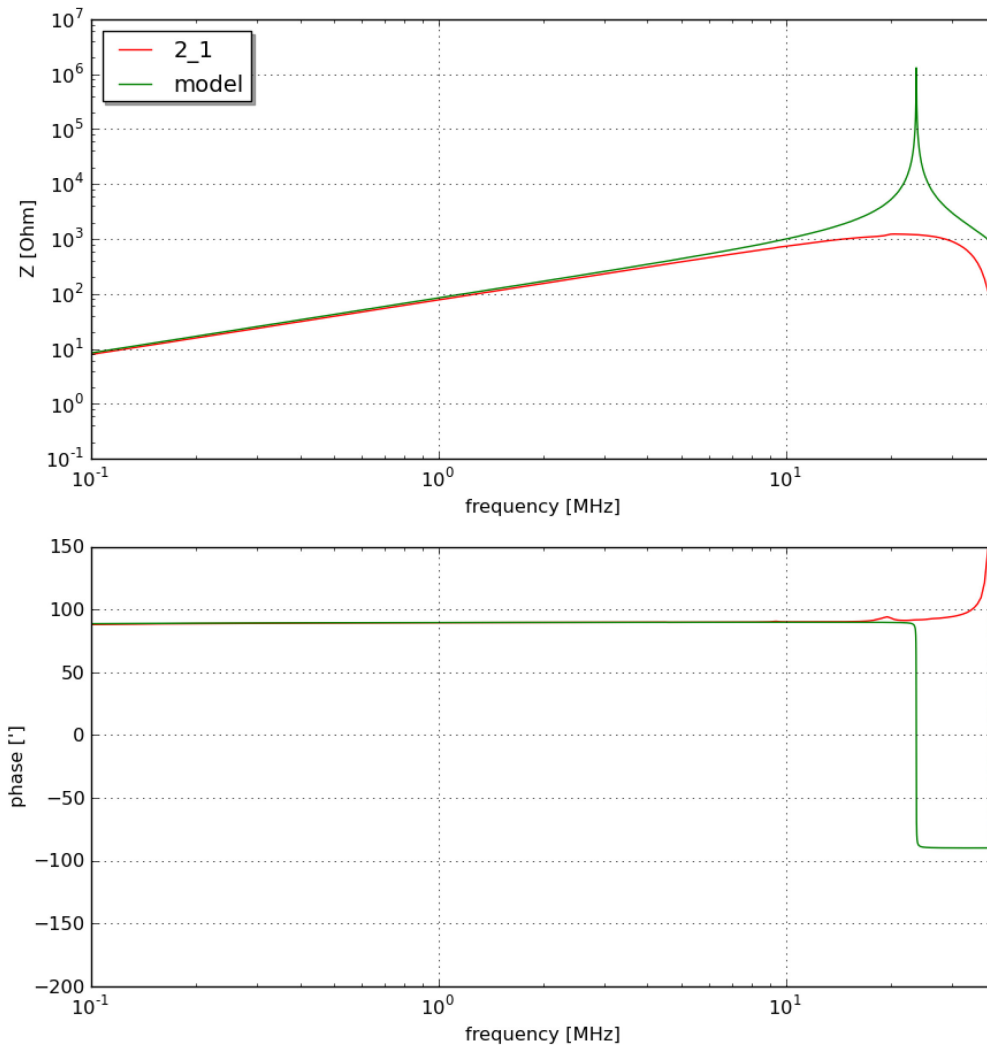
Figure 7-8 - Impedance of inductor 2, measured (red), simulated (green)

Table 7-7 - Electrical parameters of inductor 2

parameter	id	Measured @ 1 MHz	Simulated @ 1 MHz	unit
Impedance	ZL	77.3	84.4	Ω
Effective resistance	Re	n.a.	555	mΩ
Effective inductance	Le	12.2	13.4	μH

The effective resistance derived from direct measurement is not available.

Figure 7-9 - Sample inductor 3

Table 7-8 - Inductor 3 geometry

parameter	id	value	unit
Coil diameter	D	0.0475	m
Conductor radius	rc	0.0004	m
Pitch	p	0.000908	m
Number of turns	n	22	-
resistivity	ro	1.7E-8	Ωm

Table 7-9 - Calculated electrical parameters at 1 MHz of inductor 3

parameter	id	value	unit
Resistance	RL	1381	mΩ
Inductance	L	26.12	µH
Turn to turn capacitance	Ctt	8.08	pF
Turn to shield capacitance	Cts	0.90	pF
Impedance	ZL	164.5	Ω
Simulated effective resistance	Re	1387	mΩ
Simulated effective inductance	Le	26.2	µH
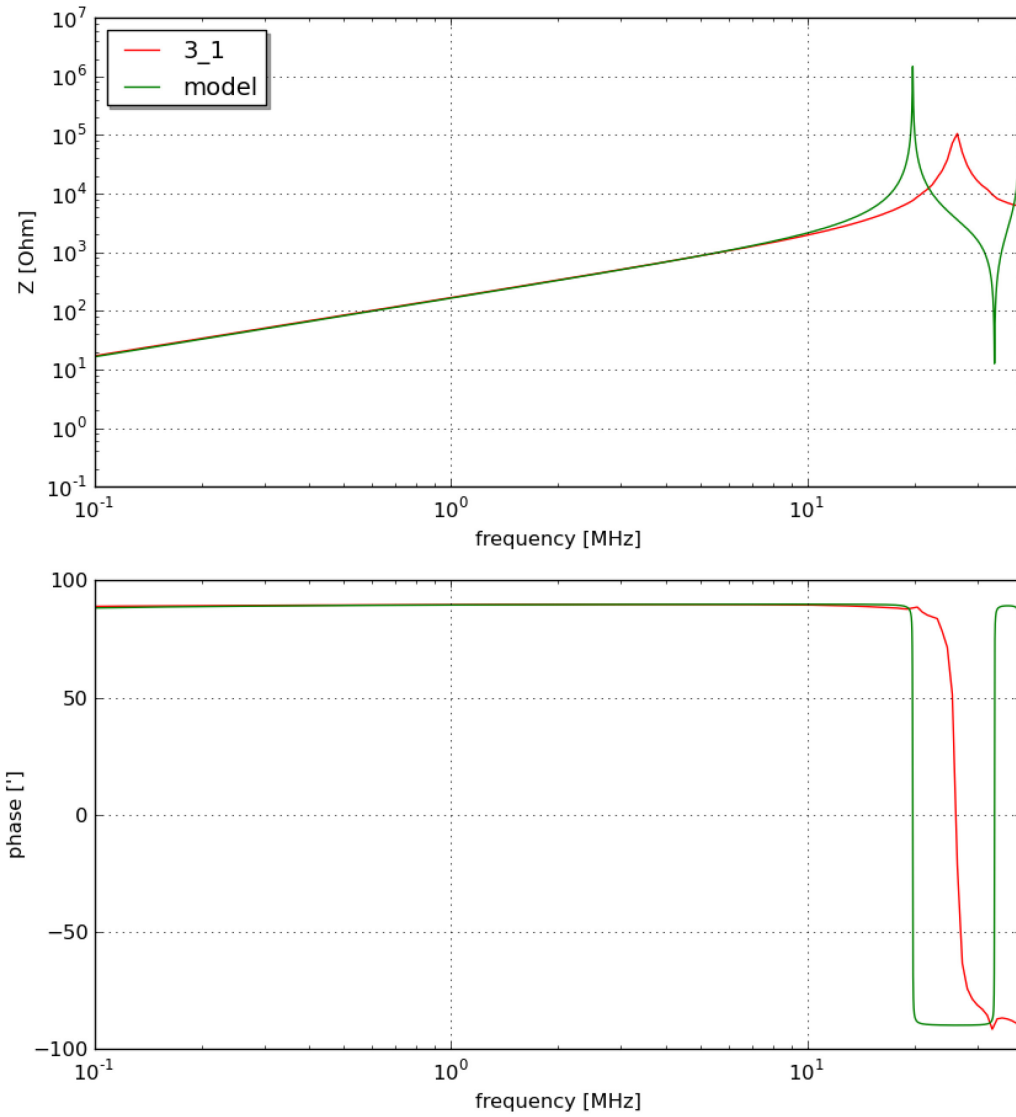
Figure 7-10 - Impedance of inductor 3, measured (red), simulated (green)

Table 7-10 - Electrical parameters of inductor 3

parameter	id	Measured @ MHz	Simulated @ MHz	unit
Impedance	ZL	164.0	164.5	Ω
Effective resistance	Re	n.a.	1387	mΩ
Effective inductance	Le	26.0	26.2	μH

The effective resistance derived from direct measurement is not available.

II.ii.d *Inductor A*
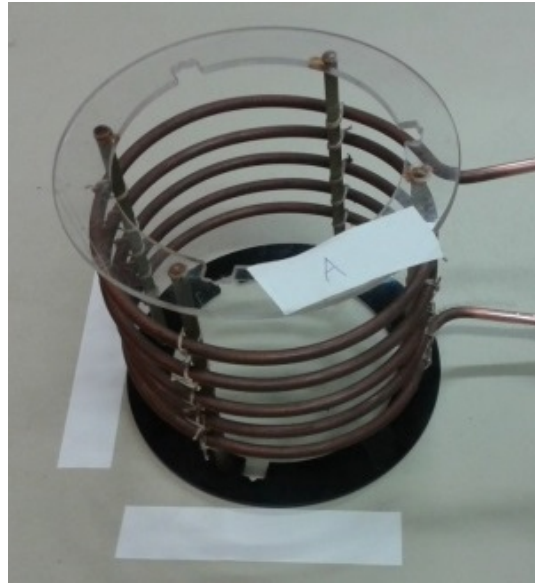
Figure 7-11 - Sample inductor A

Table 7-11 - Inductor A geometry

parameter	id	value	unit
Coil diameter	D	0.15	m
Conductor radius	rc	0.003	m
Pitch	p	0.018	m
Number of turns	n	5	-
resistivity	ro	1.7E-8	Ωm

Table 7-12 - Calculated electrical parameters at 1 MHz of inductor A

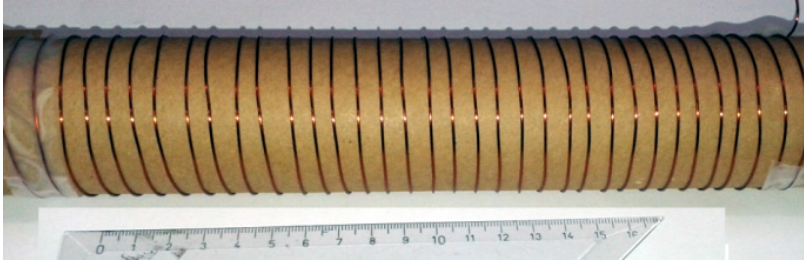| parameter	id	value	unit
Resistance	RL	39	mΩ
Inductance	L	3.69	μH
Turn to turn capacitance	Ctt	7.04	pF
Turn to shield capacitance	Cts	3.45	pF
Impedance	ZL	23.2	Ω
Simulated effective resistance	Re	39	mΩ
Simulated effective inductance	Le	3.7	μH
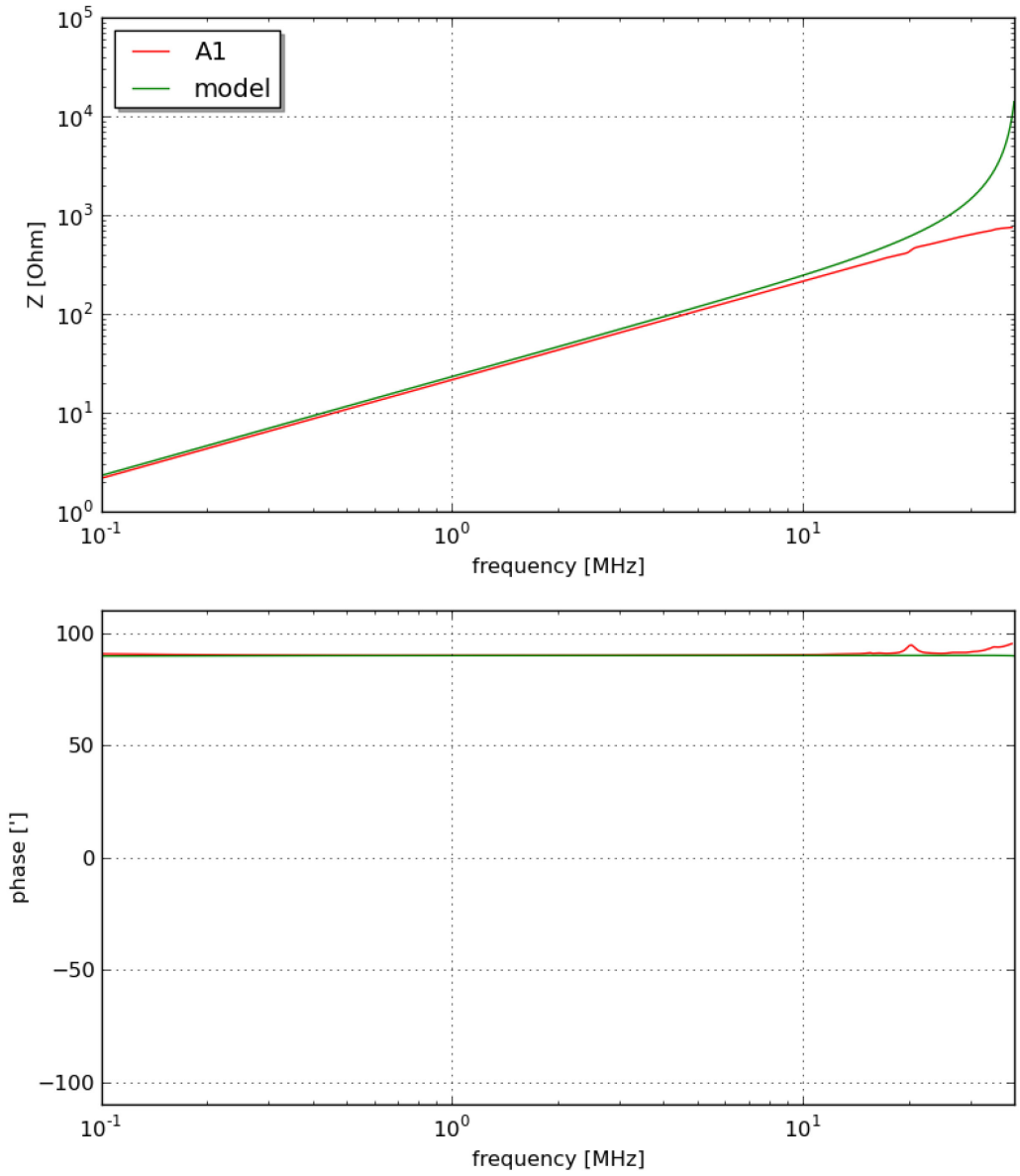
Figure 7-12 - Impedance of inductor A, measured (red), simulated (green)

Table 7-13 - Electrical parameters of inductor A

parameter	id	Measured @ 5.13 MHz	Simulated @ 5.13 MHz	unit
Impedance	ZL	112.7	120.9	Ω
Effective resistance	Re	143	91	mΩ
Effective inductance	Le	3.49	3.8	µH

Figure 7-13 - Sample inductor B

Table 7-14 - Inductor B geometry

parameter	id	value	unit
Coil diameter	D	0.115	m
Conductor radius	rc	0.0025	m
Pitch	p	0.007	m
Number of turns	n	43	-
resistivity	ro	1.7E-8	Ωm

Table 7-15 - Calculated electrical parameters at 1 MHz of inductor B

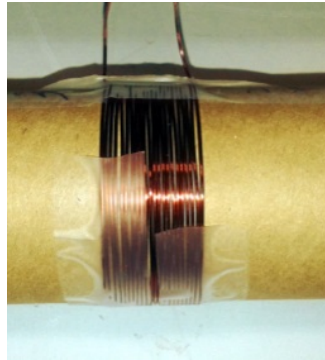| parameter	id	value	unit
Resistance	RL	566	mΩ
Inductance	L	63.8	µH
Turn to turn capacitance	Ctt	11.09	pF
Turn to shield capacitance	Cts	2.62	pF
Impedance	ZL	411.3	Ω
Simulated effective resistance	Re	596	mΩ
Simulated effective inductance	Le	65.5	µH
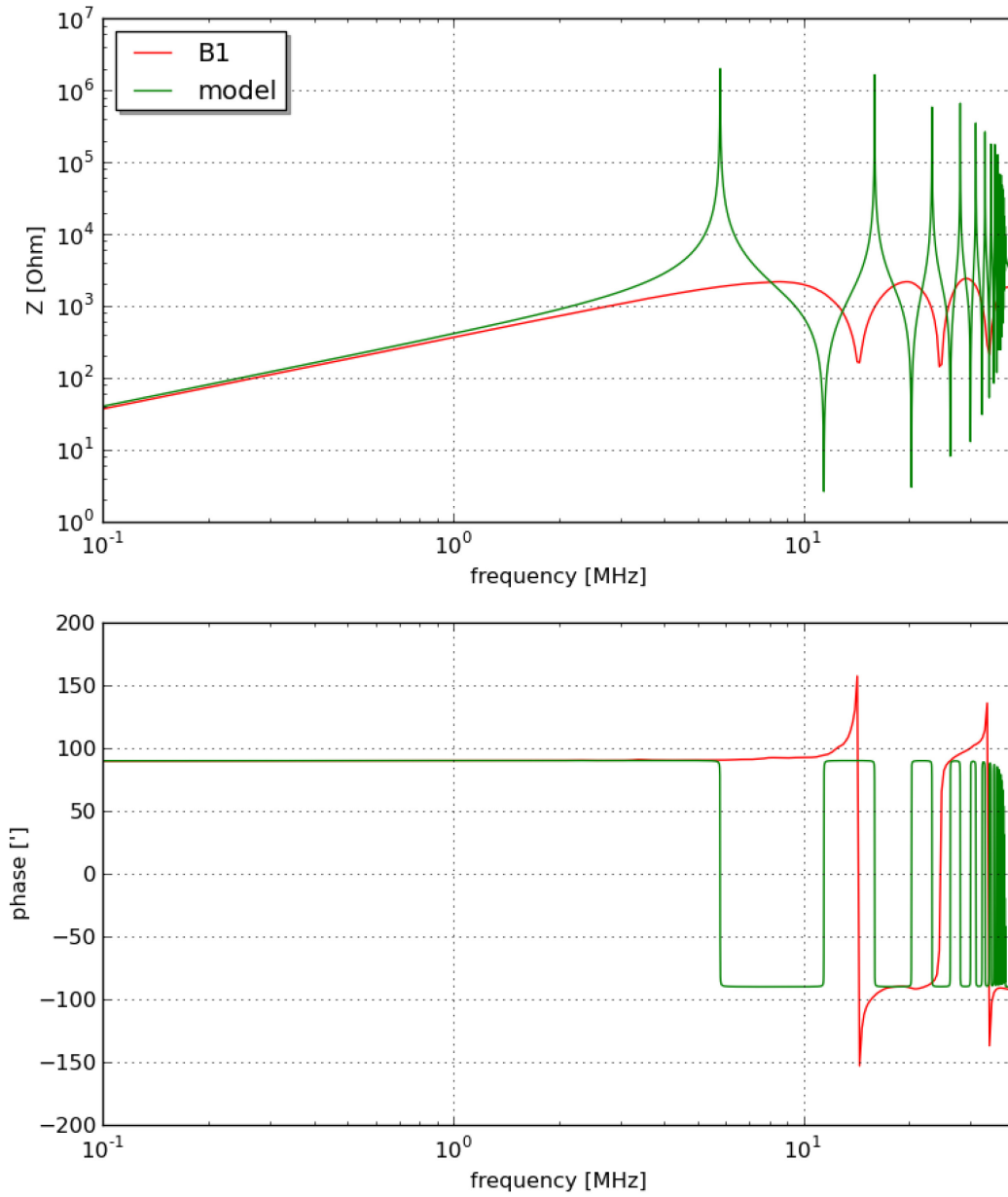
Figure 7-14 - Impedance of inductor B, measured (red), simulated (green)

Table 7-16 - Electrical parameters of inductor B

parameter	id	Measured @ 1.24 MHz	Simulated @ 1.24 MHz	unit
Impedance	ZL	468	517.4	Ω
Effective resistance	Re	616	682	mΩ
Effective inductance	Le	60.2	66.4	µH

II.ii.f *Inductor C*

Figure 7-15 - Sample inductor C

Table 7-17 - Inductor C geometry

parameter	id	value	unit
Coil diameter	D	0.225	m
Conductor radius	rc	0.005	m
Pitch	p	0.01625	m
Number of turns	n	9	-
resistivity	ro	1.7E-8	Ωm

Table 7-18 - Calculated electrical parameters at 1 MHz of inductor C

parameter	id	value	unit
Resistance	RL	116	mΩ
Inductance	L	20.45	μH
Turn to turn capacitance	Ctt	20.89	pF
Turn to shield capacitance	Cts	6.67	pF
Impedance	ZL	129.4	Ω
Simulated effective resistance	Re	117	mΩ
Simulated effective inductance	Le	20.6	μH
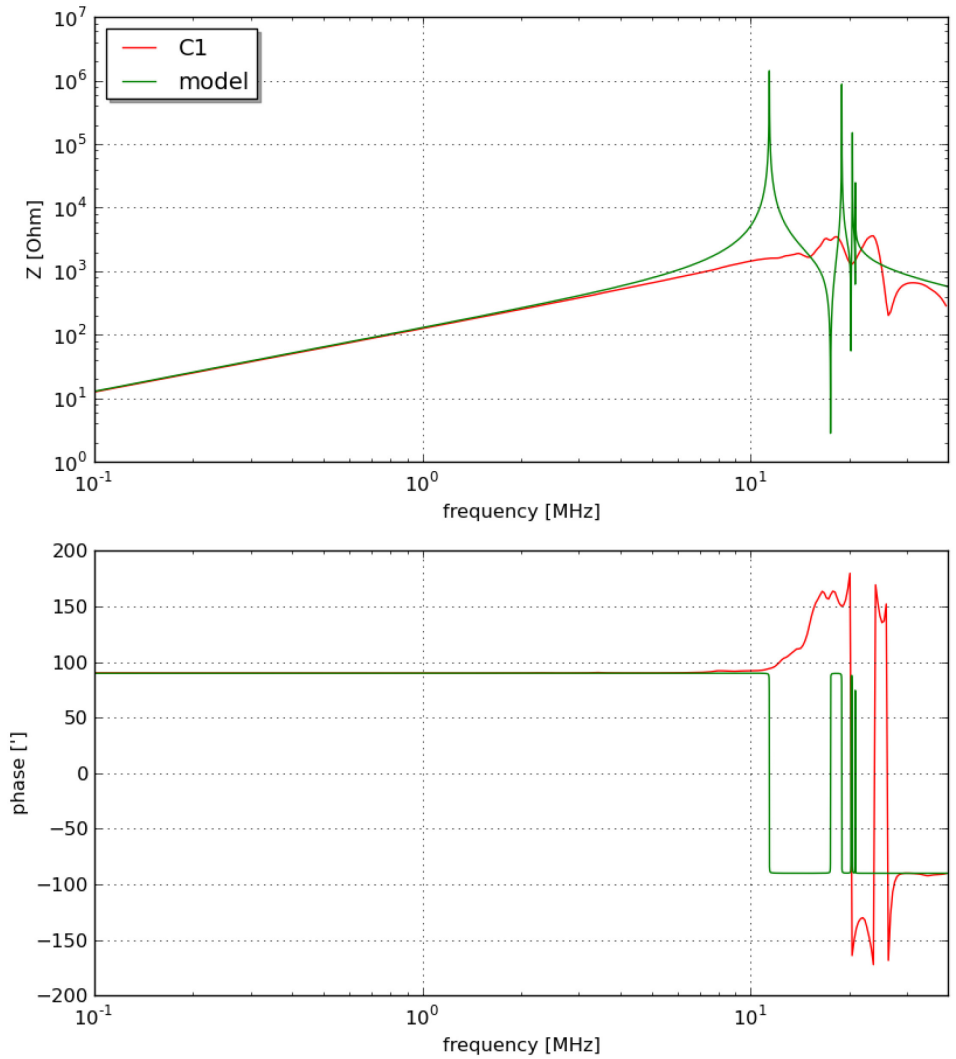
Figure 7-16 - Impedance of inductor C, measured (red), simulated (green)

Table 7-19 - Electrical parameters of inductor C

parameter	id	Measured @ 2.11 MHz	Simulated @ 2.11 MHz	unit
Impedance	ZL	274.5	280.1	Ω
Effective resistance	Re	357	179	mΩ
Effective inductance	Le	20.7	21.1	μH

II.ii.g *Inductor D*

Figure 7-17 - Sample inductor D

Table 7-20 - Inductor D geometry

parameter	id	value	unit
Coil diameter	D	0.125	m
Conductor radius	rc	0.003	m
Pitch	p	0.008	m
Number of turns	n	5	-
resistivity	ro	1.7E-8	Ωm

Table 7-21 - Calculated electrical parameters at 1 MHz of inductor D

| parameter	id	value	unit
Resistance	RL	69	mΩ
Inductance	L	4.15	μH
Turn to turn capacitance	Ctt	13.73	pF
Turn to shield capacitance	Cts	3.04	pF
Impedance	ZL	26.1	Ω
Simulated effective resistance	Re	69	mΩ
Simulated effective inductance	Le	4.2	μH
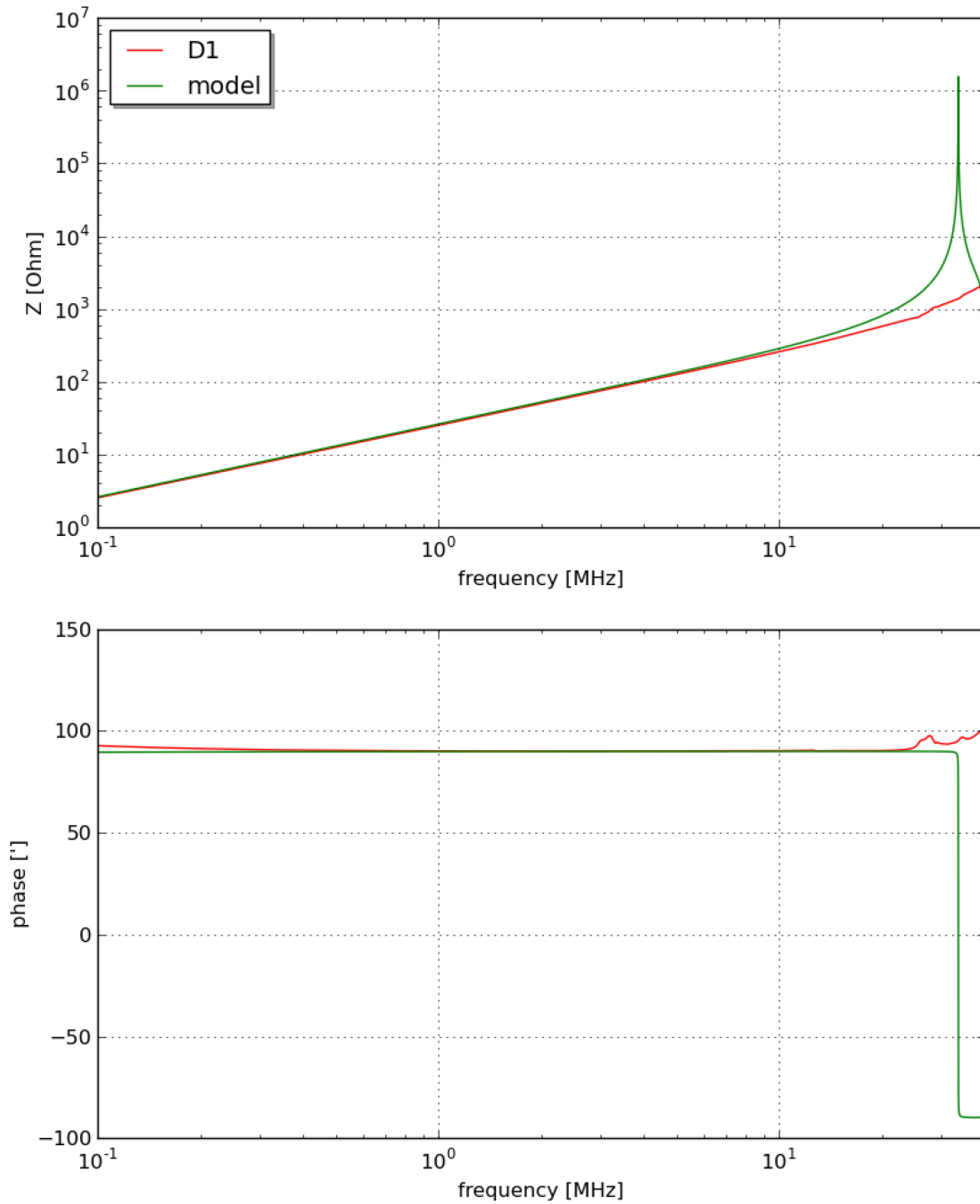
Figure 7-18 - Impedance of inductor D, measured (red), simulated (green)

Table 7-22 - Electrical parameters of inductor D

parameter	id	Measured @ 4.64 MHz	Simulated @ 4.64 MHz	unit
Impedance	ZL	124.9	123.2	Ω
Effective resistance	Re	217	154	mΩ
Effective inductance	Le	4.29	4.2	µH

PICTURE NOT AVAILABLE
(The coil has been disassembled)

Figure 7-19 - Sample inductor E

Table 7-23 - Inductor E geometry

parameter	Id	value	unit
Coil diameter	D	0.16	m
Conductor radius	rc	0.0004	m
Pitch	p	0.005	m
Number of turns	n	24	-
resistivity	ro	1.7E-8	Ωm

Table 7-24 - Calculated electrical parameters at 1 MHz of inductor E

parameter	id	value	unit
Resistance	RL	1433	mΩ
Inductance	L	80	μH
Turn to turn capacitance	Ctt	5.56	pF
Turn to shield capacitance	Cts	3.04	pF
Impedance	ZL	514.0	Ω
Simulated effective resistance	Re	1498	mΩ
Simulated effective inductance	Le	81.8	μH
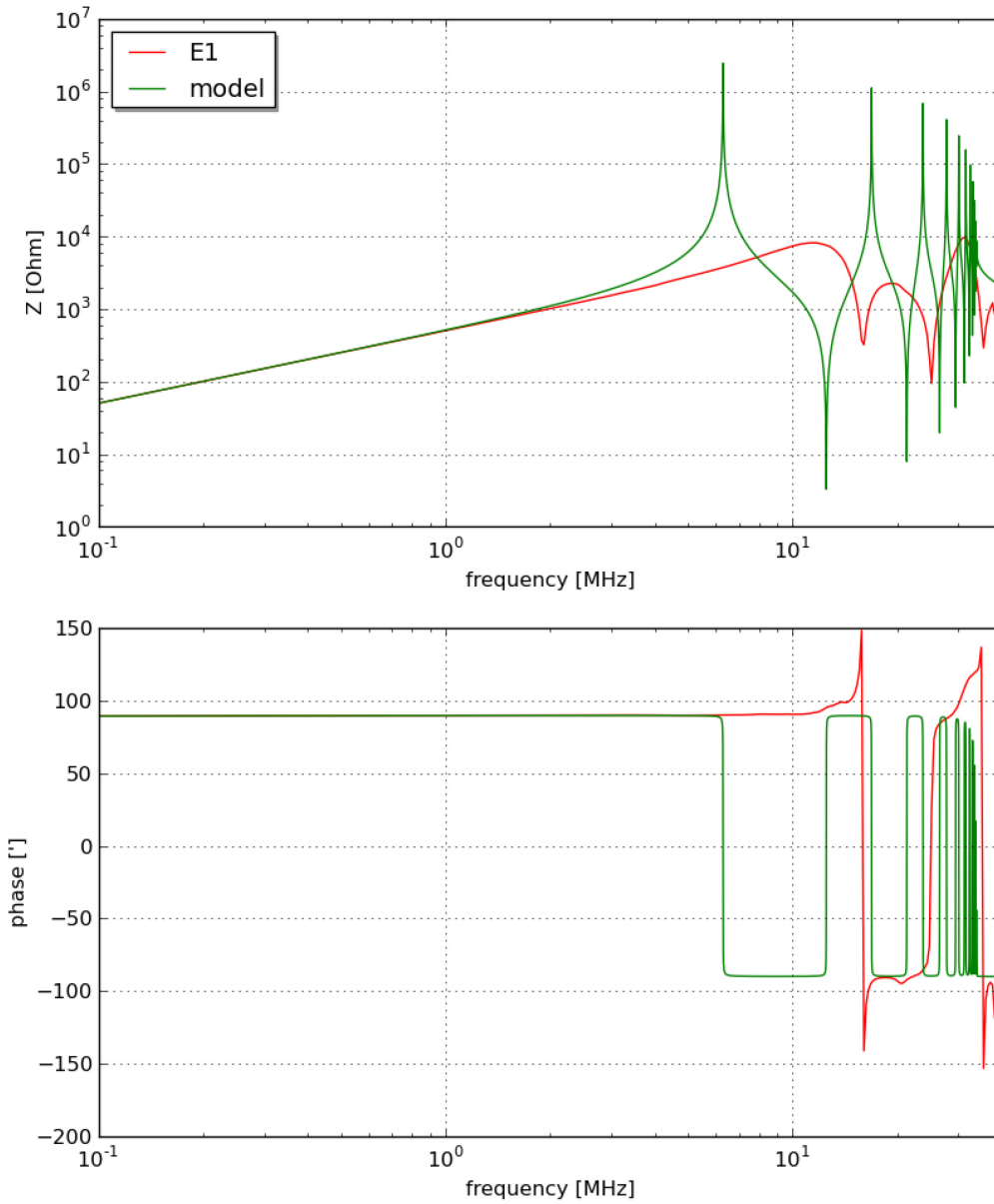
Figure 7-20 - Impedance of inductor E, measured (red), simulated (green)

Table 7-25 - Electrical parameters of inductor E

parameter	id	Measured @ 2.29 MHz	Simulated @ 2.29 MHz	unit
Impedance	ZL	505.2	514.0	Ω
Effective resistance	Re	n.a.	1498	mΩ
Effective inductance	Le	80.1	81.8	μH

The effective resistance derived from direct measurement is not available.

II.ii.i *Inductor F1*

Figure 7-21 - Sample inductor F1

Table 7-26 - Inductor F1 geometry

parameter	Id	value	unit
Coil diameter	D	0.16	m
Conductor radius	rc	0.0004	m
Pitch	p	0.01	m
Number of turns	n	10	-
resistivity	ro	1.7E-8	Ωm

Table 7-27 - Calculated electrical parameters at 1 MHz of inductor F1

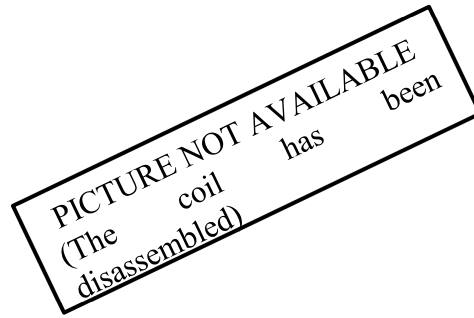| parameter	id	value	unit
Resistance	RL	576	mΩ
Inductance	L	17.1	µH
Turn to turn capacitance	Ctt	4.35	pF
Turn to shield capacitance	Cts	3.04	pF
Impedance	ZL	107.7	Ω
Simulated effective resistance	Re	579	mΩ
Simulated effective inductance	Le	17.1	µH
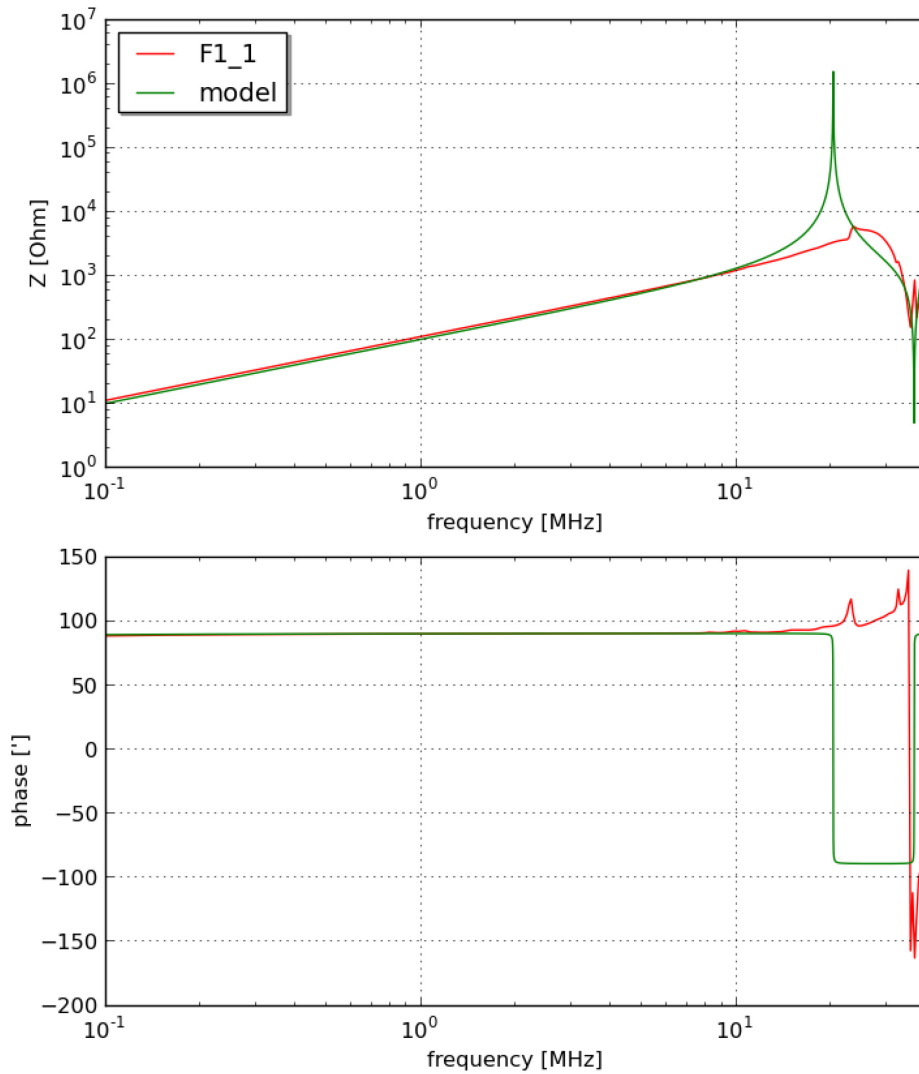
Figure 7-22 - Impedance of inductor F1, measured (red), simulated (green)

Table 7-28 - Electrical parameters of inductor F1

parameter	id	Measured @ 2.29 MHz	Simulated @ 2.29 MHz	unit
Impedance	ZL	252.7	249.2	Ω
Effective resistance	Re	974	872	mΩ
Effective inductance	Le	17.6	17.3	µH

II.ii.j   *Inductor F2*

The inductor F2 is composed of two insulated wires wound around the support without twisting them. The idea is to increase the equivalent cross section without increasing the turn to turn capacitance. The insulation is needed to avoid current exchange between the two coupled solenoids.

For F2 only the measurement results are reported since there is not a model for this type of inductor.
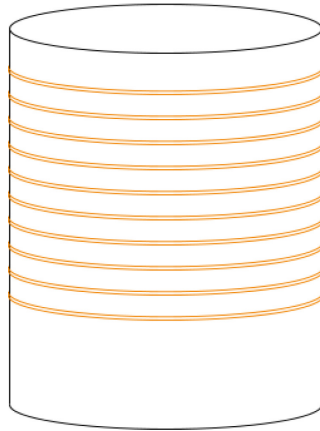
Figure 7-23 - Sample inductor F2

Table 7-29 - Inductor F2 geometry

parameter	Id	value	unit
Coil diameter	D	0.16	m
Conductor radius	rc	2x0.0004	m
Pitch	p	0.01	m
Number of turns	n	10	-
resistivity	ro	1.7E-8	Ωm

Table 7-30 - Calculated electrical parameters at 1 MHz of inductor F2

parameter	id	value	unit
Resistance	RL	n.a.	mΩ
Inductance	L	n.a.	μH
Turn to turn capacitance	Ctt	n.a.	pF
Turn to shield capacitance	Cts	n.a.	pF
Impedance	ZL	n.a.	Ω
Simulated effective resistance	Re	n.a.	Ω
Simulated effective inductance	Le	n.a.	μH
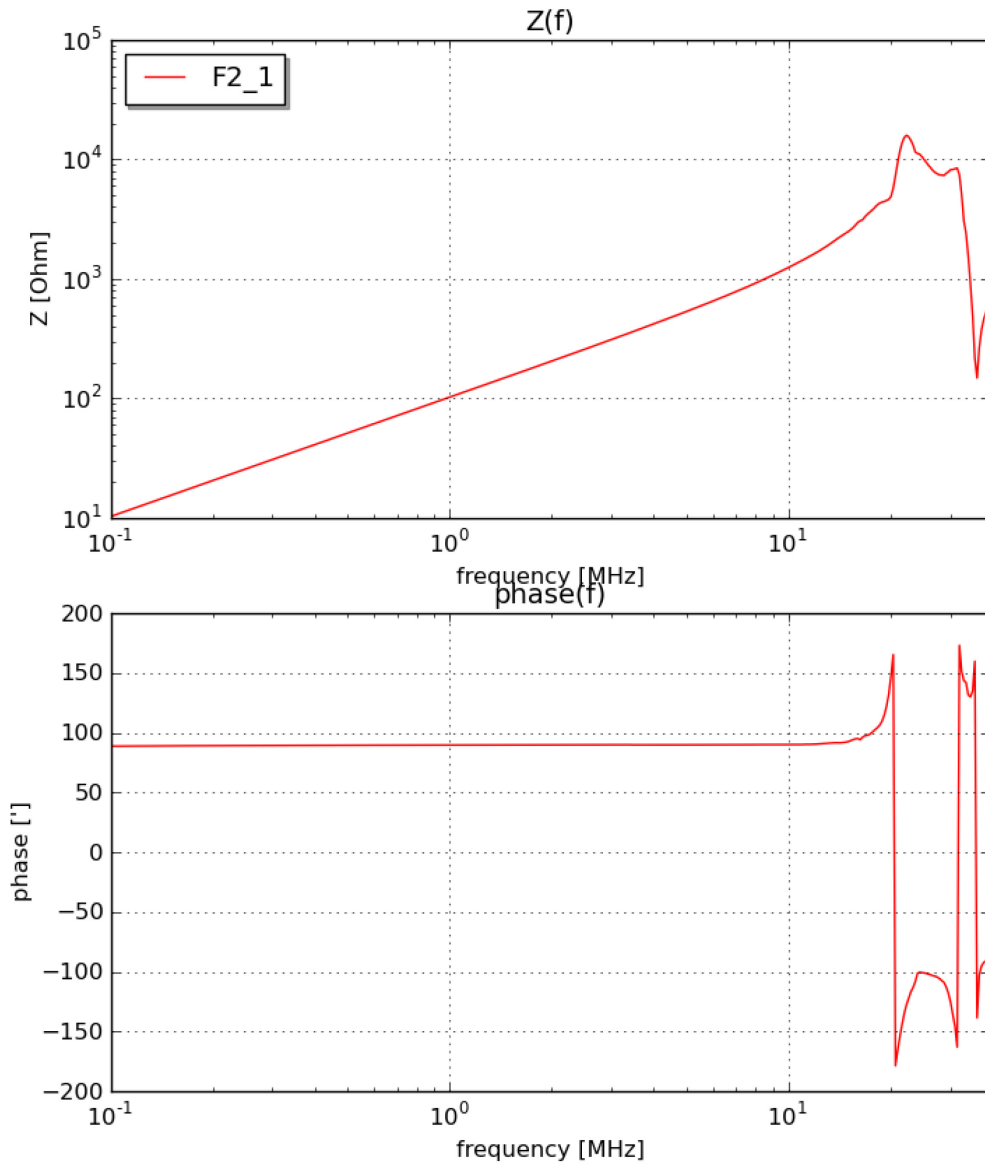
Figure 7-24 - Measurement of the impedance of inductor F2 (red)

Table 7-31 - Electrical parameters of inductor F2

parameter	id	Measured @ 2.33 MHz	Simulated	unit
Impedance	ZL	248.5	n.a.	Ω
Effective resistance	Re	581	n.a.	mΩ
Effective inductance	Le	17.0	n.a.	µH

The simulated electrical parameters are not available.

II.ii.k   *Inductor F4*

The inductor F4 is composed of four wires wound around the support without twisting them.

For F4 only the measurement results are reported since there is not a model for this type of inductor.

Figure 7-25 - Sample inductor F4

Table 7-32 - Inductor F4 geometry

parameter	Id	value	unit
Coil diameter	D	0.16	m
Conductor radius	rc	4x0.0004	m
Pitch	p	0.01	m
Number of turns	n	10	-
resistivity	ro	1.7E-8	Ωm

Table 7-33 - Calculated electrical parameters at 1 MHz of inductor F4

parameter		id	value	unit
Resistance		RL	n.a.	mΩ
Inductance		L	n.a.	μH
Turn to turn capacitance		Ctt	n.a.	pF
Turn to shield capacitance		Cts	n.a.	pF
Impedance		ZL	n.a.	Ω
Simulated effective resistance		Re	n.a.	Ω
Simulated effective inductance		Le	n.a.	μH
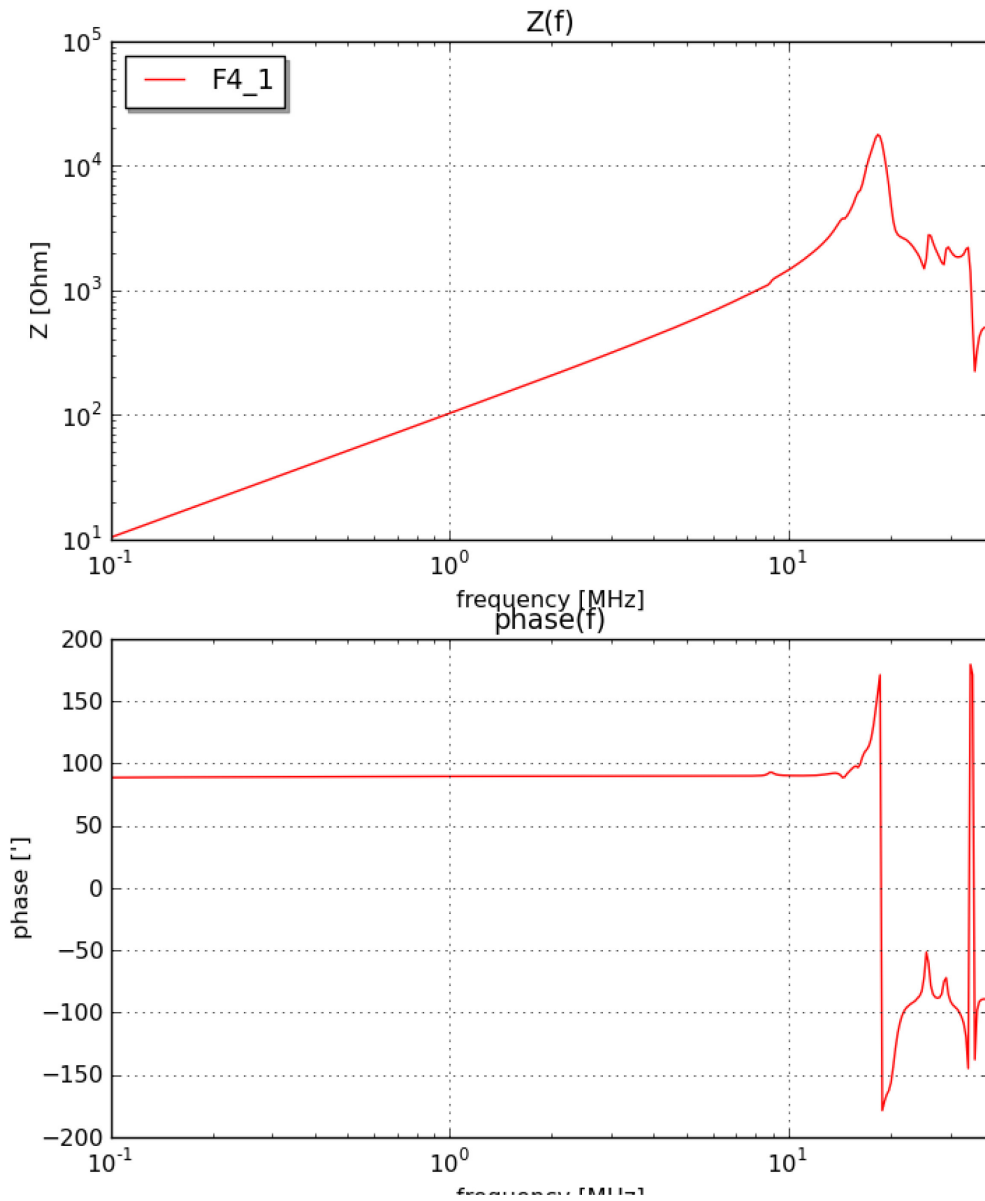
Figure 7-26 - Measurement of the impedance of inductor F4 (red)

Table 7-34 - Electrical parameters of inductor F4

parameter	id	Measured @ 2.38 MHz	Simulated	unit
Impedance	ZL	243.7	n.a.	Ω
Effective resistance	Re	427	n.a.	mΩ
Effective inductance	Le	16.3	n.a.	μH

The simulated electrical parameters are not available.

II.ii.1 *Inductor G*

For inductor G only the measured results are reported since there is not a model for this type of inductor. In fact it is based on litz wire (individually insulated wires twisted in a strand), which should allow a reduction of the ratio between the resistance at high frequency and the dc resistance.

Figure 7-27 - Sample inductor G

Table 7-35 - Inductor G geometry

parameter	Id	Value	unit
Coil diameter	D	0.49	m
Equivalent conductor radius	rc	0.0017	m
Pitch	p	0.03	m
Number of turns	n	13	-
resistivity	ro	1.7E-8	Ωm

Table 7-36 - Calculated electrical parameters at 1 MHz of inductor G

parameter	id	value	unit
Resistance	RL	n.a.	mΩ
Inductance	L	n.a.	μH
Turn to turn capacitance	Ctt	n.a.	pF
Turn to shield capacitance	Cts	n.a.	pF
Impedance	ZL	n.a.	Ω
Simulated effective resistance	Re	n.a.	Ω
Simulated effective inductance	Le	n.a.	μH
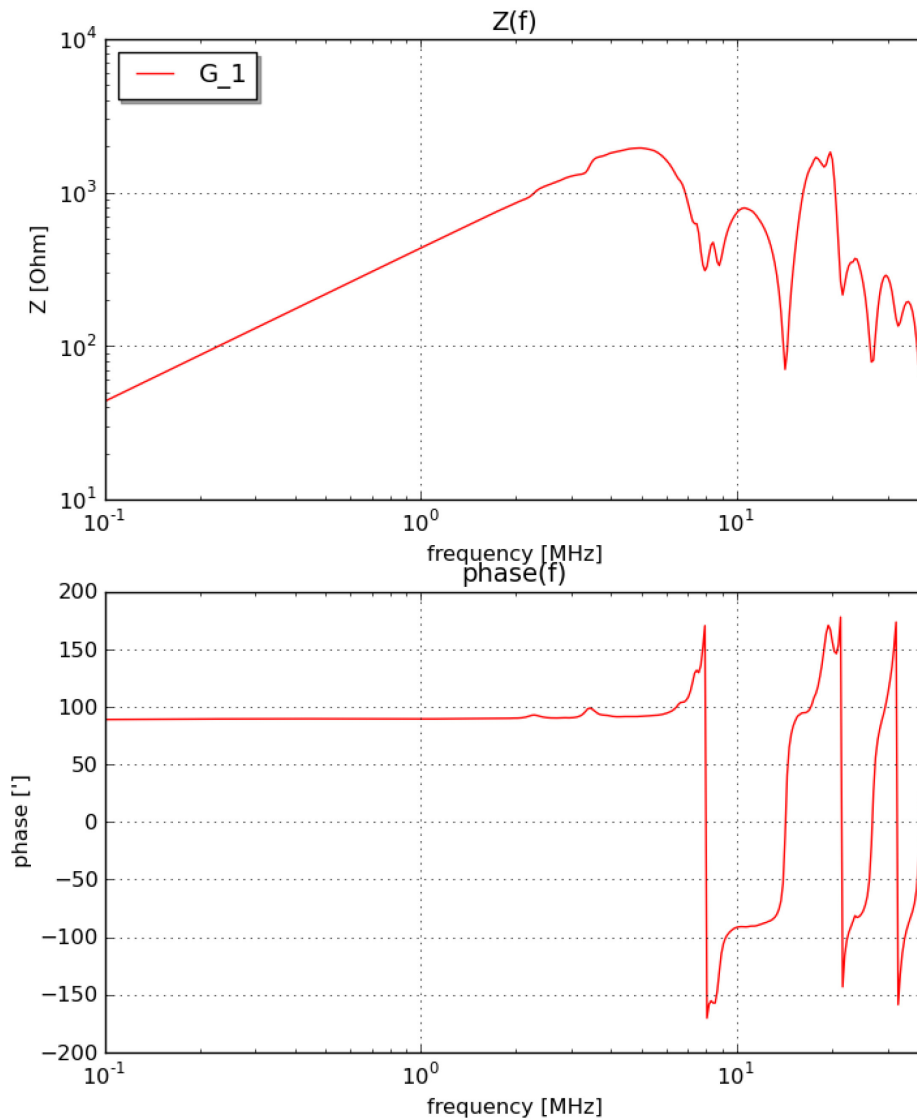
Figure 7-28 - Measurement of the impedance of inductor G (red)

Table 7-37 - Electrical parameters of inductor G

parameter	id	Measured @ 1.09 MHz	Simulated	unit
Impedance	ZL	529.7	n.a.	Ω
Effective resistance	Re	2168	n.a.	mΩ
Effective inductance	Le	77.1	n.a.	μH

The simulated electrical parameters are not available.

II.ii.m *Inductor H*

For inductor H only the measured results are reported since there is not a model for this type of inductor. This inductor is made of a copper braid of rectangular cross section wound on a wood support.

The use of rectangular cross section should reduce turn to turn capacitance with respect to a circular cross section.

Figure 7-29 - Sample inductor H

Table 7-38 - Inductor H geometry

parameter	Id	Value	unit
Coil diameter	D	0.49	m
Equivalent conductor radius	rc	0.007	m
Pitch	p	0.045	m
Number of turns	n	9	-
resistivity	ro	1.7E-8	Ωm

Table 7-39 - Calculated electrical parameters at 1 MHz of inductor H

parameter	id	value	unit
Resistance	RL	n.a.	mΩ
Inductance	L	n.a.	μH
Turn to turn capacitance	Ctt	n.a.	pF
Turn to shield capacitance	Cts	n.a.	pF
Impedance	ZL	n.a.	Ω
Simulated effective resistance	Re	n.a.	Ω
Simulated effective inductance	Le	n.a.	μH
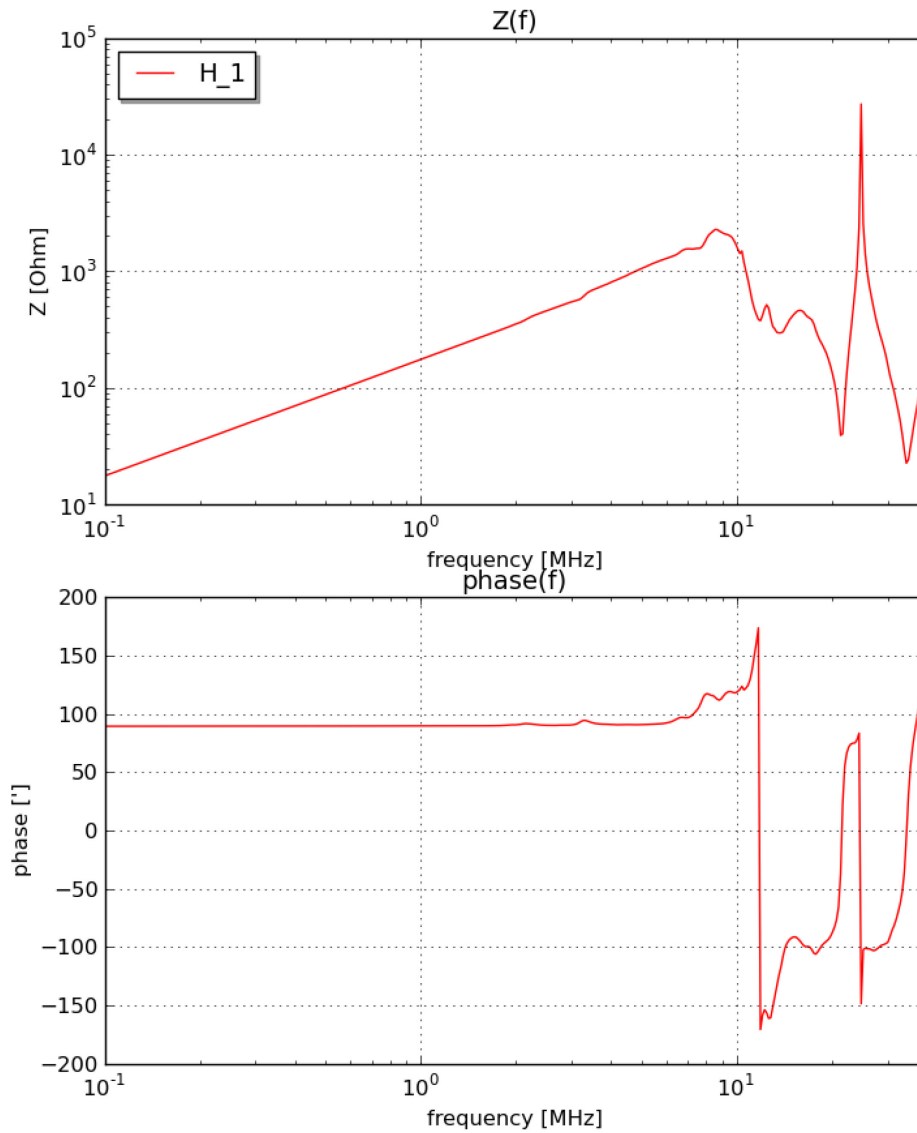
Figure 7-30 - Measurement of the impedance of inductor H (red)

Table 7-40 - Electrical parameters of inductor H

parameter	id	Measured @ 1.7 MHz	Simulated	unit
Impedance	ZL	340.4	n.a.	Ω
Effective resistance	Re	760	n.a.	mΩ
Effective inductance	Le	31.9	n.a.	μH

The simulated electrical parameters are not available.

II.iii Summary and comments

The geometry of the inductors which have been tested is summarized in Table 7-41 and plotted in Figure 7-31.

Table 7-41 - Geometry of the tested inductors

| Inductor	n	p	rc	D	L	note
	-	[m]	[m]	[m]	[m]	
1	22	0,000908	0,00045	0,022	0.039	
2	35	0,006	0,00045	0,0475	0.236	
3	22	0,000908	0,00045	0,0475	0.039	
A	5	0,018	0,003	0,142	0.102	
B	43	0,007	0,0025	0,11	0.509	
C	9	0,01625	0,005	0,255	0.220	
D	5	0,008	0,003	0,125	0.062	
E	24	0,005	0,0004	0,1604	0.134	
F1	10	0,01	0,0004	0,16	0.098	
F2	10	0,01	0,0004	0,16	0.098	2 coupled insulated solenoids
F4	10	0,01	0,0004	0,16	0.098	4 coupled insulated solenoids
G	13	0,02	0,004	0,49	0.344	Litz wire
H	9	0,01	0,006	0,49	0.504	rectangular conductor (0.003 m x 0.035 m)
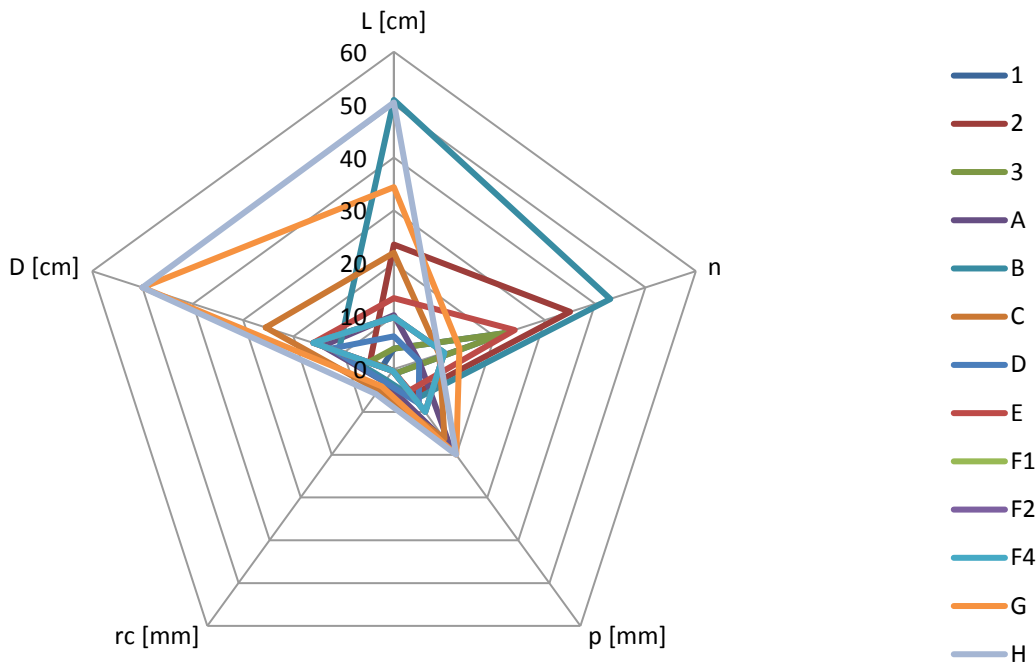
Figure 7-31 - Geometry of the tested inductors

As can be seen from Figure 7-31 the geometrical parameters of the coils cover a wide range of size, except the radius of the conductor.

A quantitative comparison between model and measures is summarized in Table 7-42, Table 7-43, Table 7-44, Table 7-45; the relative difference is plotted in Figure 7-32 as a function of the ratio coil length/coil diameter and in Figure 7-33 as a function of the number of turns.

The measurement is taken as reference and the model result is subtracted in the calculation of Δ.

Table 7-42 - Summary: Effective impedance [Ω] at 1 MHz

Inductor	Model	Measured	Δ	%
1	45.5	46.0	-0.5	-1.1
2	84.4	77.3	7.1	9.2
3	164.5	162.0	2.5	1.5
A	23.2	21.4	1.8	8.7
B	411.3	361.7	49.6	13.7
C	129.4	123.8	5.6	4.5
D	26.1	24.8	1.3	5.4
E	514	505.2	8.8	1.7
F1	107.7	105.5	2.2	2.1

Table 7-43 - Summary: Effective inductance [μH] at 1 MHz

Inductor	Model	Measured	Δ	%
1	7.2	7.3	-0.1	-1.2
2	13.4	12.2	1.2	9.5
3	26.2	26.0	0.2	0.9
A	3.7	3.4	0.3	9.0
B	65.5	57.5	8.0	13.9
C	20.6	19.7	0.9	4.6
D	4.2	3.9	0.3	6.7
E	81.8	80.0	1.8	2.3
F1	17.1	16.8	0.3	1.9

Table 7-44 - Summary: Effective resistance [mΩ]

Inductor	f [MHz]	Model	Measured	Δ	%
1	n.a	-	n.a	-	-
2	n.a	-	n.a	-	-
3	n.a	-	n.a	-	-
A	5.1	91	143	-52	-36.4
B	1.2	682	616	66	10.7
C	2.1	179	357	-178	-49.9
D	4.6	154	217	-63	-29.0
E	n.a.	-	n.a.	-	-
F1	2.3	872	973.9	-101.9	-10.5

Table 7-45 - Summary: natural resonance frequency [MHz]

Inductor	Model	Measured	Δ	%
1	>40	>40	-	-
2	23.3	38.3	-15	-39.2
3	19.6	25.9	-6.3	-24.3
A	>40	>40	-	-
B	5.69	14.1	-8.41	-59.6
C	11.3	20	-8.7	-43.5
D	33.4	>40	-	-
E	6.3	15.8	-9.5	-60.1
F1	19.1	35.5	-16.4	-46.2
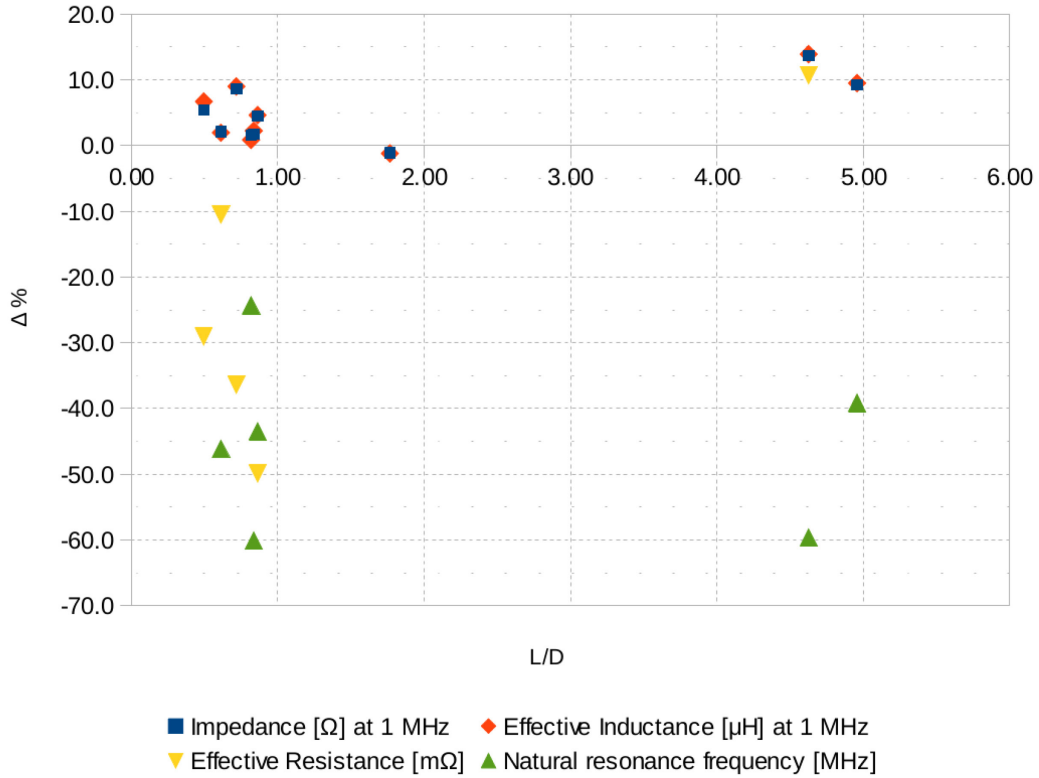
Figure 7-32 - Relative difference between model and measures as a function of the ratio coil length/coil diameter
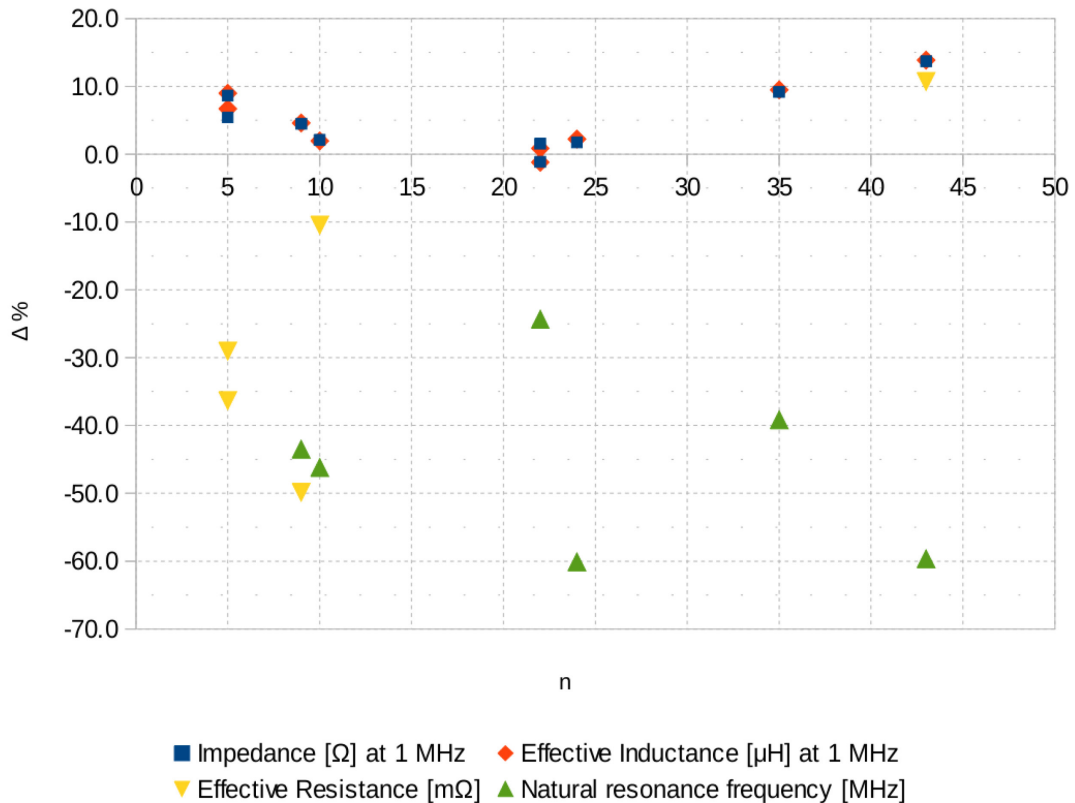
Figure 7-33 - Relative difference between model and measures as a function number of turns

The ratio length/diameter L/D for a coil expresses if it is relatively "short" or "long".

The model predicts the impedance and the inductance with a relative error lower than 10% for short coils, while it is below 15 % for long coils.

There is a correlation (direct proportionality) between the L/D and the ability of the model to estimate the resistance. In particular for "short" coils the model underestimates the resistance, while for long coils the model predicts higher values with respect to the one measured.

There is a similar correlation to the number of turns.

For the natural resonance frequency the model always predicts frequencies which are about half with respect to the measured one; this is due to the fact that the model overestimates the stray capacitances.

The model of the solenoid gives anyway good results for the frequencies near to 1 MHz, which is the operating frequency of the matching resonant circuit, as far as the inductance and impedance is concerned.

The calculation of the resistance is still far from the measured one (the maximum error is 50%), but the measurements may also be affected by the connections to the impedance meter.

The model predicts multiple natural resonance frequencies as found experimentally, even if not at the right frequency.

II.iv Litz wire

The litz wire (LW) is made by twisting a big amount of thin (with respect to the skin depth penetration at the operating frequency) coated insulated wires in order to push the current to flow in the entire cross section of the LW. The final effect of this assembly procedure is the reduction of the equivalent resistance of the wire with respect to a conductor with same cross section.

The datasheet of the litz wire available at Consorzio RFX presents the following characteristics:

- Strand of 1200 filaments of 0.1 mm diameter;
- dc resistance p.u.l.: 1.8 mΩ/m (calculated with $\rho = 1.7 \ 10^{-8}$ Ωm);
- dc resistance: 36.1 mΩ (calculated);

The ratio between the resistance measured at 1.09 MHz and the calculated dc resistance is 60.

This ratio is not so far from the one obtained with the copper tube used for inductor C, in fact at 2.11 MHz the ratio is about 94, which scaled to 1 MHz (with the square root of the frequency) is about 65.

II.v Squared cross section wire

The use of a squared cross section wire for winding a coil reduces the facing area between turns at equal cross section, compared to a circular cross section. The reduction of facing area, with the same air gap, results in the reduction of the turn to turn stray capacitance, which affects the resistance of the coil at high frequency.

The characteristics of the wire are:

- Cross section: 1.4 10^{-4} m^2;
- dc resistance p.u.l.: 0.121 mΩ/m (calculated with $\rho = 1.7 \ 10^{-8}$ Ωm);
- dc resistance: 1.68 mΩ (calculated);

The ratio between the resistance measured at 1.7 MHz and the calculated dc resistance is 440.

The results on inductor H are not satisfactory.

II.vi *"Coupled solenoids" inductors*

This paragraph summarizes the studies and the experimental verification of the opportunity to wound many inductors with same inductance and inserted in a circuit where they are mutually coupled and electrically paralleled. The aim is to decrease the overall resistance without changing the value of the inductance seen from the circuit. It will be clear that this behaviour is respected if the current sharing among the inductors is good and other major effects do not appear.
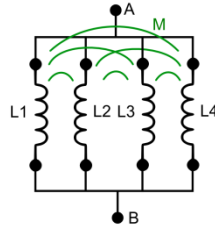
Figure 7-34 – "Coupled solenoids" inductors scheme (no parasitic elements)

Three inductors called F1, F2, F4 have been prepared:
- F1 is the inductor with only one wire wound on a support,
- F2 is the inductor with two wires;
- F4 is the inductor with four wires.

Each inductor has been tested to characterize the impedance as a function of frequency and the resistance with the resonant circuit as described in II.i.
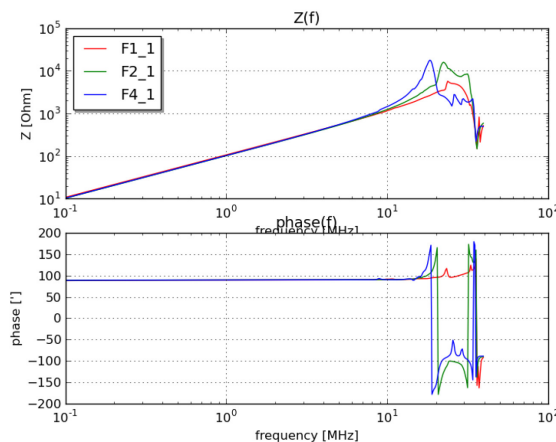
Figure 7-35 - Impedance of the "coupled solenoids" inductors
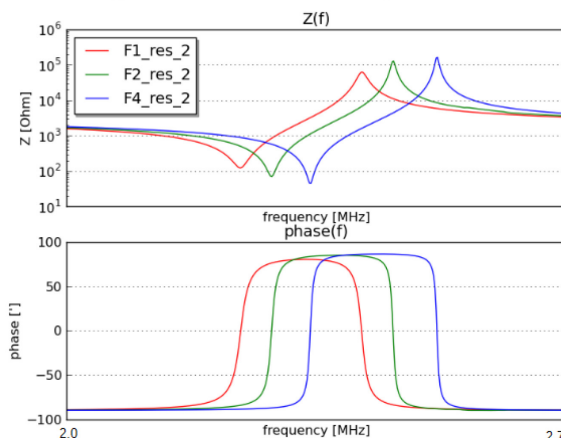
Figure 7-36 - Impedance seen at the input of the resonant circuit

As can be appreciated from Figure 7-35 the inductance is almost the same for the three inductors, while from figure Figure 7-36 the resistance seen from the input of the resonant circuit (at the resonance frequency) decreases: the value is lower and the bandwidth is smaller for F4 than F2 and F1.

The values of the effective inductance L_e and effective resistance R_e of the three inductors has been calculated taking into account the effect of the capacitors used in the resonant circuit; the results are shown in Figure 7-37.
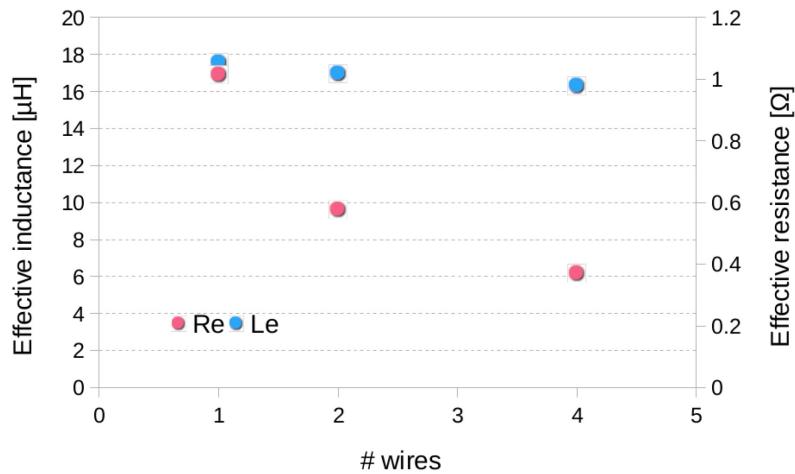
Figure 7-37 - Inductance and resistance of the "coupled solenoids" inductors

The results are promising since there is a slight reduction on the inductance value while the resistance decreases, even if not linearly, increasing the number of wires; in particular the Q factor increases by a factor of 1.6 with just two wires and by a factor of 2 with four wires.

III HVRFTF inductor

The HVRFTF inductor is indicated as inductor "I" (capital "i") and it is composed of two solenoids called "I1" and "I2" electrically insulated, mutually coupled and with their terminals connected in parallel.

The aim of this configuration is to reduce the stray resistance, for a given inductance, thanks to the current sharing between the two inductors.

To characterize the inductor the following measurements were done with the inductor placed on a desk, far from conducting passive structures:

- Measure of the impedance of "I", "I1", "I2" with an impedance meter;
- Assessment of its stray resistance with a resonant circuit (see Appendix paragraph II.i).
-

III.i Measurement of the inductor impedance

III.i.a *Floating terminals*

The plots of the impedance (modulus and argument) of the inductor "I", solenoid "I1" and "I2" are shown in Figure 7-38.
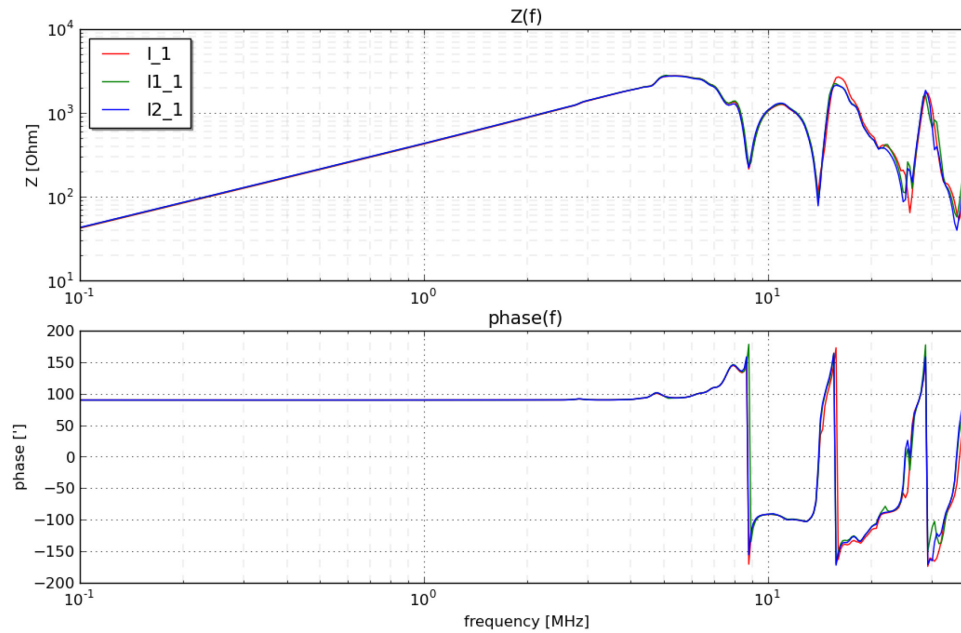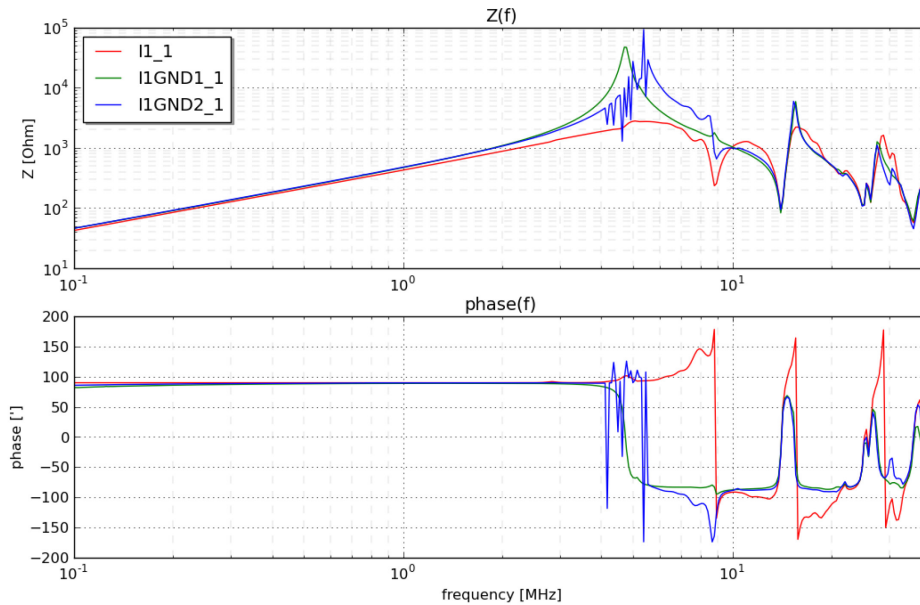

Figure 7-38: Measured impedance and argument of the inductor with floating terminals

Table 7-46 - Measured impedance and inductance with floating terminals

Inductor	Natural resonance frequency [MHz]	Impedance [Ω] @ 1 MHz	Inductance [µH] @ 1MHz
I1	8.9	416.1	66.2
I2	8.8	418.5	66.6
I (I1 and I2 in parallel)	8.9	410.7	65.4

The plots of the impedance (modulus and argument) of the solenoid "I1" with floating terminals (red curve) and with one terminal grounded (green curve top terminal grounded, blue curve bottom terminal grounded) are shown in Figure 7-39.

Figure 7-39: Measured impedance and argument of the solenoid I1 with floating terminals (red curve), with top terminal grounded (green curve) and with bottom terminal grounded (blue curve)
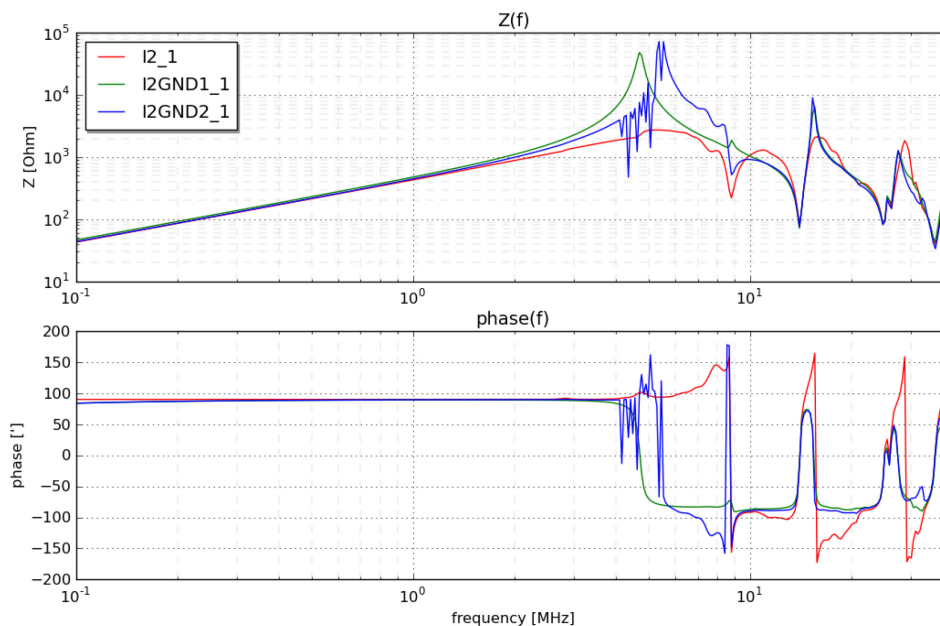
The plots of the impedance (modulus and argument) of the solenoid "I2" with floating terminals (red curve) and with one terminal grounded (green curve top terminal grounded, blue curve bottom terminal grounded) are shown in Figure 7-39.

Figure 7-40: Measured impedance and argument of the solenoid I2 with floating terminals (red curve), with top terminal grounded (green curve) and with bottom terminal grounded (blue curve)

The plots of the impedance (modulus and argument) of the inductor "I" with floating terminals (red curve) and with one terminal grounded (green curve top terminal grounded, blue curve bottom terminal grounded) are shown in Figure 7-41.
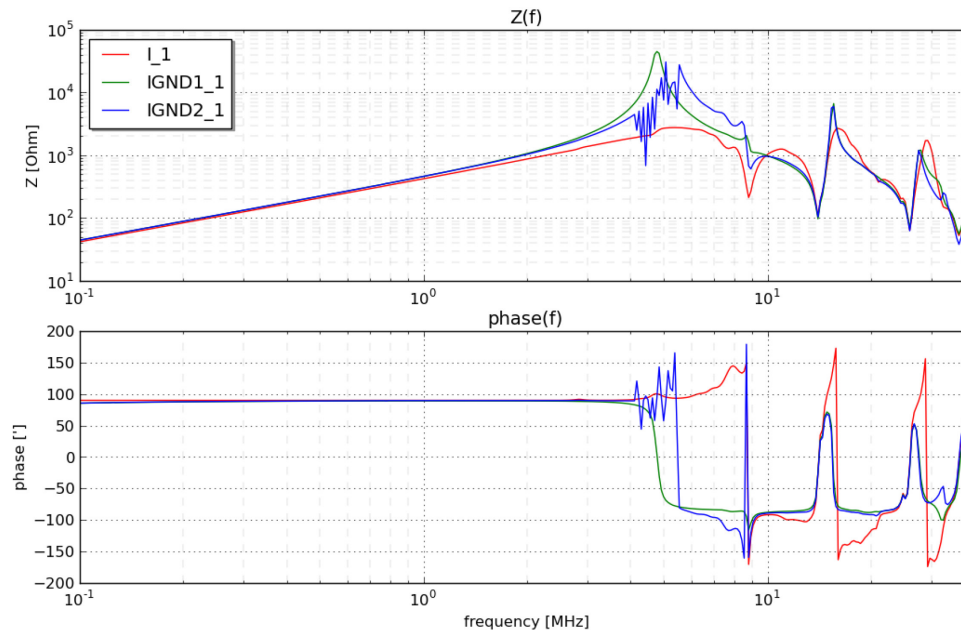

Figure 7-41: Measured impedance and argument of the inductor "I" with floating terminals (red curve), with top terminal grounded (green curve) and with bottom terminal grounded (blue curve)

The summary of the measurements are reported in Table 7-47:

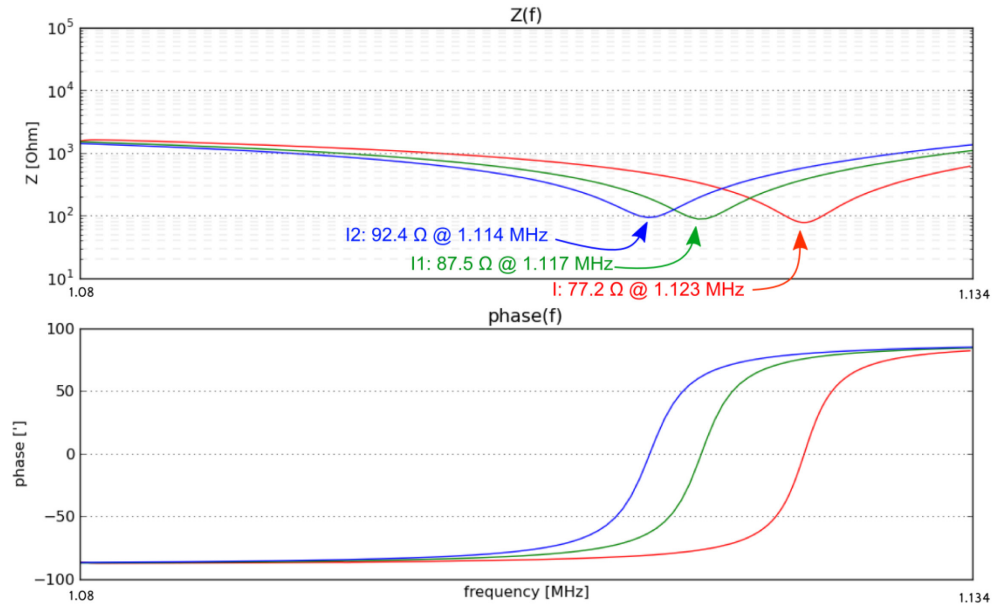**Table 7-47 - Measured impedance and inductance with a grounded terminal**

Inductor	Natural resonance frequency [MHz]	Impedance [Ω] @ 1 MHz	Inductance [µH] @ 1MHz
I1 Top terminal grounded	4.7	451.6	71.9
I1 Bottom terminal grounded	5.5	470.0	74.8
I2 Top terminal grounded	4.7	454.2	72.3
I2 Bottom terminal grounded	5.5	462.0	73.5
I (I1 and I2 in parallel) Top terminal grounded	4.7	462.2	73.6
I Bottom terminal grounded	5.4	460.0	73.2

The inductance of the inductor "I" have an increment of 7.8-8.2 µH, corresponding to 12-12.5 %, with respect to the inductance shown with floating terminals.

III.ii Evaluation of the inductor stray resistance
III.ii.a *Floating terminals*
The impedance meter has been connected to the port AB of the circuit of Appendix paragraph II.i, the measured impedance is reported in Figure 7-42, the resulting parameters are listed in Table 7-48.

Figure 7-42: Measured Impedance and Phase seen from port AB with floating terminals

Table 7-48 – Inductor "I" characteristics with floating terminals

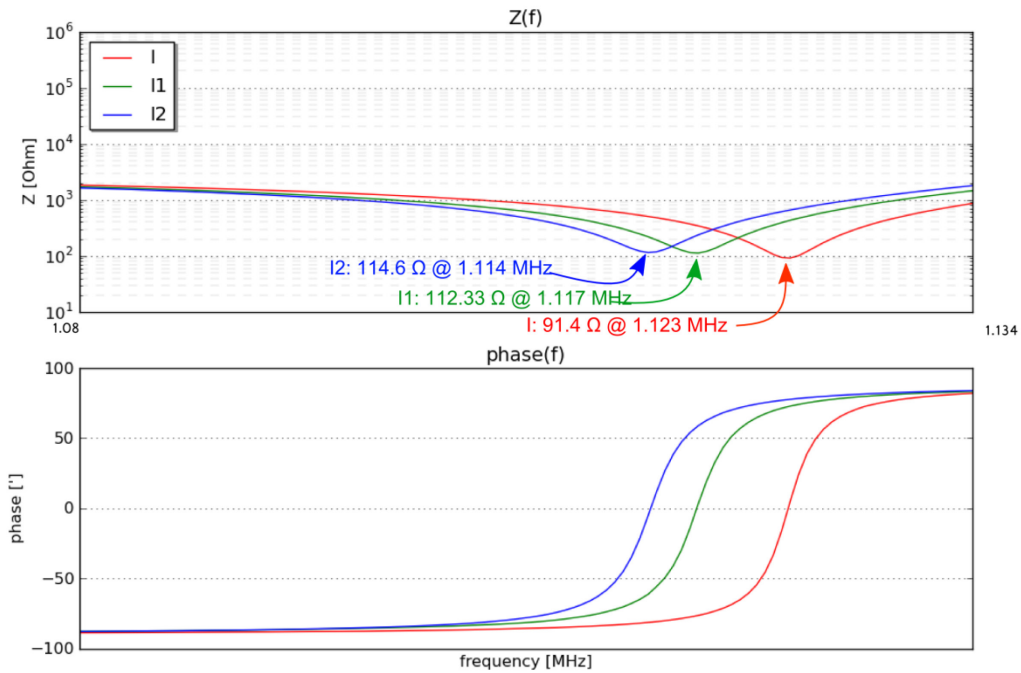| Circuit	Resonance frequency (fr) [MHz]	Input Impedance [Ω] / argument [°] @ fr	Inductance of [µH] @ fr	Resistance [Ω] @ fr
Resonant circuit with I1	1.117	87.8 (∟-7.35°)	72.5	0.86
Resonant circuit with I2	1.114	93.0 (∟-1.43°)	72.9	0.92
Resonant circuit with I (I1 and I2 in parallel)	1.123	77.3 (∟-7.36°)	71.7	0.76

The inductance value derived from the measurement with the resonant circuit is higher than the value derived from the direct measurement on the inductor alone: about 72 µH versus 66 µH.
The resistance value is similar for I1 and I2, it slightly decreases when the two solenoids are connected in parallel.

III.iii Grounded bottom terminal
Only the measurements with bottom terminal grounded are reported in this paragraph, since in the actual circuit the bottom terminal of the inductor is grounded.
The impedance meter has been connected to the port AB of the circuit of Appendix paragraph II.i, the measured impedance is reported in Figure 7-42 and the resulting parameters are listed in Table 7-49.

138

Figure 7-43: Measured Impedance and Phase seen from port AB with grounded terminal

Table 7-49 – Inductor "I" characteristics with grounded terminal

Circuit	Resonance frequency (fr) [MHz]	Impedance [Ω] / argument [°] @ fr	Inductance of [µH] @ fr	Resistance [Ω] @ fr
Resonant circuit with I1	1.117	112.3	72.6	1.10
Resonant circuit with I2	1.114	114.6	72.9	1.13
Resonant circuit with I (I1 and I2 in parallel)	1.123	91.4	71.8	0.90

In this case (with the bottom terminal grounded, corresponding to the point of the circuit which is grounded by the voltage source) the inductance value derived from the measurement with the resonant circuit is similar to the value derived from the measurement on the inductor alone: about 72 µH.

The resistance value is similar for I1 and I2, it slightly decreases when the two solenoids are connected in parallel. With a grounded terminal the resistance of the inductor "I" increases of about 18 % with respect to the case of floating terminals

139

III.iv Summary of the results

Table 7-50 list the summary of the results of the measures on inductor "I"

Table 7-50 - Summary of the results of inductor "I"

Inductor	Inductance measured directly L [µH] @ 1 MHz	Resistance RL [Ω] @ fr
I1 Floating terminals	66.2	0.86
I2 Floating terminals	66.6	0.92
I Floating terminals	65.4	0.76
I1 bottom terminal grounded	74.8	1.10
I2 bottom terminal grounded	73.5	1.13
I bottom terminal grounded	73.2	0.90

The inductance value derived from direct measure on the inductor with floating terminals is lower than the inductance value derived from the measurement on the resonant circuit with floating terminals. The difference is about 9%. However, no significant difference is observed between the two inductance values when one of the terminals is grounded.

The measured inductance of the two solenoids I1 and I2 is similar and it is similar to the inductance of the inductor "I", in the same conditions.

Ringraziamenti

Dopo 4 anni densi e sofferti, i miei più sentiti ringraziamenti:
A Grazia e alla mia famiglia.
A chi mi è sempre stato vicino.
A chi ha saputo lasciarmi spazio.
A chi mi ha supportato moralmente e sopportato.
A chi ha letto e rivisto il lavoro di analisi e progetto.
A chi a contribuito con il proprio impegno a mettere in piedi e operare la test facility.
A chi mi ha regalato ore di svago.
A chi apprezza quello che fa.
A chi dà.
A chi ha il coraggio di cambiare.
A chi critica per migliorare.
A chi si impegna per migliorare.